NAVAL POSTGRADUATE SCHOOL

MONTEREY, CALIFORNIA

DISSERTATION

A PERSONAL NAVIGATION SYSTEM BASED ON INERTIAL AND MAGNETIC FIELD MEASUREMENTS

by

James Calusdian

September 2010

Dissertation Supervisor: Xiaoping Yun

THIS PAGE INTENTIONALLY LEFT BLANK

REPORT DOCUMENTATION PAGE		*Form Approved OMB No. 0704-0188*

1. AGENCY USE ONLY *(Leave blank)*	2. REPORT DATE September 2010	3. REPORT TYPE AND DATES COVERED Dissertation

4. TITLE AND SUBTITLE: A Personal Navigation System Based on Inertial and Magnetic Field Measurements	5. FUNDING NUMBERS
6. AUTHOR(S) James Calusdian	

7. PERFORMING ORGANIZATION NAME(S) AND ADDRESS(ES) Naval Postgraduate School Monterey, CA 93943-5000	8. PERFORMING ORGANIZATION REPORT NUMBER

9. SPONSORING / MONITORING AGENCY NAME(S) AND ADDRESS(ES) N/A	10. SPONSORING / MONITORING AGENCY REPORT NUMBER

11. SUPPLEMENTARY NOTES The views expressed in this thesis are those of the author and do not reflect the official policy or position of the Department of Defense or the U.S. Government. IRB Protocol Number: _____N/A_____.

12a. DISTRIBUTION / AVAILABILITY STATEMENT Approved for public release; distribution is unlimited	12b. DISTRIBUTION CODE

13. ABSTRACT (maximum 200 words)

This work describes the development and testing of a personal navigation system (PNS) for use during normal walking on level ground surfaces. A shoe-worn miniature inertial/magnetic measurement unit (IMMU), which is comprised of accelerometers, magnetometers, and angular rate sensors, provides the measurement data for the PNS algorithm. The well-known strapdown navigation algorithm is adapted for use in the PNS, which further incorporates the error correction technique commonly referred to as zero-velocity updates. A gait-phase detection algorithm estimates instances of foot stance and swing and establishes the appropriate times to apply the velocity error correction technique within the PNS algorithm.

A main contribution of the work described herein pertains to the design and analysis of a quaternion-based complementary filter for estimation of three-dimensional attitude of the IMMU. This complementary filter algorithm builds on an earlier three-dimensional attitude estimator known as the Factored Quaternion Algorithm (FQA). The complementary filter is further tailored for the PNS application through the use of an adaptive gain switching strategy based on knowledge of the gait phase.

A novel and incidental effort described here pertains to the design and implementation of a locomotion interface for a virtual environment using the shoe-worn IMMU. In this application, one IMMU is worn on each foot. A set of foot gestures was conceived and a custom software program was developed to decode the user's foot motions. This unique interface gives the user freedom to navigate through a virtual environment in any direction he/she chooses for those applications utilizing large-screen displays.

14. SUBJECT TERMS personal navigation, accelerometer, magnetometer, angular rate sensor, quaternion, complementary filter, zero-velocity update, gait-phase detection algorithm	15. NUMBER OF PAGES 235
	16. PRICE CODE

17. SECURITY CLASSIFICATION OF REPORT Unclassified	18. SECURITY CLASSIFICATION OF THIS PAGE Unclassified	19. SECURITY CLASSIFICATION OF ABSTRACT Unclassified	20. LIMITATION OF ABSTRACT UU

THIS PAGE INTENTIONALLY LEFT BLANK

**A PERSONAL NAVIGATION SYSTEM BASED ON
INERTIAL AND MAGNETIC FIELD MEASUREMENTS**

James Calusdian
Civilian, United States Navy
B.S., California State University–Fresno, 1988
M.S., Naval Postgraduate School, 1998

Submitted in partial fulfillment of the
requirements for the degree of

DOCTOR OF PHILOSOPHY IN ELECTRICAL ENGINEERING

from the

**NAVAL POSTGRADUATE SCHOOL
September 2010**

Author: _____

James Calusdian

Approved by:

_____   _____

Xiaoping Yun   Carlos F. Borges
Professor of Electrical   Professor of Mathematics
& Computer Engineering
Dissertation Committee Chair

_____   _____

David C. Jenn   Harold Titus
Professor of Electrical   Professor Emeritus of Electrical
& Computer Engineering   & Computer Engineering

_____

Murali Tummala
Professor of Electrical and Computer Engineering

Approved by: _____

R. Clark Robertson, Chairman, Department of Electrical & Computer
Engineering

Approved by: _____

Douglas Moses, Vice Provost for Academic Affairs

THIS PAGE INTENTIONALLY LEFT BLANK

ABSTRACT

This work describes the development and testing of a personal navigation system (PNS) for use during normal walking on level ground surfaces. A shoe-worn miniature inertial/magnetic measurement unit (IMMU), which is comprised of accelerometers, magnetometers, and angular rate sensors, provides the measurement data for the PNS algorithm. The well-known strapdown navigation algorithm is adapted for use in the PNS, which further incorporates the error correction technique commonly referred to as zero-velocity updates. A gait-phase detection algorithm estimates instances of foot stance and swing and establishes the appropriate times to apply the velocity error correction technique within the PNS algorithm.

A main contribution of the work described herein pertains to the design and analysis of a quaternion-based complementary filter for estimation of three-dimensional attitude of the IMMU. This complementary filter algorithm builds on an earlier three-dimensional attitude estimator known as the Factored Quaternion Algorithm (FQA). The complementary filter is further tailored for the PNS application through the use of an adaptive gain switching strategy based on knowledge of the gait phase.

A novel and incidental effort described here pertains to the design and implementation of a locomotion interface for a virtual environment using the shoe-worn IMMU. In this application, one IMMU is worn on each foot. A set of foot gestures was conceived and a custom software program was developed to decode the user's foot motions. This unique interface gives the user freedom to navigate through a virtual environment in any direction he/she chooses for those applications utilizing large-screen displays.

THIS PAGE INTENTIONALLY LEFT BLANK

TABLE OF CONTENTS

THIS PAGE INTENTIONALLY LEFT BLANK

LIST OF FIGURES

LIST OF TABLES

THIS PAGE INTENTIONALLY LEFT BLANK

EXECUTIVE SUMMARY

The art of navigation has existed in many forms for thousands of years. Early travelers used terrestrial waypoints and celestial bodies to explore vast distances. In modern times, the Global Positioning System, or GPS, has come to the forefront as one of the primary methods for navigation. Undoubtedly, GPS may be regarded as one of the most significant developments of the 20th century. Originally conceived and developed by the Department of Defense, GPS has been successfully integrated into navigation systems installed within aircraft, ships, submarines, and weapons of various types. It has also found many civilian applications, including a number of consumer products, such as cellular phones, automobiles, and personal navigation. In the latter, this term is meant to describe the tracking of one's position while the user moves about under his/her own locomotion (walking, running).

In spite of the many successful applications of GPS in land, sea, and air, the navigational aid has some considerations that limit its use. One of these deals with the reception of the essential signals from the system's orbiting satellites. Since it is necessary to receive signals from at least four GPS satellites to calculate position fixes, GPS-based positioning may not be possible at some locations. It has been widely established that places such as dense urban environments, valleys and canyons, and heavily forested regions suffer from occlusion problems. The GPS signal also is attenuated as it propagates through the exterior walls of building structures to the point that indoor navigation becomes difficult. Hostile or inadvertent radio-frequency jamming could also deny the user the proper reception of these essential GPS signals.

This work deals specifically with the development of a personal navigation system (PNS) for tracking one's position. It seeks to address the limitations of GPS for personal navigation through the use of inertial and magnetic measurements. Low cost, light weight, and low power devices, such as accelerometers, angular rate sensors, and magnetometers, have been integrated into commercially-available miniature modules. These inertial magnetic measurement units (IMMU), however, come with some disadvantages that limit their performance—namely, a significant amount of random

error (noise), which, in turn, affects their overall accuracy. Therefore, additional techniques and methods must be developed to expand the breadth of their utility.

With regard to the PNS application, which is to be presented within the body of this work, a navigation algorithm is developed. It requires that the IMMU be attached to the user's foot to provide measurements during normal walking motion. The algorithm is adapted from the familiar strapdown navigation algorithm and integrates the error-correction technique known as zero-velocity updates. This work also presents a gait-phase detection algorithm for identifying the two primary phases of the human walking cycle: the swing phase and the stance phase. The operation of the PNS algorithm requires knowledge of the walking state at any given time.

To determine the foot attitude during each iteration of the navigation algorithm, a quaternion-based complementary filter is introduced. It builds upon the Factored Quaternion Algorithm (FQA), which was developed previously at the Naval Postgraduate School, to yield a more robust method for computing attitude in instances where there are abrupt changes in body dynamics. A gain-switching scheme is further developed for the complementary filter that is shown to give better performance than a constant-gain version of the same filter. Testing of the attitude filter is accomplished by simulation and through the use of an instrumented pendulum built in the laboratory.

The resulting PNS algorithm is composed of the parts introduced in the previous paragraphs. That is, it integrates the strapdown navigation algorithm with the zero-velocity updates, the gait-phase detection algorithm, and the quaternion-based complementary filter with the adaptive gain-switching strategy. Performance of the PNS is examined by simulation and by the use of real data collected during walks around an athletic track, and demonstrates the viability of the PNS in some GPS-denied situations. Some limitations are noted here, such as, the PNS is only demonstrated for normal walking over level developed walking surfaces. Other types of locomotion (running or crawling, for example) were either not considered or shown to be incompatible with the PNS algorithm in its present form. PNS performance was also limited by magnetometer accuracy, which was easily influenced by sources of hard- and soft-iron interference.

As an incidental by-product of this effort, a novel utilization for the IMMU was also developed: a locomotion interface for a virtual environment. As in the PNS application, it used the shoe-worn IMMU. In this application, however, two IMMUs are required, one on each foot. A set of foot gestures was conceived and a custom software program was developed to decode the user's foot motions. This unique interface gave the user freedom to navigate through a virtual environment in any direction he/she chose for those applications utilizing large-screen displays.

THIS PAGE INTENTIONALLY LEFT BLANK

ACKNOWLEDGMENTS

As a one-time student and current employee of the Naval Postgraduate School, I have gained an appreciation for its mission within the Department of Defense, which is undoubtedly distinct among the many prominent government facilities located around the country. I consider myself fortunate to have been able to participate in its commitment to military higher education and engage in some of the fascinating research work conducted here.

Behind all great institutions, however, must reside a cadre of dedicated and talented individuals. I humbly thank my immediate supervisor, Mr. Bob McDonnell, who gave me a vast amount of latitude to complete my job duties so that I might pursue my academic goals. I am also indebted to Professor Emeritus John Powers, who initially brought me on board to work in the labs and fostered an atmosphere that permitted me the freedom to tinker and explore to my heart's content electronics, optics, and many other engineering concepts and demonstrations that sparked my curiosity.

I also wish to extend my appreciation to my dissertation committee members for their continued support and patience during this phase of the PhD process. In particular, I would like thank Professor Carlos Borges and Professor Emeritus Harold Titus for many words of encouragement. They were very uplifting during those times when I thought I would not be able to make any headway into my research topic.

I would also like to gratefully acknowledge the assistance of Professor Robert McGhee. At the most appropriate time, he pointed out the fact that the quaternion, q, represents the same three-dimensional orientation as $-q$ and that the FQA can give this as a result. His suggestion to include a check of this occurrence in my program code relieved me of countless hours investigating the cause of an odd loop in my position tracks, which had perplexed me up to this point.

I owe a special word of thanks to Professor Xiaoping Yun. In addition to his tireless patience and enthusiasm, he has taught me many valuable engineering lessons. As an example, in a recent conversation we had regarding the problem of the box cart and the inverted pendulum, he related the motor torque required for stability to the effort

exerted by a tight-rope walker and whether he chose to use a long or short balancing stick. Over the years, I have enjoyed many examples of his clever engineering analogies, such as this, to help explain difficult and abstract concepts. I will always be grateful for his mentoring during these many years. I also want to recognize his original suggestion to build the complementary filter upon the FQA. He provided the right idea at the right time and opened up the path for the rest of this work.

In the sudden passing of my father, I found solace in those moments when I reflected upon his life. The son of Armenian immigrants during the 1930s, he grew up during a very difficult time in our nation's history. There was a great deal of unemployment and many families struggled to find a means of economic stability. At an early age of 8 years old, he worked selling pumpkin seeds and shinned shoes in the local park to help his parents and other siblings scrape together the most basic of necessities. I believe it was childhood experiences such as these that sparked within my father a yearning for success and independence gained through labor and industry—a tenet he maintained throughout his life. Very early, he learned that through diligence and perseverance he could indeed overcome the adversity that surrounded him. I was blessed to have been provided with the fruits of dad's hard work and thankful to him for his nurturing and guidance all my life.

for my dad
George H. Calusdian

THIS PAGE INTENTIONALLY LEFT BLANK

I.   INTRODUCTION

A.   EARLY AND PRESENT-DAY NAVIGATION

Early travelers and explorers recognized the need to track one's position as they voyaged across distant lands and oceans. The technique employed at the time is, as the saying goes, "as old as the hills." Ancient cultures were resourceful and used landmarks, such as mountains, canyons, rivers, and other significant topographical features, to determine their position as they journeyed from one place to another. Ancient travelers were also skilled in the art of celestial navigation. It is believed that Phoenician seafarers as early as 600 BC determined their position in the open water from observations of heavenly bodies [1]. In the Pacific, Polynesians traveled across great ocean distances in 400 AD by observing the position of the sun, moon, and stars to ensure safe voyages to distant islands [2]. To sail across the Atlantic, explorers of the New World practiced the art of celestial navigation by surveying the position of the heavenly bodies in the nighttime skies. It is somewhat of a coincidence that modern-day travel rely on a man-made form of celestial navigation—the Global Positioning System (GPS).

GPS may be considered one of the most notable inventions of the 20th century. Originally conceived and developed by the Department of Defense, GPS has been successfully integrated into navigation systems installed within aircraft, ships, submarines, and weapons of various types. GPS has also found many civilian applications, including a vast amount of consumer products that range from navigation for automobiles, boats, and aircraft, to the location of an individual with a GPS-equipped cellular telephone [3].

While the applications of GPS in both military and civilian domains are vast, the system does have some drawbacks. One limitation of GPS concerns the availability of the transmitted signals. Since it is necessary to have signal reception from at least four GPS satellites to calculate position fixes, some locations may not receive adequate satellite coverage. It has been widely established that places such as dense urban environments, valleys and canyons, and heavily forested regions suffer from occlusion

problems. The GPS signal also is attenuated as it propagates through the exterior walls of building structures to the point that indoor navigation becomes difficult. Hostile or inadvertent radio-frequency jamming could also deny the user the proper reception of these essential GPS signals.

A second limitation of GPS is that the update rate for some applications may not be sufficient [4], [5]. For example, a vehicle traveling at high speed, such as a tactical or strategic aircraft, or one capable of accelerated maneuvering, will traverse a substantial distance in a short amount of time. It is necessary that some means of exacting position in between the GPS updates be implemented. In practice, many modern navigation applications combine GPS and an Inertial Navigation System (INS) with a Kalman filter, as depicted in Figure 1, [6], [7]. The INS and GPS work in a complementary manner. An INS provides position information in between those times when a GPS solution is unavailable. When a GPS fix is available, it is used to correct the errors that have accumulated in the INS solution. Other aiding systems that have been used in conjunction with GPS and INS include radar updates, celestial measurements, static and dynamic pressure measurements, and magnetic compass heading [8].
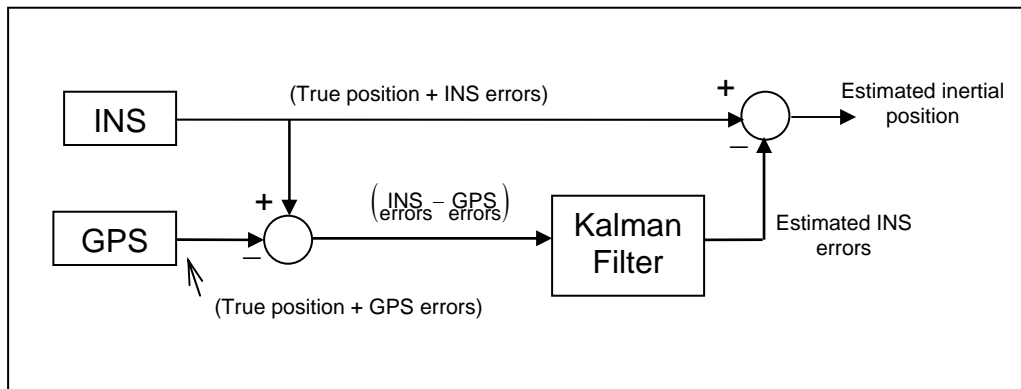
Figure 1. Aided inertial navigation system (From [7]).

In general, navigation systems can be classified into one of two types. The first may be thought of as an absolute navigation system. In this type, the navigation system makes position estimates that are referenced to an installed infrastructure. Each new position update, therefore, is derived wholly from a new set of measurements. An

attractive feature of this type of system is that errors that occurred in past position estimates do not propagate into future estimates. A disadvantage, however, is that this type of navigation system requires good "line-of-sight" to the infrastructure. Examples of theses types of systems include GPS, Loran-C, and celestial navigation.

Alternatively, a relative (or incremental) navigation system is one where new position estimates are computed with respect to previous ones. Often, this is called dead-reckoning navigation. The INS is an example of this type of position tracking system, wherein acceleration measurements are doubly integrated at the end of each sample interval to derive position. A well-known limitation of this type of system is that position errors tend to grow, and the system must be periodically reinitialized. An advantage, on the other hand, is that the relative navigation system does not require the use of an infrastructure; therefore, it can be used in those places where the infrastructure of the absolute navigation system is unavailable.

Lastly, a third and final form of the navigation system is a hybrid, as shown in Figure 1. It combines the attributes of the absolute navigation system with those of the relative navigation system.

B. SENSORS FOR INERTIAL NAVIGATION

Perhaps the first to recognize the utility of a self-contained system for guidance and navigation of a vehicle were the Germans during WWII, when they assembled gyros and accelerometers into a platform and installed the resulting inertial measurement unit (IMU) into V-2 rockets to deliver a deadly payload to targets lying across the English Channel in England [9]. Immediately after the war, the United States, impressed by the German's technological achievement of the rocket's IMU, initiated an engineering program to further study and improve the design. As a result, the modern IMU has evolved into a highly complex system of precision mechanical assemblies, electronics, and advanced algorithms. In their present form, the IMU is manufactured in one of two varieties: the platform IMU and the strapdown IMU. Both variants contain two or three mutually perpendicular accelerometers for measurement of motion along a defined set of reference directions.

A main distinction between the two architectures, however, lies with the manner in which the acceleration measurements are accomplished. In the platform IMU, gyros are used to stabilize the axis of an accelerometer and align it with that of a navigation reference frame. More specifically, the spin axes of a set of mutually perpendicular gyros—having a very large angular momentum and tending to resist any change in their orientation—are aligned with the axes of a navigation reference frame. The gyros are mounted into a cage such that their axes may tilt freely relative to the cage (and vehicle) in which they are mounted [9]. As the vehicle orientation changes during the course of a mission, the gyro axes remain fixed and aligned with the navigation reference frame. Consequently, the accelerometers, whose alignment have been preserved with that of the navigation frame, produce measurements of motion already referenced in the desired navigation coordinate system. It then becomes a simple matter to doubly integrate these measurements to derive the new position.

Alternatively, a strapdown IMU is one in which the accelerometers are "strapped" to the vehicle body. As such, as the vehicle pitches, rolls, and yaws, so do the axes of the mutually perpendicular accelerometers. The resulting measurements of acceleration are consequently referenced in a body frame and not in the required navigation frame. Gyros are used in this mechanization to measure body rotational rates [10]. From these measurements, the vehicle orientation is derived and subsequently used to reference the acceleration measurements in the navigation frame. Then, in a similar fashion to the platform IMU, the properly referenced accelerations are doubly integrated to derive a position.

Platform IMUs tend to be large and heavy. They are constructed of mechanical moving parts and require periodic maintenance to maintain the mechanical hardware in good working order. Their use is primarily reserved for high-accuracy applications and long range missions. Strapdown IMUs, on the other hand, tend to be smaller and lighter than the platform IMU. They also require less power to operate and cost less than the platform IMU. A disadvantage of the strapdown IMU, however, is that greater computational effort is required because of the requirement to resolve the accelerometer measurements in the navigation frame before integration.

C.   MEMS TECHNOLOGY

Micro-electro-mechanical systems (MEMS) technology has enabled the miniaturization of various types of common sensors. Sensors that have been manufactured with MEMS technology, such as accelerometers, rate gyroscopes, and pressure sensors, are much smaller than those manufactured with conventional macroscale techniques (welding, casting, machining). MEMS-based sensors are manufactured with mature microelectronic manufacturing processes. As a result, the sensing element can be combined into the same substrate with required signal conditioning and signal processing electronics. Typical electronic processes that may be applied to a sensor signal include biasing, low-pass or high-pass filtering, amplification (scale and offset), analog-to-digital conversion, or even self-diagnostics of the sensor [11].

The MEMS-based sensor has found a wide array of applications due to its smaller size, lighter weight, and lower power consumption. For instance, the automobile industry has successfully integrated MEMS accelerometers into their vehicles for crash detection. More recently, the rate gyroscope has been used in a new feature of automobiles called vehicle stabilization [12], [13].

1.   Survey of MEMS Devices

MEMS devices beyond those of accelerometers and gyroscopes have been developed. Honeywell, Inc., manufactured an infra-red thermal imaging sensor that is capable of operation at room temperature [14]. A carbon monoxide gas sensor called the MGS1100 was manufactured by Motorola, Inc. [15]. Knowles Acoustics, Inc., developed the SiSonic microphone. The major advantage of this type of microphone is the fact that it can be integrated into automated printed circuit board fabrication assembly lines that operate at elevated temperatures [16]. The more common electret microphone, which is not capable of withstanding these elevated temperatures, must be installed by a secondary assembly process, adding time and cost to the overall assembly.

Still, other devices beyond sensors have been manufactured with MEMS technology. Texas Instruments invented a micromachined steerable mirror that it has

successfully marketed for use in projection displays, [17], [18]. A more ubiquitous use of MEMS technology is found in the ink jet printer. IBM patented a number of designs for silicon nozzles used to reliably deliver precise amounts of ink [19], [20], [21]. An optical switch for use in a fiber optic network employing wavelength division multiplexing has been patented by several companies including Optic Net, Inc. [22], Fujitsu Laboratories [23], Agere [24], and Xerox [25]. If a MEMS device is built upon a gallium arsenide substrate rather than silicon, then devices suitable for operation above 1 GHz can be manufactured. Radio frequency MEMS, or RF MEMS, such as switches, antennas, and variable capacitors have been developed in the laboratory [26]. A thorough discussion of the many MEMS applications is exhaustive, nevertheless, [11] and [27] are good references to begin an in-depth survey of the many areas that have benefited from MEMS technology or are postured to benefit in the future.

2.   An IMU Based on MEMS Technology

The widespread use of the MEMS-based accelerometers and gyros in the automotive industry has reduced the cost of these sensors to the point that they become attractive for use in other applications—most notably the Apple iPhone and the Nintendo Wii-mote. The former uses these sensors to determine the orientation of the display and to detect finger taps. Nintendo's Wii-mote incorporates this type of sensor for motion sensing and gesture recognition to interface with a video game [28].

In 2001, Marins et al. began building prototypes of a miniature strapdown IMU with accelerometers and gyros [29]. The prototypes also included magnetometers for measurement of heading. This concept appealed to a number of manufacturers, including XSense, Microstrain, and MEMSense, which developed their own versions of the miniature IMU for the commercial market; see Figure 2. These units alleviated the researcher from having to design his/her own custom printed circuit boards for integration and packaging of the sensors. The commercial units addressed all of the technical issues related to the filtering and sampling of the sensor signals, as well as the precise mechanical alignment required for the sensors. These units generally incorporated a microcontroller to handle the analog-to-digital conversion, processing, and

6

formatting of the sampled data for subsequent transmission via any number of means, including RS-232 or I2C. Upon assembly at the manufacturer facility, all of the essential calibration and compensation constants could also be programmed into the microcontroller to improve the overall accuracy of the reported sensor data.

Because of their light weight, small size, and low power, one of the applications for which these units are suitable is personal navigation. A miniature inertial/magnetic measurement unit (IMMU) may be worn by a user, and as he/she moves about from one place to another, the sensed accelerations could then be processed to track their position in a manner that is very similar to strapdown navigation. A limitation of this approach, however, deals with the quality of the MEMS-based sensors compared to their conventional counterparts found in the navigation-grade IMU. The MEMS-based accelerometers and gyros exhibit more noise than those sensors used in navigation-grade systems [30], [31]. Table 1 compares the MEMS-derived accelerometers and gyros with those of the LN-200, which is a navigation-grade IMU manufactured by the Northrup-Grumman; it is used in a number of military systems such as Predator, Global Hawk, and the AIM-120 Advanced Medium Range Air-to-Air Missile [32]. The added noise possessed by the MEMS-based sensors will cause the position error in the personal navigation application to grow rapidly. Consequently, the development of innovative algorithms beyond that of the accepted strapdown navigation algorithm will be required.
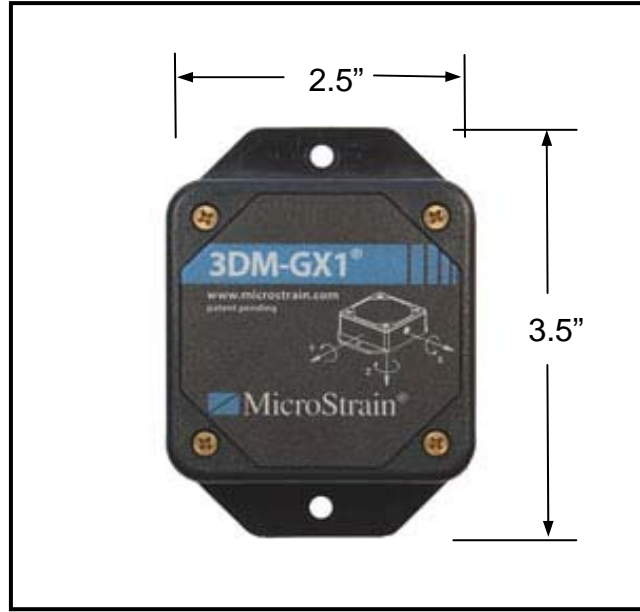
Figure 2.   Miniature IMMU from Microstrain, Inc. (From [33]).

Table 1.   Comparison of Noise in Navigation-Grade Sensors and MEMS Sensors.

	Accelerometer		Angular Rate Sensor	
Nav-grade	Northrop-Grumman A-4 Triad	$5\mu g / \sqrt{\text{Hz}}$	Fiber-Optic Gyro (LN-200)	$0.07° / \sqrt{\text{hr}}$
MEMS	Analog Devices ADXL325	$250\mu g / \sqrt{\text{Hz}}$	Analog Devices[*] ADXRS610 [33]	$3.0° / \sqrt{\text{hr}}$

---

[*] Analog Devices, Inc., specified the noise density of its sensor in units of [$°/s/\sqrt{\text{Hz}}$]. The ADXRS610 has a noise density of $0.05°/s/\sqrt{\text{Hz}}$. This figure was converted into units of $°/\sqrt{\text{hr}}$ using the following expression:

$$ARW[°/\sqrt{\text{hr}}] = \tfrac{1}{60} NoiseDensity[°/\text{hr}/\sqrt{\text{Hz}}]$$

where the noise density specified by Analog Devices was first multiplied by 3600 sec/hr to set the figure into the proper units.

D.   PERSONAL NAVIGATION

While position tracking solutions utilizing GPS and the INS have been implemented with great success on maritime and aerospace vehicles, the transition of this concept to the problem of tracking the position of an individual is in its infancy. One may argue that such an approach to this problem is unnecessary and that a personal navigation system based solely on GPS is sufficient. However, for reasons stated previously, namely the availability of the GPS signal (or lack thereof), there is a strong case for using inertial/magnetic measurements in a personal navigation application. This concept is valid in situations where the GPS signal can not be received. Additionally, since it is uncertain how long the GPS signal may be unavailable during the course of a pedestrian trip, there exists the need for an IMMU implementation that is reliable and robust to compensate for the GPS downtime.

A main component of this body of work deals with the subject of personal navigation. Subsequently, it is worthwhile to spend a moment expanding on the definition of the subject. Personal navigation in this context refers to the tracking of one's position. A recent article found on the internet [34] suggests that modern personal navigation is based solely on the use of handheld GPS devices. However, there are other ways that one could perform the task of personal navigation. Making observations of landmarks and correlating them to a map of the region, as had been done for millennia, is certainly a valid approach. Therefore, the term, personal navigation, does not imply which technique is used to accomplish this task. In the context of this work, however, personal navigation refers to the use of inertial measurements in a dead reckoning scheme to establish the position of an individual.

1.   Applications for Personal Navigation

There are a number of potential applications for the personal navigation technology, both military and civilian. The Marine infantry learn in training how to track their position using nothing more than a map and a magnetic compass. However, this technique is limited by the fact that good line-of-sight to mapped landmarks is required. In dense jungle or heavily forested areas, the line-of-sight to these landmarks may not

exist, and the aid of GPS may be unavailable. A personal navigation system tailored for infantry use could prove itself useful in this situation. Still another military application could be found in the potential increase in situational awareness offered to a team of marines or soldiers in a tactical situation. Knowledge of the location of fellow team members in a building or other urban combat setting could improve the overall situational awareness and increase the likelihood of a successful mission outcome.

Still another potential application for a personal navigation system pertains to assistance for the vision impaired [35]. GPS-based solutions have been developed. In [36] and [37], GPS information is integrated with a location database to give the user audible cues to a desired destination. The IMMU-derived data could be integrated with the GPS information to give the user a more accurate position solution and provide a means of navigation during those times when the GPS signal is unavailable, for example, when walking inside a residence or a shopping mall.

The coordination of emergency rescue operations is yet another area to benefit from the development of a personal navigation capability. Given accurate location information of emergency medical technicians, an emergency dispatcher can effectively direct the services to the location of those in need. The position data could be superimposed onto a building floor plan, if desired, to assist the dispatcher in guiding the rescuers to the appropriate location.

A personal navigation system would not necessarily be limited to these applications. With the advancement of engineering control systems applications, a new type of robot has emerged, a true walking robot, like Asimo manufactured by Honda Corp. Asimo is one of the first robots of this type to integrate a feedback control system to ensure that the robot is able to maintain its balance as it walks. Furthermore, the robot is able to shift its center of gravity and rotate its hips, as required, to coordinate turns as it travels [38]. This provides the robot with a smoother, more human-like motion. Wheeled robots, which are the predominant type of robot with a locomotion capability, use encoders on their wheels to track their position as they move about a space. However, walking robots, such as ASIMO, must use some kind of "step counting" technique to determine their position in a room. As the robot emerges from the

10

laboratory and into the real world, a personal navigation system could potentially offer some alternative means of navigation within a larger space.

The impetus for research in this area came from ongoing work by Yun et al. at the Naval Postgraduate School in support of a U.S. Army sponsored program to develop a posture tracking capability for training in a virtual environment. A detailed description of this work is found in [39], [40], [41], [42], and [43]. With the development of a personal navigation capability, another level of realism can be created within the virtual environment. Through the incorporation of accurate position data into the virtual environment, a more realistic training experience may be envisioned.

2. Objective for Personal Navigation

The primary objective of this dissertation is to develop a personal navigation system (PNS) that uses the miniature IMMU. The PNS will require the user to carry an IMMU on his/her foot. Accelerations induced by natural walking motion will be processed to derive an updated position of the user. The strapdown navigation algorithm will be adapted for this application. It will utilize an adaptive-gain quaternion-based complementary filter that was specifically tailored for the PNS. Furthermore, the strapdown algorithm will incorporate the concept of zero-velocity updates and a custom gait-phase detection algorithm to determine the instances of the foot swing and stance periods.

The PNS will be constrained for use only during normal biped walking. Locomotion by other means (i.e., limping, skipping, hopping) was not considered in this dissertation, but are topics for further study and development. Performance of the PNS was initially examined for the case of running motion. It was found that the data sample rate was insufficient to identify the necessary features of this type of locomotion and was not considered beyond this point.

An additional operational limitation of the PNS deals with the walking surface. Only flat, level walking surfaces were examined, such as concrete or other types of manufactured flooring (tile, rubberized asphalt). Walking on softer surfaces such as grass made it difficult for the gait-phase detection algorithm to determine the essential features of natural walking motion.

One more limitation of the PNS deals with the fact that it was only tested by the author. Therefore, all the parameters that were adjusted in the PNS—there are a number of thresholds and gains used throughout the system—were chosen to give the best tracks for data that was collected by the author while walking with the miniature IMMU attached to his foot. Additional consideration will be required to determine whether or not the selected parameters are suitable for a larger set of users.

E. LOCOMOTION INTERFACE FOR THE VIRTUAL ENVIRONMENT

A virtual reality is a computer-generated environment intended to provide a medium for one or more persons to interact in some manner—either with one another or with the environment itself. The virtual reality incorporates features such as computer graphics, sound, tactile feedback (haptics), smell, and any number of other user interfaces, including keyboard and computer mouse to enhance the interaction with the user [44]. Undoubtedly, the most common application of virtual reality is entertainment [45]. Popular with the younger generation, the annual global sales of video games are estimated to be $12 billion [46]. Another use of virtual reality is found on the World Wide Web. Approximately 50 million people have created avatars to engage in this virtual social network [47]. Non-entertainment applications of virtual reality exist, as well, for use as training simulators, educational tools, as part of a therapeutic regimen, or to aid in the visualization of an engineering or scientific problem [48], [49], [50].

The military has a demonstrated interest in using virtual reality. Military training programs that have a component within virtual reality can be provided at reduced cost and with the added benefit of enhanced safety [51]. For example, combat training with live ammunition is costly and presents additional risks to soldiers. Training in a virtual environment can reduce some of the costly burden and mitigate some of the safety risks associated with this type of training. While training entirely in the virtual world is not a suitable substitute for real-world training, it offers an opportunity for an acceptable level of compromise. Another attraction of training in a virtual environment is that many soldiers of the younger generation have grown up playing video games. In this regard, they feel quite comfortable interacting with a simulated reality for training purposes, see Figure 3 and [52].

Figure 3.　　　Navy personnel in a virtual reality parachute trainer wearing a head-mounted display (From [53]).

Furthermore, the military, both U.S. and foreign, has employed training simulators to educate personnel in the operation of advanced weapons systems, such as tanks and aircraft.　For these types of weapon systems, training in the virtual environment reduces overall cost because it decreases fuel consumption and maintenance requirements due to the reduced operation of the real weapon system.　Moreover, the safety of personnel and equipment is increased because they have some exposure to the system operation before the actual hands-on experience.　An added benefit of this type of training is that it reduces the overall environmental impact because the actual weapon system does not have to be used in the field as often [53], [54].

Another military application for virtual reality is in the treatment of post traumatic stress disorder (PTSD) [55].　In this approach to PTSD therapy, the patient is gradually introduced to the sensory details (visual, sound, and scent) in a virtual reality of the trauma with the motivation that he/she will learn to manage the effects of the disorder. This type of regimen, also known as a form of prolonged exposure therapy, has the benefit in that it can be administered in the safe environment of the doctor's office.　In the past, treatment for this type of disorder may have required that the patient confront the source of the trauma or fear in a real-world setting, thus placing the patient (and attending staff) in a potentially hazardous situation.　With virtual reality therapy, however, the

13

exposure can be accomplished in a safe location with all of the sensory stimuli introduced in a controlled manner at the doctor's discretion. An initial experiment of this approach was conducted in 1997 on Vietnam veterans suffering from PTSD. The experiment showed positive results, and the treatment has been advanced for use in Iraq war veterans suffering from the same disorder [56].

1. Immersion and Presence

For a user to feel as an integral part of the computer-created virtual world, he/she must have a sense of presence when interacting with the virtual environment. That is, presence is the subjective measure of one's feeling that he/she is in the virtual reality [57]. Furthermore, presence is dependent on the level of immersion that a virtual environment is able to offer. Immersion, on the other hand, is the objective measure of the amount of sensory stimuli that is provided by the virtual environment. For example, a virtual reality that uses detailed graphics displays, sound, and advanced user interfaces will offer a higher level of immersion than one that only provides a low-resolution display of the virtual environment without any other sensory stimuli. Consequently, for a user of a virtual training program (or therapeutic regimen) to have a positive or rewarding experience in a virtual environment, he/she must have a high sense of presence. In turn, the high presence can only be achieved through an adequate level of immersion, which is provided by the various forms of interfaces available to the user.

To that end, researchers and commercial developers have made interfaces of various types to heighten the experience within the virtual environment. Sound and graphics systems are the most common, but locomotion interfaces have also been developed. A locomotion interface gives the user control of his movement through the virtual environment. Many are variations of treadmill designs, assumedly because this requires user body motions most like those required in the real world and would most likely result in a high sense of user presence. Other designs for locomotion interfaces are based on step-in-place devices where the user steps on pads located on the floor to direct his/her motion through the environment.

2. Objective for the Locomotion Interface

In dealing with the subject of virtual reality, an objective for this dissertation is to develop a locomotion interface for the virtual environment incorporating the miniature IMMU. The locomotion interface will allow a user to navigate within a virtual environment. A miniature IMMU will be worn on each foot; a custom C++ application called MOVESMover interprets the user's foot gestures to direct his translation through the virtual environment. The user is allowed to move forward, walk left/right, side-step left/right, and turn-in-place clockwise or counter-clockwise. Systems that utilize large displays where the user remains fixed in one location are suitable for this type of interface. Specifically, the locomotion interface was designed for a marksmanship training system that projects virtual targets onto a large projection display located immediately in front of the trainee.

A limitation of this interface, however, is that the user is not allowed to move backwards through the virtual environment. In spite of this, the user can turn-in-place to face the opposite direction, then walk forward to achieve a similar translation. A second limitation is that the interface only operates in one speed. The pace of the foot gestures could not be interpreted accurately with our MOVESMover program. Consequently, the speed was programmed to one value only.

F. DISSERTATION OUTLINE

This dissertation primarily focuses on the development of the PNS, but a chapter is dedicated to explaining the design and operation of the locomotion interface that was developed for a virtual environment, which also utilizes the miniature IMMU. Background material relevant to the subsequent chapters is presented in Chapter II. It introduces the zero-velocity updates and the gait-phase detection algorithm. An introduction to the quaternion and its role in the strapdown navigation algorithm is also included here. The Factored Quaternion Algorithm (FQA), which is used for orientation estimation, is presented in Chapter III. Additionally, the manner in which the FQA is integrated into the complementary filter to give improved dynamic performance is also discussed in this chapter. The PNS and all of its component algorithms are presented in

Chapter IV, along with a summary of its performance. In Chapter V, the novel locomotion interface is presented, which was a by-product of the research work carried out in pursuit of the PNS. Lastly, conclusions and recommendations for future research are provided in Chapter IV.

II. BACKGROUND AND PRELIMINARY WORK

This chapter presents material relevant to the development of the PNS. Since the subject of this dissertation deals in large part with human walking motion, it is worthwhile to begin this chapter with an examination of the salient features of ambulatory locomotion. After this, a brief review of related work is outlined, as well as,previous work that was conducted at the Naval Postgraduate School. This chapter also introduces the concept of the zero-velocity updates and the gait-phase detection algorithm, two essential components that are integrated into the strapdown navigation algorithm and adapted for use in the PNS. The chapter concludes with some initial trials of the PNS and highlights the need for a quaternion-based orientation algorithm that is tailored for this particular application.

A.   HUMAN GAIT CYCLE

Walking is the most natural form of locomotion. It is a highly complex coordinated movement of our feet, legs, hips, arms, and torso to propel our center of mass in a forward direction. Walking is an innate ability we acquire not too long after we have developed sufficient motor skills to perform this articulated motion. The average age one learns to walk is 11 months. Generally, the details of walking are given very little consideration. That is to say, most of us pay little attention to how the different parts of our body move when we are walking, what muscles are involved, or how we balance and control the location of our center of gravity. Walking is second nature. However, an understanding of human walking motion is important because it relates to the analysis of the normal gait cycle and to the identification and treatment of neurological and physiological disorders. A detailed study of this complex motion would be exhaustive, involving at the very least the fields of anatomy, physiology, and biomechanics. Fortunately, for our purposes, we require only a simplified analysis of this complex body motion.

The gait cycle of normal human walking is defined as the interval of motion from heel strike to heel strike of the same foot [58]. Figure 4 shows an example of one cycle

of normal human walking motion. At the left of this diagram, the human figure begins a gait cycle at the moment the heel of the right foot strikes the ground. The gait cycle continues through several distinct phases, such as, the toe-off phase of the left foot, heel strike of the left foot, toe-off phase of the right foot, and concludes with another heel strike of the right foot. Alternatively, the gait cycle may be analyzed with regard to the motion of the left foot. Figure 4 further shows how ambulatory motion consists of two fundamental phases: a stance phase and a swing phase. The stance phase of either foot is the interval between its heel strike and toe-off. It represents the period that this foot is in contact with the ground. A complete gait cycle, therefore, has two stance phases, one corresponding to each foot. The stance phase occupies approximately 60% of the normal gait cycle.
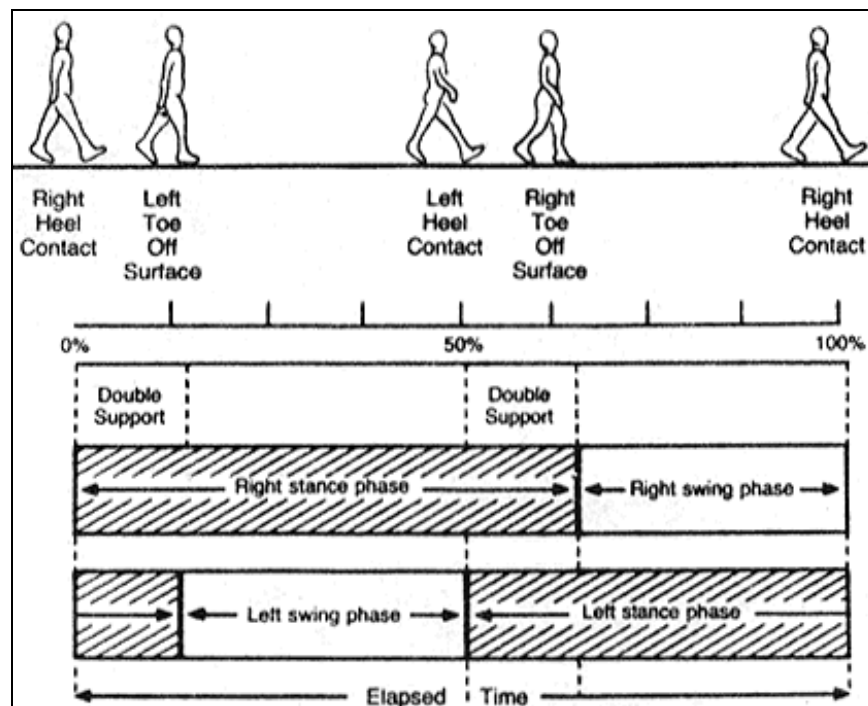
Figure 4.   Phases of the human gait cycle (From [59]).

The swing phase is characterized by the fact that the foot does not bear any weight during this interval. In this phase, the foot begins accelerating at the moment of toe-off until a maximum acceleration is reached somewhere in mid-swing, at which time

18

deceleration begins to slow the foot velocity in preparation for the subsequent heel strike. There will be two swing phases in a given gait cycle. This interval occupies approximately 40% of the normal gait cycle.

A double support phase is another characteristic of normal walking motion. This is the interval of normal walking when both feet are in contact with the ground. There are two such periods of double support in each gait cycle. At faster walking speeds, the double support period decreases and disappears altogether at the onset of running motion.

Whether the motion is walking at slow or moderate speeds, or running at fast speeds, most of the motion generally occurs in the sagittal plane of the human body. The predominant amount of motion of the feet and legs coincides with this plane. Figure 5 shows the location of the sagittal plane, along with the transverse (or horizontal) plane and the frontal plane. Normal walking consists of body motion beyond that of the feet and legs, however. The pelvic bone also exhibits some motion in support of normal walking. The pelvis will rotate in the transverse plane and tilt downward in the frontal plane during the course of walking. The torso will also exhibit some motion in these planes. Because of their inertia, the arms will appear to rotate in the sagittal plane as the center-of-mass moves forward—creating the appearance that the arms are swinging.

Some of the more common parameters used to describe the normal gait cycle are the stride length, walking speed, and cadence. Stride length measures the distance traversed of a given foot in a particular gait cycle. It is approximately half of the step length, where the step length is the distance separating the feet during the double support phase. Walking speed is a scalar quantity that gives the rate of travel of the center-of-mass. Lastly, cadence is reported in number-of-steps per unit of time. These parameters are used in the analysis of the human gait cycle and diagnostics of related disorders. They are highly dependent on individual features, such as, stature, weight, age, and gender.
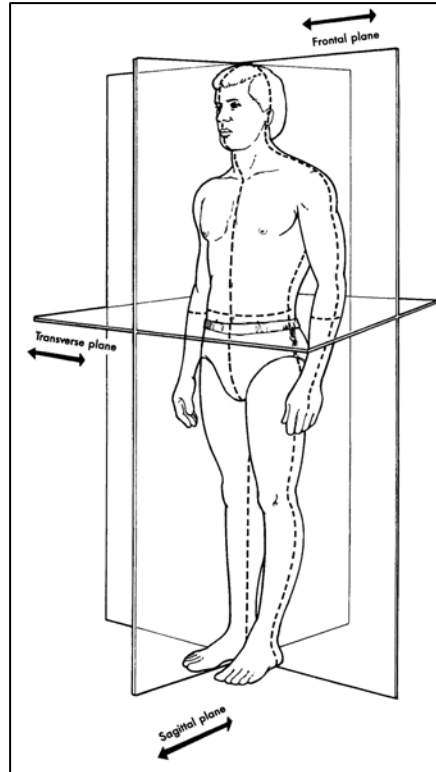
Figure 5.   Planes of body motion (From [59]).

B.   RELATED WORK

Small, lightweight accelerometers and gyros have been used in the past to study human body kinematics. Among the various motivations for this research was a need to assess physical activity and its relationship to energy expenditure [59]. Others have sought to classify body motion patterns and relate these measurements to biological and psychological data, such as, gender, emotion, and personality [60].   Still, other applications concern the rehabilitation of those suffering from injuries or disorders affecting normal walking behavior, for example, as in the development of a neuroprosthesis to alleviate "dropped-foot" syndrome, as described by Pappas et al. [61].

1.   Related Works Using Small Lightweight Sensors

In Pappas et al., the researchers demonstrated a gait phase detection system that merged angular rate data from a gyro attached at the heel of a shoe with data from a set of force sensitive resistors glued to the insole of the same shoe. These data were then fed

into a state machine to determine the corresponding phase of a particular gait cycle: stance phase, heel-off phase, swing phase, or heel-strike phase. The system was reported to have an accuracy of 99% for determining the gait phase during walking motion, ascending or descending stairs, walking on inclines, and running for short periods. This information was then used to stimulate muscles used to elevate the foot during a given swing phase.

With regard to personal navigation, various approaches have been introduced. Some have the sensors attached at the waist or torso and used a combination of inertial sensors and other navigational aids. For example, Lee from Korea and Mase from Japan collaborated on several papers that explored different techniques to assess walking features, determine distance, or compute position. In [62], they utilized a two-axis accelerometer, a digital compass, and an infra-red beacon system to aid in landmark recognition. The sensors were arranged in a small enclosure worn on the waist of the test subject. The researchers focused on a scheme to count steps and identify whether the test subject was walking on level ground, walking up, or walking down a stairway. They examined the use of the cross-correlation of the x-axis and z-axis accelerometer as a means to establish one of the three types of ambulatory motion. The researchers reported the ability to identify level walking and climbing down stairs with more than 95% success and climbing up stairs with 83% success. They also proposed an algorithm to determine stride length based on the time between observations of peak accelerations, but no experimental results were presented.

In [63], the same collaborators used an arrangement of four orientation sensors (one on each thigh and one on each leg) to determine stride length. The orientation sensors manufactured by NEC Tokin, model MDP-A3U9 consisted of three accelerometers, three angular rate sensors, and three magnetometers to provide three-dimensional orientation of each limb. They used the data from these devices in a biped stick model of the human figure to calculate the stride length after each step. The model related the measured orientation (Euler angles) of each limb in a trigonometric manner to

21

tep length. The authors reported a 2.3% average error in step length estimation based on the limited testing of this sensor arrangement on one test subject during a trial that consisted of walking 30 steps.

In another work by the same researchers, they explored some techniques to recognize whether the subject was sitting or standing, climbing stairs, descending stairs, or walking on level ground [64]. When the algorithm identified level walking, it then tried to establish walking speed (slow, normal, or fast). The sensors used were a two-axis accelerometer and one rate gyro, which were carried in a small box and inserted into the pocket of one's trousers. An electronic compass whose output consisted of one of four discrete values representing the directions of north, south, east, or west was worn on the waist. In order to classify the type of motion (i.e., sitting, standing, walking) Lee and Mase organized the sensor data into a "feature vector" that was used in a fuzzy logic scheme. They reported better than 92% success for the task of motion recognition.

In this same work, the researchers developed a method for location recognition that was based on a table look-up of presurveyed locations in an office space. A displacement vector with the number of steps taken in each direction was used for input to the look-up table. The authors also reported good results with this technique from the testing of one individual.

Researchers have also investigated attaching sensors to the foot. While this may be considered a more inconvenient location for the sensors than the waist or torso, this offers the opportunity for mitigating some of the errors in the computed position due to the occurrence of the foot's zero velocity during the stance phase. Sagawa et al. in [65] reported good results when they computed distance walked using this drift correction technique that was applied to data derived from a foot-mounted three-axis accelerometer. In addition to the three-axis accelerometer, the experimenters used an angular rate gyroscope, also attached to the same foot. The phase of the gait was detected by comparing the foot angular velocity with a specified threshold. The acceleration was integrated to produce velocity, and then a correction was applied to this result to compensate for the error that had accumulated during the swing phase. Another integration of the corrected velocity data produced the calculated distance. An average

computed distance of 30.0 $\pm$ 0.8 m was reported for eight test subjects walking at various speeds over a 30.0 m path. The error correction applied to the velocity data was based on the fact that at the end of the swing phase, the foot comes to rest on the ground and will have a zero velocity. By identifying this point in the velocity profile (i.e., where the foot had come to rest) an opportunity was provided for correcting the error that had accumulated during the integration of the acceleration data.

Similar work was described by Cavallo and Sabatini in [66]. This work sought a technique to identify gait cycles with a foot-mounted IMU that consisted of a two-axis accelerometer and a single-axis angular rate gyro. Tests were conducted on a number of subjects walking on a treadmill machine. The authors determined velocity and incline of the treadmill from the measurements of acceleration and angular velocity. They employed a "resetting" algorithm to account for the sensor errors resulting from the integration of the noisy sensor data. This algorithm made use of the zero foot velocity and provided an opportunity for recalibration of the sensor. In a subsequent work, the same group of researchers explored a GPS/INS implementation of a personal navigation system [67]. They compared IMU-calculated distance with GPS-computed distance to verify that good results could be achieved through the integration of the accelerometer data. Heading was derived from the GPS information to produce a position tracking capability.

Randell, Djiallis, and Mueller presented an alternative approach to personal navigation in [68]. They experimented with different configurations of a two-axis magnetic compass and a single-axis accelerometer to determine position. The accelerometer was attached to the foot and used to make estimates of stride length. The authors proposed that there was a correspondence between the peak vertical acceleration of the foot and the stride length. In this manner, the technique avoided the integration of any sensor noise in the accelerometer. The authors reported good results in the assessment of traveled distance, but stated that the two-axis magnetic compass did not yield reliable heading information, especially in the urban environment. The authors indicated that this was likely due to anomalous variations in the magnetic sensor data and

that the sensor could not be maintained in a level position during the experiments. They further reported that a three-axis magnetic compass would be able to provide a means of tilt compensation and yield better results.

2. Related Work at the Naval Postgraduate School

At the Naval Postgraduate School, in Monterey, California, researchers have been involved with the development and testing of sensors for the purpose of inserting one's body orientation into a virtual training environment. The prototype devices were miniature IMMUs, which were assembled with accelerometers, gyros, and magnetometers.

Bachmann in [39] described the development and testing of a miniature IMMU for use in posture tracking. The devices were attached to the limbs of the subject. Data from the sensors were merged in a complementary filter to produce a 3-D measurement of orientation for each instrumented body segment. A virtual image (avatar) was then generated that reproduced the posture of the individual. Figure 6 shows the concept of the system, and Figure 7 shows Bachmann demonstrating the use of the miniature IMMU sensors to orient the virtual avatar. This work was the impetus for the study and development of the PNS at the Naval Postgraduate School.
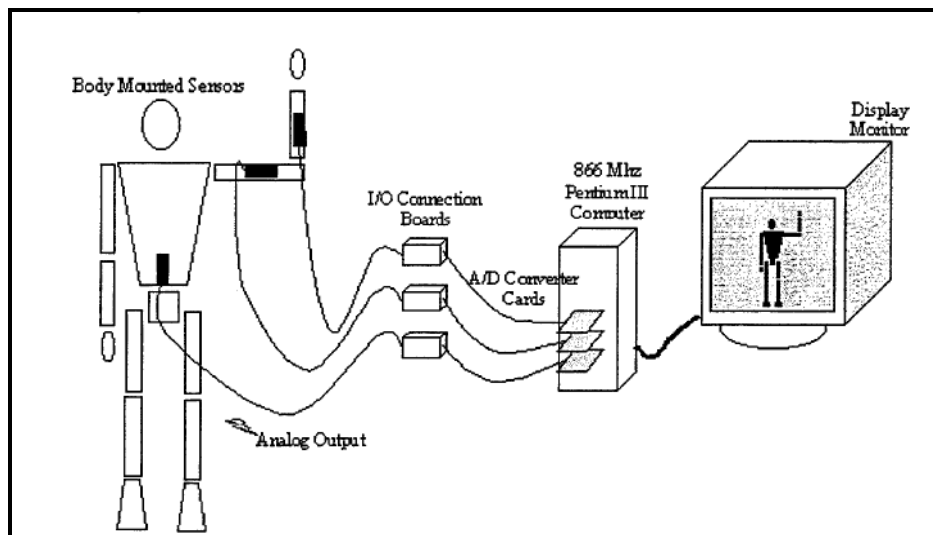
Figure 6.   Conceptual tracking system (From [39]).
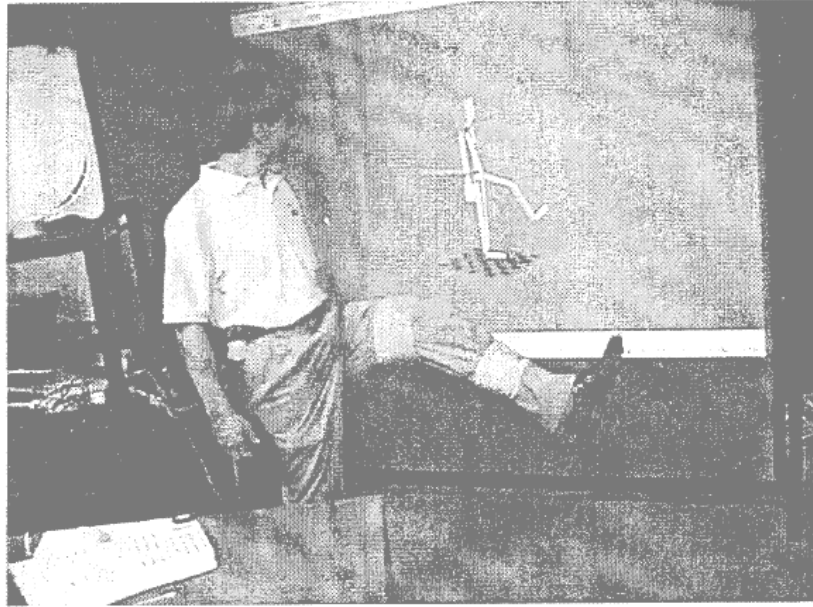
Figure 7.   Bachmann demonstrating the MARG sensor and the avatar. Sensors are attached to subject's leg to measure its orientation (From [39]).

Recently, Moore in [69] explored the use of the Microstrain 3DM-GX1 sensor (Figure 2). Like the custom prototypes used by Bachmann, the commercially-available 3DM-GX1 was a miniature IMMU. However, its built-in microcontroller calculated sensor body orientation from the raw data and made this data available through its serial communications port. This alleviated the user from having to develop an algorithm to calculate the orientation angles.   The raw sensor data from the accelerometers, magnetometers, and rate gyros were also available to the user through the same communications port.   Moore initially used this sensor in the same fashion as Bachmann to provide orientation or posture data for an avatar. Later he attached the sensor to his foot to collect dynamic data of ambulatory motion. The data collected from these latter experiments were analyzed to determine his position (distance and direction traveled) from an arbitrary starting point. Moore concluded in his thesis that these sensors were viable for use in personal navigation applications. However, due to the errors inherent in the sensor data and the numerical integration of the corresponding data, additional effort would need to be expended to develop their use in a practical personal navigation system.

Two important ideas that Moore explored were the application of the zero velocity updates and the use of the gyro to detect the swing and stance phases of the foot.

In the next two sections, the concept of the zero velocity updates and the gait-phase detection algorithm are presented. They will become essential components in the PNS.

C. ILLUSTRATION OF ZERO VELOCITY UPDATES

One of the first tests that Moore conducted was to simply move the MARG sensor through a straight line. Here, the sensor was placed on a table top and slid through a linear distance of one meter. Figure 8 shows the results from this test. Acceleration is seen in the top-most plot. In this test, the sensor was stationary for approximately six seconds prior to its translation across the table. After its trajectory was completed, the sensor was kept stationary for another seven seconds, approximately. The acceleration appears relatively small during the stationary periods, while the acceleration occurring during the sensor's translation is clearly observed within the time period between six and eight seconds. A numerical integration of this data (using Matlab's *cumtrapz( )* function) produced the velocity plot, also shown in Figure 8. Similarly, integrating the resulting velocity data gives the final distance of 12.44 meters—a considerable error when compared to the actual distance of one meter.
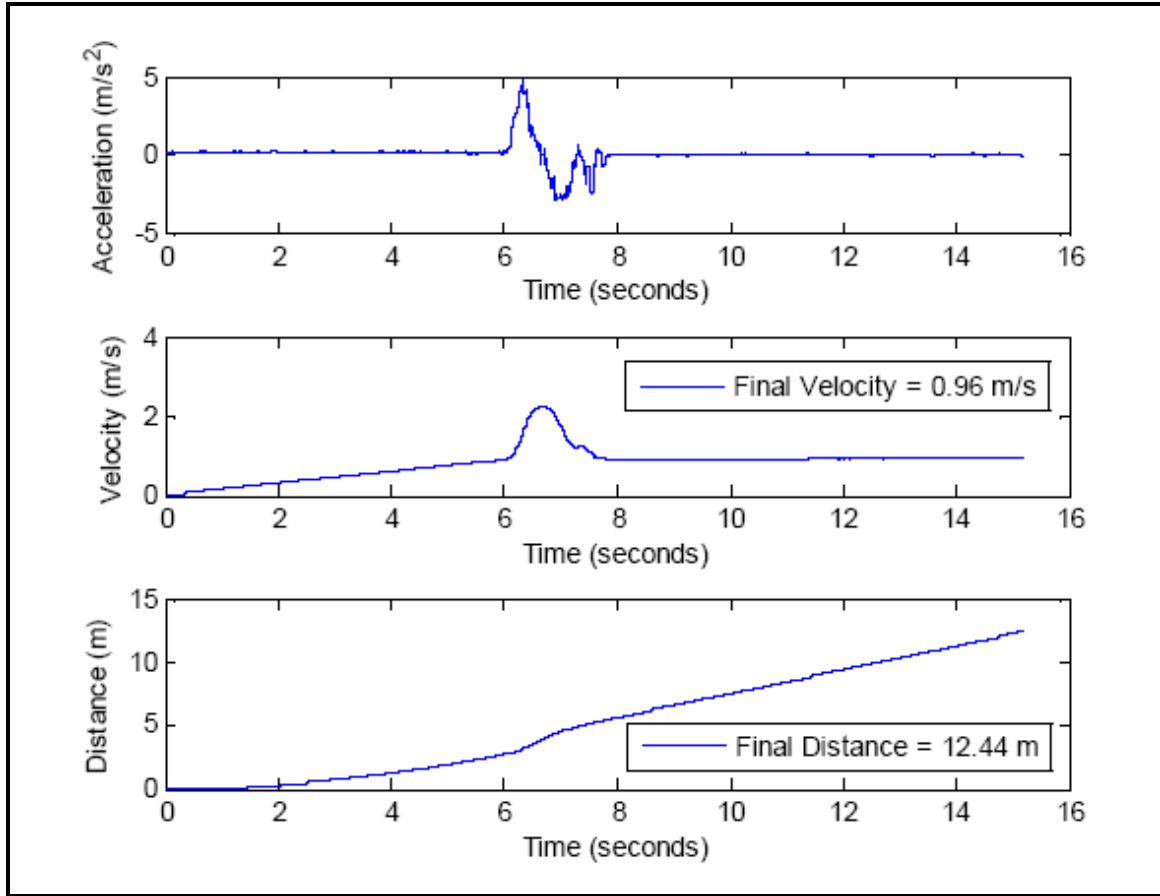
Figure 8.   Result of one meter translation of IMMU (From [69]).

Upon closer inspection of the velocity plot, one observes that prior to the sensor's motion, as well as immediately after its motion, the velocity is nonzero. Integration of this nonzero data in the velocity is responsible for the gross error in the computed distance. These errors arise because the accelerometer's output exhibits two behaviors that must be taken into consideration—bias and drift. Bias is the nonzero output measured when the accelerometer undergoes no acceleration. Drift is the randomly varying portion of the sensor output often referred to as noise.

These errors may be mitigated through a two-step process. First, since the sensor undergoes no acceleration outside of the time period between six and eight seconds, the acceleration during those times may be equated to zero. Subsequent numerical integration of the data will eliminate this component of error.

27

Secondly, the measured acceleration between six and eight seconds will also be influenced by the sensor bias and drift. To minimize this effect, the zero velocity update was employed. The measured acceleration, $a_m(t)$, consists of two components such that

$$a_m(t) = a_a(t) + \varepsilon, \qquad t = [0,T] \tag{2.1}$$

where $a_a(t)$ is the actual or true acceleration and ε is a bias error that is assumed constant in the time interval over which the acceleration occurred. In the example under consideration, $t=[0,T]$ corresponds to the time period between six and eight seconds. Integration of $a_m(t)$ will yield a calculated velocity, $v_c(t)$, as shown in (2.2).

$$\begin{aligned} v_c(t) &= \int a_m(t)\,d\tau \\ &= \int a_a(t)\,d\tau + \int \varepsilon\,d\tau \\ &= v_a(t) + \varepsilon t, \qquad t = [0,T] \end{aligned} \tag{2.2}$$

The calculated velocity, $v_c(t)$, is comprised of two parts. One component, $v_a(t)$ is the true velocity that is derived from the true acceleration. The other component, which is the product of ε and t, arises from the error in $a_m(t)$. However, at the end of the accelerated motion, when $t=T$, the motion has stopped, and the true velocity, that is $v_a(t)$, is known to be zero. Substitution of this fact ($v_a(T) = 0$ m/s) into the latter part of (2.2) gives the expression for the error that is valid during the interval $t=[0,T]$.

$$\varepsilon = \frac{v_c(T)}{T} \tag{2.3}$$

The numerator in (2.3) is taken from the last sample of $v_c(t)$, when $t=T$. Substitution of (2.3) into (2.2) and solving for $v_a(t)$ gives an expression that is used to correct the velocity data for the error encountered during the interval of the accelerated motion, as shown in (2.4).

$$v_a(t) = v_c(t) - \frac{v_c(T)}{T}t, \qquad t = [0,T] \qquad\qquad (2.4)$$

With the actual velocity data in hand, a final integration of the data produces a revised figure for the distance traveled. Figure 9 shows the corrected data plots and a new calculated distance that is more acceptable than previously calculated. Moore repeated this test for distances of two and three meters, the results of which are shown in Table 2. The distance errors of 0.5% and 0.33% for the two- and three-meter tests, respectively, are noteworthy in that they validate the technique for correcting the drift and bias inherent in the accelerometer data.
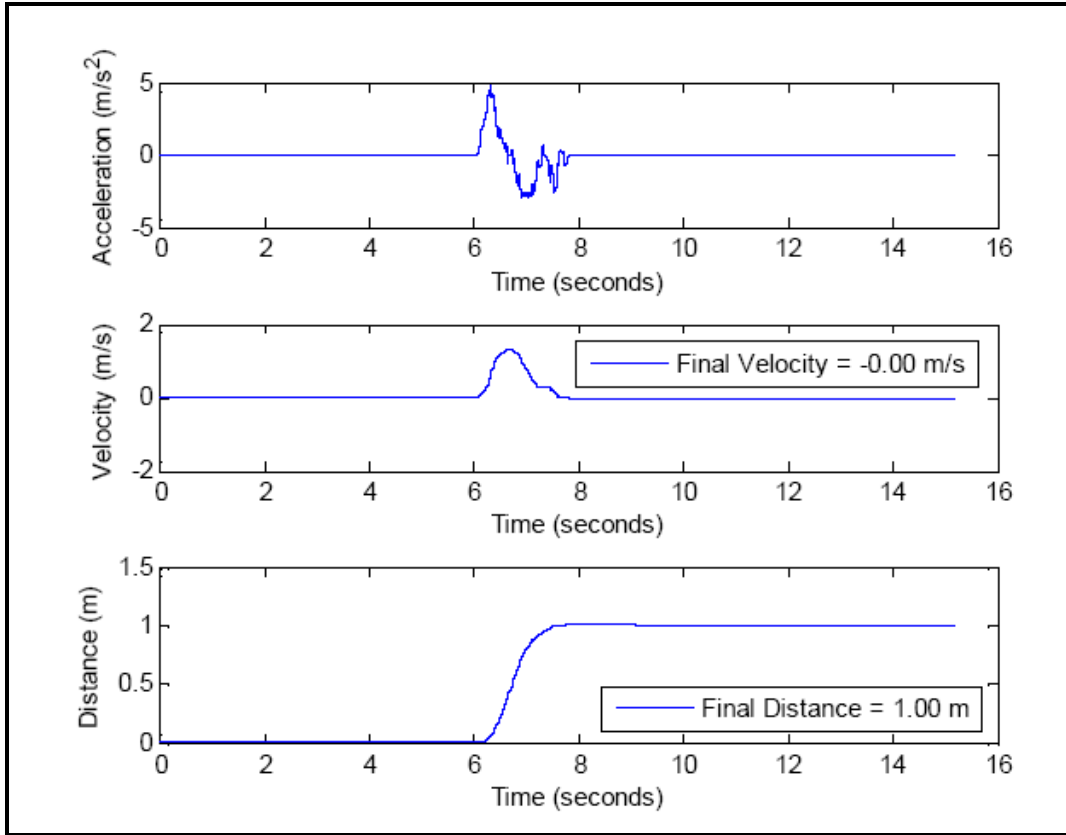
Figure 9.   Result of one-meter displacement of IMMU after data was corrected for error (From [69]).

Table 2.   Results of linear displacement of IMMU (From [69]).

True Distance (m)	Measured Distance (m)		Corrected Distance Error
	Uncorrected	Corrected	
1	12.44	1.00	0.0%
2	-1.45	2.01	0.5%
3	-2.57	2.99	0.33%

D.   GAIT-PHASE DETECTION ALGORITHM

To utilize the zero velocity updates in a PNS, the IMMU was attached to the user's foot. It is here that a zero velocity is certain to occur during the stance phase of normal walking. In this brief moment, the zero velocity can be identified and the correction to the velocity profile applied as illustrated in the previous section. The first trial of this concept in the navigation application required one to examine the acceleration data and manually locate the intervals of motion within the plotted data. This rapidly became tedious and highlighted the need for an automated technique for motion detection. The angular rate of the foot measured by the installed gyros was found to be a reliable signal to discriminate the periods of the swing and stance phase motion.

The algorithm that was developed was essentially a state machine with two states—STANCE and SWING. Figure 10 shows the two states of the gait phase detection algorithm and the allowed transitions between them. The operation of the state machine was required to be synchronized with the user's foot motion. That is, when the user's foot was in the stance phase, then the state machine must be in this state. Conversely, when the user's foot is in the swing phase, then the state machine should reflect this state, as well. Two parameters were monitored during the execution of the algorithm. The first was a composite signal, $|\omega|$, that was the magnitude of the angular rate measurements

$$|\omega| = \sqrt{\omega_x^2 + \omega_y^2 + \omega_z^2} \qquad (2.5)$$

where ω_x, ω_y, and ω_z were the individual angular rate measurements about the body axes of the IMMU. This parameter was simply compared against a threshold, Ω_{th}. The second parameter was a sample count, γ, that was incremented until a specified number of samples had satisfied the threshold condition.
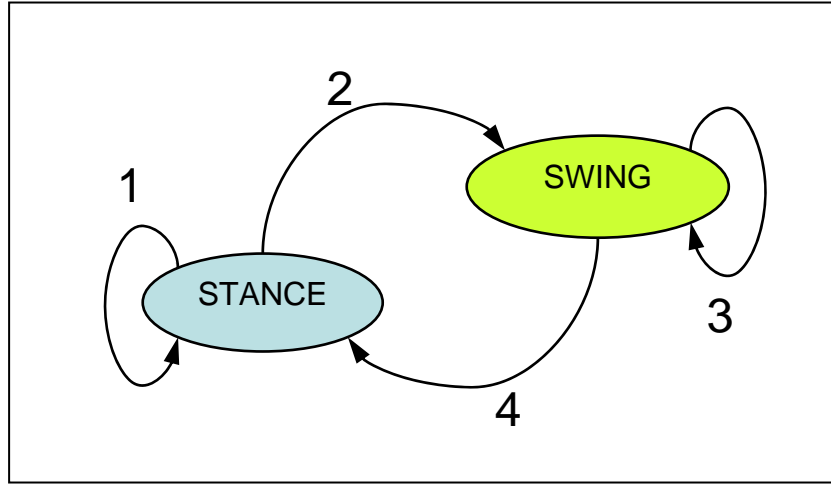
Figure 10.   State machine in the gait phase detection algorithm.

Figure 11 shows $|\omega|$ identified as the angular rate length on the vertical axis of the plot, as well as, the output of the gait phase detection algorithm, shown in blue and red, respectively. The value of the threshold, Ω_{th}, is identified on the plot, as well. Examination of the plot shows that the gait phase detection algorithm accurately locates the periods of the swing and stance phase. This was achieved by the use of the sample count parameter, γ, which worked to minimize the effect of the wide excursions observed in $|\omega|$. A simple threshold detection scheme would have resulted in the swing phase being interpreted as two or possibly more steps within a given swing phase.

Figure 12 shows a pseudo-code of the algorithm. A switch-case structure, which is suitable for any type of state machine design, was used here. The variable, *gaitPhase*, tracked the state of the state machine.

Lastly, the performance of the gait phase detection algorithm was tested using data from several walks around an oval athletic track. For each walk, the total number of steps taken was recorded and compared with the number of times transition 4 occurred in the state machine. This transition marked the end of a step and incremented a counter for subsequent analysis. Table 3 shows the performance of the gait phase detection algorithm. For the five walks examined here, the algorithm consistently detected each step. While the algorithm was proven to work reliably, occasionally, a step was missed. This tended to occur during the first step of a walk and was likely due to the fact that user had not achieved full cadence at this point in a given walk.
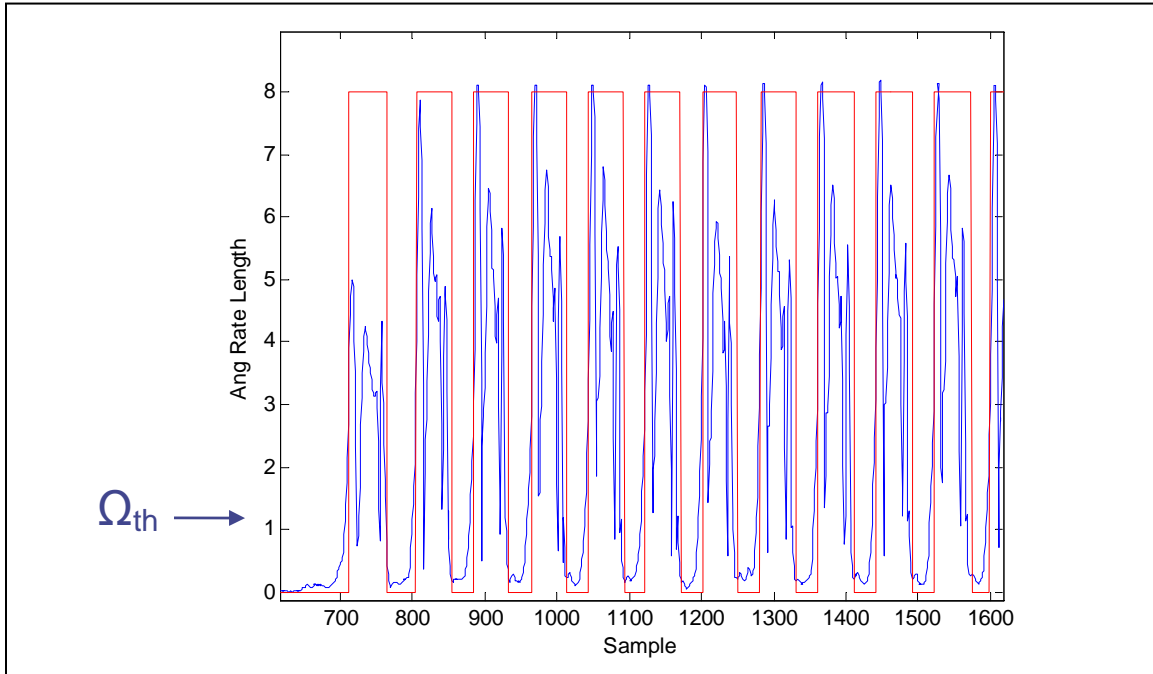
Figure 11.   Angular rate length, $|\omega|$ (blue), and the SWING/STANCE phases (red).

```
switch gaitPhase

case STANCE
      if ( |ω| < Ω_th )
         gaitPhase = STANCE        % transition 1
      else
         if ( γ > COUNT_Threshold )
            gaitPhase = SWING     % transition 2
         else
            γ = γ + 1

case SWING
      if ( |ω| > Ωth )
         gaitPhase = SWING          % transition 3
      else
         if ( γ > COUNT_Threshold )
            gaitPhase = STANCE  % transition 4
         else
            γ = γ + 1
```

Figure 12.   Pseudocode for the Gait-Phase Detection algorithm.

Table 3.   Performance of Gait-Phase Detection algorithm.

	Actual Steps	Detected Steps (Transition 4)
Walk 1	286	286
Walk 2	293	293
Walk 3	289	289
Walk 4	290	290
Walk 5	291	291

E. STRAPDOWN NAVIGATION ALGORITHM

Now that we have a means of correcting the error in the computed velocity and an automated tool for detecting the user's steps, we turn our attention to the task of computing our position. Since the IMMU is of the strapdown variety, the strapdown algorithm will be employed. This algorithm is at the heart of any inertial navigation system that uses a strapdown IMU. Many modern vehicles, such as, missiles and aircraft, use a strapdown IMU as a major component of the installed navigation system. Perhaps the best way to examine this algorithm is with a block diagram, as shown in Figure 13.
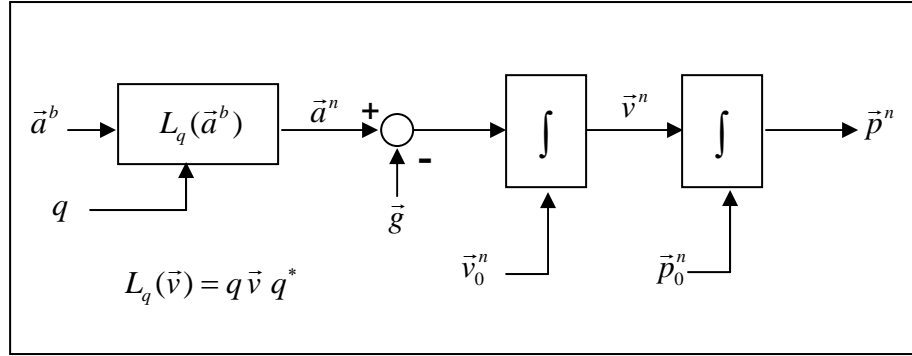
Figure 13.   Strapdown navigation algorithm.

The strapdown navigation algorithm begins with acceleration measurements made in a body reference frame designated as $\left\langle x^b \; y^b \; z^b \right\rangle$. This reference frame coincides with the axes of the strapdown IMU. Furthermore, it is aligned with the axes of the vehicle in which the strapdown IMU is installed. The accelerations are designated by the vector, $\vec{a}^b$, because there are three acceleration measurements to consider, a_x^b, a_y^b, and a_z^b. As the vehicle moves, $\vec{a}^b$ gives the resulting accelerations for this motion. Next, the algorithm requires that $\vec{a}^b$ be referenced in the navigation reference frame, identified as $\left\langle x^n \; y^n \; z^n \right\rangle$. It is in this frame into which one wishes to plot his or her position.

Before going any further in the discussion of the strapdown navigation algorithm, it is necessary to digress for a moment to consider the illustration shown in Figure 14 and

to give a relationship between $\left\langle x^b \; y^b \; z^b \right\rangle$ and $\left\langle x^n \; y^n \; z^n \right\rangle$. The two reference frames under consideration are shown. The body frame, $\left\langle x^b \; y^b \; z^b \right\rangle$ is aligned with the IMU and the vehicle. As the vehicle pitches, rolls, and yaws, so do the axes of this reference frame. The other reference frame shown is the navigation frame, $\left\langle x^n \; y^n \; z^n \right\rangle$. In general, the navigation frame is fixed and is aligned with some stationary point, the North pole or a star, for example. In order to resolve $\vec{a}^b$ in the navigation frame, some method of tracking the relationship between $\left\langle x^b \; y^b \; z^b \right\rangle$ and $\left\langle x^n \; y^n \; z^n \right\rangle$ is required. Perhaps the most familiar and intuitive way is the use of the Euler angles, also referred to as roll, pitch, and yaw. Euler angles are easily interpreted, and they will be useful to examine the relative orientation of the axes. An alternate way of expressing the relation between the two reference frames is with the direction cosine matrix. However, for this work, which builds on previous efforts, the quaternion will be used to express the relative orientation. An advantage offered by the quaternion is the benefit of reduced computational burden compared to that required when using Euler angles. A drawback, however, is that they are not very intuitive. It is difficult to visualize the relative orientation by inspection of the quaternion. Nevertheless, in embedded systems applications, the quaternion is favored for its computational efficiency.
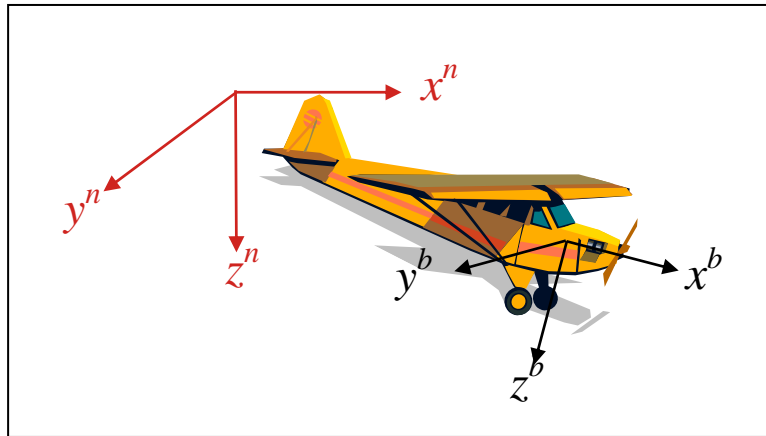
Figure 14.   Navigation and body reference frames.

In very simple terms, the quaternion, q, can be thought of as an extension of complex numbers. They are written as a four-element vector, such that, $q = [q_0, q_1, q_2, q_3]$. An alternate representation of the quaternion is one that is comprised of a scalar component and a three-element vector component, as $q = [q_0 \; \vec{q}]$. The most common use of the quaternion is in the rotation of vectors. The quaternion rotation operator, $\vec{w} = L_q(\vec{v})$, rotates $\vec{v}$ into $\vec{w}$ while preserving its length. For this application, q is required to be a unit quaternion, such that $|q| = 1$. In the strapdown navigation algorithm, $\vec{w} = L_q(\vec{v})$ will be used to rotate $\vec{a}^b$ into the $\langle x^n \; y^n \; z^n \rangle$ reference frame giving $\vec{a}^n$. The implementation of $L_q(\vec{v})$ is as shown

$$\vec{a}^n = L_q(\vec{a}^b) = q \; \vec{a}^b \; q^* \tag{2.6}$$

where $\vec{a}^b$ is written in the form of a "pure quaternion" as $\left[0, a_x^b, a_y^b, a_z^b\right]$, and q^* is the quaternion conjugate defined as $q^* = [q_0, -q_1, -q_2, -q_3]$. Furthermore, the product of the terms in (2.6) is carried out as a quaternion multiplication.[†]

Returning to the strapdown navigation algorithm in Figure 13 and with the accelerations properly referenced in $\vec{a}^n$, the next step is to correct these measurements for the local gravity, $\vec{g}$. Since the accelerations measured in $\vec{a}^b$ also have a component of gravity, it is necessary to remove this part of the measurements in preparation for the subsequent integration. The magnitude of the gravity vector is known to vary with location, and in practice, this would be accounted for in the algorithm. Lastly, a double integration of the acceleration yields the desired position in $\langle x^n \; y^n \; z^n \rangle$ given initial conditions $\vec{v}_0^n$ and $\vec{p}_0^n$.

[†] Multiplication of two quaternions, $p = [p_0 \; \vec{p}]$ and $q = [q_0 \; \vec{q}]$ is defined as
$$p \, q = p_0 \, q_0 - \vec{p} \cdot \vec{q} + p_0 \, \vec{q} + q_0 \, \vec{p} + \vec{p} \times \vec{q}.$$
The result of this operation is another quaternion of the form $r = [r_0 \; \vec{r}]$.

F.   STRAPDOWN NAVIGATION FOR PERSONAL NAVIGATION

The strapdown navigation algorithm is adapted for use in the personal navigation application, as shown in Figure 15. The diagram shows the insertion of the zero velocity updates (ZUPT) into the algorithm, which will work to reduce the errors that have accumulated in the computed velocity, $\vec{v}^n$. Corrected velocity will now be available at the output of the ZUPT block for use in the derivation of the desired position, $\vec{p}^n$. Also shown in the figure is the location of the gait-phase detection algorithm, which triggers the ZUPT at the appropriate time. Angular rate measurements of the foot are processed by the gait-phase detection algorithm to indicate the instances of the stance phase and swing phase. When the stance phase is detected, marking the interval of zero velocity, then the ZUPT is employed in a manner similar to that which was discussed previously.
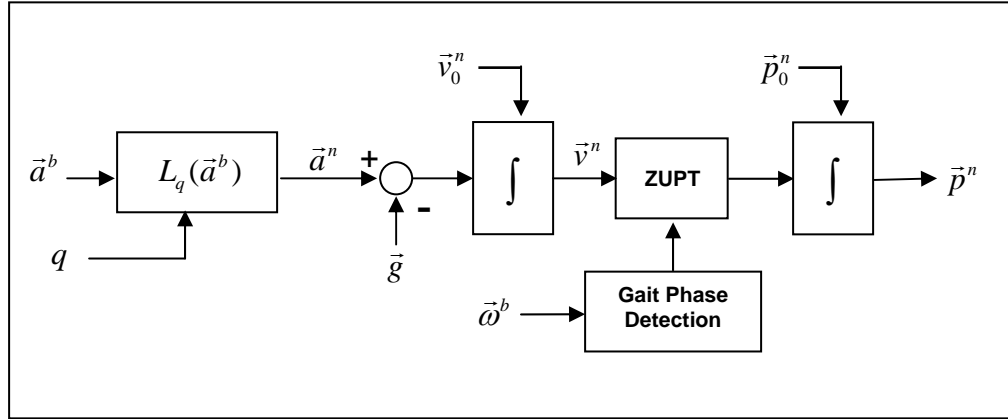
Figure 15.   Strapdown navigation adapted for personal navigation.

Also shown in Figure 15 is the use of the quaternion rotation operator, $L_q(\vec{a}^b)$. The algorithm requires that a quaternion, q, be provided. Generally, this would be computed by the integration of angular rate measurements from the gyros.[‡] However, in this particular implementation, q is provided by a proprietary algorithm residing within

---

[‡] The quaternion may be computed from the dynamic equation $\dot{q}(t) = \frac{1}{2}\Omega(\vec{\omega})q(t)$, where $\Omega(\vec{\omega})$ is a skew-symmetric matrix comprised of the instantaneous angular rate measurements. During each iteration of the strapdown algorithm, the navigation computer must solve this equation to compute $q(t)$.

the 3DM-GX1. Microstrain did not share the details of its algorithm for examination. Suffice it to say, this was a very convenient feature of the 3DM-GX1 that relieved the user from having to compute this figure.

G.   INITIAL TRIALS OF THE PERSONAL NAVIGATION SYSTEM

The configuration of the hardware used in the personal navigation system is shown in Figure 16. An IMMU was attached over the user's shoe with a homemade adapter fashioned from a recycled yogurt container, duct tape, and shoe laces. A cable carrying power and data was routed from the IMMU to the small hip sack secured around the user's waist. The hip sack contained the 6-volt DC battery that supplied power to the IMMU and an RS232-to-USB adapter, which interfaced the IMMU data to the mini-computer, also shown in the figure. The mini-computer was a SONY VGN-UX180P that had an Intel Core Solo U1400/1.2GHz processor, 512 Mbytes of RAM, and a 20.0 Gbyte hard drive. It also was equipped with the Microsoft Windows XP operating system. To collect data from the IMMU, a custom C++ data acquisition program was used. It logged the IMMU data to a file on the SONY mini-computer. The data file was later transferred to a desktop PC for post-processing.[§] Data collected during each sample interval consisted of a timer value that was provided by the 3DM-GX1 processor, the quaternion, acceleration, angular rates, and magnetometer measurements. The sample rate was approximately 50 samples per second.

[§] This configuration was for development purposes. Later, the SONY mini-computer was programmed to compute the position and transmit this data via wireless connection for real-time plotting and tracking at a central location, for example.

Figure 16.   User with IMMU attached to foot and SONY mini-computer.

Several trials were conducted walking on an athletic track. Figure 17 shows three walks of a straight line course of approximately 150 meters. The plots identified as "MARG trial" are the tracks resulting from the navigation algorithm described in the previous section. These tracks tended to drift from the very beginning of the walk and did not reproduce a straight line, as had been expected. An attempt to make a comparison with a set of GPS tracks is also shown. A small hand-held GPS device was carried simultaneously during the walks to provide another source of track data.
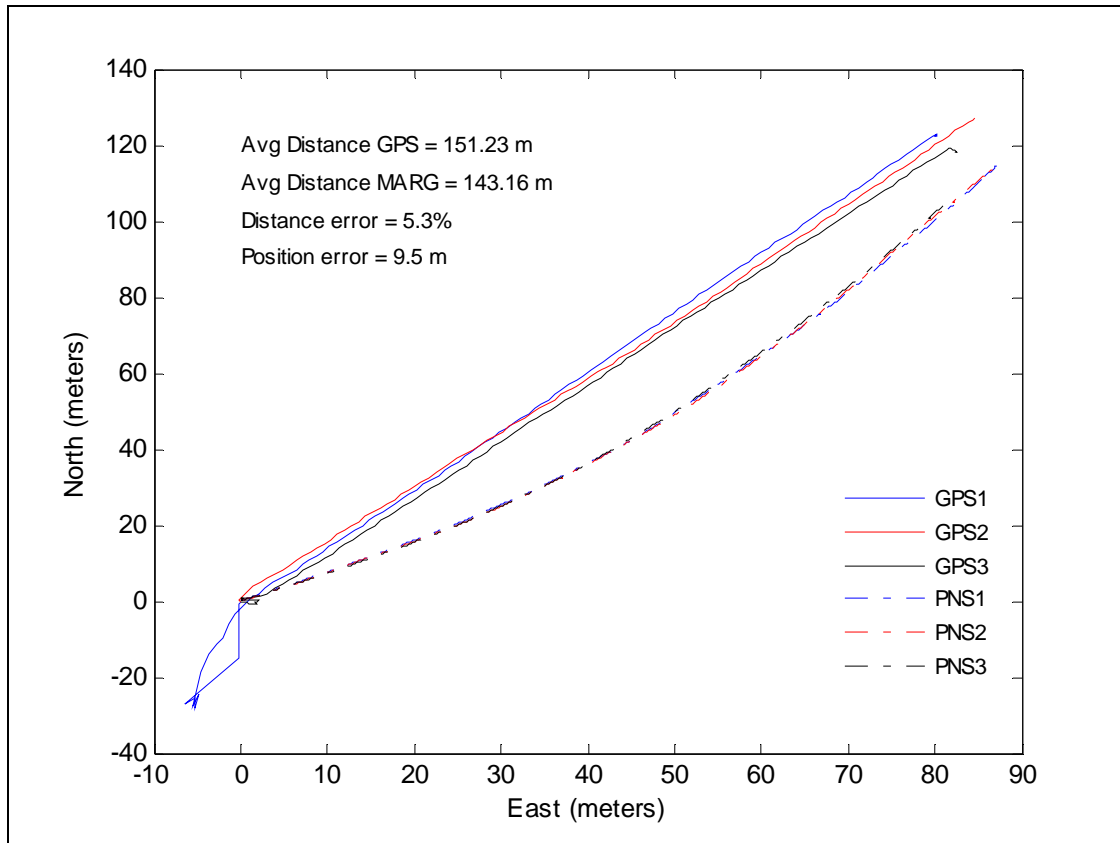
Figure 17.   Straight line track of approximately 150 meters.

In another walk, this time around the circumference of the athletic track, the drift in the computed position is again observed. Figure 18 shows this result. The walk, shown in blue and identified as MEMS-IMU in the legend, started in a north-easterly direction and continued in a counter-clockwise fashion returning to complete the oval path at the origin. Immediately at the start of the track, the position is seen to drift from a straight line where the course was known to consist of a straight section. On the downward side of the track, where another straight section of the course exists, the computed track does seem to reproduce this part reasonably well. This plot also attempts to make a comparison with a GPS track, however, this is provided with the caveat that a certain degree of post-processing of the GPS data was required, the accuracy of which is uncertain. The GPS data is provided in terms of latitude and longitude with respect to true north. To make the comparison with the inertial track, one must first convert the

latitude and longitude coordinates into x-y coordinates, which involves a gross estimate of the earth's radius. Then the data must be rotated from true north to magnetic north using the local angle of magnetic declination.
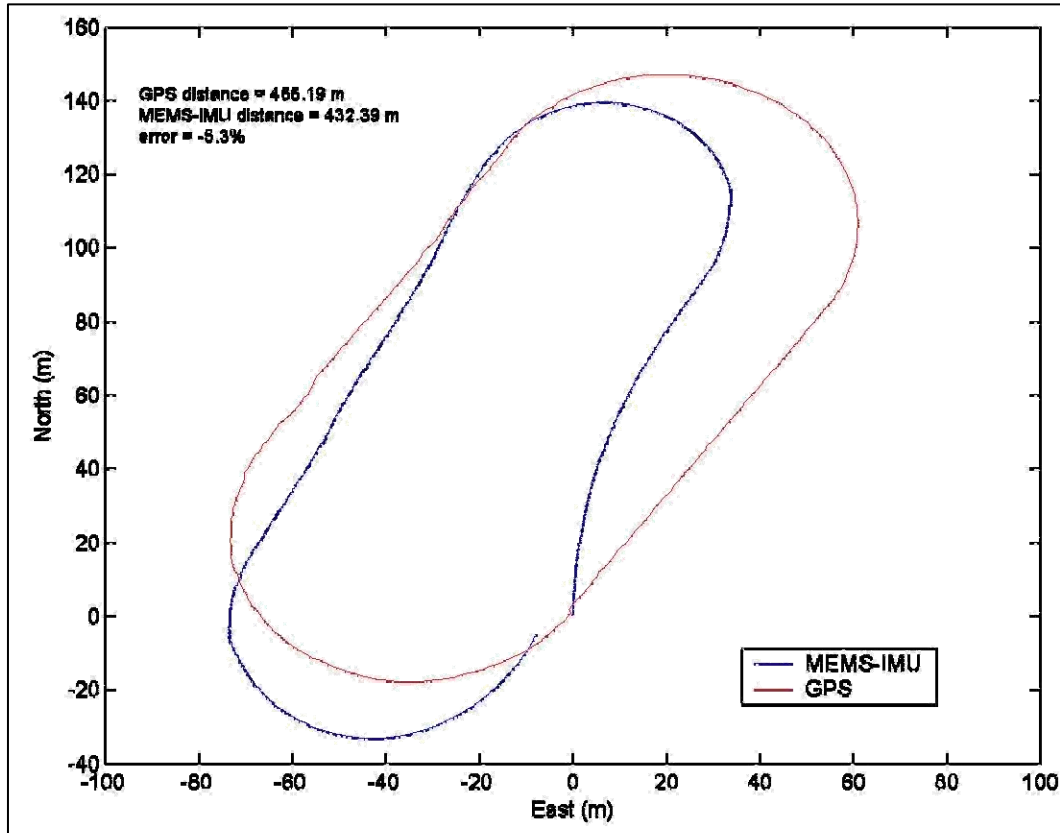
Figure 18.   Walk around the circumference of an athletic track.

H.   ANOMALOUS QUATERNION BEHAVIOR

In the previous section, some initial results were presented of the PNS while walking around an athletic track. The track showed a drift that began from the onset of the walk. It is widely understood that inherent in all inertial navigation systems there exists a tendency for growth in the position error, and the PNS was certainly expected to exhibit a certain amount of this behavior. Nevertheless, it was deemed necessary to investigate whether or not the observed drift could be reduced.

41

1. Initial Investigation of Quaternion Performance

A component of the algorithm that was given consideration after these initial trials of the PNS was the quaternion used in the quaternion rotation operator, $\vec{a}^n = L_q(\vec{a}^b)$. Recall that the quaternion used here was conveniently computed within the IMMU by a proprietary algorithm within the unit and provided to the user. In [70], an investigation of the dynamic accuracy of this quaternion was accomplished. A test stand was constructed that consisted of a simple vertical pendulum with a length that was adjustable from a few centimeters to approximately one meter. A 16-bit absolute encoder was located on the pendulum axis to measure its angular displacement. This encoder provided an angular resolution of 0.005 degrees and a maximum angular velocity rate of 180 deg/sec. The 3DM-GX1 was attached at the swinging end of the pendulum. As the pendulum swung back and forth, dynamic data were collected simultaneously from the encoder and the 3DM-GX1. Analysis of the resulting data showed a dynamic angular difference less than ± 2 degrees, which was consistent with the manufacturer's stated performance.

With the results of the pendulum experiments in mind, it was surmised—albeit incorrectly at first—that the Microstrain quaternion was not the source of the anomalous drift observed in the personal navigation application (see Figure 17 and Figure 18). At this time, other possible sources of the drift were investigated, such as, errors in the accelerometer and angular rate measurements, as well as, the magnetometers. Various possible solutions were investigated including low-pass and high-pass filtering of the data, Kalman filtering, and even the integration of a second shoulder-mounted 3DM-GX1 to serve as a source of heading information. It was not until some time later while another application for the 3DM-GX1 was being developed that the true source of the anomalous drift was discovered. Indeed, it was the quaternion that was computed from within the Microstrain 3DM-GX1. The quaternion was found to exhibit a slow wandering drift similar to that observed previously in the initial PNS trials. Furthermore, the anomalous drift was repeatable in laboratory experiments.

2.   Quaternion Tracking During Arbitrary Motion

A simple experiment was conducted in the laboratory to further investigate the drifting orientation. This experiment began with the 3DM-GX1 sitting undisturbed on a flat surface. Then, after a few seconds, the sensor was raised and moved swiftly through the air in an arbitrary fashion for approximately four seconds. After the motion, the sensor was placed on the flat surface again in the original orientation, all the while logging the sensor data and the computed quaternion from the 3DM-GX1. Figure 19, Figure 20, and Figure 21 show the three-dimensional sensor measurements acquired during the experiment. The stationary periods can be identified on the plots, as well as, the period of motion that occurred between approximately 15 seconds and 20 seconds. The time periods when the 3DM-GX1 was stationary did not exhibit any significant discernible drift in either of the accelerometers, angular rates, or magnetometer measurements. However, examination of Figure 22, which shows the individual elements of the Microstrain quaternion for the same experiment, reveals the slow wandering drift in all four elements of the quaternion. Figure 23 shows the quaternion converted into Euler angles. One observes that the individual elements of the Microstrain quaternion (and Euler angles) did not return to the original values after the motion stopped, but instead exhibited the slow wandering behavior similar to what had been seen in the initial trials of the personal navigation application. This experiment was repeated numerous times and with other 3DM-GX1 sensor modules; identical results were observed in all cases.

While the results of the pendulum experiments in [70] indicated that the Microstrain quaternion was accurate to within the manufacturer's stated specification, in the end, it was shown to be deficient for our application. Since the manufacturer's algorithm was not available for analysis, one could only speculate as to the underlying cause of this performance limitation. Many works on the study of biological motion have modeled the act of human walking as consisting of a set of single or double inverted pendulums, see [71], [72], and [73], for example. The individual sections of the leg (femur and tibia) corresponded to one of the lengths in the double-pendulum system. It was this thinking that led to the idea that the pendulum experiments would be adequate to

43

quantify the quaternion accuracy for the personal navigation application. However, it became apparent that true human walking motion was more complex than that which had been modeled with the double pendulums, at least with regard to the motion of the foot where the IMMU was attached. Instead, foot motion is comprised of as a series of abrupt start and stop events, with accelerations of ± 5 G's or more and angular rates in excess of 300 degrees/sec. The motion of the foot was unlike that of the vertical pendulum, where the pendulum's velocity will increase and decrease gradually without the sudden discontinuous changes that the foot experiences. Furthermore, one may speculate that when the foot motion data was input into the IMMU quaternion algorithm, this motion would appear more like impulses and the slow wandering drift was an indication of the algorithm's impulse response.
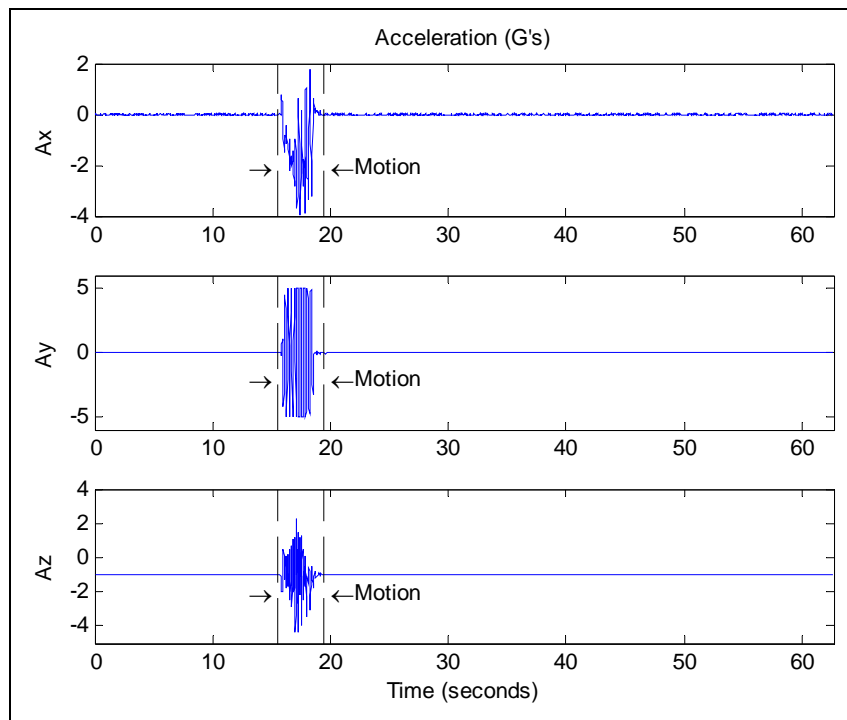
Figure 19.   Accelerometer data for the arbitrary motion.

44
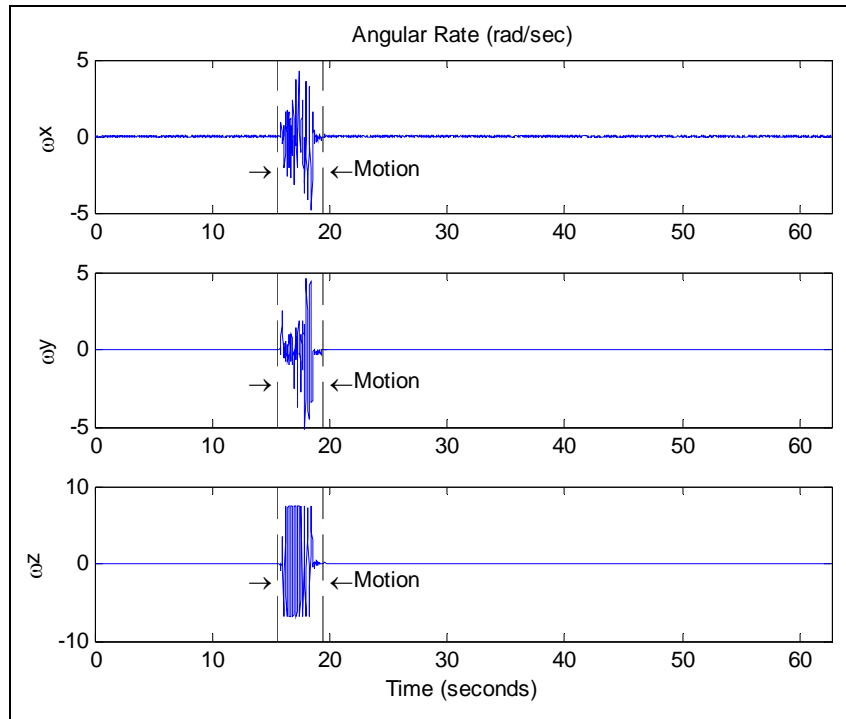
Figure 20.   Angular rate data for the arbitrary motion.
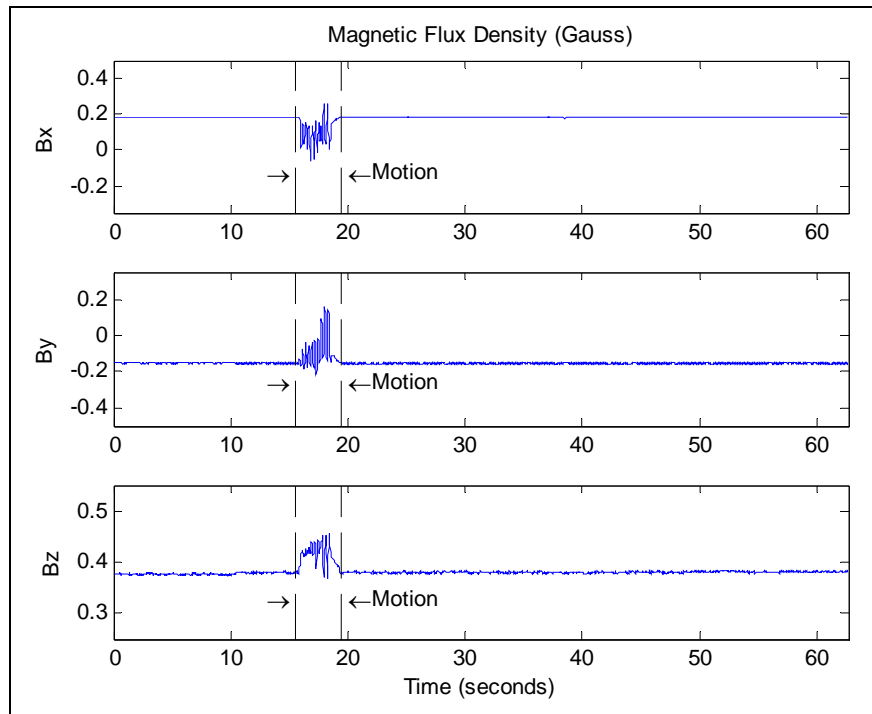
Figure 21.   Magnetometer data for the arbitrary motion.
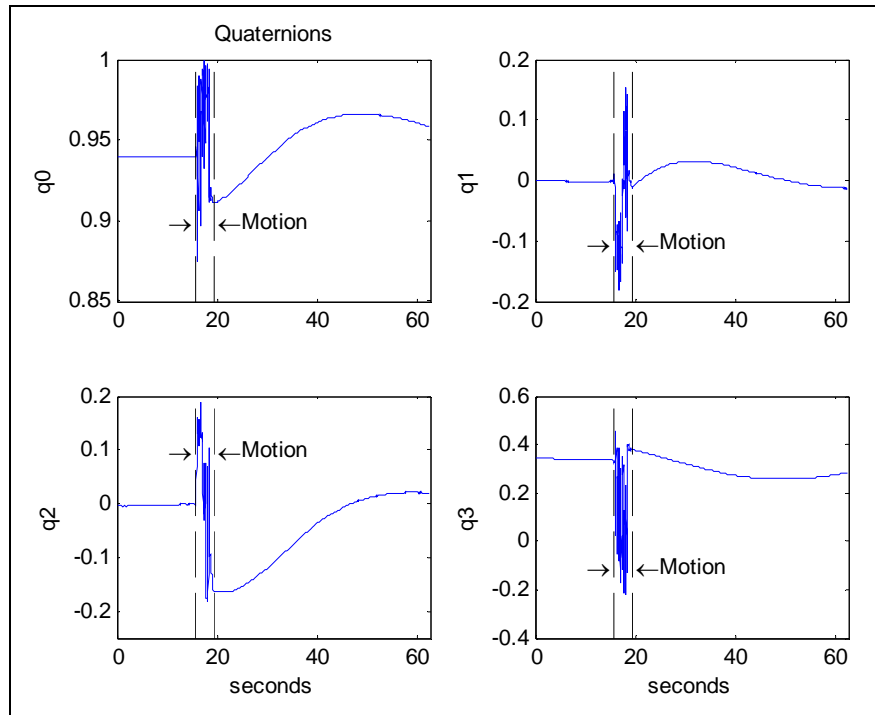
Figure 22.   Quaternion for the arbitrary motion.
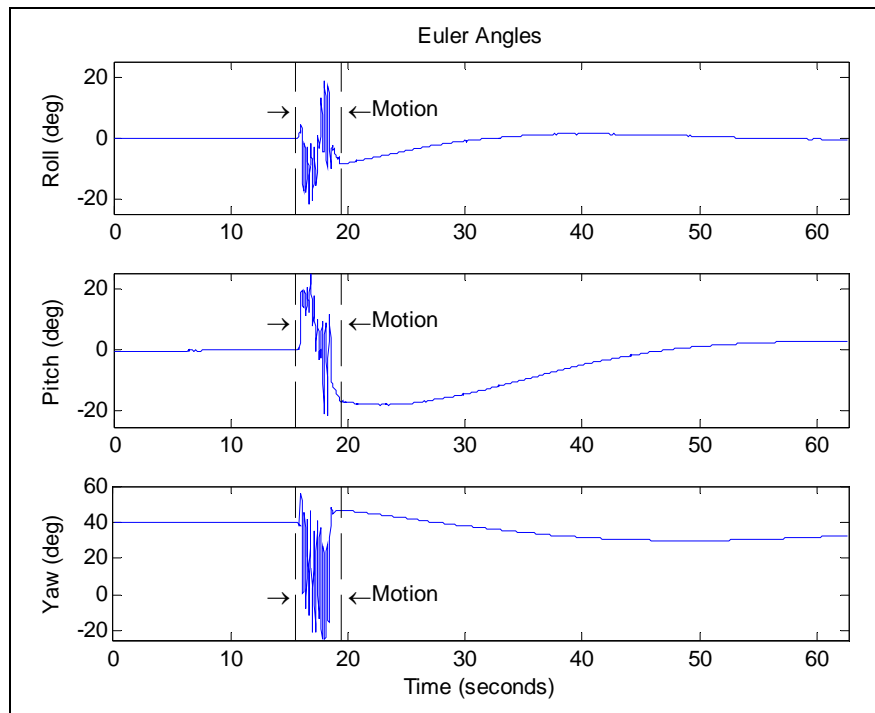
Figure 23.   Euler angles for the arbitrary motion.

I.   SUMMARY

This chapter presented background material relevant to the development of the PNS. It began with an examination of the main features of human walking motion. For our purposes, however, it was only necessary to consider the motion of the foot and its two fundamental states—the swing phase and the stance phase. A brief review of related work was also included in this chapter including preliminary work conducted at the Naval Postgraduate School. Two essential components of the PNS were also introduced here. The first being the zero-velocity updates, which provide a means of reducing the error in the computed velocity and subsequently the computed position. A second component of the PNS that was included in this chapter was the gait-phase detection algorithm that works to identify those periods of the stance phase and swing phase of the foot. The strapdown inertial navigation algorithm was also presented here and the use of the quaternion in relating the body reference frame to the navigation frame. Lastly, this chapter examined the dynamic performance of the proprietary IMMU quaternion. It showed that for the PNS, the performance of this quaternion was not sufficient and highlighted the need for an alternative means of acquiring this essential element of the strapdown navigation algorithm.

THIS PAGE INTENTIONALLY LEFT BLANK

III. QUATERNION-BASED COMPLEMENTARY FILTER

The last chapter introduced the strapdown navigation algorithm and its adaptation to the PNS by incorporation of the zero-velocity updates and the gait-phase detection algorithm. Moreover, it highlighted the need for an orientation algorithm (or attitude filter) that was capable of tracking the dynamic motion of the foot.

In a typical strapdown navigation system—our PNS falls into this category—an accurate determination of the sensor body orientation is required. Consequently, the proposed PNS required that the three-dimensional attitude of the foot be determined as accurately as possible during each sample interval of the motion. Accurate knowledge of the foot orientation was essential for the rotation of the sensor body acceleration measurements into the appropriate reference frame prior to integration and the eventual computation of position.

This chapter presents the attitude filter that was developed specifically for the PNS. Firstly however, this chapter begins with a discussion of the two main approaches to the problem of attitude estimation. One of them can be considered a relative or incremental technique that is based on measurements of body rotation rates. Gyroscopes, or more appropriately, angular rate sensors, provide the essential body rotational rate measurements for this category of attitude filters. The alternate methodology for attitude determination, which can be thought of as an absolute technique, comes from direct or indirect measurements of angular displacement with respect to two or more reference axes. Sensors, such as, accelerometers, magnetometers, and star trackers, are some of the common devices used in this class of angle-referencing algorithms.

However, as will be shown in this chapter, due to the inherent limitations of the accelerometers and gyros within the IMMU, a variant methodology was required. The proposed solution for the attitude determination problem was a hybrid of the two approaches just described. It had the form of a complementary filter, which is generally used to blend measurements from two or more sensors having a complementary frequency performance. This chapter examines our proposed complementary filter in detail and gives an evaluation of its performance in a dynamic setting. A simple vertical

pendulum served as the test case for this evaluation. Finally, this chapter concludes with a comparison of the manufacturer's quaternion and that produced with our complementary filter.

A.   ATTITIDE DERIVED FROM ANGULAR RATE MEASUREMENTS

1.   Direction Cosine Matrix

A PNS is not the only navigation application that requires accurate determination of attitude. In fact, any navigation application that employs the strapdown algorithm requires an accurate estimate of the orientation, regardless of whether the navigation is for a missile, submarine, aircraft, satellite, or as in our case, the human foot. The computation of the attitude turns out to be the most challenging part of the navigation algorithm [10, p. 309]. Consequently, the published literature contains a myriad of articles describing the various techniques that have been proposed for the computation of attitude [74], [75]. One of the main methodologies for the estimation of attitude is by the use of angular rate measurements. Angular rate sensors give the angular rate of rotation about one of the principal sensor body axes. Because the angular rate measurements are accomplished in the body reference frame, they can not be integrated directly to get angular displacement in the navigation reference frame. Instead, these measurements are used in a dynamic equation that relates the three-dimensional orientation to the orientation rate-of-change as shown

$$\dot{C}_b^n = C_b^n \, \Omega_{DCM} \tag{3.1}$$

where

$$\Omega_{DCM} = \begin{bmatrix} 0 & -\omega_z & \omega_y \\ \omega_z & 0 & -\omega_x \\ -\omega_y & \omega_x & 0 \end{bmatrix}. \tag{3.2}$$

The quantity C_b^n is the 3×3 direction cosine matrix that relates the body frame to the navigation frame, and Ω_{DCM} is a skew-symmetric matrix comprised of the angular

rate measurements from a triad of mutually orthogonal gyros. Eq. (3.1) may be solved within the navigation computer to give the most recent attitude update. Once C_b^n is computed, it is used to resolve the acceleration measurements into the navigation frame using

$$\vec{a}^n = C_b^n \, \vec{a}^b \, . \tag{3.3}$$

This last equation implies that C_b^n is an orthogonal matrix—a necessary condition to maintain the magnitude of $\vec{a}^b$ when it is resolved in the navigation frame.

2. Quaternion

Attitude filters based on the quaternion are also used in navigation systems. In a manner similar to that of the direction cosine matrix, a dynamic equation relates the quaternion to the quaternion rate as shown

$$\dot{q}(t) = \tfrac{1}{2} \Omega_q \, q(t) \tag{3.4}$$

where

$$\Omega_q = \begin{bmatrix} 0 & -\omega_x & -\omega_y & -\omega_z \\ \omega_x & 0 & \omega_z & -\omega_y \\ \omega_y & -\omega_z & 0 & \omega_x \\ \omega_z & \omega_y & -\omega_x & 0 \end{bmatrix} . \tag{3.5}$$

In Eq. (3.4) $q(t)$ is the quaternion that relates the body frame to the navigation frame, and Ω_q is the skew-symmetric matrix comprised of the angular rate measurements. When Ω_q is constant over the sampling interval, Δt, then the solution has the form

$$q(t + \Delta t) = e^{\frac{1}{2} \Omega_q \cdot \Delta t} \cdot q(t) \tag{3.6}$$

Once the latest quaternion has been computed, it is used in the quaternion rotation operator, $L_q(\vec{a}^b)$, to resolve the accelerations in the navigation frame. The exponential in (3.6) can be expanded using the Taylor series

$$e^{\frac{1}{2}\Omega_q \cdot \Delta t} = I_4 + \frac{1}{2}\Omega_q \cdot \Delta t + \frac{(\frac{1}{2}\Omega_q \cdot \Delta t)^2}{2!} + h.o.t \qquad (3.7)$$

where I_4 is the $[4 \times 4]$ identity matrix and "$h.o.t$" are the higher order terms of the series expansion. Substitution of the first two terms in (3.7) into (3.6) gives

$$q(t + \Delta t) = \left\{ I_4 + \frac{1}{2}\Omega_q \cdot \Delta t \right\} \cdot q(t). \qquad (3.8)$$

This last equation produces the desired quaternion update with an error that is of second order.

As a point of interest, the attitude quaternion is related to the direction cosine matrix, C_b^n, through the following equation [10, pp. 45],

$$C_b^n = \begin{bmatrix} c_{11} & c_{12} & c_{13} \\ c_{21} & c_{22} & c_{23} \\ c_{31} & c_{32} & c_{33} \end{bmatrix}$$

$$\qquad (3.9)$$

$$= \begin{bmatrix} (q_0^2 + q_1^2 - q_2^2 - q_3^2) & 2(q_1 q_2 - q_0 q_3) & 2(q_1 q_3 + q_0 q_2) \\ 2(q_1 q_2 + q_0 q_3) & (q_0^2 - q_1^2 + q_2^2 - q_3^2) & 2(q_2 q_3 - q_0 q_1) \\ 2(q_1 q_3 - q_0 q_2) & 2(q_2 q_3 + q_0 q_1) & (q_0^2 - q_1^2 - q_2^2 + q_3^2) \end{bmatrix}$$

Furthermore, the quaternion, C_b^n, and the Euler angles are related through the following expressions,

$$\phi = \arctan\left(\frac{c_{32}}{c_{33}}\right)$$

$$\theta = \arcsin\left(-c_{31}\right) \qquad (3.10)$$

$$\psi = \arctan\left(\frac{c_{21}}{c_{11}}\right)$$

Figure 24 shows the Euler angles with respect to the navigation frame. Roll, pitch, and yaw are positive rotations about the respective reference frame axes.

$$\text{roll} = \phi$$
$$\text{pitch} = \theta$$
$$\text{yaw} = \psi$$
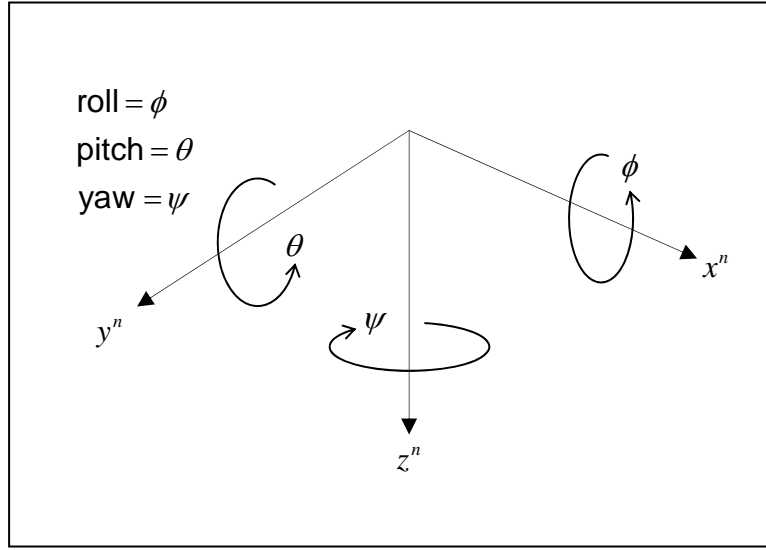
Figure 24.   Euler angles with respect to navigation frame.

B.   ATTITUDE DERIVED FROM REFERENCE ANGLE MEASUREMENTS

1.   TRIAD Algorithm

The previous section illustrated one of the main approaches to attitude determination using angular rate measurements. An alternative method is to use measurements of angular displacement relative to two or more references axes. A reference axis may be the bearing to the sun, the earth's horizon, the gravity vector, or the earth's magnetic flux density vector. With regard to satellite attitude, the horizon tracker, star tracker, sun tracker, and magnetometer are sensors commonly used in this application. One way to compute the attitude from a pair of vector measurements, for

example the gravity vector and earth's magnetic flux density vector, is to use the Three-Axis Attitude Determination (TRIAD) algorithm [76, pp. 424] [77]. This algorithm is very attractive because it is simple and straightforward to implement. It produces the attitude matrix, C_b^n. However, it is not derived from gyro measurements, as was discussed previously. Instead, it uses vector measurements of two distinct references.

Consider a pair of vector measurements from a triad of accelerometers and magnetometers, $\vec{a}^b$ and $\vec{m}^b$. Each vector has dimensions 3×1 and gives the relationship to the reference axes, $\vec{g}^n$ and $\vec{m}^n$, where the former is the gravity vector expressed in the navigation frame and the latter is the magnetic flux density vector given in the same navigation frame. An orthonormal basis can be formed from the sensor measurements as shown

$$\vec{s}_1 = \frac{\vec{a}^b}{\left| \vec{a}^b \right|}$$

$$\vec{s}_2 = \frac{\vec{a}^b \times \vec{m}^b}{\left| \vec{a}^b \times \vec{m}^b \right|} \tag{3.11}$$

$$\vec{s}_3 = \vec{s}_1 \times \vec{s}_2$$

A similar basis set may be formed from the reference vectors, such that

$$\vec{r}_1 = \frac{\vec{g}^n}{\left| \vec{g}^n \right|}$$

$$\vec{r}_2 = \frac{\vec{g}^n \times \vec{m}^n}{\left| \vec{g}^n \times \vec{m}^n \right|} \tag{3.12}$$

$$\vec{r}_3 = \vec{r}_1 \times \vec{r}_2$$

The two basis sets are related to each other by

$$M_R = C_b^n M_S \tag{3.13}$$

where $M_S = [\vec{s}_1, \vec{s}_2, \vec{s}_3]$ and $M_R = [\vec{r}_1, \vec{r}_2, \vec{r}_3]$ are orthogonal matrices in $\mathbb{R}^3$. Because of this fact, $M_S^{-1} = M_S^T$ and the above equation is solved by

$$C_b^n = M_R M_S^T. \tag{3.14}$$

A shortcoming of this algorithm is that it can only accommodate two vector measurements. When more than two vector measurements are available, such as might be the case when additional sensor types are used, they must be combined in pairs in a cumbersome manner.

2.   QUEST Algorithm

The TRIAD algorithm gives the orientation in the form of the direction cosine matrix. However, as was discussed previously, the quaternion offers some benefits in terms of computational efficiency. Another algorithm often used in this class of methods is the QUaternion ESTimator (QUEST) algorithm. It gives the attitude in the form of the quaternion, and unlike the TRIAD algorithm, is able to process $N \geq 2$ vector measurements. Furthermore, it is an optimal algorithm because it seeks to maximize the gain function

$$g(q) = q^T K q \tag{3.15}$$

with respect to the quaternion, q, where K is a 4×4 matrix that has been constructed from the N measurement vectors and N reference vectors [77]. To find the optimal quaternion requires the computation of the eigenvectors, $\{\vec{q}_1 \quad \vec{q}_2 \quad \vec{q}_3 \quad \vec{q}_4\}$, of K. However, the optimum quaternion, $\vec{q}_1$, is the one associated with the largest eigenvalue, λ_1 of K. The matrix K is found by the following sequence of steps [78]:

a.   Compute the 3×3 matrix D where

$$\underset{3 \times 3}{D} = \sum_{i=1}^{N} \vec{w}_i \cdot \vec{v}_i^T.$$

Since we only have $N = 2$ vector measurements in the present application, $\vec{w}_1 = \vec{a}^b$ and $\vec{w}_2 = \vec{m}^b$ are the vector measurements of gravity and magnetic flux density in the body frame. The reference vectors $\vec{v}_i$ are defined as $\vec{v}_1 = \vec{g}$ and

$\vec{v}_2 = \left[\left| \vec{B}_e \right| \cos \beta \quad 0 \quad \left| \vec{B}_e \right| \sin \beta \right]^T$ in the navigation frame, where $\left| \vec{B}_e \right|$ is the magnitude of the earth's magnetic flux density and β is the local angle of inclination.

    b.   Construct the matrix $S = D^T + D$

    c. $Z = D^T - D$

    d.   Obtain the vector $\vec{z}$ from the elements of the skew symmetric matrix Z such that

$$\vec{z} = \left[z_{32} \quad z_{13} \quad z_{21} \right].$$

    e. $\sigma = trace(D)$.

    f.   Construct the 4×4 matrix K,

$$\underset{4 \times 4}{K} = \begin{bmatrix} \underset{3 \times 3}{S - I\sigma} & \underset{3 \times 1}{\vec{z}} \\ \underset{1 \times 3}{\vec{z}^T} & \underset{1 \times 1}{\sigma} \end{bmatrix}.$$

The QUEST algorithm proceeds with the finding of the eigenvalues and eigenvectors of K. Interestingly, as noted in the reference, for the special case $N = 2$, the optimum quaternion, $\vec{q}_1$ is equivalent to the attitude matrix, C_b^n, which results from the TRIAD algorithm.

3.   FQA Algorithm

More recently, an alternative to the TRIAD and QUEST algorithm was introduced. The Factored Quaternion Algorithm (FQA), while not optimal, provides some attractive features. For one, unlike the TRIAD, the FQA produces a quaternion. Another feature of the FQA is that it uses magnetic vector measurements only for the computation of the yaw angle. Any errors present in this measurement are not coupled into the roll and pitch angles [79]. Furthermore, the FQA was shown to give similar

performance to the QUEST at a reduced level of computational effort. It achieves this by avoiding the use of trigonometric terms, which tend to increase the computational burden of an algorithm.

The algorithm computes three distinct quaternions—each one corresponding to the rotation about one of the principal axes. More to the point, the algorithm is rooted in the fact that any orientation can be decomposed into an ordered set of rotations about the principal axes of the reference (navigation) frame [80]. A final step of the FQA is to multiply the three principal quaternions to yield a total or composite quaternion that describes the complete three-dimensional orientation of the body as shown

$$q = q_{Yaw}\, q_{Pitch}\, q_{Roll}. \tag{3.16}$$

The roll and pitch quaternions are computed form the acceleration vector measurement, while the yaw quaternion is computed from the magnetic field vector measurement.

Given the normalized gravity vector measurement, $\vec{a}^b = \left[a_x^b, a_y^b, a_z^b \right]$ where $\left| \vec{a}^b \right| = 1$, the pitch quaternion has the form

$$q_{Pitch} = \begin{bmatrix} \cos\frac{\theta}{2} \\ 0 \\ \sin\frac{\theta}{2} \\ 0 \end{bmatrix} \tag{3.17}$$

where

$$\begin{aligned} \sin\tfrac{\theta}{2} &= \mathrm{sgn}(\sin\theta)\sqrt{(1-\cos\theta)/2} \\ \cos\tfrac{\theta}{2} &= \sqrt{(1+\cos\theta)/2} \end{aligned} \tag{3.18}$$

and

$$\begin{aligned} \sin\theta &= a_x^b \\ \cos\theta &= \sqrt{1-\sin^2\theta}. \end{aligned} \tag{3.19}$$

It is noted that in the equations provided above, the sine or cosine of the angle is never actually computed. Beginning with the value for $\sin\theta$, it is carried through the remaining expressions until the two half-angle terms are populated in the elements of the pitch quaternion. In this manner, the FQA achieves a reduction in the amount of numerical computations.

The roll quaternion is computed in a similar manner, but it accounts for any rotation in the pitch angle. This quaternion has the form

$$q_{Roll} = \begin{bmatrix} \cos\frac{\phi}{2} \\ \sin\frac{\phi}{2} \\ 0 \\ 0 \end{bmatrix} \tag{3.20}$$

where

$$\sin\tfrac{\phi}{2} = \mathsf{sgn}(\sin\phi)\sqrt{(1-\cos\phi)/2}$$
$$\cos\tfrac{\phi}{2} = \sqrt{(1+\cos\phi)/2} \tag{3.21}$$

and

$$\sin\phi = -a_y^b / \cos\theta$$
$$\cos\phi = -a_z^b / \cos\theta. \tag{3.22}$$

Next, the FQA computes the yaw quaternion using the magnetic field measurement. First in this part of the computation is to determine the horizontal components of the magnetic field vector measurement. This is done using the previously computed pitch and roll quaternions

$$\vec{m}^n = q_{Pitch}\, q_{Roll}\, \vec{m}^b\, q_{Roll}^*\, q_{Pitch}^* \tag{3.23}$$

where $\vec{m}^n$ and $\vec{m}^b$ are expressed in the form of pure quaternions, that is $\vec{m}^n = \begin{bmatrix} 0 & m_x^n & m_y^n & m_z^n \end{bmatrix}$ and $\vec{m}^b = \begin{bmatrix} 0 & m_x^b & m_y^b & m_z^b \end{bmatrix}$. After normalization of the resulting vectors, the yaw angle, ψ, is related to the horizontal components of the

magnetic reference vector, $\begin{bmatrix} N_x & N_y \end{bmatrix}$, and the corresponding components of the magnetic measurement vector, $\begin{bmatrix} M_x & M_y \end{bmatrix}$ by

$$\begin{bmatrix} \cos\psi \\ \sin\psi \end{bmatrix} = \begin{bmatrix} M_x & M_y \\ -M_y & M_x \end{bmatrix} \begin{bmatrix} N_x \\ N_y \end{bmatrix}. \tag{3.24}$$

In the above equation, $\begin{bmatrix} N_x & N_y \end{bmatrix} = \begin{bmatrix} 1 & 0 \end{bmatrix}$ and $\begin{bmatrix} M_x & M_y \end{bmatrix} = \left(m_x^n \ m_y^n \right) \big/ \sqrt{\left(m_x^n \right)^2 + \left(m_y^n \right)^2}$. Lastly, the yaw quaternion is given by

$$q_{Yaw} = \begin{bmatrix} \cos\frac{\psi}{2} \\ 0 \\ 0 \\ \sin\frac{\psi}{2} \end{bmatrix}. \tag{3.25}$$

In a fashion similar to the roll and pitch quaternions, $\cos\psi$ and $\sin\psi$ are related to the elements of the yaw quaternion through the half-angle formulas used previously.

The FQA uses vector measurements from the accelerometers and magnetometers. The TRIAD and QUEST algorithms would use these same vector measurements, if they were to be used in this application. Because of this, these algorithms require accurate measurements from these sensors. For the magnetometers, it is widely understood that errors can be introduced into the corresponding measurements due to magnetic disturbances. Examples include electric machinery and electronics which generate their own magnetic fields and add to the earth's magnetic field. This type of interference is known as hard-iron interference. Other examples include metallic objects, which do not generate magnetic fields but can cause local variations in the magnetic field. Not surprisingly, this is referred to as soft-iron interference [81]. As mentioned earlier, an attractive feature of the FQA is that it isolates these unknown and unpredictable errors from the pitch and roll angle computations.

In the absence of magnetic field interference and under static (or quasi-static) conditions the FQA will produce an accurate attitude quaternion. However, if the sensor

59

body is accelerated, then the accelerometers will measure this acceleration in addition to the component of the gravity vector. This latter component of the acceleration measurement corresponds to the desired body orientation, but the former contributes an unknown error into the FQA and to the resulting attitude quaternion.

C. QUATERNION-BASED COMPLEMENTARY FILTER

In the previous sections, several examples of algorithms were presented for the computation of attitude. These algorithms were classified into two categories: those that were based on angular rate measurements, which involved the solution of a dynamic differential equation, and those that were based on angular measurements relative to two or more reference axes.

In the present section, an alternative solution is presented, one that incorporated both types of algorithms in the form of a complementary filter. As will be shown in the remainder of this chapter, this architecture combined the attributes of both types of algorithms, which in turn, helped to mitigate the inferior performance of the MEMS-based IMMU.

Our proposed complementary filter had the architecture shown in Figure 25. The filter blended a quaternion computed with the FQA (static branch) and another that was computed using the angular rates (dynamic branch). The filter gain, k, had the effect of adjusting the weight of either branch that was used in the final computation of a given quaternion estimate, $\hat{q}(t)$. During each iteration of the filter loop, an error, $e(t)$, was computed, which was the difference between the most recent quaternion computed with the FQA, $q_s(t)$, and the estimate, $\hat{q}(t)$, that had been computed during the previous filter loop iteration. In the dynamic branch, a quaternion rate, $\dot{q}_d(t)$, was computed from the angular rates and combined with the error. The resulting differential equation was solved numerically to yield the most recent estimate of $\hat{q}(t)$. More details on the operation of the filter will be presented in the following subsections.
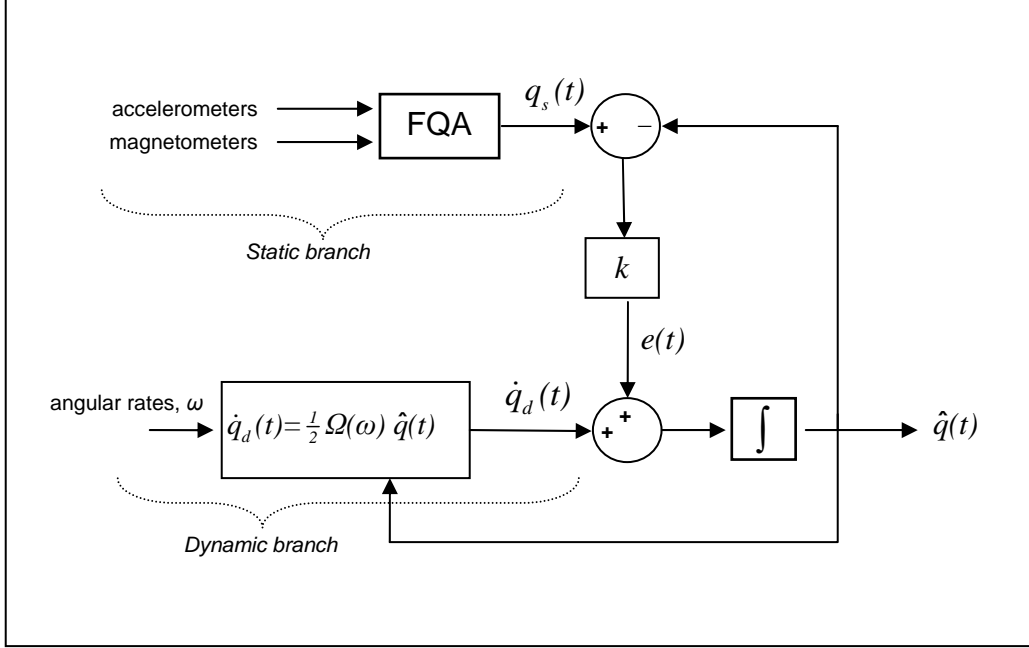
Figure 25.   Quaternion-based complementary filter.

D.   FREQUENCY RESPONSE OF THE COMPLEMENTARY FILTER

The filter gain, k, played an important role in the performance of the complementary filter. As will be shown, it determined the weighting in the filter's output of one branch over the other. In order to begin this discussion, the complementary filter was redrawn in the frequency domain, as shown in Figure 26. This was done to derive a transfer function of the filter and facilitate analysis of the frequency response, which in turn, would reveal the true action of the filter gain within the system. In the figure, $Q_s(s)$, is the quaternion derived from the FQA, and $Q_d(s)$ is a quaternion computed from the angular rates.
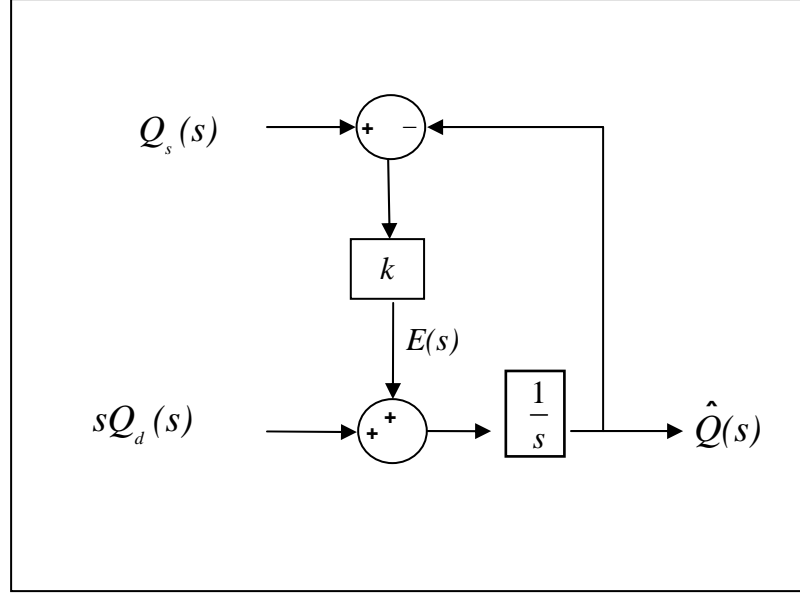
Figure 26.   Complementary filter in the frequency domain.

First, we seek to derive the transfer function for the static branch. Applying the principle of superposition and neglecting the filter input from the dynamic branch, we get expressions for *E(s)* and $\hat{Q}(s)$, as shown in (3.26) and (3.27)

$$E(s) = k\{Q_s(s) - \hat{Q}(s)\} \tag{3.26}$$

$$\hat{Q}(s) = \frac{1}{s}E(s) \tag{3.27}$$

Substitution of   (3.26) into   (3.27) and rearranging terms yields the desired transfer function for the static branch of the complementary filter

$$\frac{\hat{Q}(s)}{Q_s(s)} = \frac{k}{s+k} \tag{3.28}$$

In terms of the magnitude frequency response, $M_s(\omega)$, and the phase frequency response, $\phi_s(\omega)$, for the static branch we have that

$$M_s(\omega) = \frac{\left|\hat{Q}(j\omega)\right|}{\left|Q_s(j\omega)\right|} = \frac{k}{\sqrt{\omega^2 + k^2}} \tag{3.29}$$

$$\phi_s(\omega) = \frac{\angle\hat{Q}(j\omega)}{\angle Q_s(j\omega)} = \angle k - \angle(j\omega + k) = 0 - \tan^{-1}(\omega\!/_k)$$
$$= -\tan^{-1}(\omega\!/_k) \tag{3.30}$$

Figure 27 and Figure 28 show $M_s(\omega)$ and $\phi_s(\omega)$ for three different values of gain (plotted in blue). The horizontal axis on these plots are in terms of frequency (rad/sec), but can be thought of as the rate of change of the input orientation or true quaternion. $M_s(\omega)$ has a low-pass response, which suggests that as the rate of change of the input orientation increases, the static branch would tend to attenuate this signal and not reproduce the true desired orientation. Moreover, we also note that $\phi_s(\omega)$ increases from zero to $-\pi/2$ as the orientation rate of change increases. Thus, there exists a phase difference of $-\pi/2$ between the input and output of the static branch at high input frequency.

Turning our attention to the dynamic branch, we once again apply the superposition principle, but this time we ignore the input, $Q_s(s)$. Expressions for $E(s)$ and $\hat{Q}(s)$ are given by

$$E(s) = -k\hat{Q}(s) \tag{3.31}$$

$$\hat{Q}(s) = \frac{1}{s}(sQ_d(s) + E(s)) \tag{3.32}$$

Substitution of (3.31) into (3.32) and rearranging terms produces the transfer function for the dynamic branch of the complementary filter:

$$\frac{\hat{Q}(s)}{Q_d(s)} = \frac{s}{s+k} \tag{3.33}$$

The magnitude frequency response, $M_d(\omega)$, and the phase frequency response, $\phi_d(\omega)$, for the dynamic branch are

$$M_d(\omega) = \frac{\left|\hat{Q}(j\omega)\right|}{\left|Q_d(j\omega)\right|} = \frac{\omega}{\sqrt{\omega^2 + k^2}} \tag{3.34}$$

$$\begin{aligned}\phi_d(\omega) &= \frac{\angle\hat{Q}(j\omega)}{\angle Q_d(j\omega)} = \angle j\omega - \angle(j\omega + k) \\ &= \frac{\pi}{2} - \tan^{-1}(\omega/\!k)\end{aligned} \tag{3.35}$$

Figure 27 and Figure 28 show these responses for the dynamic branch for three values of gain (shown in red). We see that the magnitude response, $M_d(\omega)$, of the dynamic branch has a high-pass response, which suggests that this branch would be appropriate for tracking orientation in situations where the attitude tended to change rapidly. The phase frequency response, $\phi_d(\omega)$, reinforces this idea about the ability to track rapidly changing orientation because we see that the phase change approaches zero as the input frequency increases.
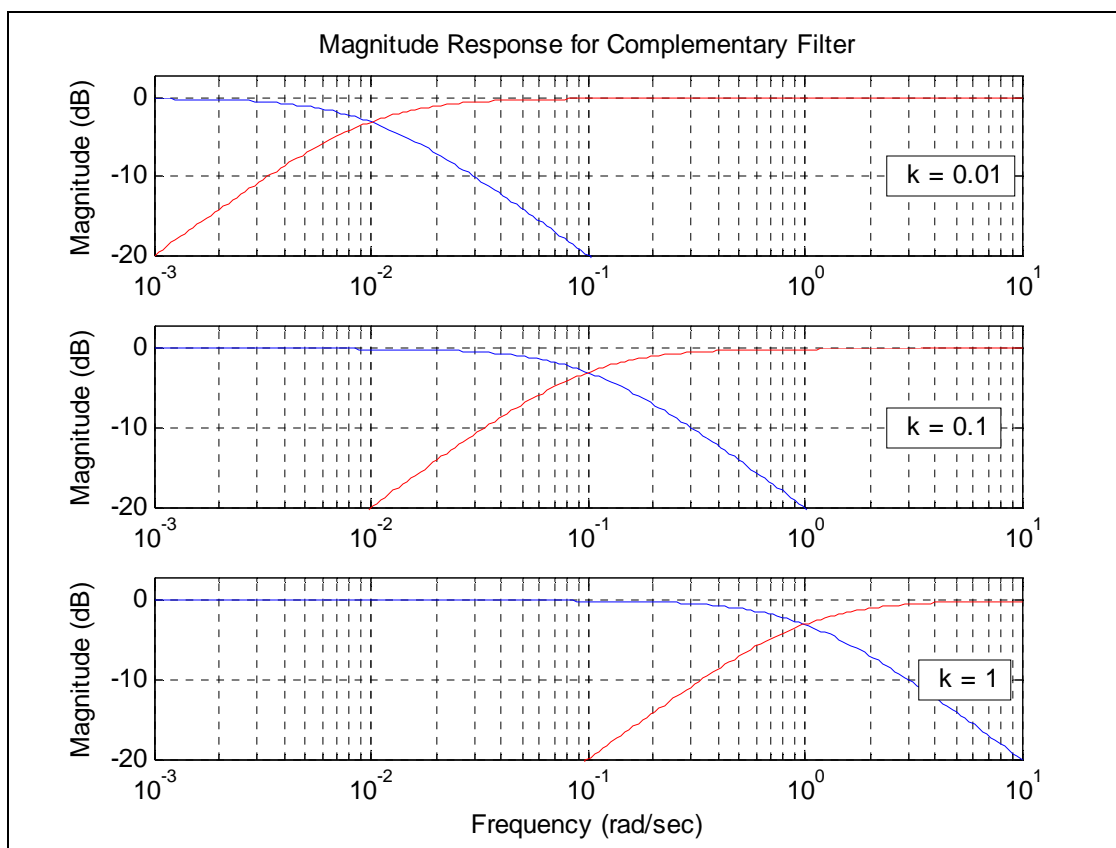
Figure 27.   Magnitude response of static branch (blue) and dynamic branch (red).
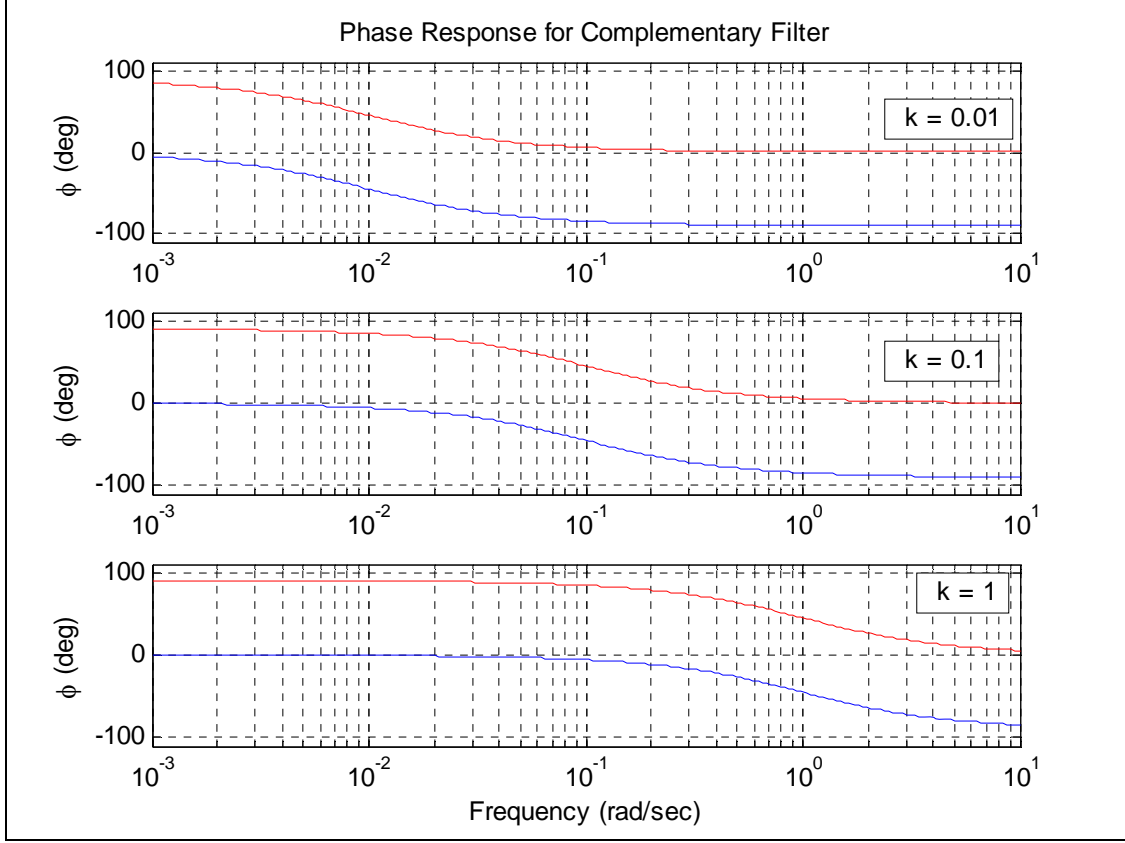
Figure 28.   Phase response of static branch (blue) and dynamic branch (red).

With the superposition principle in mind, we have that the output of the complementary filter is the sum of the static branch and the dynamic branch transfer functions, such that,

$$\hat{Q}(s) = \frac{s}{s+k} Q_d(s) + \frac{k}{s+k} Q_s(k) \tag{3.36}$$

If we assume that $Q_d(s)$ and $Q_s(s)$, which are computed from the angular rates and the FQA, respectively, are in fact equal to the true quaternion, $Q_T(s)$, then we have

$$\hat{Q}(s) = \left[\frac{s}{s+k} + \frac{k}{s+k} \right] Q_T(s) = [1] \, Q_T(s) \tag{3.37}$$

66

Therefore, our complementary filter has an overall transfer function of unity or an all-pass response. There will not be any input frequency that is preferentially attenuated in our complementary filter, and the phase of the output will be zero over all input frequencies. These characteristics make the complementary filter suited to those applications where a high-frequency measurement is to be blended with a low-frequency measurement of the same process or physical quantity.

Before concluding this discussion on the frequency response of the complementary filter, it is worthwhile to make one more examination of the frequency response plots. Figure 27 shows the magnitude frequency response for $k = 0.01$, 0.1, and 1. From the plots we see that the gain is not only the corner frequency for the individual branches in the complementary filter, but can also be thought of as a crossover frequency for the filter—the point where the magnitude response in both branches are equal. The plots serve to illustrate the concept that as the gain is increased, this crossover frequency also increases. Consequently, the total output of our complementary filter has a correspondingly larger portion derived from the static branch or $Q_s(s)$. Conversely, as the filter gain is decreased, the output will be weighed more greatly by the quaternion derived from the dynamic branch, $Q_d(s)$. In this fashion, the complementary filter can be tuned to allow a greater or lesser amount of its output to be influenced by one branch or the other.

E.   ERROR ANALYSIS OF THE COMPLEMENTARY FILTER

With a preliminary understanding of the complementary filter and in preparation for the filter performance analysis to be presented later, it is timely to consider the relationship between the filter output and the sensor errors, which are certain to be found within the accelerometers, magnetometers, and angular rate sensors. For this analysis, the sensor errors are assumed to be small and constant over the time period of interest, generally less than one second. These errors have a variety of sources including variations in scaling coefficients over time, misalignment of the individual sensors, cross-coupling between sensor axes, temperature dependence of the scaling coefficients, g-dependent variations in gyro sensitivity, just to name a few of these factors.

1.   Filter Performance Due to Gyro Error

The error analysis begins with the angular rate sensors.   Measurements, $\{\hat{\omega}_{xb}, \hat{\omega}_{yb}, \hat{\omega}_{zb}\}$, are expressed as the sum of the true angular rate, $\{\omega_{xb}, \omega_{yb}, \omega_{zb}\}$, and the sensor error, $\{\delta\omega_{xb}, \delta\omega_{yb}, \delta\omega_{zb}\}$ as in

$$
\begin{aligned}
\hat{\omega}_{xb} &= \omega_{xb} + \delta\omega_{xb} \\
\hat{\omega}_{yb} &= \omega_{yb} + \delta\omega_{yb} \\
\hat{\omega}_{zb} &= \omega_{zb} + \delta\omega_{zb}
\end{aligned}
\tag{3.38}
$$

The dynamic three-dimensional attitude is derived from these measurements by the differential equation

$$
\dot{\hat{q}}_d(t) = \tfrac{1}{2}\Omega(\hat{\omega})\,\hat{q}_d(t)
\tag{3.39}
$$

where $\Omega(\hat{\omega})$ is the skew-symmetric matrix formed with the angular rate measurements such that

$$
\Omega(\hat{\omega}) =
\begin{bmatrix}
0 & -\hat{\omega}_{xb} & -\hat{\omega}_{yb} & -\hat{\omega}_{zb} \\
\hat{\omega}_{xb} & 0 & -\hat{\omega}_{zb} & \hat{\omega}_{yb} \\
\hat{\omega}_{yb} & \hat{\omega}_{zb} & 0 & -\hat{\omega}_{xb} \\
\hat{\omega}_{zb} & -\hat{\omega}_{yb} & \hat{\omega}_{xb} & 0
\end{bmatrix}.
\tag{3.40}
$$

Substituting (3.38) into (3.39), we have that

$$
\begin{aligned}
\dot{\hat{q}}_d(t) &= \tfrac{1}{2}\Omega(\omega)\,\hat{q}_d(t) \;+\; \tfrac{1}{2}\Omega(\delta\omega)\,\hat{q}_d(t) \\
&= \dot{q}_d(t) \;+\; \delta Q_\omega
\end{aligned}
\tag{3.41}
$$

The first term on the right hand side of (3.41) is the true dynamic rate quaternion that is derived from the error-free component of the angular rate measurements. The second term is a constant in the expression for the quaternion rate; it comes from the small constant sensor error in the angular rate measurements. Next, assuming zero initial conditions, we take the Laplace transform of (3.41) and have that

68

$$s\hat{Q}_d(s) = sQ_d(s) + \frac{\delta Q_\omega}{s} \qquad (3.42)$$

Referring to Figure 26 and deriving the transfer function for the complementary filter output as was demonstrated in the previous section with (3.42) as an input, we have that the filter output is

$$\hat{Q}(s) = \frac{s}{s+k}Q_d(s) + \frac{s}{s+k}\frac{k}{s}Q_s(s) + \frac{s}{s+k}\frac{\delta Q_\omega}{s^2}$$

$$= \frac{s}{s+k}Q_d(s) + \frac{k}{s+k}Q_s(s) + \frac{1}{s+k}\frac{\delta Q_\omega}{s} \qquad (3.43)$$

If we have that $Q_d(s)$ and $Q_s(s)$ are equal to the true quaternion, then the filter output becomes

$$\hat{Q}(s) = Q_T(s) + \frac{1}{s+k}\frac{\delta Q_\omega}{s} \qquad (3.44)$$

The last term in (3.44) is the error in the filter output that is due to the small constant error assumed in the angular rate measurements. Applying the inverse Laplace transform to this term, we have that the error response in the complementary filter output due to the errors in these measurements is

$$error_{\delta\omega}(t) = \mathscr{L}^{-1}\left\{\frac{1}{s+k}\frac{\delta Q_\omega}{s}\right\} = \frac{\delta Q_\omega}{k}(1-e^{-kt}) \qquad (3.45)$$

This last result indicates that the error in the complementary filter output is related to the constant error in the angular rate sensors, δQ_ω, and inversely proportional to the filter gain. A non-zero gain will give an error that settles to a nominal value of $\delta Q_\omega/k$ after approximately five time constants or $5/k$ seconds. Furthermore, as (3.45) suggests, the error can be reduced by choosing k sufficiently large. However, as will be explained in a later section, it is not a simple matter of making k large in the

complementary filter to control the effects of the angular rate measurement errors. When k is large, the filter relies more greatly on the static quaternion, which in turn, is derived from the accelerometer/magnetometer measurements. These sensors, not surprisingly, come with their own set of errors that must be considered in some way.

Lastly, we consider the case when $k = 0$ in (3.45). In this situation, the complementary filter output depends entirely on the angular rate measurements. Expanding the exponential term with the Taylor series gives

$$\frac{\delta Q_\omega}{k}\left(1-e^{-kt}\right) = \frac{\delta Q_\omega}{k}\left(1-\left\{1-kt+\frac{(kt)^2}{2!}-\frac{(kt)^3}{3!}+\cdots\right\}\right)$$

$$= \frac{\delta Q_\omega}{k}\left(kt-\frac{(kt)^2}{2!}+\frac{(kt)^3}{3!}-\cdots\right)$$

(3.46)

Neglecting the terms in (3.46) that have power ≥ 2 gives

$$\delta error_{\delta\omega}(t) = \delta Q_\omega t$$

(3.47)

This last result indicates that when $k = 0$ in the complementary filter, there will be a linearly increasing error at the filter output due to the small angular rate sensor error.

2. Filter Performance Due to Accelerometer Error

Next, we turn our attention to the static quaternion that is derived from the FQA and consider the impact of small constant errors in the accelerometers and magnetometers of which there are three each. Within the FQA, the accelerometer measurements are used to compute the pitch and roll angles of the orientation, while the magnetometers are used to compute the yaw angle component. These angles are each cast into a quaternion form, such that q_{Yaw}, q_{Pitch}, and q_{Roll} contain the yaw, pitch, and roll angles, respectively. A final step in the FQA is to multiply these quaternions to give the complete orientation as shown

$$q_s = q_{Yaw}\, q_{Pitch}\, q_{Roll}$$

(3.48)

To begin the analysis, it is assumed there is a small constant error in the x^b–axis accelerometer, such that

$$\hat{a}_x^b = a_x^b + \delta a_x^b \qquad (3.49)$$

The remaining sensors are assumed free of any error in the ensuing analysis. After [79], the pitch angle, $\hat{\theta}$ is related to the x^b–axis acceleration by

$$\hat{a}_x^b = \sin \hat{\theta} \qquad (3.50)$$

Furthermore, we have that $\hat{\theta} = \theta + \delta\theta$, and using the familiar trigonometric identity $\sin(x + y) = \sin x \cos y + \cos x \sin y$, (3.50) becomes

$$\begin{aligned} \hat{a}_x^b &= \sin(\theta + \delta\theta) \\ &= \sin \theta \cos \delta\theta + \cos \theta \sin \delta\theta \end{aligned} \qquad (3.51)$$

We expect that a small accelerometer error, δa_x^b, will lead to small angular error, $\delta\theta$. Additionally, when $\delta\theta$ is small, $\cos \delta\theta \approx 1$ and $\sin \delta\theta \approx \delta\theta$, which simplifies (3.51) to

$$\hat{a}_x^b \approx \sin \theta + \delta\theta \cos \theta \qquad (3.52)$$

Lastly, taking (3.49) and (3.52) into consideration we have that

$$a_x^b = \sin \theta \qquad (3.53)$$

$$\delta a_x^b = \delta\theta \cos \theta \qquad (3.54)$$

Eq. (3.53) simply states that the error-free part of the acceleration measurement goes into computing the true pitch angle, while (3.54) relates the accelerometer error to the resulting pitch angle error. With this understanding of how δa_x^b introduces error into

the computed pitch angle, we seek to explore its impact on q_{Pitch} and ultimately on the static quaternion, q_s. First, we write the pitch quaternion as

$$\hat{q}_{Pitch} = \begin{bmatrix} \cos\frac{\hat{\theta}}{2} \\ 0 \\ \sin\frac{\hat{\theta}}{2} \\ 0 \end{bmatrix} = \begin{bmatrix} \cos\frac{\theta+\delta\theta}{2} \\ 0 \\ \sin\frac{\theta+\delta\theta}{2} \\ 0 \end{bmatrix} \tag{3.55}$$

Next, expanding cosine and sine terms with a first-order Taylor series, we have that

$$\hat{q}_{Pitch} = \begin{bmatrix} \cos\frac{\theta}{2} \\ 0 \\ \sin\frac{\theta}{2} \\ 0 \end{bmatrix} + \begin{bmatrix} -\frac{\delta\theta}{2}\sin\frac{\theta}{2} \\ 0 \\ \frac{\delta\theta}{2}\cos\frac{\theta}{2} \\ 0 \end{bmatrix}$$

$$= q_{Pitch} + \delta q_{Pitch} \tag{3.56}$$

We recognize that the first quaternion in the right hand side of (3.56) is the true pitch quaternion and that the second is an error quaternion that comes from the pitch angle error, $\delta\theta$. Since we have in (3.54) that the $\delta\theta$ is related to δa_x^b, then we can infer that δq_{Pitch} arises from the small accelerometer error that exists in $\hat{a}_x^b$.

The last step in this portion of the analysis is to establish how δq_{Pitch} manifests itself in the static quaternion. Starting with (3.48) and substituting (3.56) into this expression gives

$$\hat{q}_s = q_{Yaw}(q_{Pitch} + \delta q_{Pitch})q_{Roll}$$
$$= q_{Yaw} q_{Pitch} q_{Roll} + q_{Yaw} \delta q_{Pitch} q_{Roll} \tag{3.57}$$
$$= q_s + \delta Q_s$$

Eq. (3.57) shows that the output of the FQA is composed of the sum of a true static quaternion, q_s, and an error quaternion, δQ_s. This latter component is directly the

72

result of the small accelerometer error, δa_x^b, introduced at the beginning of this analysis. Since δa_x^b was assumed to be a constant in this analysis, then δQ_s will also be a constant if we make the additional assumption that there is no rotation in the roll and yaw angles. Taking the Laplace transform of (3.57) we have that

$$\hat{Q}_s(s) = Q_s(s) + \frac{\delta Q_s}{s} \tag{3.58}$$

Turning to the frequency domain representation of our complementary filter in Figure 26, and applying (3.58) as an input to the filter, we have that the output of the filter is now given by

$$\hat{Q}(s) = \frac{s}{s+k}Q_d(s) + \frac{k}{s+k}Q_s(s) + \frac{k}{s+k}\frac{\delta Q_s}{s} \tag{3.59}$$

Once again as before, assuming that the $Q_d(s)$ and $Q_s(s)$ are equal to the true quaternion, then the filter output becomes

$$\hat{Q}(s) = Q_T(s) + \frac{k}{s+k}\frac{\delta Q_s}{s} \tag{3.60}$$

The last term in (3.60) is recognized as the error in the quaternion output of the complementary filter. Taking the inverse Laplace transform of this term gives the time-domain representation of the error

$$error_{\delta Q_s}(t) = \delta Q_s(1 - e^{-kt}) \tag{3.61}$$

This result indicates that the error in the complementary filter output due to small δa_x^b settles to a steady-state value after approximately $5/k$ seconds. Furthermore, this result differs from (3.45), which described the filter error in terms of the gyro error, $\delta \omega$, in that the magnitude of the error does not depend on the filter gain and therefore can not be minimized or affected by a proper selection of k.

F.   MATLAB IMPLEMENTATION

The complementary filter shown in Figure 25 represents the architecture of a filter in continuous time. However, this filter can not be directly synthesized on a computer. Instead, to permit analysis in MATLAB, the filter was programmed as shown in Figure 29. The filter loop began with an initial estimate of the quaternion, $\hat{q}(n-1)$, which was computed from the static acceleration and magnetometer measurements using the FQA. For the initialization to be as accurate as possible, it was essential that $\hat{q}(n-1)$ be computed when the subject was stationary. It was during those times when the FQA was known to yield a reliable orientation estimate.

The algorithm then proceeded with the computation of a static quaternion, again using the FQA. The next step in the iteration was to compute the error signal incorporating the desired filter gain. The third step in the filter loop computed a dynamic quaternion rate using the three-dimensional angular rate. The dynamic quaternion rate and the error signal were then added in the subsequent step to produce another quaternion rate, which was the rate of change of the quaternion we wish to estimate. Finally, using a numerical integration technique, such as Euler's method, the estimated quaternion was derived. This result was then used to initialize the filter loop in a recursive fashion to produce the next estimated quaternion.

$\hat{q}(n-1)$

Begin
Complementary
Filter

$q_s(n) = fqa(a(n), m(n))$

Use accelerometer, magnetometer
measurements in FQA to get static
quaternion

$e(n) = k * \left[q_s(n) - \hat{q}(n-1) \right]$

Apply filter gain, k

$q'_d(n) = \frac{1}{2} \Omega(\omega(n)) * \hat{q}(n-1)$

Use angular rates to get dynamic
quaternion

$\hat{q}'(n) = e(n) + q'_d(n)$

Compute the estimate of the
quaternion rate

$\hat{q}(n) = \hat{q}'(n) * \Delta T(n) + \hat{q}(n-1)$

Use Euler's method to integrate previous
result
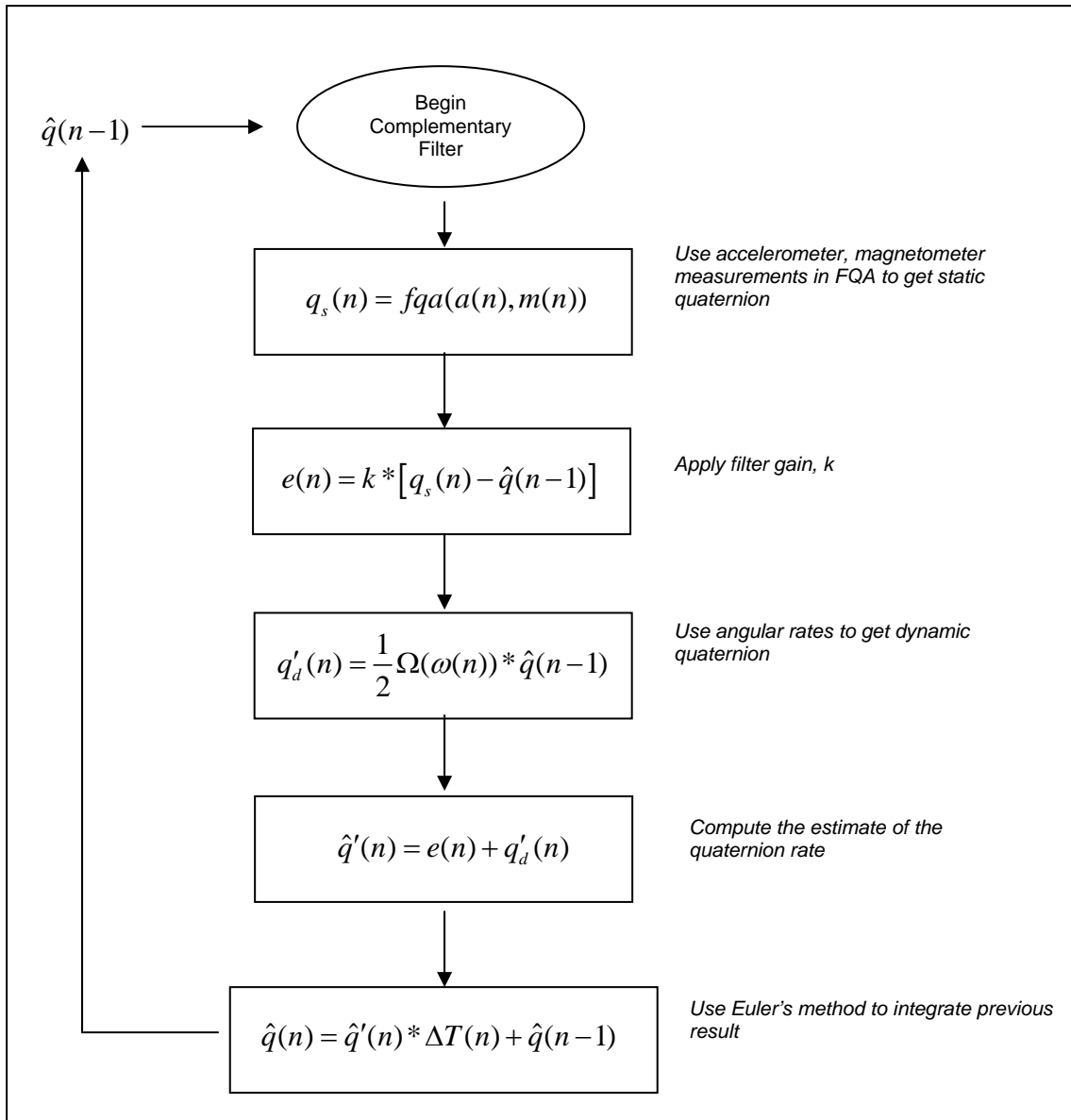
Figure 29.   Flow chart for MATLAB implementation of the complementary filter.

G.   A MODEL FOR PENDULUM MOTION SENSOR DATA

The previous section described how the complementary filter was programmed in MATLAB. In the present section, we introduce a model of the vertical pendulum. The purpose of this model was to generate data to aid in the study of the performance of the complementary filter. In this synthetic pendulum, we consider a sensor module, like the 3DM-GX1 for example, to be attached at the swinging end. Expressions for the sensor data were derived that described what the output of each sensor would be once the pendulum was set into motion.   In this manner, all of the real-world sensor artifacts, such as gyro bias, accelerometer offset, and motion-induced acceleration, which undesirably influenced the orientation estimate, could be controlled and examined in this simulated experiment.

1.   Pendulum Model for MATLAB Simulation

Figure 30 shows the pendulum with length, L; mass, m; viscous damping, c; and angular displacement, θ. The coordinate system, $\langle x^b \ y^b \ z^b \rangle$, shown at A coincides with the sensor body coordinate system, where the y^b axis is not shown because it is directed orthogonal to the $\langle x^b z^b \rangle$ plane and projects inward into the plane of the paper. The axis of rotation for the pendulum lies along the positive y^b axis, such that a positive rotation is in the clockwise direction.

Summation of the forces acting at point A along the x^b axis gives the dynamic equation

$$\sum F_{x^b} = mL\ddot{\theta} = -mg\sin\theta - c\dot{\theta} \tag{3.62}$$

Equation (3.62) is a non-linear second-order differential equation. An analytical solution is not straightforward, but using one of MATLAB's solvers for ordinary differential equations, such as, *ode45( )* for example, a numerical solution can be easily determined.

76
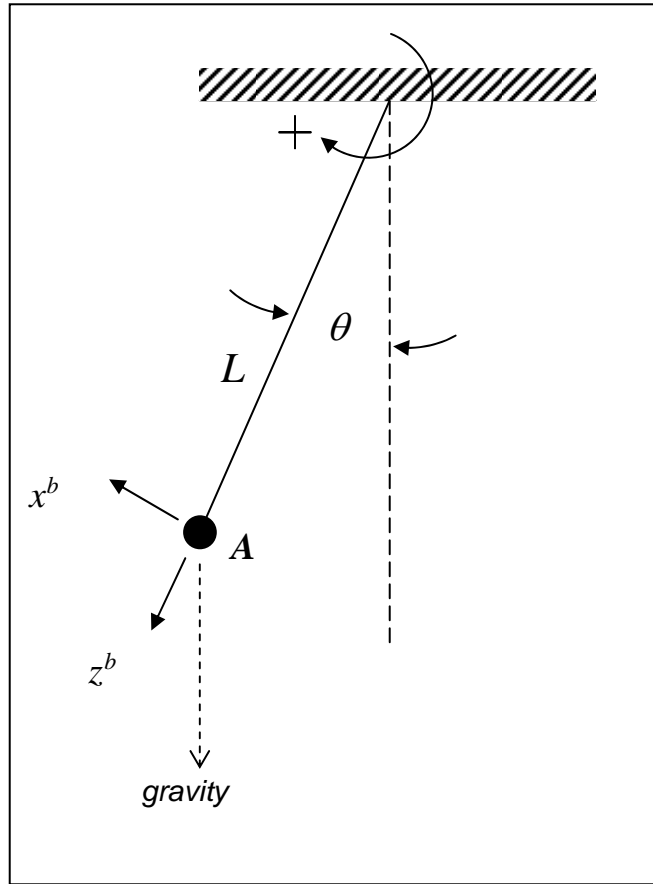
Figure 30.   Pendulum model for MATLAB simulation.

With the parameters for our pendulum defined as $L = 1$ meter, $g = 9.81$ m/s^2, $m =$ 1 kg, $c = 0.313$ N·sec, and initial conditions $\theta(0) = 10°$, $\dot{\theta}(0) = 0$, the pendulum angle with respect to time, along with the angular velocity and angular acceleration are shown in Figure 31.
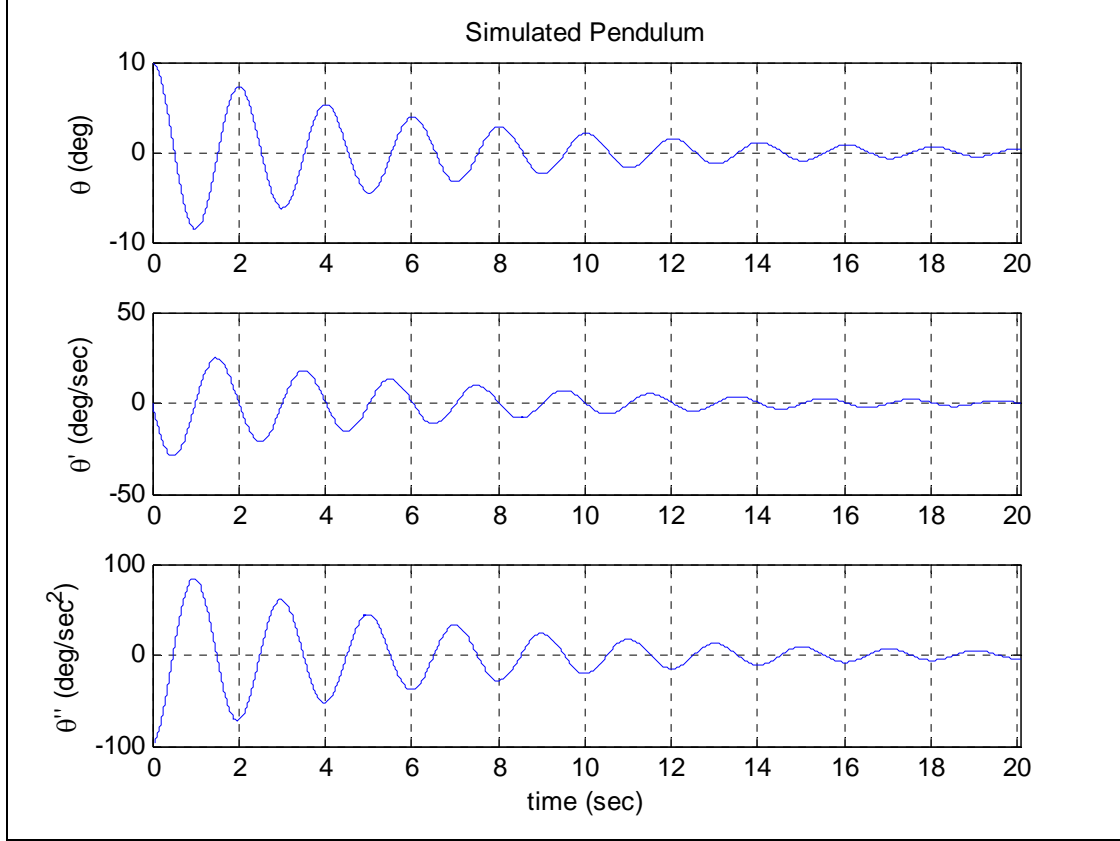
Figure 31. Pendulum motion with $\theta(0) = 10^{\circ}$, $L = 1$ meter, g = 9.81 m/s^2, $m = 1$ kg, and $c = 0.313$ N·sec.

2. Sensor Data Generated with the Pendulum Model

The previous section provided the pendulum's angular displacement, velocity, and acceleration. Next, we consider a sensor module, such as the 3DM-GX1, attached to point *A* of the pendulum. Recall that the sensor module was equipped with three accelerometers, three magnetometers, and three angular rate sensors. In this section, we seek expressions that describe each of these sensor outputs when the module is stimulated by the pendulum motion. Given these expressions for the sensor data outputs, we will have a well understood set of data that can be used in the study of the complementary filter.

First, we consider the accelerometers. In the 3DM-GX1, there were three orthogonally mounted accelerometers. When the pendulum is stationary at some angle, θ, the three accelerometers sense a component of the gravity vector that is projected onto each of the sensor body axes,

$$
\begin{aligned}
g_{x^b} &= -g \sin \theta \\
g_{y^b} &= 0 \\
g_{z^b} &= g \cos \theta
\end{aligned}
\tag{3.63}
$$

Under static conditions, the accelerometer outputs would be solely comprised of the gravitational acceleration, and (3.63) could be used to compute the pendulum angle. However, when the pendulum is in motion, the accelerometers at point A sense an added acceleration due to this motion. There will be a centripetal (normal) acceleration directed toward the center of rotation and coincident with the z^b axis. Additionally, there exists a tangential acceleration orthogonal to the centripetal acceleration that lies along the x^b axis. Therefore, (3.63) will not suffice to describe the accelerometer outputs correctly.

To determine how the accelerations due to motion combine with the acceleration due to the gravity vector, we consider a simple model of the accelerometer, as shown in Figure 32. The simple model has a proof mass, m, suspended in a case by a spring with a spring constant, k. Although not shown in the figure, there is also a viscous damping with a constant coefficient, c. When the proof mass is accelerated due to some externally applied force, it will be displaced by an amount, x, relative to the case structure. This displacement will be proportional to the applied force and the corresponding acceleration. By means of an indirect measurement of this displacement, the accelerometer then makes available to the user the value of the applied acceleration. However, the influence of gravity on the proof mass must be taken into consideration.
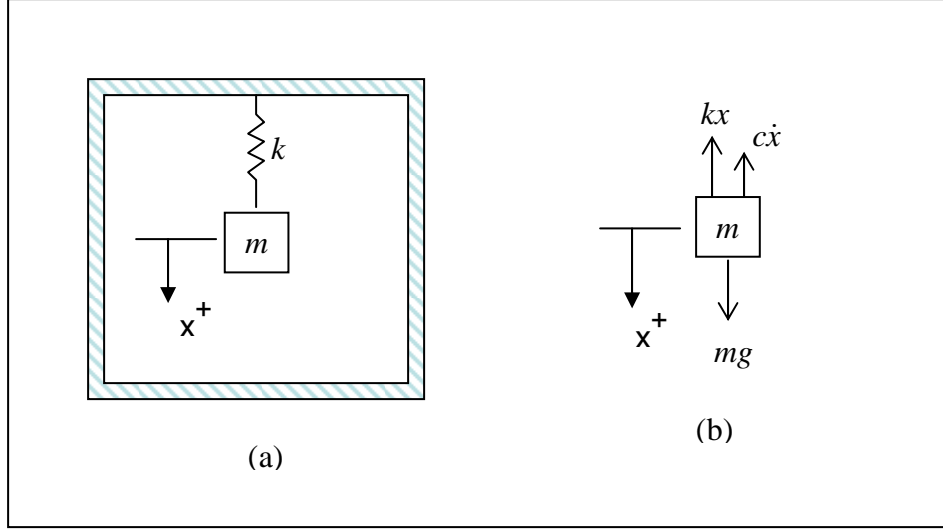
Figure 32. Accelerometer model. (a) Simple mass and spring model, and (b) free body diagram of the accelerometer proof mass.

Figure 32 also shows the free body diagram of the proof mass suspended within the accelerometer case and the following equation accounts for all the forces acting on the proof mass:

$$\sum F_{x^+} = ma = mg - kx - c\dot{x} \tag{3.64}$$

Dividing (3.64) by the proof mass, we have an expression in terms of the acceleration

$$a = g - \frac{k}{m}x - \frac{c}{m}\dot{x} \tag{3.65}$$

Furthermore, we recognize that the accelerometer produces at its output a value that is proportional to x, so we define f as the accelerometer output, and we have that

$$f = -\frac{k}{m}x$$

$$\dot{f} = -\frac{k}{m}\dot{x} \tag{3.66}$$

Substituting (3.66) into (3.65), we have an expression that gives the dynamic output of the accelerometer in terms of the applied acceleration, a, and the gravity, g,

$$a = g + f + \frac{c}{k}\dot{f} \tag{3.67}$$

To conclude the analysis of the accelerometer, we take the Laplace transform of (3.67) to get

$$A(s) = G(s) + F(s) + \frac{c}{k}sF(s) \tag{3.68}$$

Rearranging (3.68), we have the accelerometer output as

$$F(s) = \frac{A(s)}{1 + \frac{c}{k}s} - \frac{G(s)}{1 + \frac{c}{k}s} \tag{3.69}$$

Next, regarding the applied acceleration and the gravity as step inputs into the accelerometer for $t > 0$ such that

$$\begin{aligned} \mathscr{L}^{-1}[A(s)] &= a\,u(t) \\ \mathscr{L}^{-1}[G(s)] &= g\,u(t) \end{aligned} \tag{3.70}$$

then, if we apply the Laplace final value theorem to (3.69), we have that

$$\begin{aligned} f(\infty) = \lim_{s \to 0} sF(s) &= \lim_{s \to 0} s\left[\frac{\frac{a}{s}}{1 + \frac{c}{k}s} - \frac{\frac{g}{s}}{1 + \frac{c}{k}s} \right] \\ &= a - g \end{aligned} \tag{3.71}$$

Thus, we conclude that the accelerometer output is equal to the difference between the applied acceleration and the gravity vector. For the case of the triad of orthogonally-mounted accelerometers, (3.71) is tailored to the situation when only a component of the gravity vector is aligned with the sensor body axis. Therefore, (3.71) becomes the set of equations

81

$$f_{x^b} = a_{x^b} - g_{x^b}$$
$$f_{y^b} = a_{y^b} - g_{y^b} \qquad (3.72)$$
$$f_{z^b} = a_{z^b} - g_{z^b}$$

Finally, substituting (3.63) into (3.72) and accounting for the centripetal acceleration and the tangential acceleration of the pendulum, we have the accelerometer outputs given by

$$f_{x^b} = L\ddot{\theta} + g \sin\theta$$
$$f_{y^b} = 0 \qquad (3.73)$$
$$f_{z^b} = -L\dot{\theta}^2 - g \cos\theta$$

Eq. (3.73) provides the accelerometer outputs for the pendulum motion within the earth's gravity field. Conveniently, the accelerometer outputs are expressed in terms of the pendulum angular displacement, angular velocity, and angular acceleration.

Next, we consider the three angular rate sensors. Since the pendulum was constrained to swing in the $x^b z^b$ plane, then only the angular rate sensor aligned with the y^b axis would sense any rotation. The angular rate sensors oriented along the x^b axis and the z^b axis would not sense the pendulum's movement. Thus, we have that for the angular rate sensors, their outputs would be as

$$\omega_{x^b} = 0$$
$$\omega_{y^b} = \dot{\theta} \qquad (3.74)$$
$$\omega_{z^b} = 0$$

Finally, we come to the magnetometers. These sensors measure the component of the earth's magnetic flux density that has been projected onto each of the sensor body axes. To simplify this part of the pendulum model, we consider that the plane of motion of the pendulum is aligned with magnetic north. Doing this simplifies the analysis of the magnetometers. Figure 33 examines this aspect of the pendulum model. In the figure, the earth referenced coordinate system is shown as $\langle x^n y^n z^n \rangle$. The vector, $\vec{B}_e$, is the earth's magnetic flux density, which makes an angle, β, with the x^n axis; it is commonly referred to as the angle of inclination. This vector is known to vary both in magnitude and direction around the globe, however, for the local area, the values of $\vec{B}_e = 0.486$ gauss and $\beta = 60.483$ degrees were noted from the National Oceanic and Atmospheric Administration (NOAA) Web site. Finally, referring again to Figure 33, we derive the following expressions for the magnetometer sensors:

$$
\begin{aligned}
m_{x^b} &= \left|\vec{B}_e\right| \cos(\beta + \theta) \\
m_{y^b} &= 0 \\
m_{z^b} &= \left|\vec{B}_e\right| \sin(\beta + \theta)
\end{aligned}
\tag{3.75}
$$
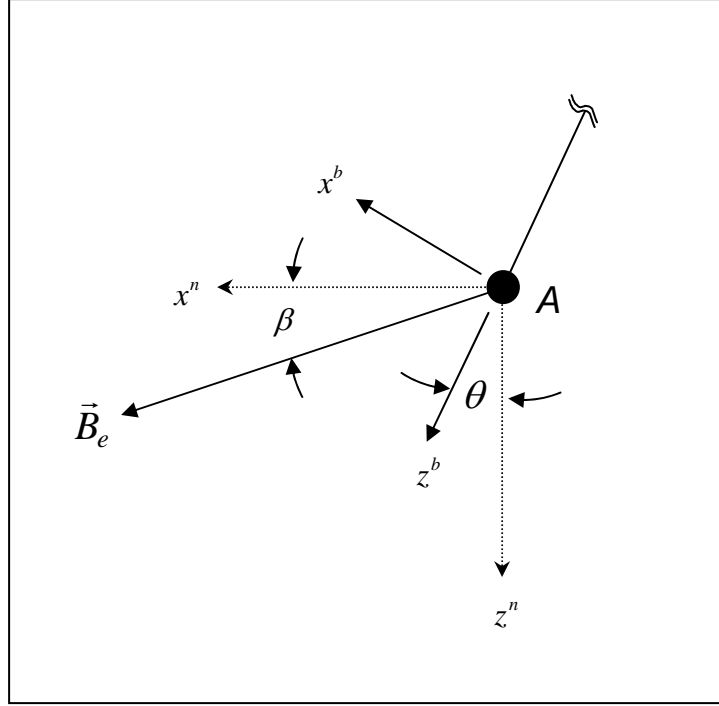
Figure 33.   Magnetic flux density vector relative to the sensor body axes ($x^b z^b$) and the navigation frame ($x^n z^n$).

With expressions for all nine sensors in hand, the next step was to generate simulated pendulum motion data and insert this synthetic data into our complementary filter. If the complementary filter was to work correctly, then the filter would produce the pendulum motion as described by our simulation model.

3. MATLAB Plots of Simulated Sensor Data

Given the expressions for the sensor outputs in (3.73), (3.74), and (3.75), the next task was to use these equations to generate synthetic sensor data. A MATLAB script was written that produced the synthetic sensor data set using these equations. A time increment was chosen to give an approximate sampling rate of 50 samples per second—similar to that provided by the 3DM-GX1. The script produced an array of incremental time and sensor data samples; it then saved the array in a data file called SimData.mat. The format of the data file was similar to that which was normally generated using the actual 3DM-GX1 sensor, except that the quaternion was not included here. Each row in the array corresponded to a sample time and the relevant sensor data from that sample time instant. The accelerometer sensor data was computed with (3.73) as shown in Figure 34. Figure 35 shows the angular rate sensor data that was derived from (3.74). Lastly, Figure 36 shows the magnetometer data generated with (3.75).
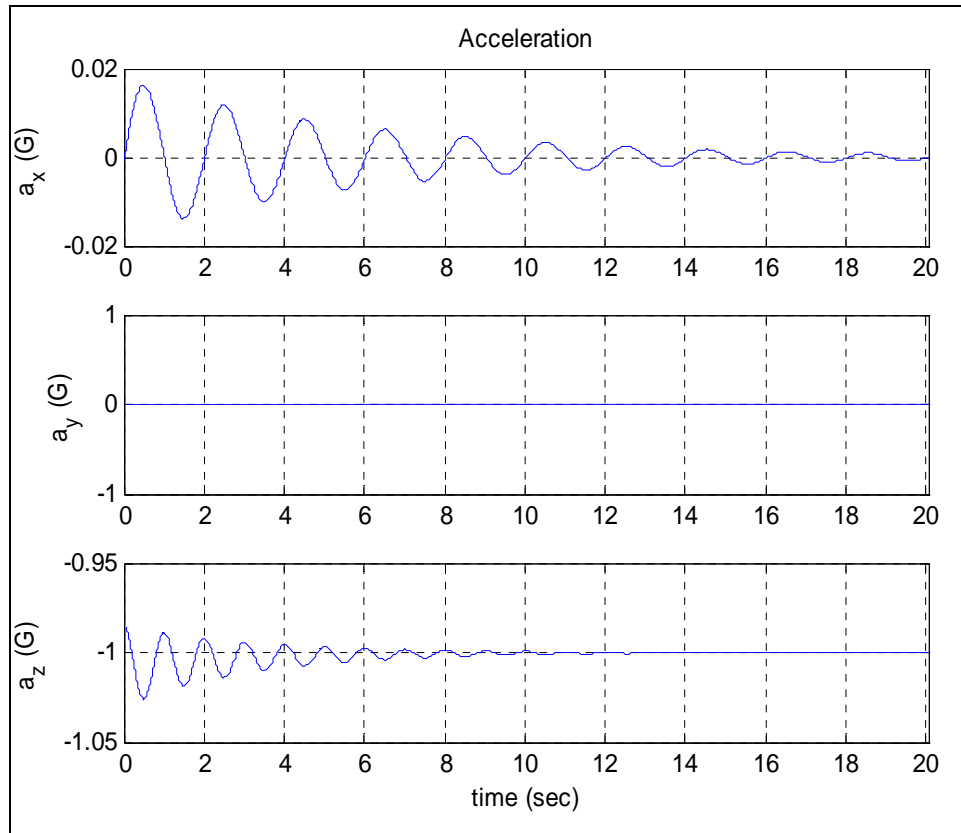
Figure 34.   Simulated accelerometer data from the pendulum model.
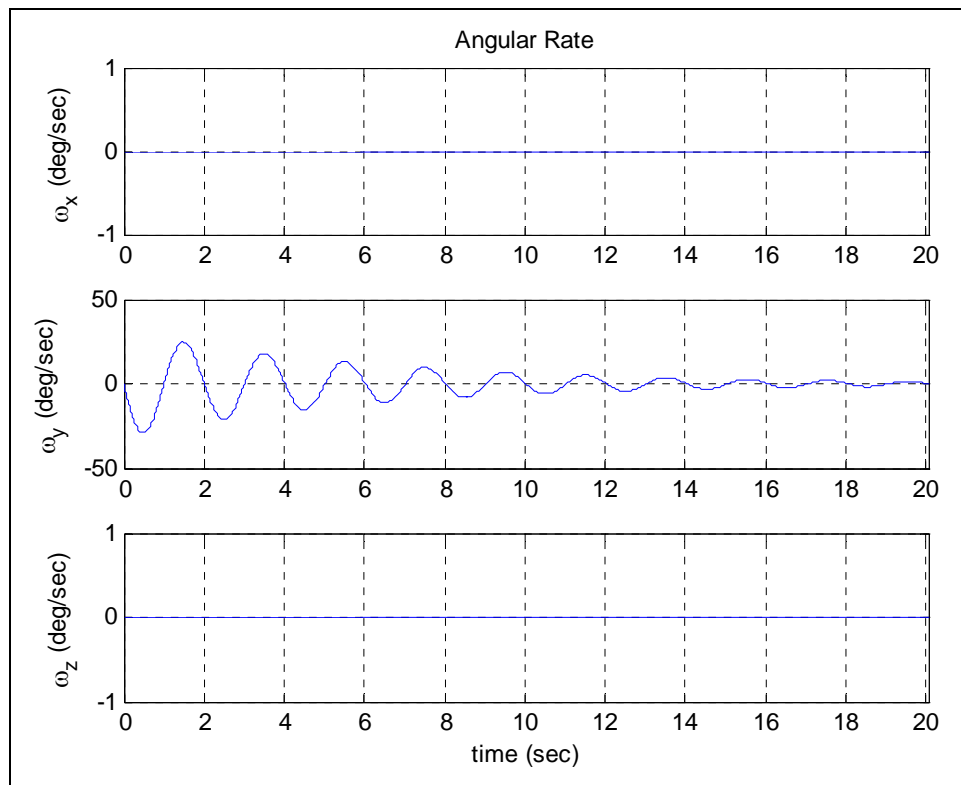
Figure 35.   Simulated angular rate data from the pendulum model.
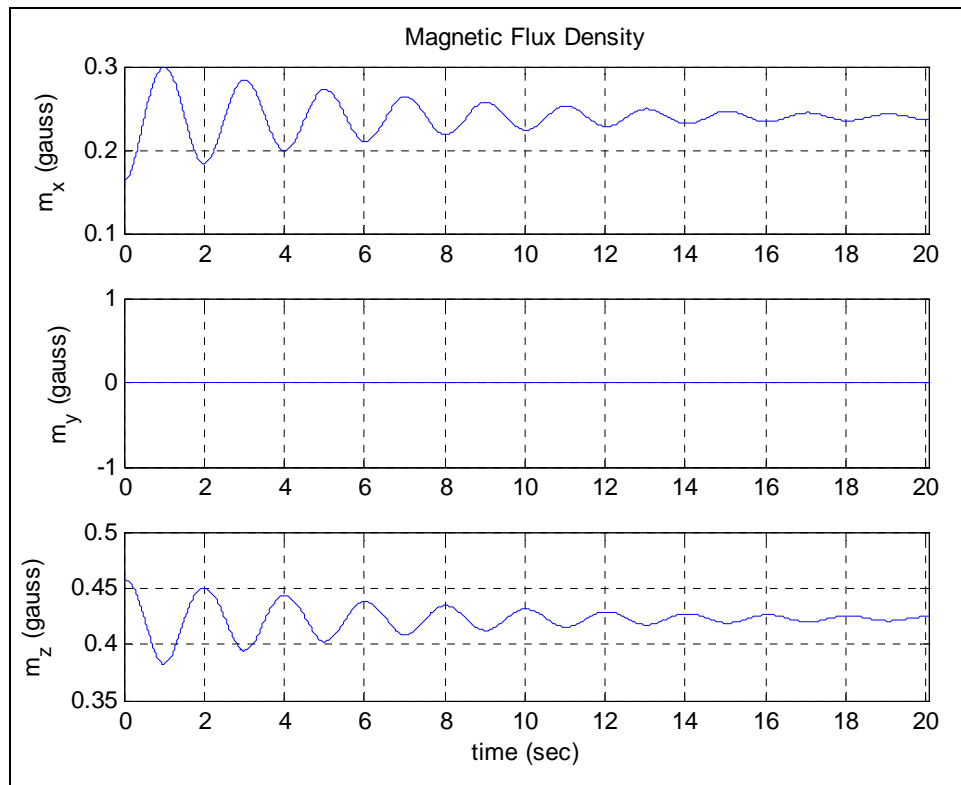
Figure 36.   Simulated magnetometer data from the pendulum model.

H. COMPLEMENTARY FILTER STUDY WITH SIMULATED PENDULUM

Leading up to this point, we have modeled the sensor outputs of the 3DM-GX1 attached to point *A* of the vertical pendulum. With the corresponding sensor data now available, we were able to begin a study of the performance of the complementary filter. The filter algorithm was programmed in MATLAB as shown in Figure 29. To begin iteration of the filter, we required an initial value for $\hat{q}(0)$ and to set the filter gain, *k*, to some desired value. Using the FQA, $\hat{q}(0)$ was computed using $\left\{ f_{x^b}(0) \; f_{y^b}(0) \; f_{z^b}(0) \right\}$ and $\left\{ m_{x^b}(0) \; m_{y^b}(0) \; m_{z^b}(0) \right\}$, which were derived with (3.73) and (3.75). For $k = 0$, the complementary filter only weighs the angular rate measurements in its output, neglecting $q_s(t)$ that was derived from the FQA. This was considered a good starting place to begin looking at the filter performance. Figure 37 shows the output of the complementary filter for the case $k = 0$. It shows the individual elements of the quaternion, $\hat{q}(t)$. However, since the performance of the filter is difficult to interpret by inspection of the quaternion, $\hat{q}(t)$ was converted into equivalent Euler angles and the result plotted in Figure 38.
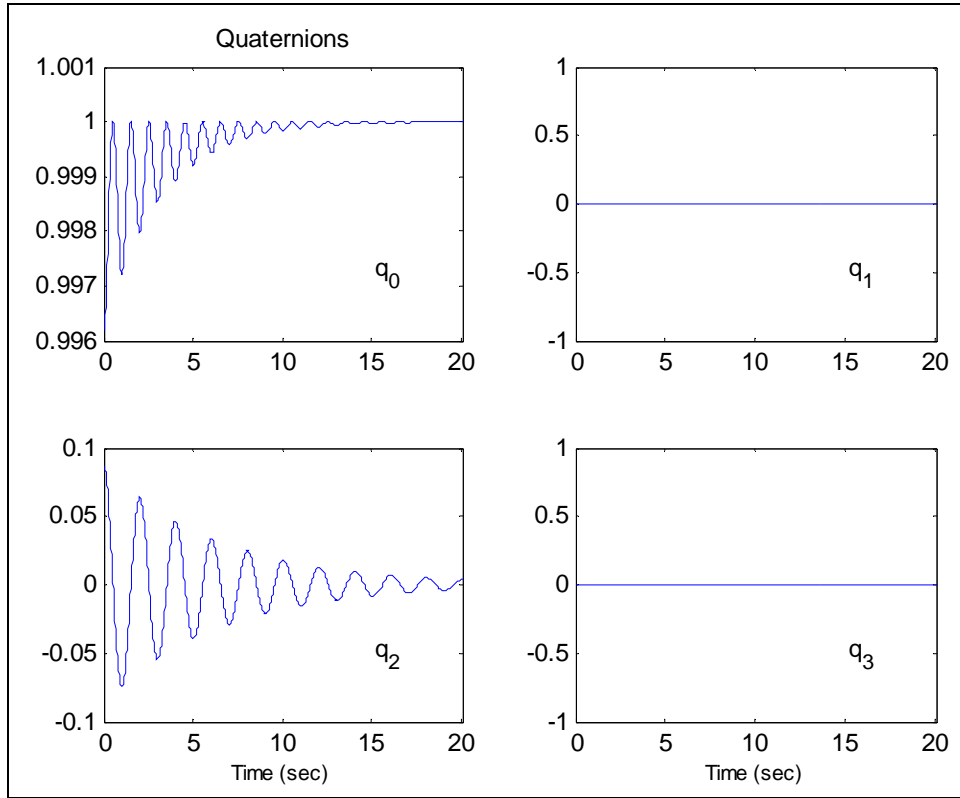
Figure 37.   Complementary filter output for $k = 0$.
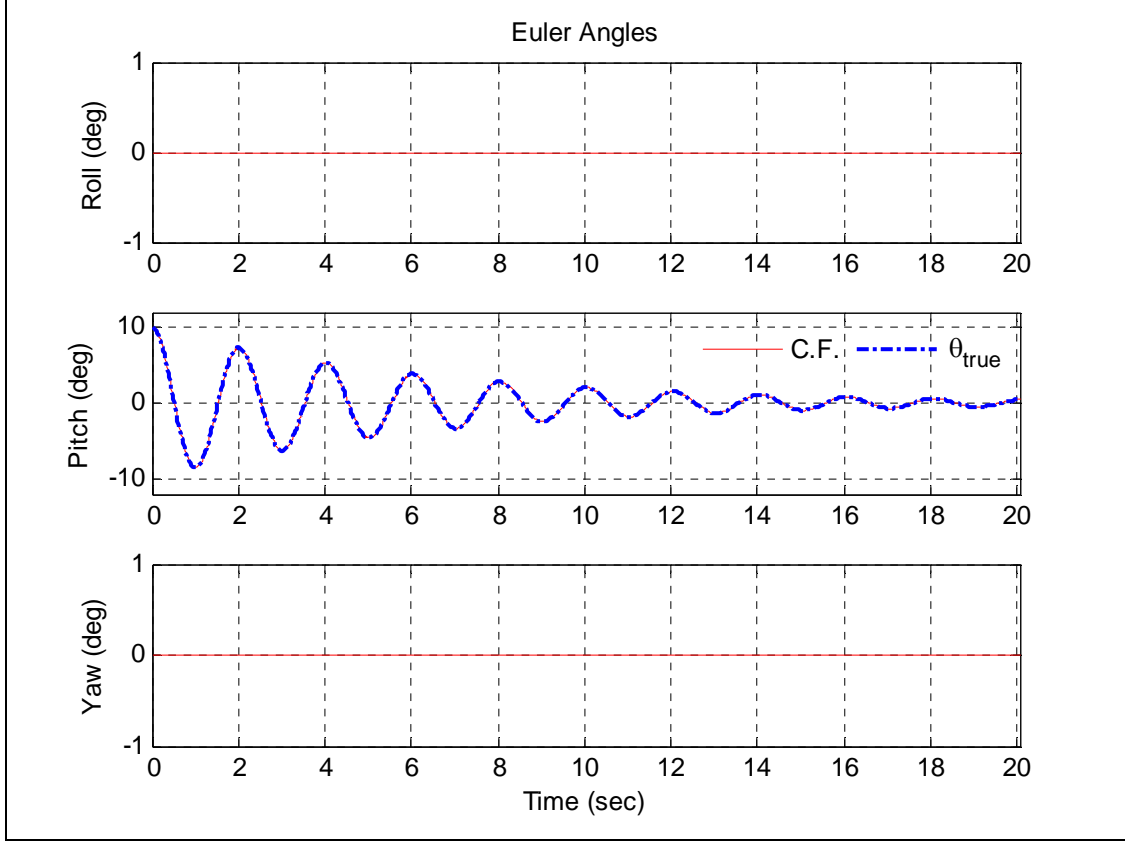
Figure 38.   Complementary filter output (red) shown in Euler angles, $k = 0$. True pendulum angle (blue). No difference between true angle and computed angle.

Figure 38 shows that the complementary filter (red) with $k = 0$ accurately tracks the true pendulum angle (blue) as given by the simulation model. Since there was no difference between the true pendulum angle and that computed by the complementary filter, the curves are shown superimposed in the pitch plot. The computed pitch angle reproduced all of the features of the true pendulum motion from the initial value of $\theta = 10$ deg to the end of the simulation period. The complementary filter also computed zero for the roll and yaw angles because there was no movement in those axes.

This example assumed ideal angular rate sensors that did not have any noise or bias in their output. In practice, however, all angular rate sensors possess some amount of error in sensitivity and bias. Therefore, to examine these types of sensor errors, we introduce a small bias error into the angular rate sensors. Microstrain specified in their documentation a 0.033% bias error for the 3DM-GX1. This value was used to create a new set of pendulum sensor data as described in the previous section.   The

complementary filter algorithm was repeated using the new sensor data to produce the pendulum angles shown in Figure 39. This figure reveals the effect of the small bias error on the computed angles when $k = 0$. The pitch angle tracked the true angle during the first few cycles, but began to drift away from the true track towards the end of the motion period. Where the roll and yaw angles were zero in the previous example, they now exhibited an error that grew without bound. This result is consistent with the error predicted in (3.47). With $k = 0$, the error due to the small angular rate sensor error is unbounded. However, if the filter gain were to be increased, then the error is expected to be contained to within some constant value. The next example explores this idea in more detail.
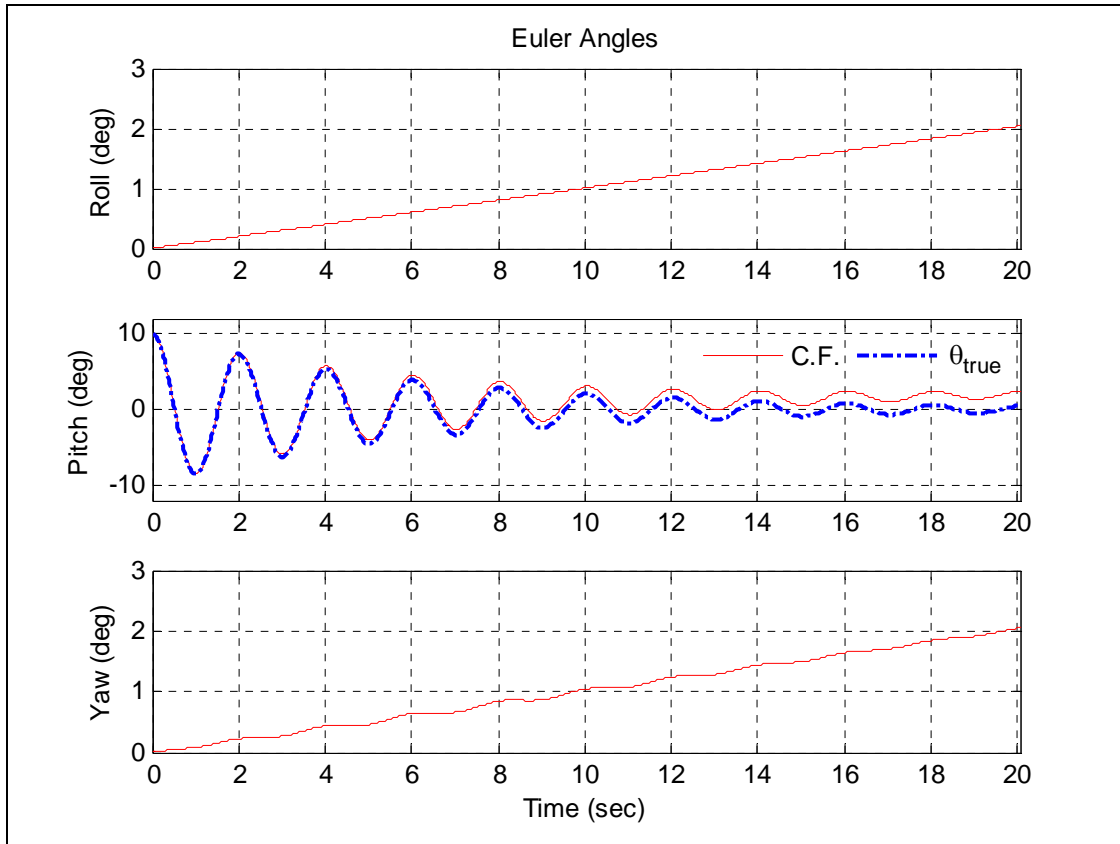
Figure 39.   Complementary filter output with small bias error in angular rate sensors and $k = 0$.

Next, we consider the performance of the complementary filter due to the FQA. For this example, the gain will be set to a value that weighs the static branch more greatly than the dynamic branch. Figure 40 shows the magnitude frequency response for $k = 50$. With this particular gain value programmed in the complementary filter, the pendulum angle, which has a radian frequency of 3.128 rad/sec, is computed mainly from the FQA. At this frequency, the dynamic branch is attenuated by more than 20 dB. Thus, its contribution to the filter output is suppressed more than 100 times than that of the static branch.
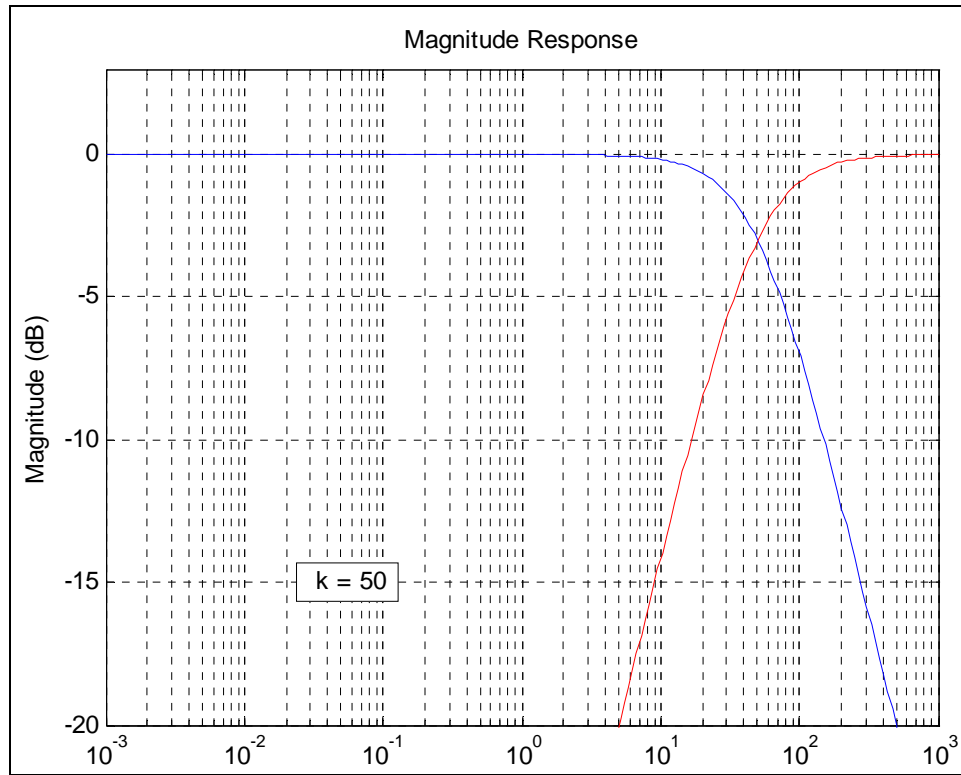
Figure 40. Magnitude response of the complementary filter with $k = 50$. Static branch (blue), dynamic branch (red).

Using this gain value, the complementary filter output is examined in Figure 41. The roll and yaw angles show a small error on the order of 0.002 degrees. This is the result of the small bias error introduced into the angular rate sensors. Furthermore, it is noted that the error does not seem to grow in time as it does in Figure 39. But instead, the error remains constant throughout the period of the pendulum motion, as indicated by (3.45). Lastly, the figure also shows the pitch angle of the pendulum. Examination of this plot shows that the complementary filter (red) is not able to track the true pendulum angle (blue). However, this is not due to the filter algorithm, but is an artifact of the accelerometer measurements which not only sense the acceleration due to gravity, but also have the response due to the centripetal and tangential acceleration, see (3.73).
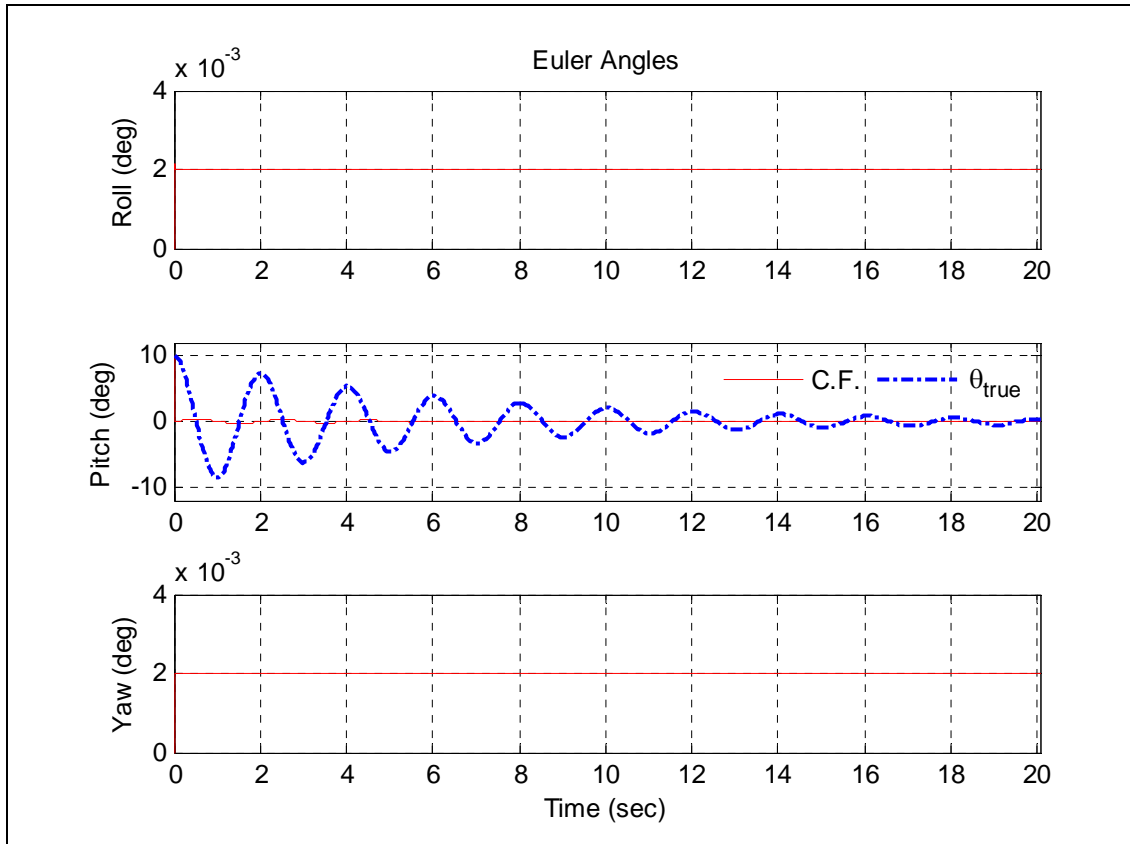
Figure 41.   Filter output (red) with $k = 50$. True pendulum angle (blue).

To explore this last notion in greater detail, the simulated pendulum data was generated once again, however the centripetal acceleration and tangential acceleration were omitted from the expressions for the accelerometer output, see (3.73). With this new data provided to the complementary filter, Figure 42 shows that the static branch does give an accurate orientation when it is given accelerometer measurements that are comprised only of acceleration due to the sensed gravity vector. As seen in the figure, the true pendulum angle (blue) and the complementary filter angle (red) are superimposed in the pitch angle plot. Interestingly, the roll angle shows a small oscillation where none had existed previously. This is explained by considering the tangential acceleration. Coincidentally, it oscillates in a similar fashion, but with an opposite phase. When both components of acceleration are accounted for, as they are in Figure 41, the oscillation cancels and only the error due to the gyro bias persists.
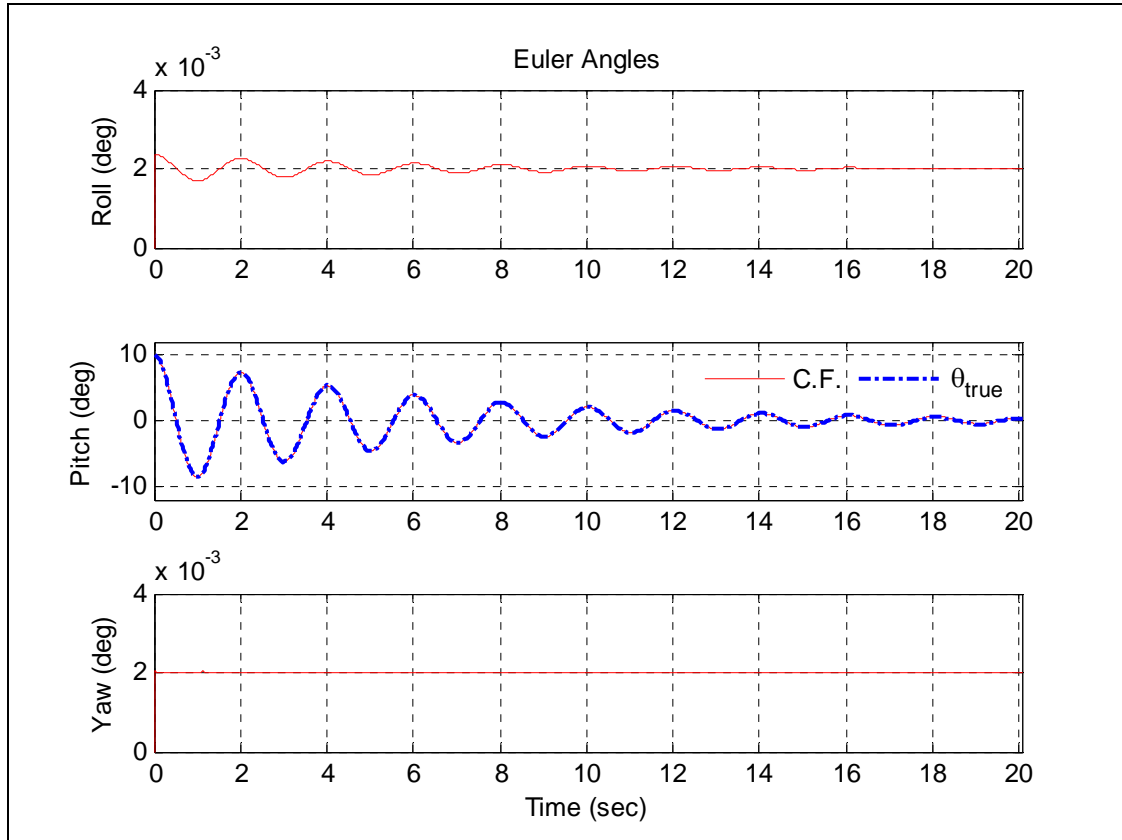
Figure 42.   Filter output (red) with $k = 50$. Tangential and centripetal acceleration omitted from accelerometer measurements. True pendulum angle (blue).

Figure 42 illustrated that the source of angular error in the FQA is due to non-gravitational accelerations. Practically speaking, however, the accelerometers respond to any and all acceleration and are not capable of discriminating between those accelerations due to the changing orientation and those arising from linear or rotational accelerations. Thus, if the accelerometers are to be a part of the orientation sensing solution, some means of mitigating the error in $q_s(t)$ that arises because of the non-gravitational accelerations must be identified.

Continuing our study of the complementary filter performance, the situation for pendulum motion with large damping is investigated. Here, the viscous damping is increased to 5.95 N·sec to produce the pendulum motion shown in Figure 43. Comparing this with the pendulum motion shown in Figure 31, which was the case for viscous damping equal to 0.313 N·sec, we see that the pendulum moves much more slowly and does not oscillate about the vertical. Next, the simulated sensor data is applied to the complementary filter with $k = 50$. The complementary filter output is shown in Figure 44. Recall that this value of gain caused the filter to weigh $q_s(t)$ more greatly than $q_d(t)$, as seen in Figure 40. The accelerometers have a response due to gravity, as well as, the centripetal and tangential accelerations. However, since these latter accelerations are smaller because of the pendulum's retarded motion, the accelerometer outputs have a larger component due to the sensed gravity vector. This in turn improves the filter's overall ability to determine the pendulum angle. The pitch angle error is less than two degrees at $t = 1$ sec, and decreases to less than 0.2 deg at $t = 2$ sec. The error in the roll and yaw angles was due to the small bias error introduced earlier into the angular rate measurements. Furthermore, we note that the error does not grow in time, but remains constant as shown in the figure.
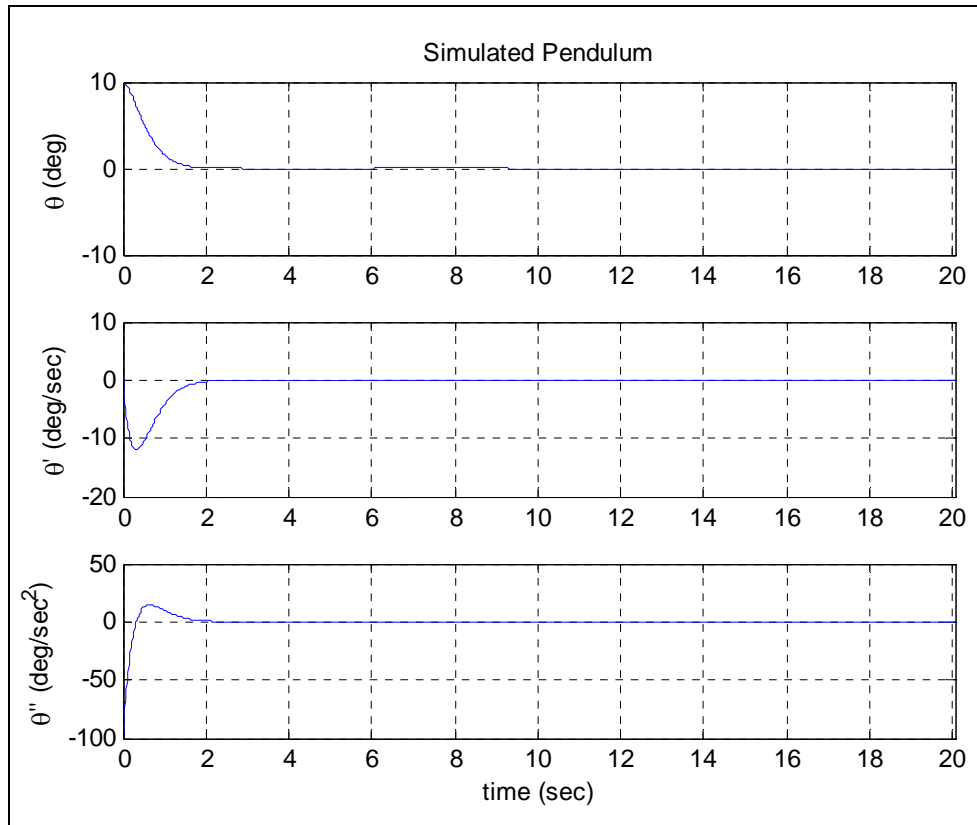
Figure 43.   Pendulum motion with viscous damping, c = 5.95 N·sec.
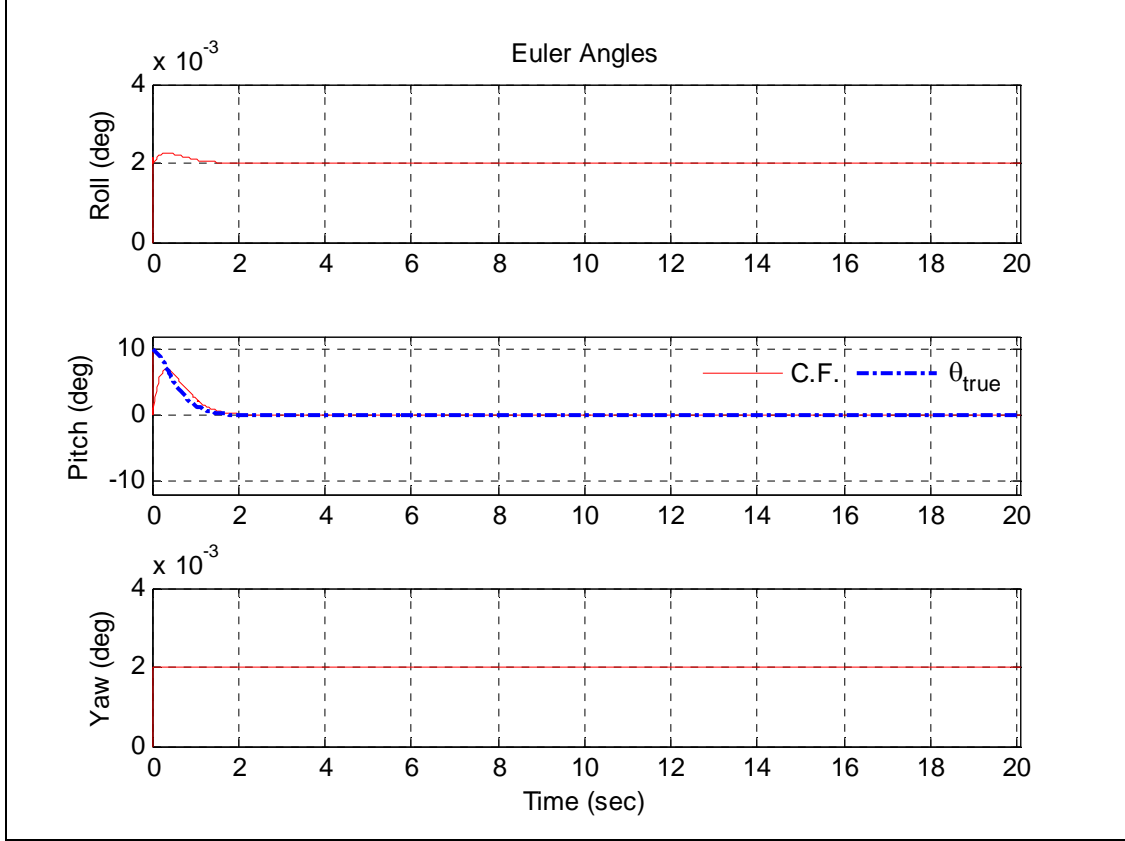
Figure 44.   Complementary filter output (red) with $k = 50$. True pendulum angle (blue).

Up to this point, we have examined the complementary filter with filter gain $k = 0$ and $k = 50$. To conclude our study of the complementary filter performance using the simulated pendulum, the pendulum simulation was conducted once more, but this time the filter gain will be set to a nominal value of $k = 1$. This value was selected without regard to optimizing the performance of the filter, but rather to examine the performance at some intermediate value of filter gain.   The pendulum viscous damping is set to $c = 0.313$ N·sec, which gives the pendulum motion shown previously in Figure 31. With this value of gain, the resulting filter performance is shown in Figure 45. The roll and yaw angles have a constant error (after the transient response) on the order of 0.1 degrees, which is due to the gyro bias error that was included in the simulation. The pitch angle error is at most 1 degree, but appears to track better than the case when

$k = 50$. An effort to optimize the error was not made here, as this will be done later, but this exercise serves to illustrate the need for tuning of the filter gain to give desirable performance.
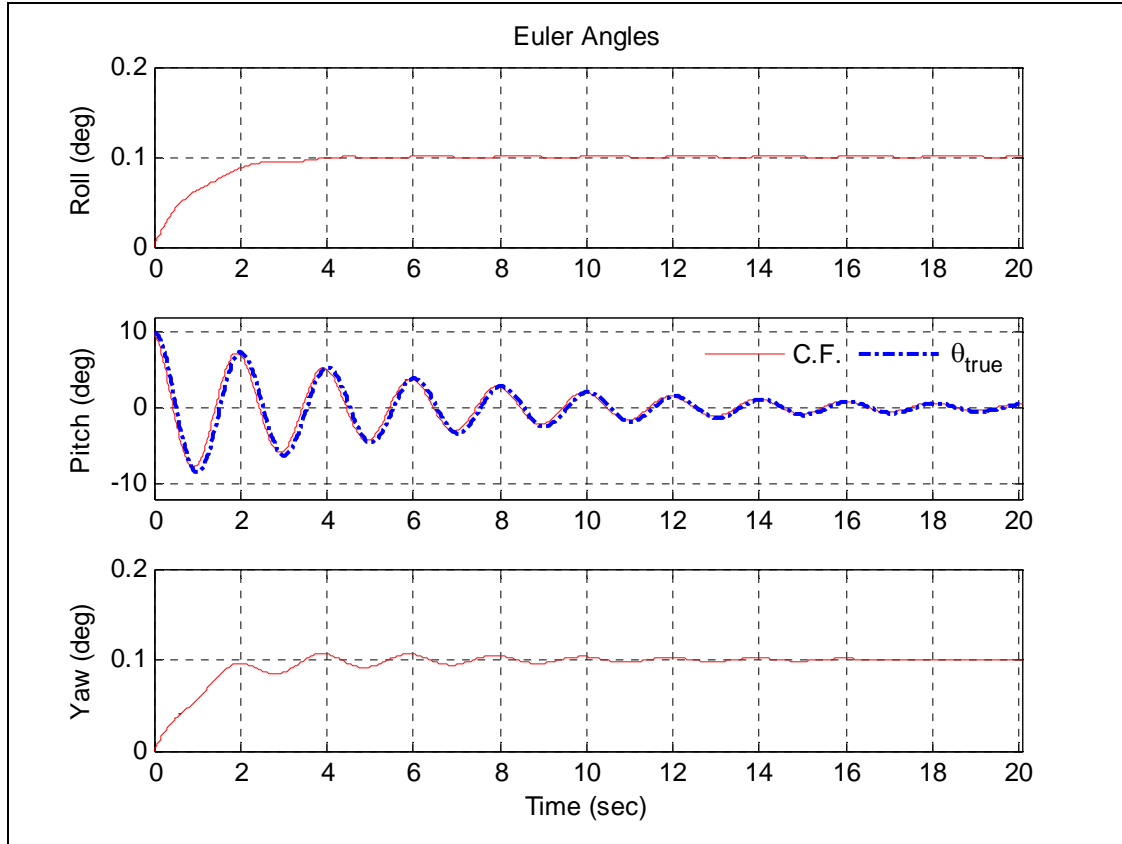
Figure 45.   Complementary filter output (red) with $k = 1$.   True pendulum angle (blue).

Summarizing, the performance of the complementary filter algorithm depends in large part on the value of gain, k, used within the filter.   A small k will place a greater weight on $q_d(t)$, so the filter output has a larger part derived from the angular rate sensors.   The ability of the filter to track the pendulum motion when this was the case was shown to be adequate during the initial period of the pendulum motion; however, any small bias errors in the angular rate sensor data results in an angle error that grows with time.   From this observation, we make the general statement that the filter gives

acceptable results with small k when it is utilized over a small period of time—before the error has grown beyond an acceptable level. Furthermore, we note that when the pendulum motion contained relatively large centripetal and tangential acceleration, a large k did not yield good angle tracking performance. But, a large k will give acceptable filter results when the pendulum motion was low with small centripetal and tangential acceleration, as was the case with large viscous damping. For this case, the filter tracked the pendulum angle after a brief transient period, and in the steady state it was able to maintain a small error. Additionally, the large k produced an output angle error that was constant and did not grow with time. Moving forward, the challenge for the application of the complementary filter is to identify a suitable value for k.

I.   FILTER PERFORMANCE WITH REAL PENDULUM DATA

The previous section described the performance of the complementary filter using simulated data. The selection of the gain, k, was discussed with regard to its effect on the ability of the filter to track the pendulum angle. In this section, we examine the complementary filter using real sensor data from the 3DM-GX1. The performance is compared against the pendulum angle measured with a 16-bit shaft encoder. To collect the data from the real pendulum, a LabView program was developed that ran on a Dell Latitude D620 laptop computer. It read the raw counts from the 16-bit shaft encoder, as well as, the sensor data from the 3DM-GX1 attached to point A. Figure 46 shows a block diagram of the data acquisition system. The LabView program controlled the operation of the National Instruments USB-6501, which provided the necessary interface for the eleven control/data lines of the A58 encoder. Additionally, the program read the sensor data from the 3DM-GX1 through the laptop's RS-232 serial communications port. All the data was arranged into a time-stamped array, which was written to a data file on the computer hard drive. Later, the data file was imported into MATLAB for processing and analysis.
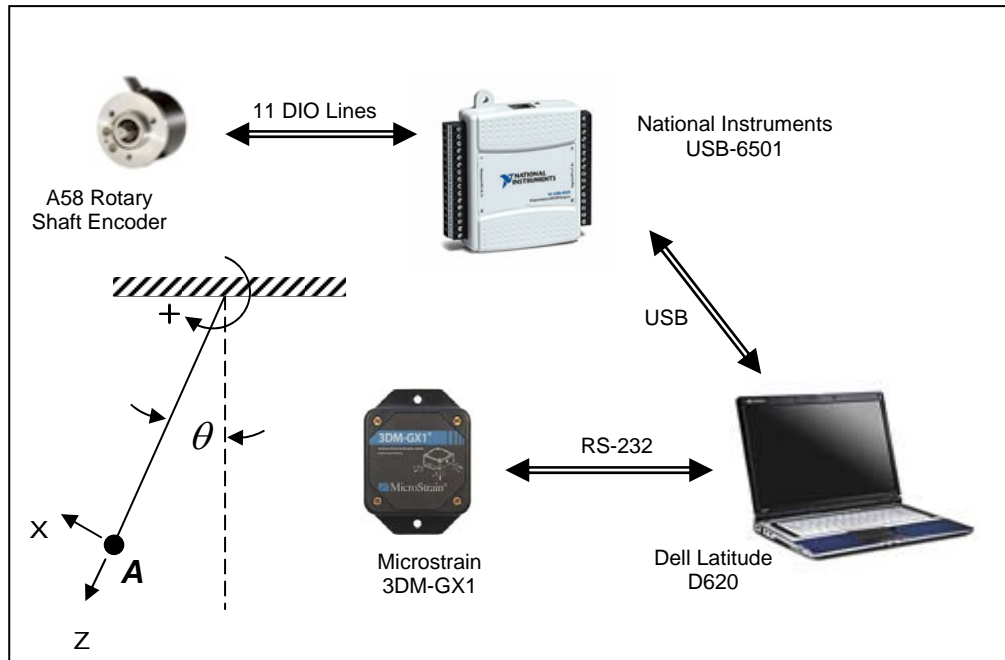
Figure 46.   Data acquisition system developed for the vertical pendulum.

The vertical pendulum provided a good platform to investigate the complementary filter performance. It was easy to change the length of the pendulum to yield different natural frequencies, and the amplitude of oscillation could be made to vary, as well. Numerous trials were conducted in the laboratory with the vertical pendulum and the 3DM-GX1. Figure 47 shows the complementary filter output with the pendulum length adjusted to 1 meter and the filter gain, k, set to 0.15. The computed pitch angle (red) appears to follow the angle measured with the A58 encoder (blue) to within two degrees. The roll and yaw angles exhibit an error of similar magnitude. The blue lines shown in the roll and yaw plots coincide with the initial computed angles; it is not an indication of an encoder measurement along those axes. The roll and yaw plots, however, show some computed motion in these angles. Since the data acquisition system does not provide a means for measurement of motion in these angles, it can not be concluded with certainty that the angular error observed in the computed roll and yaw angles is wholly due to the complementary filter algorithm. The pendulum shaft is made of a wooden dowel and may exhibit some twisting and flexing when in motion. Secondly, because no means for precise alignment of the sensor body axes with the

pendulum axes was available, the motion observed in the roll and yaw axes may in fact be due to a small pendulum alignment error. Therefore, some of the angular motion observed in these plots may be accurate. On the other hand, the 3DM-GX1, as well as, many other sensors of this type, possesses some degree of cross-coupling error. This error produces a sensor output in an axis normal to the axis of motion and is the result of the sensor axes not being completely orthogonal. Overall, the computed angles are on the order of two degrees from the expected angles and are certainly within the dynamic accuracy specified by the manufacturer for their own proprietary quaternion algorithm.
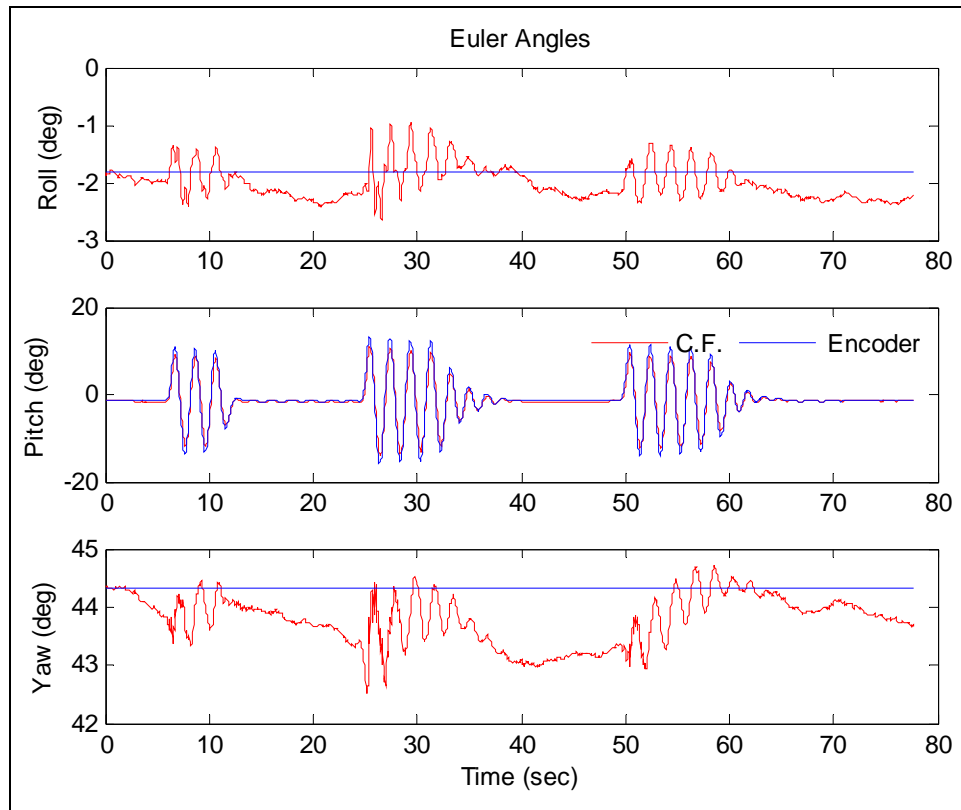
Figure 47.   Computed angles (red) vs. expected angles (blue) of the vertical pendulum, $k = 0.15$.

Figure 48 and Figure 49 compare the pendulum angles computed by the complementary filter with those acquired directly from the 3DM-GX1. The pitch angle, shown in Figure 48, indicates that the Microstrain algorithm is more accurate in this particular case since the angle is shown to be within 0.5 degrees of the encoder-measured angle. Figure 49 is similar to Figure 47, but it includes the angles derived from the

Microstrain algorithm. Comparing the roll angle computed by Microstrain's algorithm and that from our complementary filter, we note that they have similar behavior. The yaw angles differ somewhat, however, they both are within two degrees of the expected angle shown in blue. Finally, comparing the pitch angle, shown in the center of the plot, indicates that our complementary filter performs similarly to Microstrain's algorithm over the entire interval of motion.
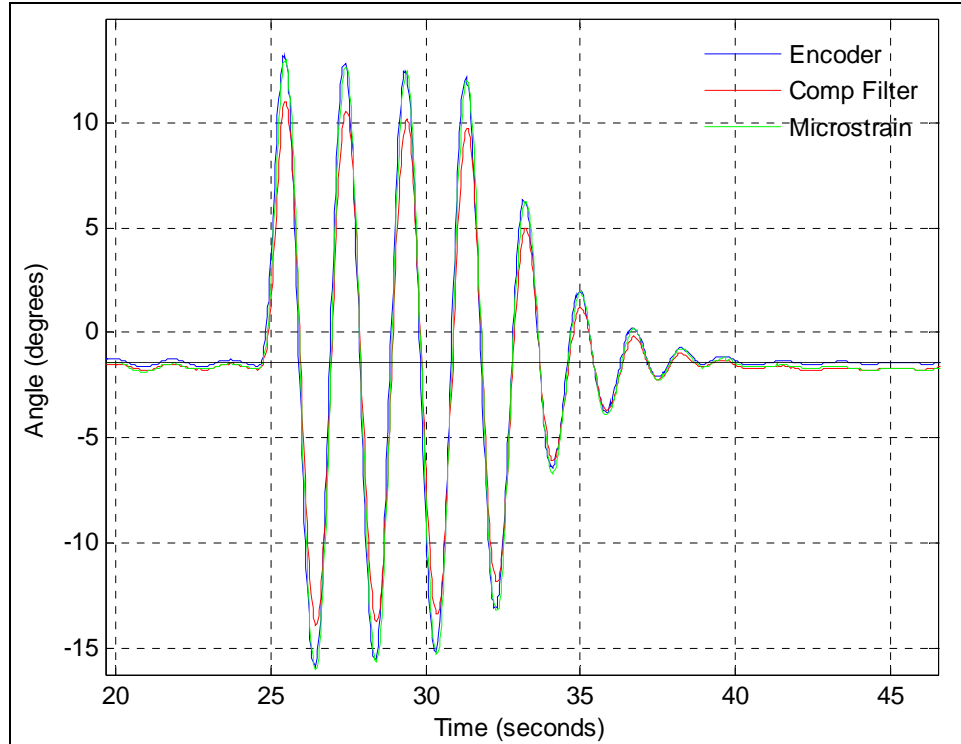
Figure 48.   Pendulum pitch angle: Complementary filter with $k = 0.15$ (red), 16-bit Encoder (blue), and Microstrain's proprietary algorithm (green).
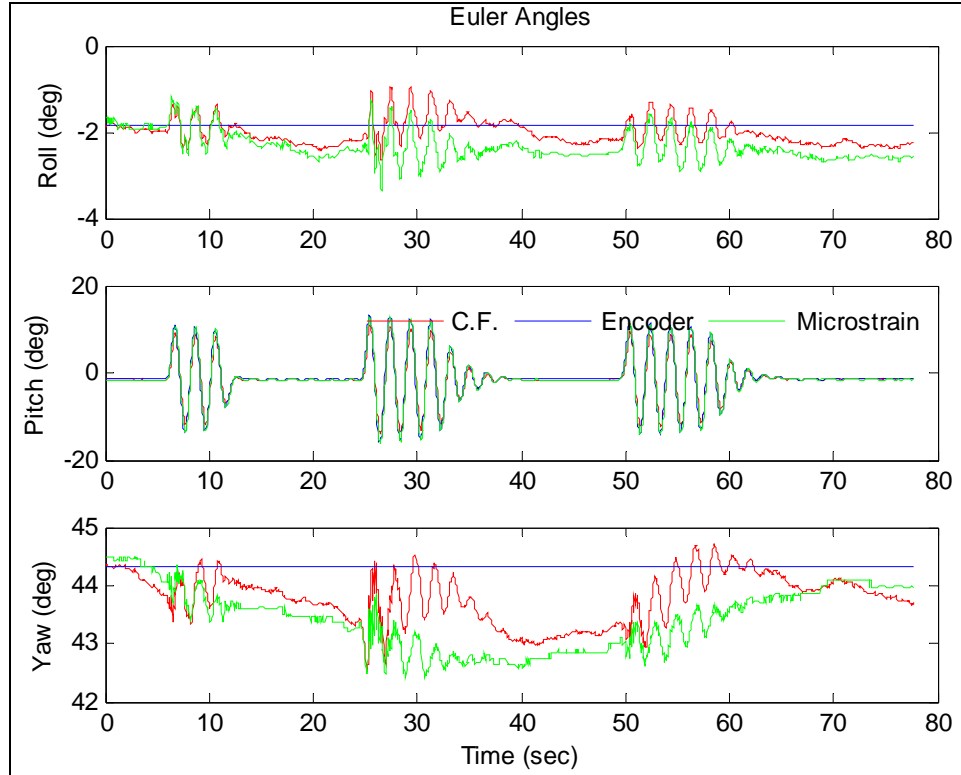
Figure 49.   Pendulum pitch angle: Complementary filter with $k = 0.15$ (red), 16-bit Encoder (blue), and Microstrain's proprietary algorithm (green).

Before leaving this section, the question arises as to what would be a reasonable value to use for the filter gain, k. The plots in Figure 47, Figure 48, and Figure 49 were all generated with our complementary filter having $k = 0.15$. In order to arrive at this value, several trials of the pendulum were conducted. The data from these trials were then processed with a MATLAB script that varied the range of k from 0 to 1. For each trial, the MATLAB script computed the total root mean square (RMS) angle error over the entire period of motion. Figure 50 shows the RMS angle error for each trial.

The plot shows that when $k = 0$, we have a large angle error. For this gain, the filter uses the gyro measurements exclusively, and the bias errors of these sensors are the source of the corresponding angular error. As the gain is increased from zero, then the angle error decreases, as predicted by (3.45); however, it begins to increase after the gain exceeds approximately 0.15. This is caused by the fact that more of the filter output is weighed by the FQA as the gain is increased. Recall that the FQA relies on the accelerometer measurements, which in turn measure the centripetal/tangential

accelerations of the pendulum, as well as, the component of the gravity vector.   As a result, the FQA introduces an ever increasing error into the filter output as the gain is increased beyond 0.15. Therefore, for the plots shown previously, $k = 0.15$ was chosen for use in our complementary filter.
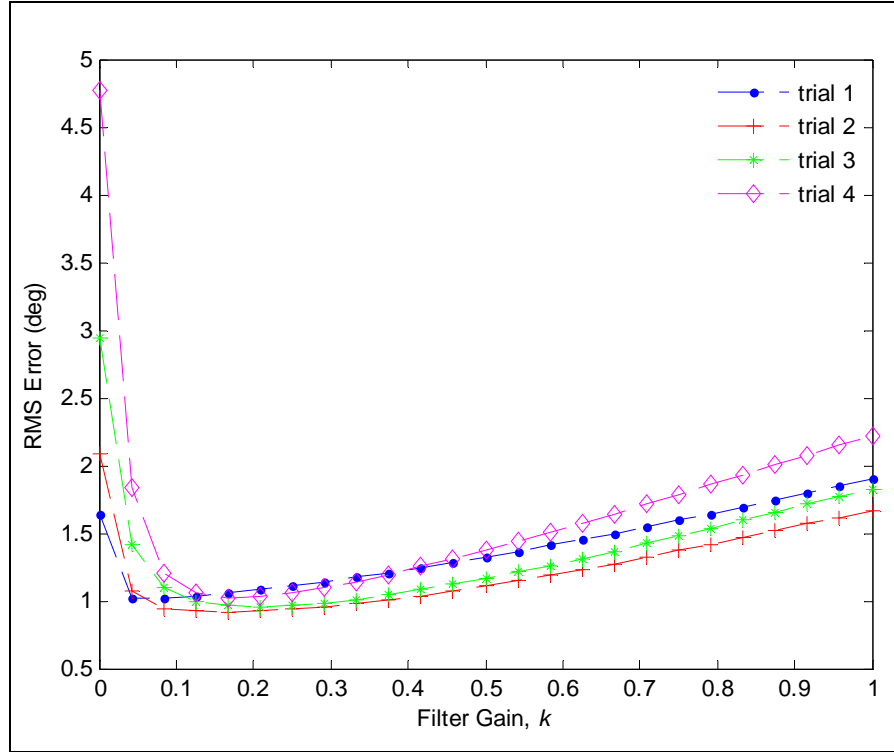
Figure 50.   Selection of filter gain using real pendulum motion data.

This section discussed the performance of the complementary filter using data that was collected from a vertical pendulum. The performance of the complementary filter was compared with the angle measured by a 16-bit rotary encoder attached to the pendulum shaft. For the filter gain of $k = 0.15$, the performance of the complementary filter was found to be comparable to that reported by Microstrain's proprietary filter and also demonstrated an ability to track the true angle to within ±2 degrees.

J. FILTER PERFORMANCE WITH RANDOM MOTION

The last chapter ended with a description of the anomalous drift observed in the Microstrain-computed quaternion. It showed how the angle was prone to drift for a substantial amount of time (on the order of 20 seconds or more) when the sensor was subjected to an energetic random motion. In the present section, this motion will be supplied to our complementary filter so that its performance can be assessed with this same type of stimulus. When the sensor body was subjected to the arbitrary motion that resulted in the drifting angle, all of the sensor data (i.e., accelerometers, magnetometers, and angular rates) were recorded to file. Subsequently, these data were available for testing with our complementary filter.

Figure 51 compares the manufacturer's quaternion with that derived from our complementary filter using $k = 0.15$ supplied with the sensor data collected from that experiment. Before the motion, $t < 15$ sec, the manufacturer's quaternion and that from our filter tend to agree. This is the time period when the sensor body is resting motionless on the workbench. During the motion interval, $15 < t < 20$ sec, it is not possible to make a comparison since we do not have a means of measuring the true orientation. Therefore, we make no statement about the filter performance during this interval. However, after the motion stops, and the sensor is returned onto the workbench in its original orientation, we observe that the components of the quaternion from our complementary filter tend to settle more quickly to their original values. Figure 52 makes the same comparison in terms of the Euler angles computed from the respective quaternion. It further illustrates how our complementary filter tends to perform better than the manufacturer's quaternion in this situation when the motion is erratic or changing abruptly.
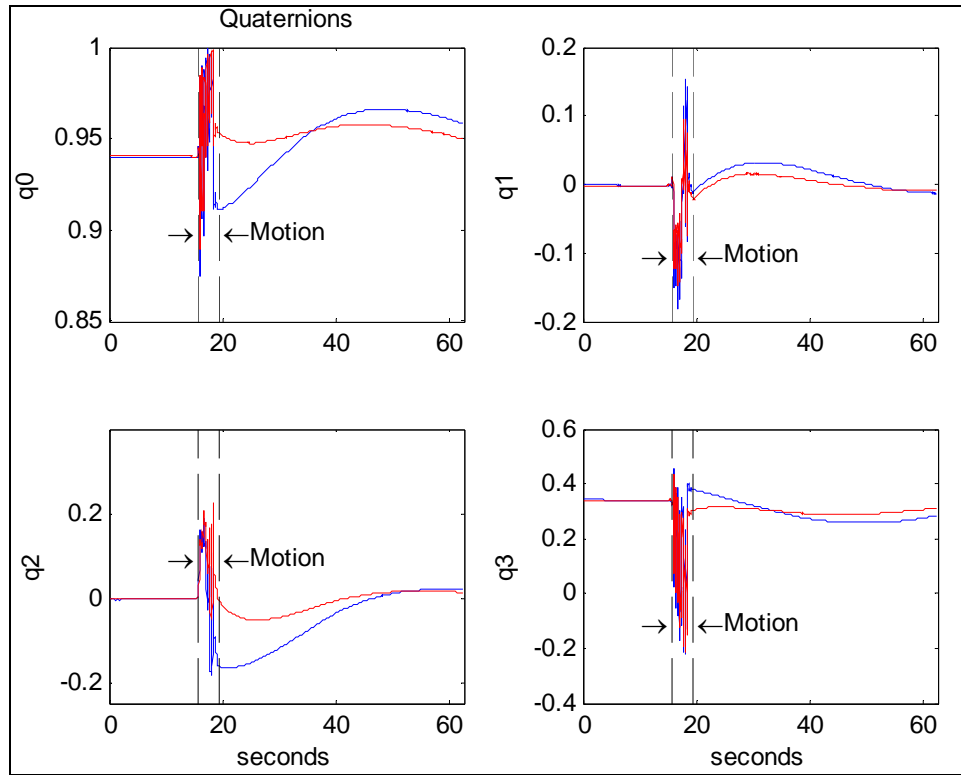
Figure 51.   Comparison of Microstrain quaternion (blue) and that from our complementary filter with $k = 0.15$ (red).
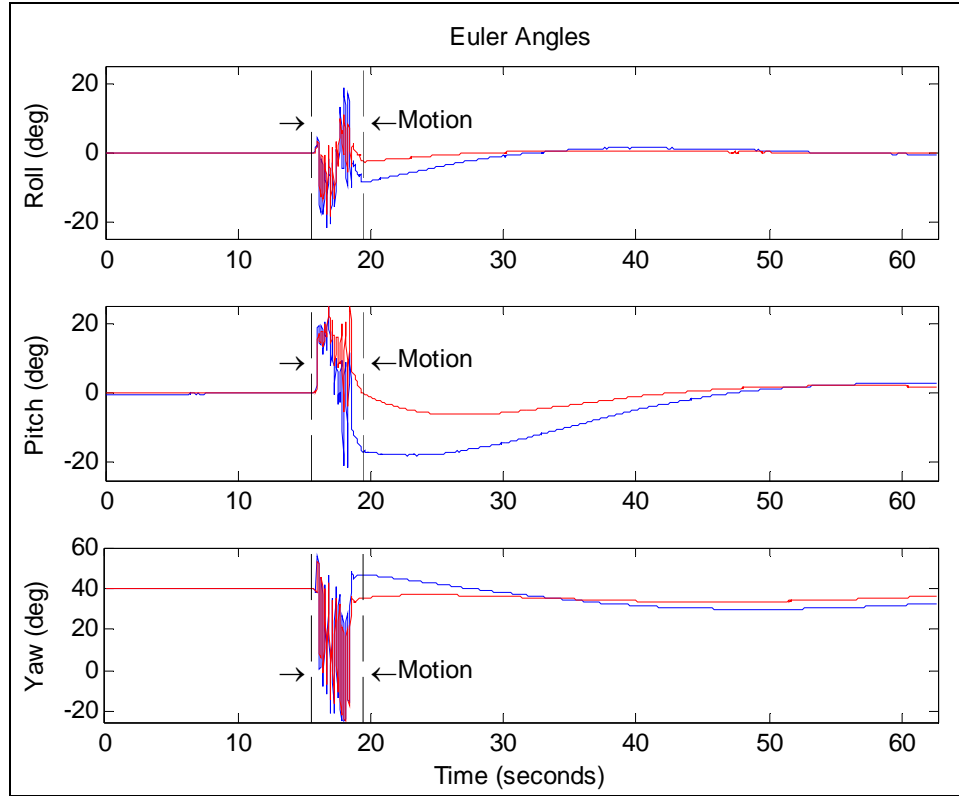
Figure 52.   Comparison of Microstrain Euler angles (blue) and those derived from our complementary filter with $k = 0.15$ (red).

Lastly, in Figure 53, we explore the idea of switching the filter gain to an alternate value based on some criterion that was monitored during the execution of the algorithm. The figure shows the same data from Figure 52, but it also includes the result of this gain switching strategy. In this approach, the filter algorithm switched the gain to a large value, relatively speaking, when the motion was considered low. This had the effect of weighing the accelerometers and magnetometers more greatly in the complementary filter output when the acceleration due to non-gravitational motion was low. To accomplish this adaptive gain strategy, the angular rate was monitored during the program iteration, and when it was observed to be below a particular threshold, the gain was raised to $k = 1$. When the motion was considered to be above the threshold, as established by the angular rate, the gain was then returned to $k = 0.15$. The figure shows this result for the period after $t = 15$ sec, as this was considered to be the more interesting interval of motion. After the motion stopped, the angles derived from the adaptive gain approach settled more quickly than those derived from the constant gain filter. During that period, $t > 20$

107

sec, the sensor was resting on the workbench, which provided an opportunity to use the accelerometers/magnetometers for the orientation computation. Because the sensor body was stationary, the accelerometers were not influenced by any motion and their response was due entirely to the gravity vector. At the end of the motion, however, both techniques appeared to yield similar results.
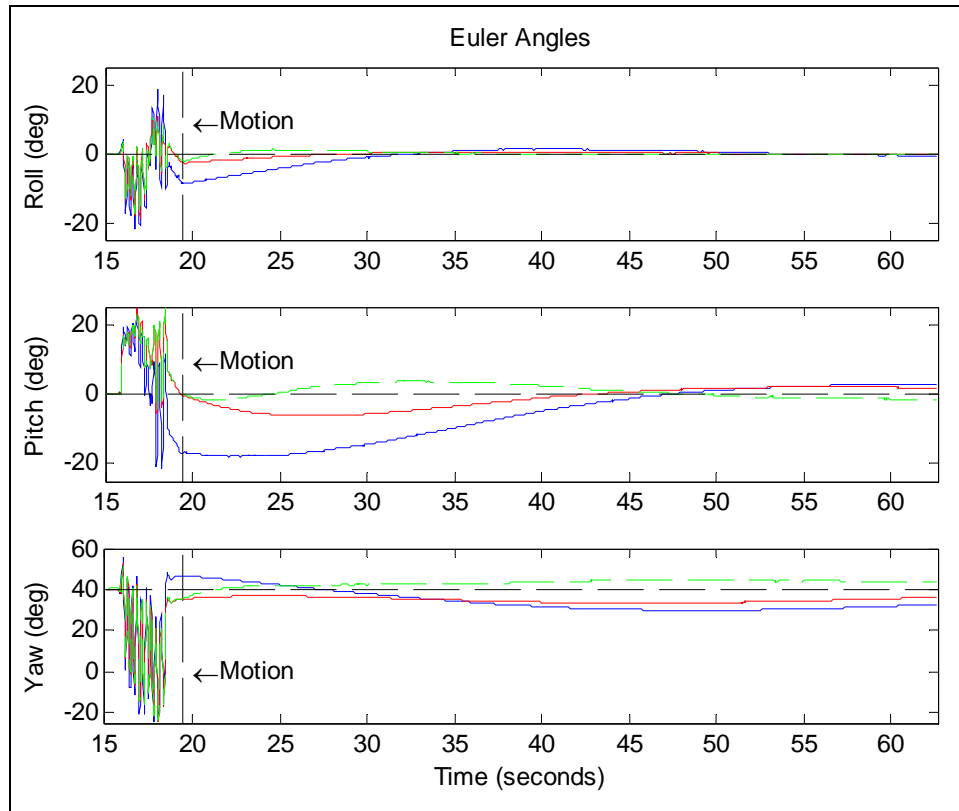
Figure 53.   Comparison of results in Figure 51 and the adaptive gain complementary filter (green).

K.   SUMMARY

This chapter presented the complementary filter and discussed its performance in terms of the gain. A vertical pendulum served as the test case for an evaluation of the filter's performance. In closing this chapter, it is noted that the adaptive-gain complementary filter appears to give slightly better results than the constant-gain filter without too much added complexity. The next chapter considers the adaptive gain filter in the personal navigation application. As will be shown, the adaptive gain

complementary filter is ideally suited to this problem. During the course of natural human walking, the motion of the foot is observed to be composed of a swing phase and a stance phase with abrupt starts and stops dividing these periods of motion. It is during these periods that the complementary filter gain can be adaptively switched to take advantage of this natural part of normal walking. Thus, during the stance phase, the gain can be set to some nominally high value to affect full use of the accelerometers (and magnetometers) for sensing orientation. Similarly, during the swing phase, the gain can be set to a low value so that the filter will utilize the angular rate sensors as much as possible to give the attitude estimate.

THIS PAGE INTENTIONALLY LEFT BLANK

IV.   PERSONAL NAVIGATION

The previous chapter introduced the complementary filter for use in estimating the attitude quaternion. It blended a "static" quaternion from the FQA with a "dynamic" quaternion that came from a differential equation involving the gyro measurements. In addition to a constant gain, the previous chapter also presented the idea of adaptively switching the filter gain based on some parameter that is monitored during the execution of the algorithm.

In this chapter, the complementary filter is applied to the strapdown navigation algorithm for use in computing one's position in a PNS application. A foot motion model is also developed here. It will be used to carry out a simulation study of the PNS algorithm and to examine some of its other relevant aspects, such as the selection of the numerical integration method used in the strapdown portion of the algorithm and the sensor sampling interval. In addition to the simulation, some example results of the PNS algorithm using actual data will also be included at the end of this chapter.

A.   STRAPDOWN ALGORITHM FOR PERSONAL NAVIGATION

The strapdown navigation algorithm with the zero-velocity updates, the gait-phase detection algorithm, and our quaternion complementary filter is shown in the block diagram in Figure 54. The inputs to this algorithm are the IMMU sensor measurements from the accelerometers, magnetometers, and gyros. A timer value is required, which is also provided by the IMMU microcontroller. The output of the algorithm is $\vec{p}^{\,n}$, a $[3 \times 1]$ vector of computed position in the navigation frame. Dashed lines from the gait-phase detection block indicate that this function controls the operation of the zero-velocity updates and the complementary filter. Recall that the zero-velocity updates were employed to correct the error that had accumulated in $\vec{v}^{\,n}$. This feature was applied when the foot was known to have a zero velocity during the stance phase. For the complementary filter, the gait-phase detection algorithm served to indicate the appropriate times to adaptively switch the filter gain.
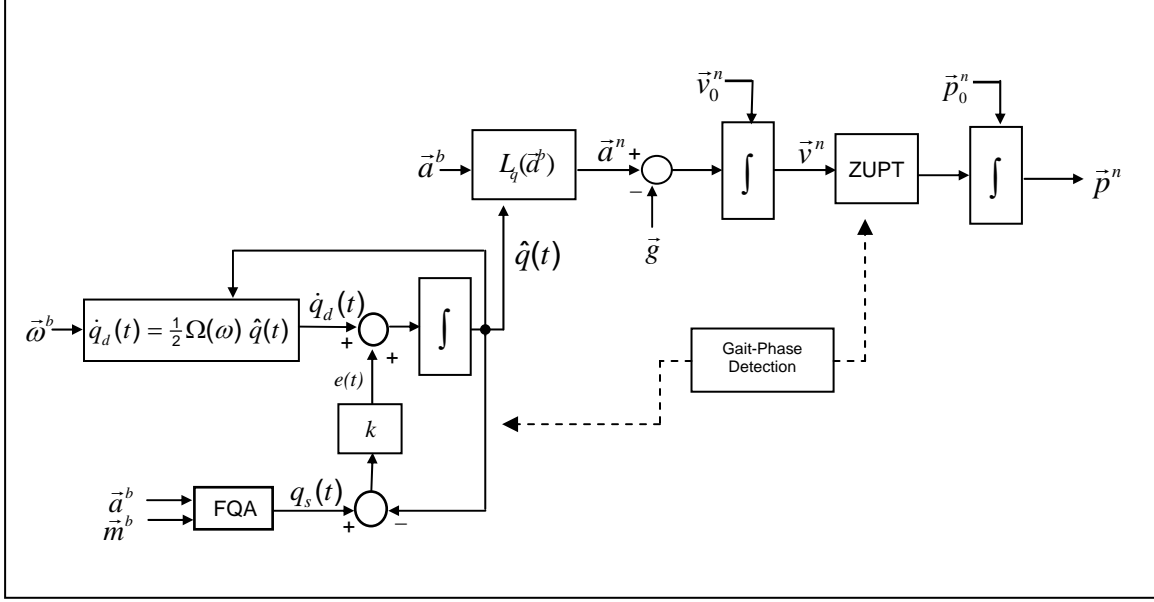
Figure 54.   Strapdown navigation algorithm with zero-velocity updates, gait-phase detection, and quaternion–based complementary filter.

B.   ANALYSIS OF NUMERICAL METHODS FOR THE PNS

With a technique in hand for the computation of one's position using the foot-mounted IMMU, it might be an appropriate time to test this algorithm with some actual foot motion data. However, this will be deferred until the end of the chapter. Instead, in this section we explore the remaining components within the PNS algorithm (see Fig. 54) that may require some additional examination, namely the integrators. For example, within the complementary filter, there is an integration operation that results in the need to solve a first-order differential equation during each iteration of the PNS algorithm. The differential equation is of the form

$$\dot{q}(t) = \frac{1}{2}\Omega(\omega)q(t). \tag{4.1}$$

In Chapter III, which dealt with the analysis and performance of this filter, this equation was solved with the numerical method known as Euler's method.   In the strapdown navigation portion of the PNS, two additional integrators can be found. The first integrator serves to generate velocity data from the derived samples of navigation

frame acceleration, while the second integrator provides the desired position updates. The resulting integral equations have the form as shown.

$$\vec{v}(t) = \int \vec{a}(t)\, dt$$

$$\vec{p}(t) = \int \vec{v}(t)\, dt. \tag{4.2}$$

Not surprisingly, some numerical integration method must be employed here, as well. Solution of these integral equations requires numerical methods known as Newton-Cotes formulas [82]. The idea behind these methods is to approximate the sampled data with a polynomial that is easy to integrate. Euler's method considers a zero-order polynomial and gives a numerical formula—for example, written to compute velocity—that is of the form

$$\vec{v}_{k+1} = \vec{v}_k + \Delta t\, \vec{a}_k. \tag{4.3}$$

This method is easy to implement in code and requires only one data sample. To improve the accuracy of the result, another popular method for numerical integration is known as the Trapezoidal Rule. It considers a first-order polynomial as an approximation for the sampled data and generally yields superior results to Euler's method. It has the convenient form

$$\vec{v}_{k+1} = \vec{v}_k + \frac{1}{2}\Delta t\left(\vec{a}_{k+1} + \vec{a}_k\right). \tag{4.4}$$

It requires two data samples, but this is generally not a limitation. Depending on the underlying nature of the data samples and the requirements for accuracy, higher-order numerical methods, such as Simpsons 1/3 and 3/8 rules, may be considered for a given application [83]. In general, the higher-order methods give more accurate results at the expense of more computational effort. Another factor affecting the accuracy is the size of the sampling interval, Δt. This parameter is the interval of time between samples, and it is often cited in terms of the sampling frequency, $f_s = 1/\Delta t$. Ordinarily, the accuracy of the solution improves as Δt decreases.

The main objective of this section is to explore the various methods available for numerical integration with regard to their application in the PNS. Specifically, we are concerned with the two integrators in the strapdown portion of the PNS, that is, those dealing with the computation of velocity and position. The reason we will not explore the integrator residing in the complementary filter is that this performance has already bees studied in Chapter III. A second objective of this section will be to determine a maximum sampling interval, Δt.

Before proceeding too much further into the analysis of the integrators, it is essential to establish a performance benchmark. This is some known quantity or result that we can use to compare the performance of the various numerical methods that will be considered, as well as, their sensitivity to the sampling frequency.

1.   Benchmark Selection Criteria

A simple benchmark might be to use the actual walking data and try different numerical methods to see which one gives the minimum distance error. While this may be the benchmark we return to at the end of this analysis, we prefer to use a carefully selected acceleration model for the ensuing analysis. This approach has validity for the following reasons:

1) An acceleration model allows the variation of the sampling frequency, f_s , either up or down. With actual data, we can only down-sample the data, and only by fixed amounts (i.e. $f_s/2$, $f_s/3$, $f_s/4$, …).

2) The analysis can be carried out in the absence of sensor noise and calibration errors. When appropriate, this parameter can be introduced as desired to study its effect on the overall performance.

3) An acceleration model, unlike real measured acceleration data, provides a known and well understood reference for the performance study. This begs the question, "What is an appropriate model for foot acceleration to use in this analysis?"

To help answer this question, consider the foot acceleration from one of the navigation frame coordinate axes shown in Figure 55. It is real data derived from the

foot-mounted IMMU during normal walking motion. Acceleration from approximately 24 steps were superimposed on the plot to show the behavior of the foot motion during the swing phase. From the moment the toe leaves the ground at the end of the stance phase, the curve peaks rapidly with some positive acceleration then quickly changes sign as the foot slows down in preparation for the end of the swing phase when the heel strikes the ground.
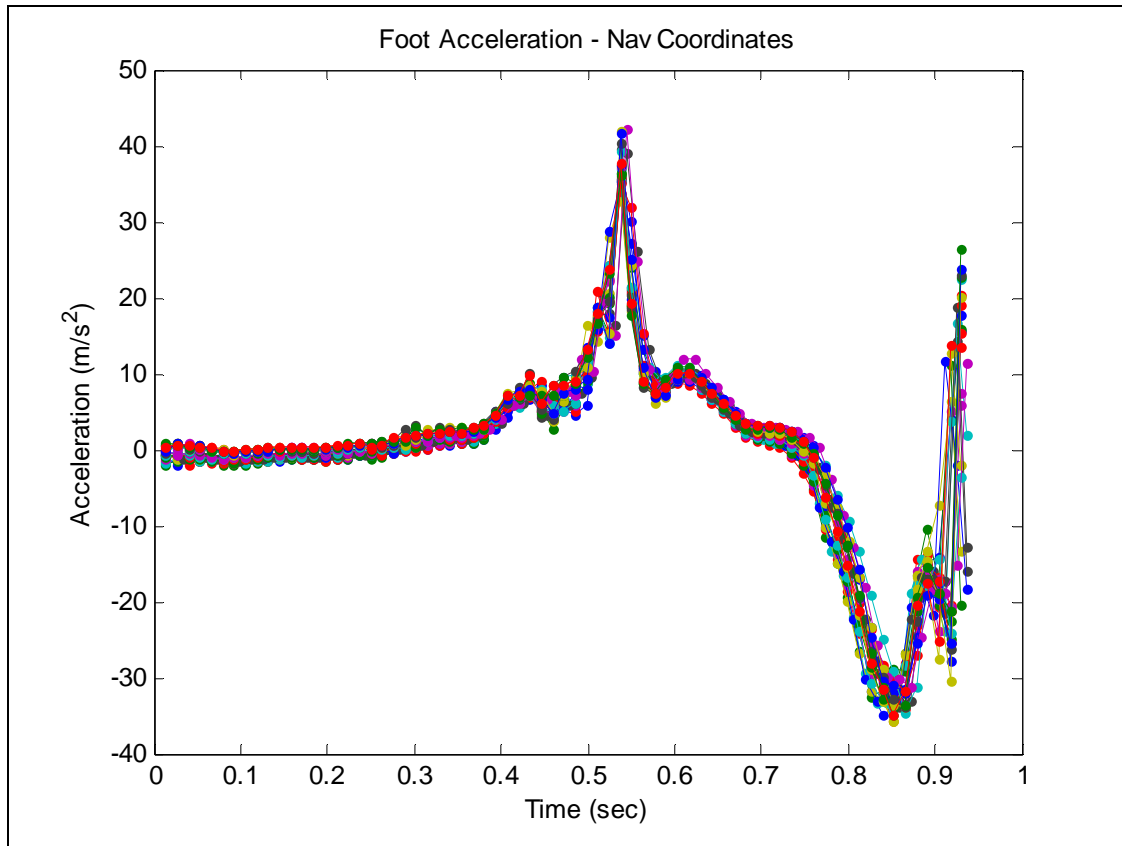
Figure 55.   Typical foot acceleration in navigation coordinates, 24 steps shown.

Integration of this data, using the Trapezoidal rule, for example, gives the velocity profile shown in Figure 56. Consistent with our intuition, the plot shows how the foot velocity increases at the beginning of the swing phase, then decreases returning to zero as it should for the stance phase. It is also noted that these curves have the correction

introduced by the zero-velocity updates. Lastly, one more integration, again by the Trapezoidal rule, gives the foot displacement in this particular navigation frame coordinate axis, as shown in Figure 57.
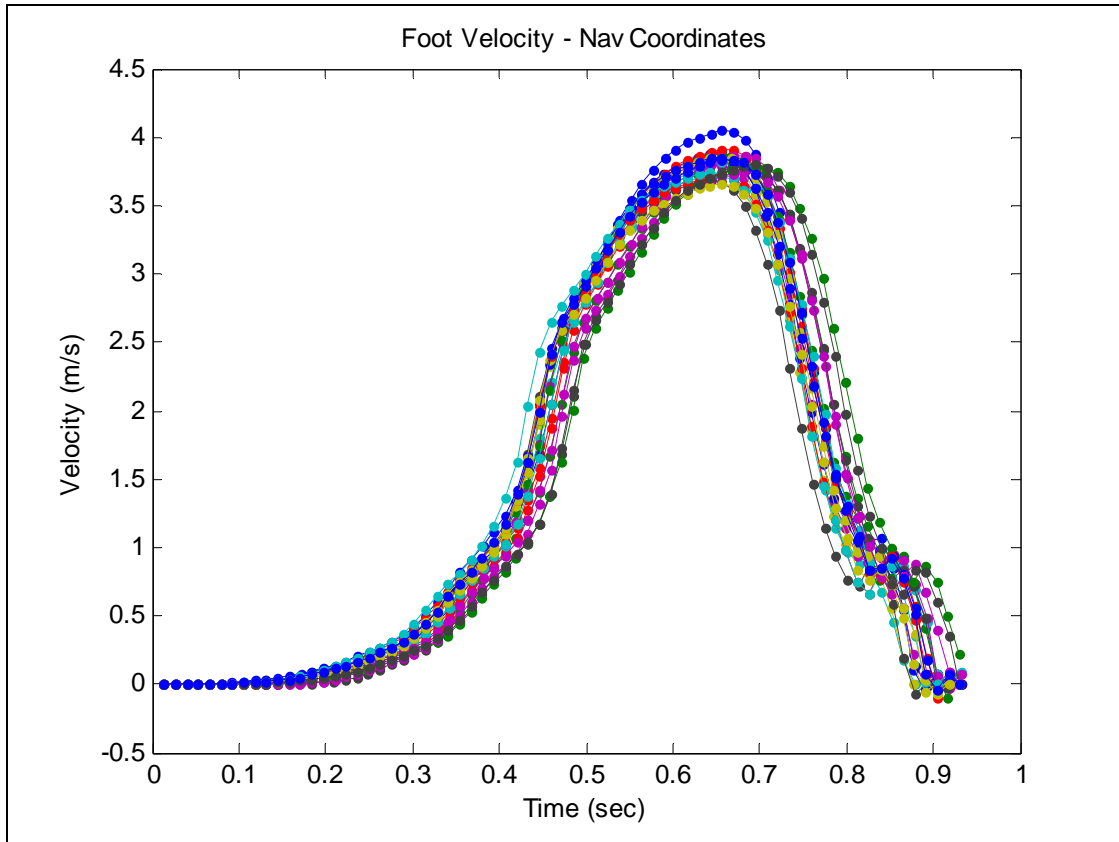
Figure 56.   Typical foot velocity in navigation coordinates.
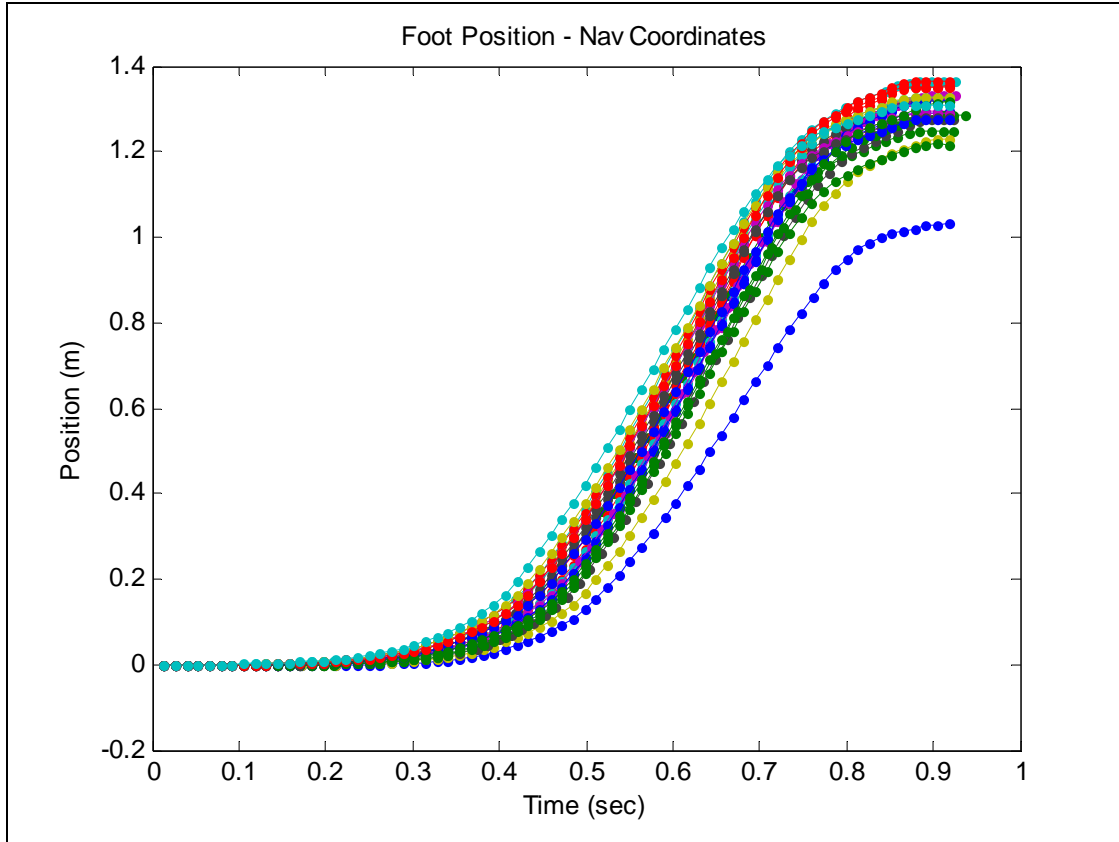
Figure 57.　　Typical foot displacement in navigation frame coordinates.

In choosing an acceleration model for our analysis, we desire it to have the behavior depicted in the previous figures for the real foot motion. That is, for the acceleration, there should be a period of zero acceleration that corresponds to the stance phase. There should also be a period of acceleration corresponding to the swing phase. The swing phase acceleration will have an interval of positive acceleration followed by a period of negative acceleration. Upon integration of the acceleration model, the result should appear similar to the curves depicting the foot velocity, as shown in Figure 56. At the end of the acceleration period, the velocity curve should be zero. Finally, for the position, we would like to see that the resulting displacement has a shape similar to that shown in Figure 57.

2.   Linear Acceleration Model

A simple model that was initially considered approximated the swing phase acceleration with a linear polynomial. This model is given as

$$a(t) = -12 \frac{L_s}{\tau^3} t + 6 \frac{L_s}{\tau^2}, \qquad 0 \leq t \leq \tau \qquad (4.5)$$

where L_s is the foot displacement, and τ is the duration of the swing phase. This polynomial is applied to a model of the foot acceleration that is comprised of a period of zero acceleration representing the stance phase and the linear acceleration during the swing phase, with another 0.1 seconds of zero acceleration representing the heel strike event at the end of the foot swing. This is better illustrated in Figure 58 where the acceleration model includes the linear polynomial $a(t)$ given in Eq. (4.5). The figure also shows a computed velocity and displacement, both of which were computed using the Trapezoidal rule. Foot displacement, L_s, was assumed equal to 180 cm, $\tau = 400$ msec, and $f_s = 1000$ Hz.

In Table 4, the velocity error (in cm) and the position error (in %) are given for several sampling frequencies ranging from 20 Hz to 1000 Hz. The velocity error, as expected, is small due to the fact that the polynomial approximation provided by the Trapezoidal rule is exact for the case of the linear acceleration model. On the other hand, the position error that we observe at the end of the swing phase clearly shows a dependence on f_s. A criticism of this simple linear model pertains to the discontinuity that exists in the acceleration profile at 0.5 sec and 0.9 sec, marking the beginning and end of the swing phase. Natural human motion can not produce acceleration profiles having such discontinuities.
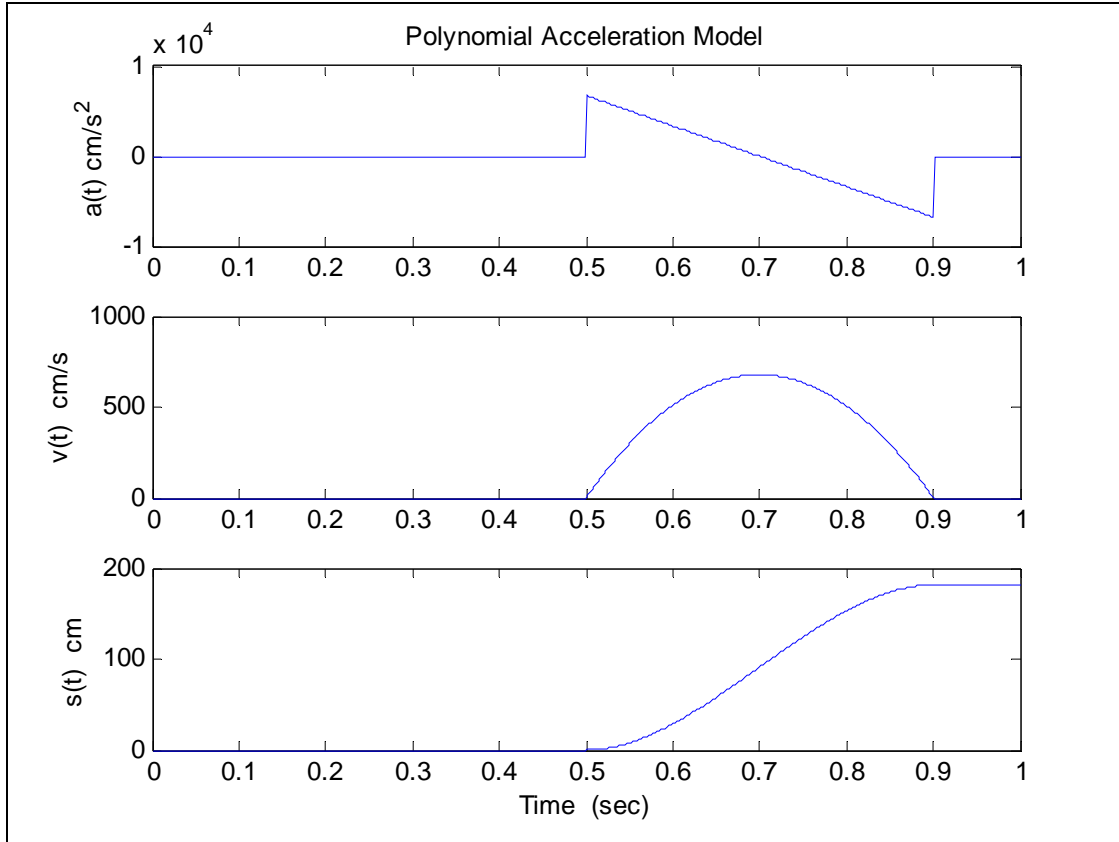
Figure 58.   Linear polynomial acceleration model for one step.

Table 4.   Position error performance for linear acceleration model and varying sampling frequency.

f_s **(Hz)**	T_s **(sec)**	**Velocity Error (cm/sec)**	**Position Error (%)**
20	0.05	1.705×10^{-13}	40.15
50	0.02	0	15.47
100	0.01	7.105×10^{-14}	7.622
200	0.005	-1.421×10^{-14}	3.781
500	0.002	-2.789×10^{-13}	1.505
1000	0.001	-3.73×10^{-14}	0.7512

3.   Sinusoidal Acceleration Model

Another model that was given ample consideration was that of a sinusoid. Here the acceleration in the swing phase had the expression

$$a(t) = \frac{L_s}{2}\cos\left(\frac{\pi t}{\tau}\right), \qquad 0 \le t \le \tau. \tag{4.6}$$

Using this expression in the model for the foot acceleration, we get the plot in Figure 59, again as before, with $L_s = 180$ cm, $\tau = 400$ msec, and $f_s = 1000$ Hz. Table 5 shows the dependence of the error to the sampling frequency using the Trapezoidal rule for integration. We also see that the velocity error performance is much worse than that for the linear model. This is due to the fact that our acceleration model is not linear, and the polynomial approximation provided by the trapezoidal rule is no longer exact.   The acceleration curve still has the discontinuity at the beginning and end of the swing phase. In experimentation with this model, it was also learned that this feature introduced an undesirable sensitivity to the distribution of the data samples. Slightly shifting the data samples forwards or backwards in time caused large swings in the resulting error. For this reason, as well as the discontinuities in the curve, this model was abandoned and not considered further in this analysis.
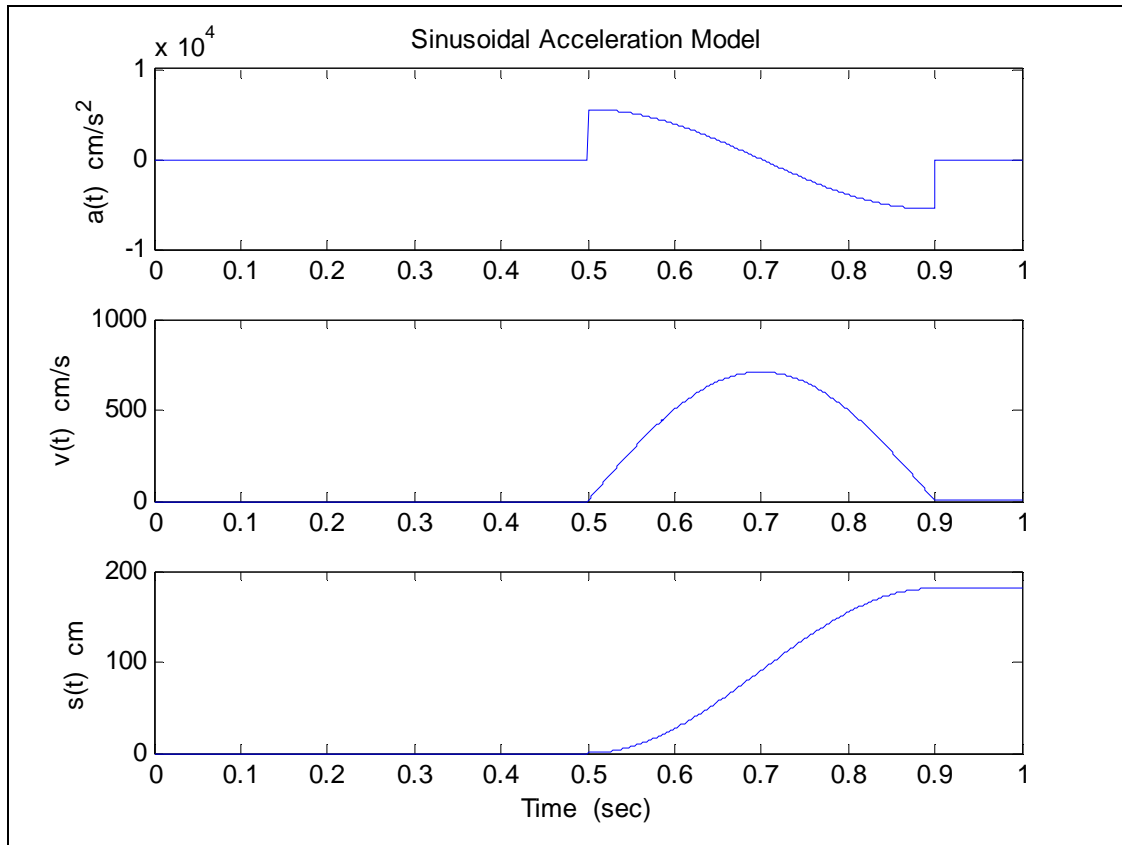
Figure 59. Sinusoidal acceleration model for one step.

Table 5. Position error performance for sinusoidal acceleration model and varying sampling frequency.

f_s (Hz)	T_s (sec)	Velocity Error (cm/sec)	Position Error (%)
20	0.05	277.6	47.56
50	0.02	111	18.71
100	0.01	55.52	9.304
200	0.005	27.76	4.639
500	0.002	11.1	1.853
1000	0.001	5.552	0.9257

## 4.	Gaussian Acceleration Model

The Gaussian (normal) function occurs often in the modeling of natural phenomenon. It was also considered here as a model for the swing phase acceleration. In our adaptation of this function, the swing phase velocity had the form of the familiar Gaussian function as shown

$$v(t) = L_s \frac{1}{\sigma\sqrt{2\pi}} e^{-t^2/2\sigma^2}, \qquad -\frac{\tau}{2} \le t \le \frac{\tau}{2} \qquad (4.7)$$

where $\sigma = 0.05$ was found by trial and error to give a curve that looked like the velocity profile derived from the actual data, and L_s is the stride length. Using $v(t)$ as shown in Eq. (4.7), the acceleration can be easily derived

$$a(t) = \frac{d\,v(t)}{dt} = \frac{L_s}{\sigma\sqrt{2\pi}} e^{-t^2/2\sigma^2} \left(-\frac{t}{\sigma^2}\right). \qquad (4.8)$$

Figure 60 shows this expression applied to the foot motion acceleration. Immediately it can be seen that this model does not have a discontinuity as large as that exhibited by the models considered previously. However, there is some minor abrupt change at the start and end of the swing phase due to the fact that the exponential function is not identically zero at these points. In spite of this, the model does show superior performance as indicated in Table 6. These results were computed using the Trapezoidal rule.
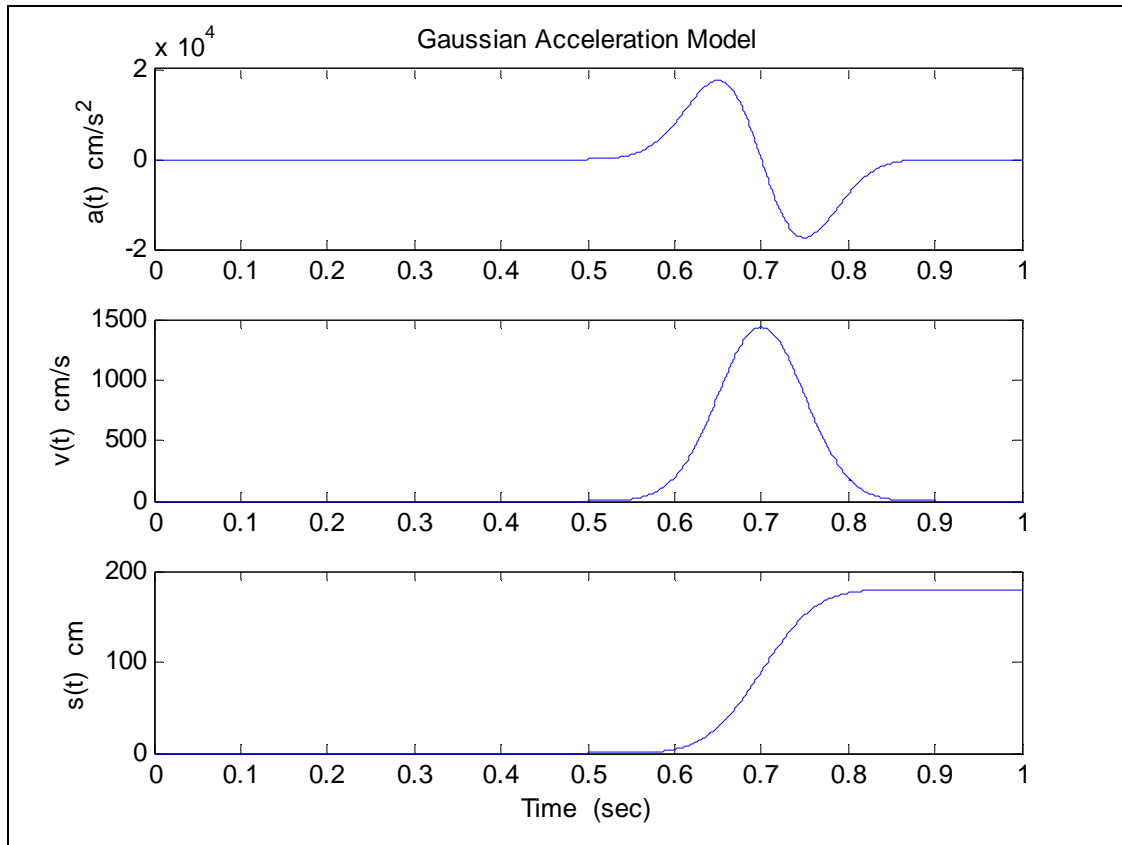
Figure 60.   Gaussian acceleration model for one step.

Table 6.   Position error performance for the Gaussian acceleration model and varying sampling frequency.

f_s **(Hz)**	T_s **(sec)**	**Velocity Error (cm/sec)**	**Position Error (%)**
20	0.05	-2.253×10^{-13}	-0.04155
50	0.02	6.122×10^{-13}	-0.04978
100	0.01	-6.908×10^{-13}	-0.07585
200	0.005	8.377×10^{-13}	-0.09327
500	0.002	-2.419×10^{-13}	-0.105
1000	0.001	1.793×10^{-13}	-0.1092

Next, we consider the performance of several numerical integration methods. Up to this point, we have only utilized the Trapezoidal rule for integration. In the following analysis, we will also employ Euler's method, Simpson's 1/3 rule, and an adaptation of Simpson's rule and Trapezoidal rule referred to here as modified Simpson's 1/3 rule. It works to preserve the sampling interval of the resulting data so that the number of samples available for a subsequent integration is maintained. These results are shown qualitatively in the following graphs.

Figure 61 shows the position derived from the double integration of the Gaussian acceleration model with f_s =100 Hz. The true position, which was derived analytically using MATLAB's *erfc( )* function, is shown in blue. The symbols in the plot are the results from the various integration methods considered. Red dots are used to identify the result using MATLAB's *cumtrapz( )* function, which accomplished the Trapezoidal rule for integration. The author also implemented his own function for the Trapezoidal rule titled *myTrapz( )*. This was done to facilitate its use in other functions used here, such as Simpson's 1/3 and the modified Simpson's 1/3 rules. As evidenced by the plot, the results from *myTrapZ( )* agree with those of MATLAB's *cumtrapz( )*, thus validating its use in the higher-order functions. The plot also shows the results from the double integration of the Gaussian acceleration model using Simpson's 1/3 rule, modified Simpson's 1/3 rule, and Euler's method. As the figure suggests, for this sampling frequency, all methods utilized here gave acceptable results for this particular acceleration model.
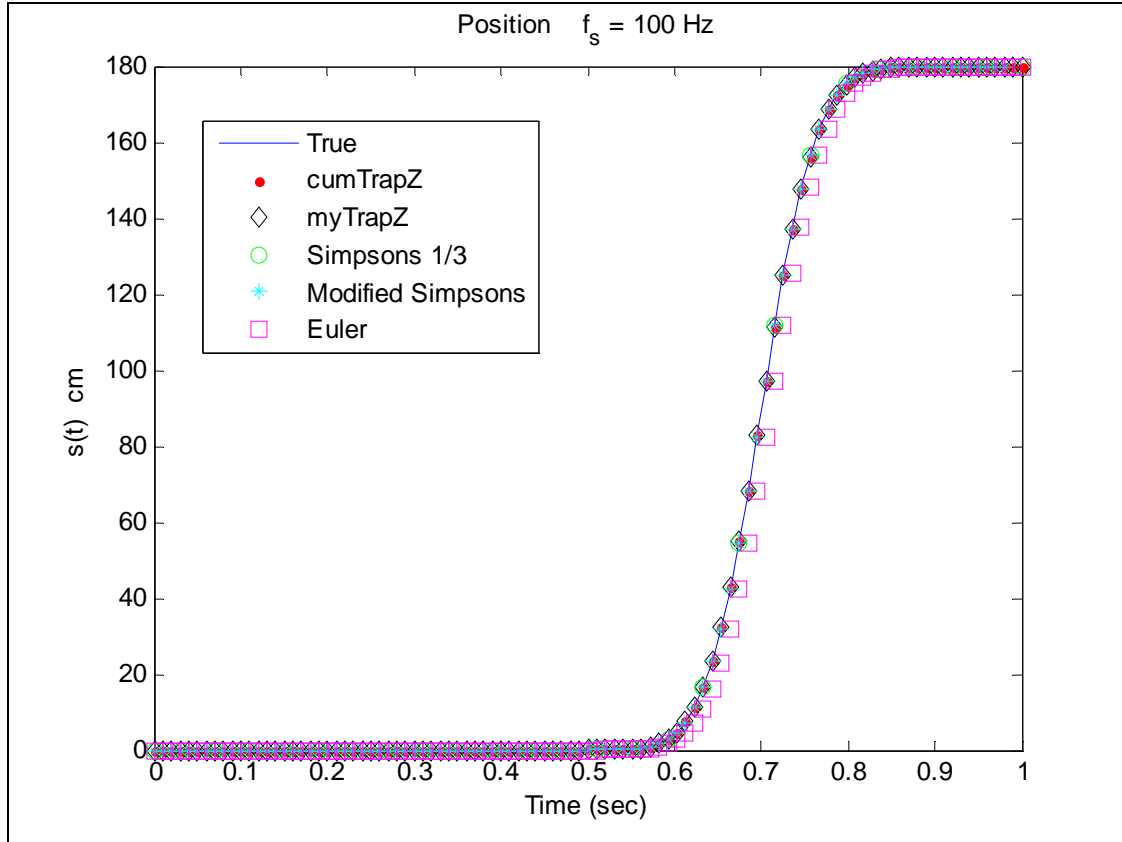
Figure 61.   Double integration of Gaussian acceleration model, $f_s = 100$ Hz.

The experiment was repeated using a reduced sampling frequency of $f_s = 50$ Hz. This result is shown in Figure 62. For this sampling frequency, all methods perform well. Euler's method begins to degrade, however, during the intermediate portion of the integration interval, but at the end, its result is consistent with those derived from the higher-order methods. Lastly, the experiment was repeated one more time, but with $f_s = 20$ Hz. As shown in Figure 63, at the end of the integration period, the Trapezoidal rule, along with Euler's method, appears to give better results. Simpson's 1/3 rule and the modified Simpson's rule, on the other hand, appear to have degraded performance for this sampling frequency. This may be due to the fact that while these higher-order methods generally yield better results, in this particular case, for the limited number of samples available, the second-order approximation utilized by these methods may tend to exacerbate the error.
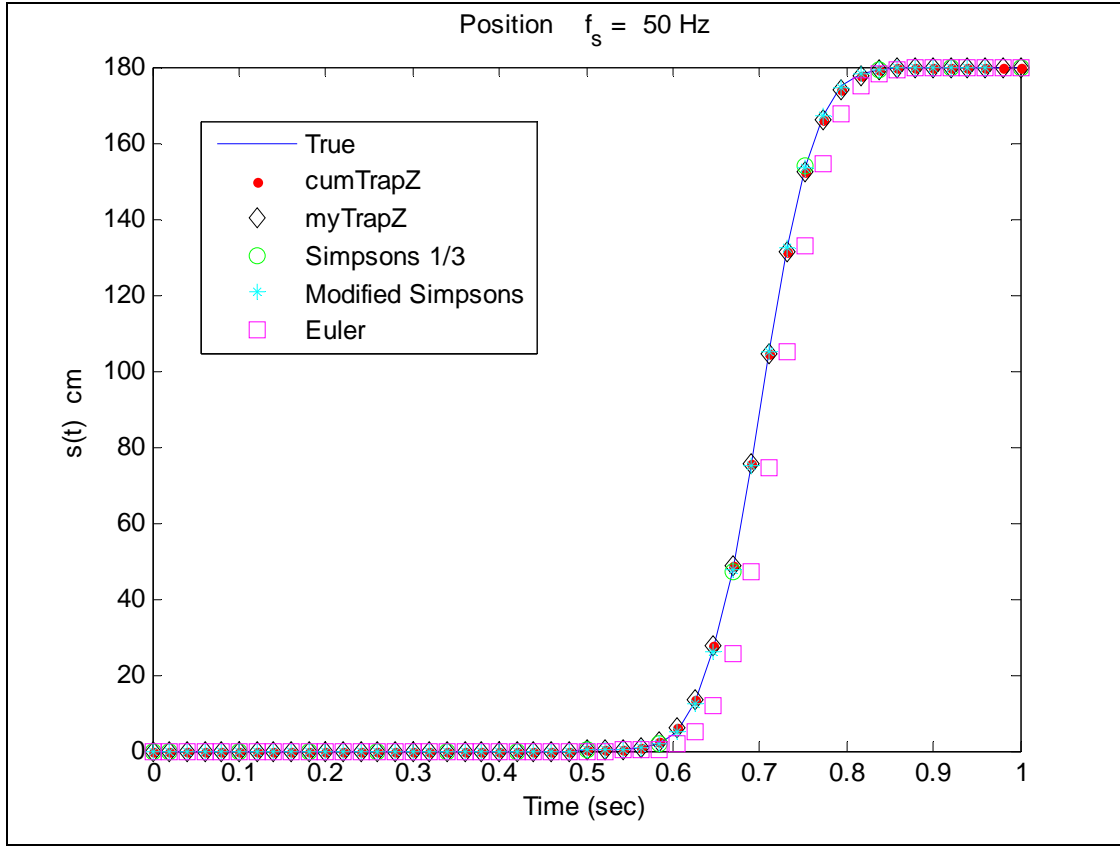
Figure 62.   Double integration of Gaussian acceleration model, $f_s = 50$ Hz.
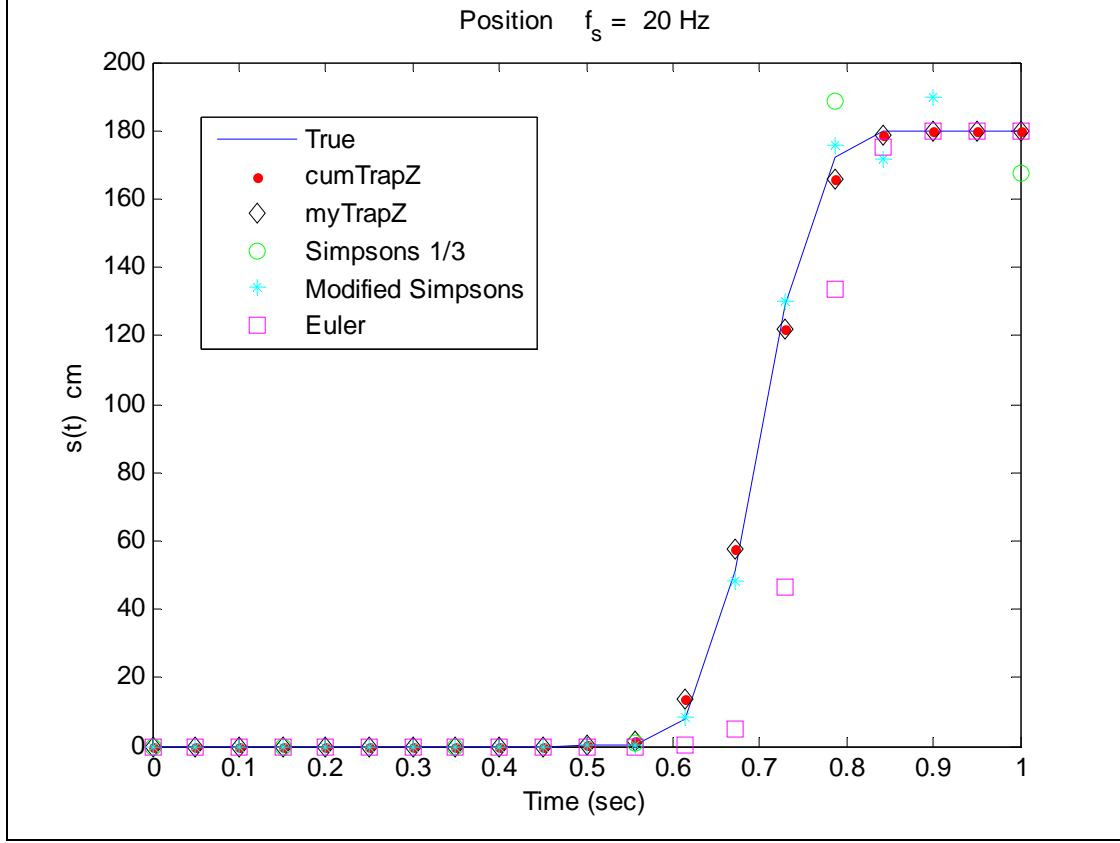
Figure 63.   Double integration of Gaussian acceleration model, $f_s = 20$ Hz.

5.   Bezier Polynomial Acceleration Model

One last model we wish to consider is derived from a well known family of functions known as Bezier polynomials. An attractive feature of these polynomials is that they can be tailored to suit a particular application. Yet another benefit is that analytical expressions for integrals and derivatives can be easily derived. Here, the polynomial chosen has a signature that is representative of the position,

$$s(t) = L_s \left(\frac{6}{\tau^5} t^5 - \frac{15}{\tau^4} t^4 + \frac{10}{\tau^3} t^3 \right), \qquad 0 \le t \le \tau. \qquad (4.9)$$

The acceleration is easily derived from the second derivative of $s(t)$.

127

$$a(t) = \frac{d^2 s(t)}{dt^2} = L_s \left(\frac{120}{\tau^5} t^3 - \frac{180}{\tau^4} t^2 + \frac{60}{\tau^3} t \right).$$
(4.10)

This acceleration model does not have a discontinuity of any kind at the beginning and end points of the modeled interval, as demonstrated by the fact that $a(0) = a(\tau) = 0$. Figure 64 shows the foot model acceleration incorporating this particular Bezier polynomial. Table 7 has the results from the variation of the sampling frequency with the Trapezoidal rule integration.
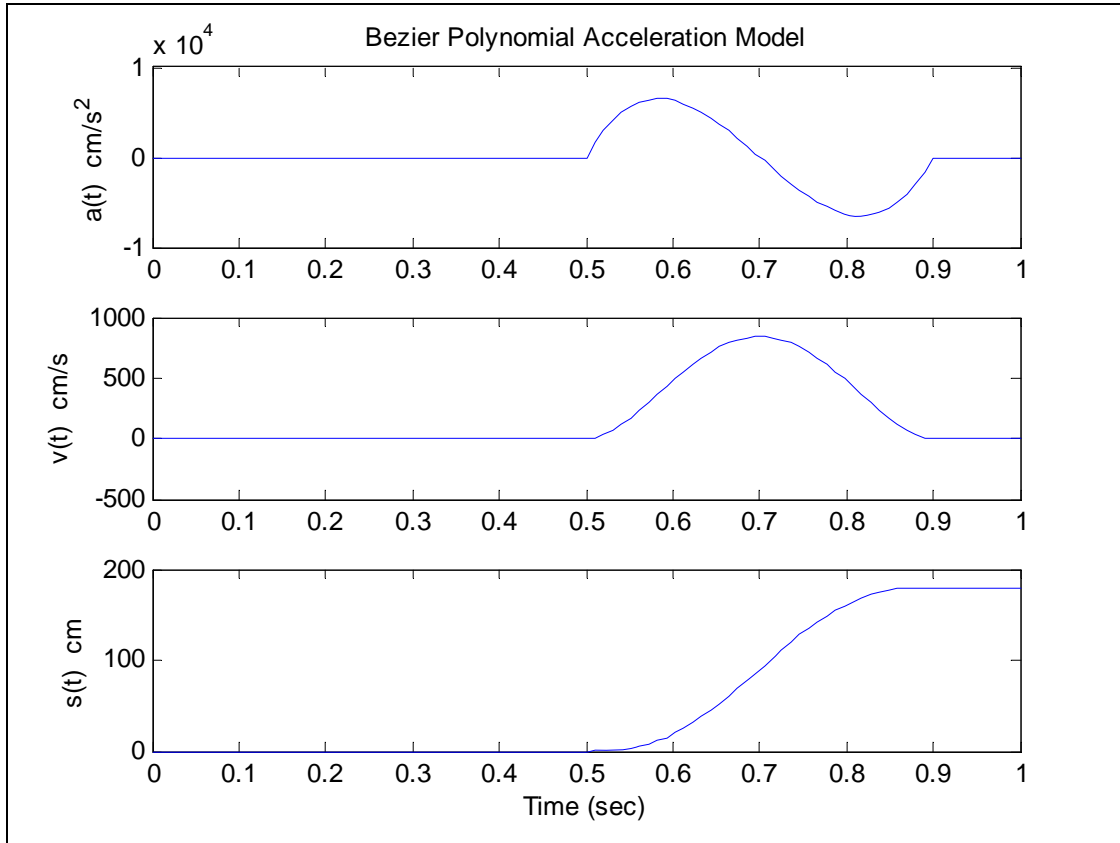
Figure 64.　Bezier polynomial acceleration model.

Table 7.   Position error performance for Bezier polynomial acceleration model and varying sampling frequency.

f_s (Hz)	T_s (sec)	Velocity Error (cm/sec)	Position Error (%)
20	0.05	-3.695×10^{-13}	-10.04
50	0.02	-4.832×10^{-13}	-1.382
100	0.01	-2.398×10^{-13}	-0.3286
200	0.005	-5.893×10^{-13}	-0.08011
500	0.002	-4.569×10^{-14}	-0.01263
1000	0.001	-5.287×10^{-14}	-0.003141

Next, we consider the various integration methods using the Bezier polynomial acceleration model. Figure 65 shows the double integration of the acceleration model data for f_s=100 Hz resulting in the foot displacement after one step.   The true or analytical curve is shown in solid blue. As the graph suggests, all of the integration methods considered in the simulation produced satisfactory results for this sampling frequency.

The simulation was repeated using a sampling frequency of f_s=50 Hz, the results of which are shown in Figure 66. Exhibiting a behavior similar to what was seen using the Gaussian acceleration model, all methods gave good results for this f_s. Euler's method had some degraded performance during the intermediate portion of the curve, but improved at the end of the integration period. Again, this is due to the fact that Euler's method is using a zero-order polynomial to approximate this portion of the curve, where clearly a first-order method would be better. Lastly, when the simulation is repeated using a f_s=20 Hz, as shown in Figure 67, we see that all the methods under consideration exhibited unsatisfactory performance, reinforcing a main tenet of numerical methods that in general, higher sampling frequencies yield better results.
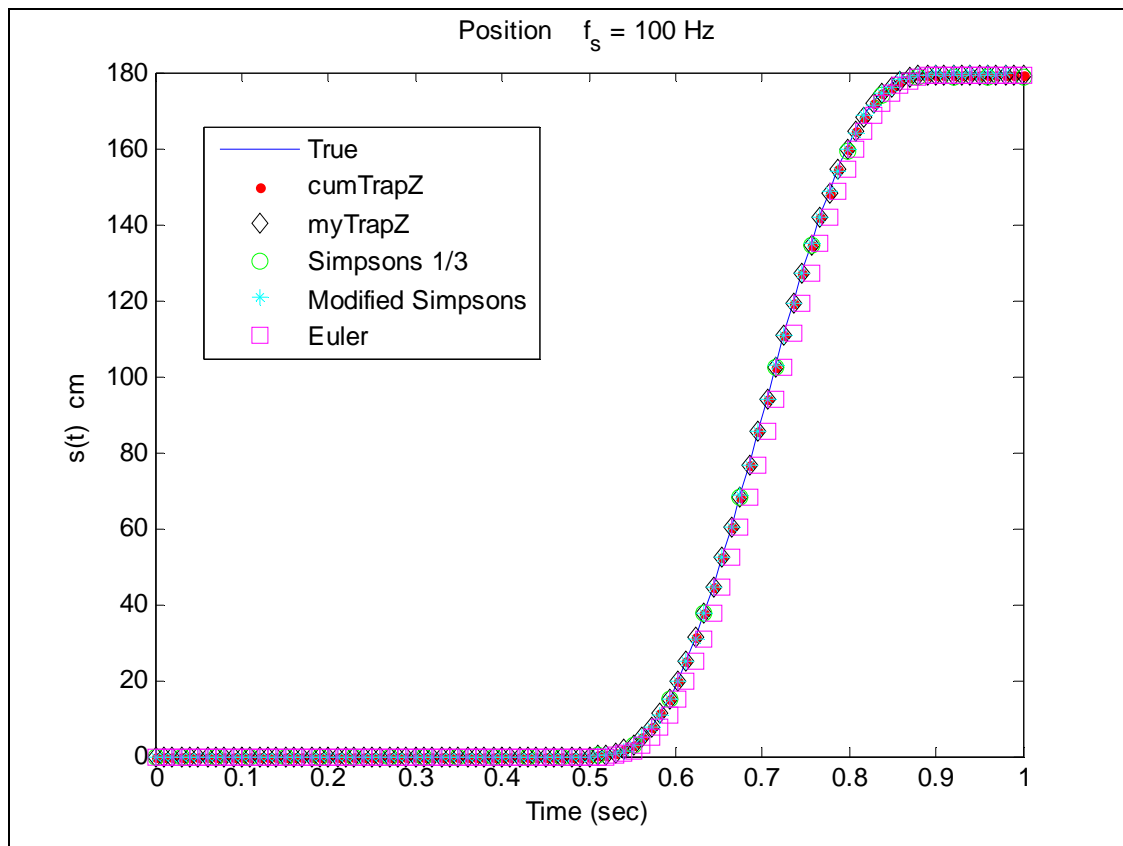
Figure 65.   Double integration of Bezier acceleration model, $f_s = 100$ Hz.
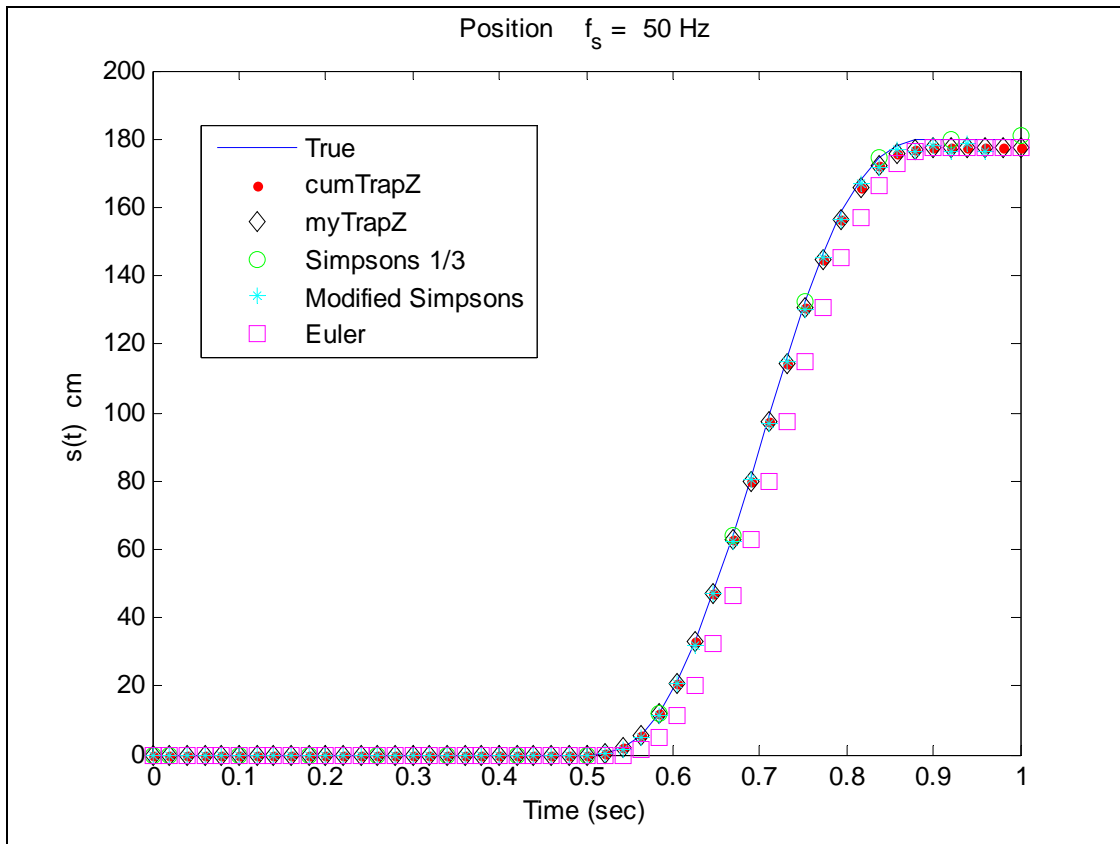
Figure 66.　　Double integration of Bezier acceleration model, $f_s = 50$ Hz.
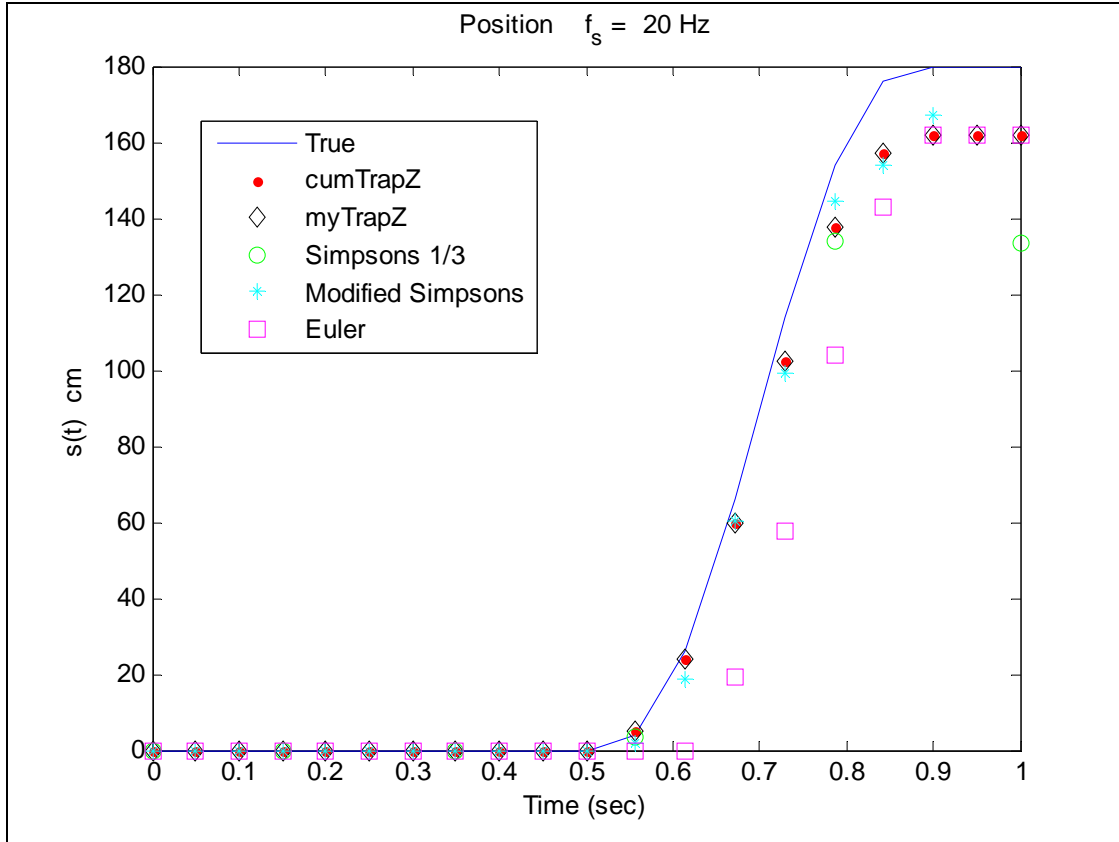
Figure 67.   Double integration of Bezier acceleration model, $f_s = 20$ Hz.

6.   Summary of Numerical Methods

To summarize the previous discussion concerning the performance study of the various numerical methods and the sampling frequency, we learned several things. First, the acceleration model used in the study does have an impact on the resulting error. As we observed early on when we experimented with the sinusoidal acceleration model, large errors had surfaced after double integration. Upon further study, we concluded that the discontinuous features of our model made the numerical method sensitive to these errors. Those models that did not have large discontinuities did not exhibit this behavior.

Another aspect of the performance of the numerical methods we considered pertains to the manner in which the data samples were distributed over the interval of integration. Slightly shifting the sample points forwards or backwards in time also

132

impacted the resulting error. If the samples were taken at carefully selected points within the acceleration model, then the error could be reduced to 10^{-12} or less.

Our study also highlighted the dependence on the sampling frequency. As borne out in many texts on the subject, the higher sampling rate generally produced better results. Lastly, while our models may not have been best suited to illustrate this point, it is widely established that the higher-order methods yield improved performance at the expense of greater computational effort.

In moving forward from this point, we wish to explore the PNS in greater depth using one of our acceleration models. The purpose now is to learn how the small errors resulting from the numerical methods evolve when considered in the larger context of the PNS. Of the various foot acceleration models evaluated, the one that demonstrated the least sensitivity to the sampling frequency was the Gaussian acceleration model. For this reason, this model will be advanced for further study in the PNS. Also, of the numerical methods that were utilized in this study, perhaps the Trapezoidal rule gave the most consistent results and presented a good compromise between Euler's method and the higher-order methods of Simpson's 1/3 rule in terms of ease of implementation and computation. Furthermore, we add that for the range of sampling frequencies, $f_s = 50$ Hz seems to be a reasonable value to use. It produced integration results that were rather accurate without the expense of excessively high sampling frequency and is representative of that which can be achieved with the real hardware. Furthermore, while a high sampling frequency may be easy to implement in a computer simulation, it is not always possible to attain in practice.

C.   A THREE-DIMENSIONAL FOOT MOTION MODEL

In this section, the Gaussian foot acceleration model presented earlier is expanded into three dimensions to generate simulated sensor data from a foot-mounted IMMU. The resulting sensor data will be used in the performance evaluation of the PNS and the study of the various aspects affecting its overall operation. For example, in the absence of any sensor calibration error or noise, the impact of numerical integration over many walking steps can be examined. Furthermore, when sensor calibration errors and noise

are ultimately incorporated into the model, an assessment of their effect can be ascertained, as well. Varying amounts of these variables can be included to gain greater insight into the sensitivity of the PNS with respect to these parameters. To develop our foot motion model, our approach is to first generate simulated sensor data of a foot-mounted IMMU for one step, then propagate this model over as many steps as desired for use in stimulating the PNS.

In Figure 68, the navigation reference frame along with a body reference frame attached to the foot center-of-mass is shown. For our motion model, the foot has been constrained to rotate only about the y^n-axis described by the pitch angle θ. This angle represents the natural rotation exhibited by the foot as it moves between the swing and stance phase. Translation or displacement of the foot is confined to the $\langle x^n \, z^n \rangle$ plane. Therefore, in our simulation, the accumulated distance traveled in the horizontal direction corresponds to magnetic North and coincides with the x^n-axis. Our model also has an acceleration along the z^n-axis to represent the vertical movement of the foot, but its net displacement is zero at the end of each step, as it should during normal walking on level ground. No acceleration occurs along the y^n-axis; thus, the net displacement in the easterly (or westerly) direction is zero.
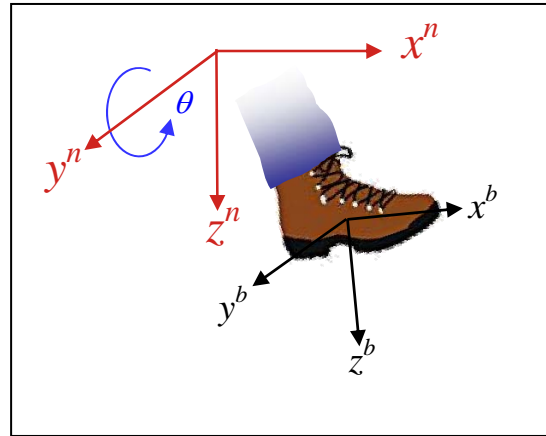
Figure 68.   Reference frames for the foot motion model.

The movement of the foot during one step can be decomposed into four distinct motions. Until now, the motion of the foot was considered only in terms of a stance phase and a swing phase, but for added realism, the stance phase will be broken down into three parts. Table 8 shows this new classification of the foot motion. For simplicity, the total duration for one step is assumed equal to one second. The foot motion model begins with the foot-flat phase; its duration is 0.4 seconds. In this phase, there is no angular rotation of the foot here, nor is there any acceleration. The next period of the model has the toe-off phase, which lasts 0.1 seconds. There is no translational motion during this phase, but there is a rotation with the heel lifting off the ground in preparation for the swing phase. Next, there is the swing phase in which the acceleration will be derived from a Gaussian model, as described shortly. Duration of this phase is 0.4 seconds and has a positive angular rate, as shown in the table. Lastly, the heel-strike phase occurs at the end of the swing phase. The acceleration here has returned to zero when the heel of the foot strikes the ground and the foot pitch angle rotates back to zero to coincide with the beginning of a new foot-flat phase.

Table 8.   Component phases of one walking step.

Phase	Duration (seconds)	Angular Rate $\dot{\theta}$ (rad/sec)	Acceleration	
			A_x	A_z
Foot-flat	0.4	0	0	0
Toe-off	0.1	-7.5	0	0
Swing	0.4	+3.5	Gaussian	Gaussian
Heel-strike	0.1	-6.5	0	0

To make the sensor data for one step of foot motion, the task is broken down into four separate parts. First, quaternions are constructed from the foot pitch angle. This angle is easily derived from the angular rate that has been assumed for each phase of the foot motion, as shown in the table above. These quaternions have the form

$$q = \begin{bmatrix} \cos\dfrac{\theta}{2} \\ 0 \\ \sin\dfrac{\theta}{2} \\ 0 \end{bmatrix}. \qquad\qquad (4.11)$$

Secondly, after the quaternions have been established for all four phases of the model, they are then used to rotate the navigation frame acceleration into the body frame, as shown in Figure 69. Unlike the quaternion rotation operator used in the strapdown navigation algorithm, the rotation operator used here works with the conjugate quaternion, q^*, as shown. A description of the navigation frame acceleration is given in the next sub-section.
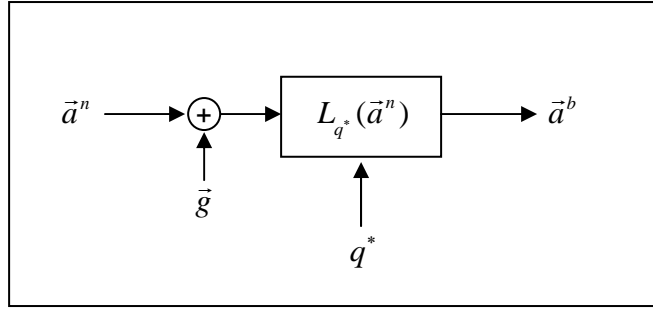
Figure 69.   Method to generate body frame acceleration from navigation frame acceleration.

The third step in this process is to use the pitch angle to construct the magnetometer measurements. This set of expressions takes on the same form as that used in Chapter III for the pendulum motion simulation, where $\vec{B}_e = 0.486$ gauss and $\beta = 60.483$ degrees,

$$\begin{aligned} m_{x^b} &= \left|\vec{B}_e\right|\cos(\beta+\theta) \\ m_{y^b} &= 0 \qquad\qquad\qquad (4.12) \\ m_{z^b} &= \left|\vec{B}_e\right|\sin(\beta+\theta) \end{aligned}$$

136

The fourth and final step of this process is to construct the gyro measurements. This is straightforward using the data in Table 8. Since rotation is confined to the y^n-axis, which is coincident with the y^b-axis, only the corresponding gyro measures any rotation. The gyro measurement designated as ω_{y^b} is equal to $\dot{\theta}$ depending on the particular phase of the foot motion, and the remaining two gyros do not sense any rotation, as shown below:

$$\omega_{x^b} = 0$$
$$\omega_{y^b} = \dot{\theta} \qquad\qquad (4.13)$$
$$\omega_{z^b} = 0.$$

1.   Three-Dimensional Acceleration Model

The previous section showed how to construct the sensor body gyro and magnetometer measurements. To construct the sensor body acceleration measurements, $\vec{a}^b$, the method illustrated in Figure 69 must be employed. However, this requires that first the navigation frame accelerations, $\vec{a}^n$, be established. Fortunately, this is straightforward because the foot motion in this frame is rather intuitive. As stated previously, the accelerated motion has been constrained to lie in the $\langle x^n\, z^n \rangle$ plane, with the foot pitch rotation required to occur along the y^n-axis. Furthermore, this leads to the convenient fact that the $\langle x^b\, z^b \rangle$ plane is parallel to the $\langle x^n\, z^n \rangle$ plane. Therefore, accelerations occurring in the $\langle x^n\, z^n \rangle$ plane reside wholly in the $\langle x^b\, z^b \rangle$ plane, and no acceleration exists along the y^n-axis nor in the y^b-axis.

For the a_x^n acceleration, we note that the velocity in the navigation frame should have a shape that is similar to the bell-shaped curve in Figure 56. Recall that this was the computed velocity of the foot in navigation-frame coordinates. For this component of the velocity, we adopt the Gaussian function, as before,

137

$$v_x^n(t) = \frac{L_s}{\sigma\sqrt{2\pi}} e^{-t^2/2\sigma^2} \tag{4.14}$$

to represent the x^n component of velocity during the swing phase. Here the constant $\sigma = 0.05$ was tailored to give a profile that looked appropriate for our simulation, and L_s is the horizontal displacement after one step. The navigation frame acceleration is derived from this velocity to give

$$a_x^n(t) = \frac{d\,v_x^n(t)}{dt} = \frac{L_s}{\sigma\sqrt{2\pi}}\, e^{-t^2/2\sigma^2}\left(-t/\sigma^2\right) \tag{4.15}$$

In (4.15), $a_x^n(t)$ applies to the acceleration during the swing phase only, and is zero for those times outside of this period. In addition, the time variable was varied as $-0.2 \le t \le +0.2$ to compute this acceleration, which had a duration of 0.4 seconds corresponding to the swing phase.

For our model, we have constrained the acceleration in the $\langle x^n\ z^n \rangle$ plane, so $a_y^n(t) = 0$. Lastly, to form an expression for the vertical acceleration, $a_z^n(t)$, we recognize that the net vertical displacement at the end of a step should be zero. With this in mind, we let the vertical displacement, $s_z^n(t)$ be equal to

$$s_z^n(t) = \frac{M_s}{\sigma\sqrt{2\pi}} e^{-t^2/2\sigma^2} \tag{4.16}$$

where $-0.2 \le t \le +0.2$, $\sigma = 0.05$, and $M_s/\sigma\sqrt{2\pi}$ equals the maximum vertical displacement of the foot in the swing phase. The corresponding acceleration is formed by

$$a_z^n(t) = \frac{d^2 s_z^n(t)}{dt^2} = \frac{M_s}{\sigma^3 \sqrt{2\pi}} e^{-t^2/2\sigma^2} \left\{ \frac{t^2}{\sigma^2} - 1 \right\}. \qquad (4.17)$$

This acceleration only applies to the swing phase and is zero outside of this period of motion. Now that we have a formulation for the navigation frame acceleration, such that $\vec{a}^n = \begin{bmatrix} a_x^n(t) & 0 & a_z^n(t) \end{bmatrix}$, it remains a matter of applying the method illustrated in Figure 69 to generate the body frame acceleration measurements. Equations (4.15) and (4.17) give the acceleration model for the swing phase. In order to construct an acceleration model for the entire cycle of one foot step, these expressions must be padded with zero data before and after the swing phase to be consistent with the assumptions made in our foot motion model. This completes the last remaining set of measurements required for the foot motion model.

2. Plots of Three-Dimensional Foot Motion Model

The previous section described how to generate acceleration in the body frame for our foot-mounted IMMU. In conjunction with the expressions for the magnetometers and gyros, namely those given in (4.12) and (4.13), we have a complete model for all nine sensors of a foot-mounted IMMU. The figures in this section show the body frame measurements produced with this model for one walking step. To generate these plots, a step duration of one second was assumed with $f_s = 50$ Hz. A horizontal displacement was assumed equal to $L_s = 180$ cm. For the vertical displacement, we chose a value of 25 cm, and solved for the appropriate value of M_s in (4.16).

Figure 70 shows the magnetometer measurements for one step, which was derived from (4.12). These equations required the foot pitch angle, θ, which in turn was generated from our model for the foot angular rate, as defined in Table 8. Figure 71 and Figure 72 show the foot pitch angle and the gyro measurements computed for one

139

walking step.   The gyro measurements came from (4.13).   As was specified for our model, no foot rotation occurred along either the x^b - or the z^b -axis.   Therefore, only the ω_y gyro shows any rotation.
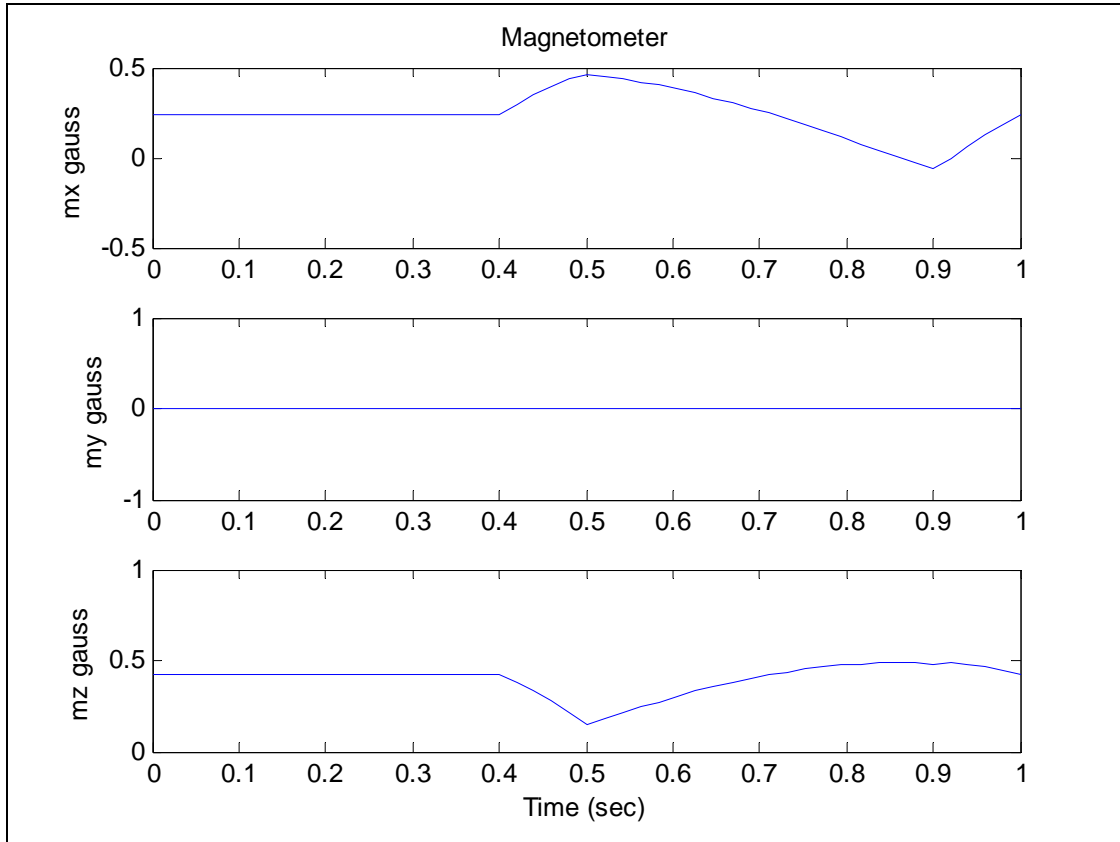
Figure 70.   Magnetometer measurement for foot motion model.
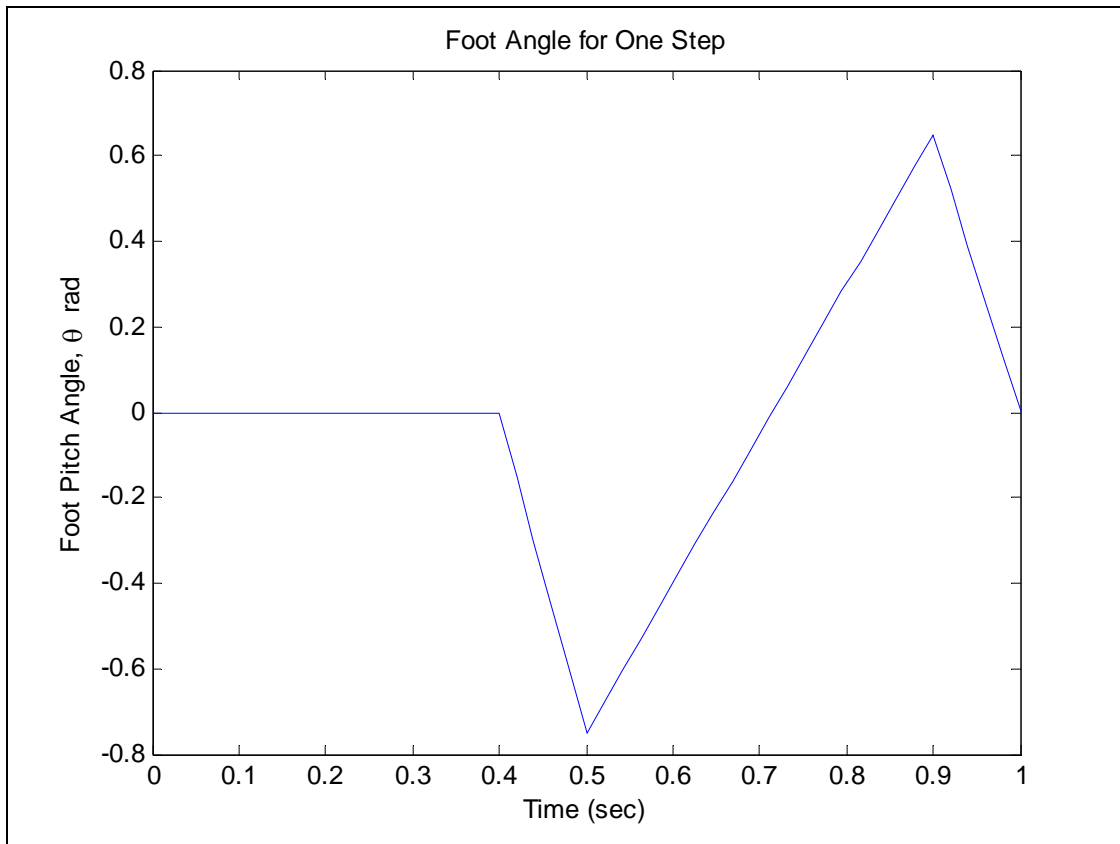
Figure 71.   Foot pitch angle, θ, for one walking step.
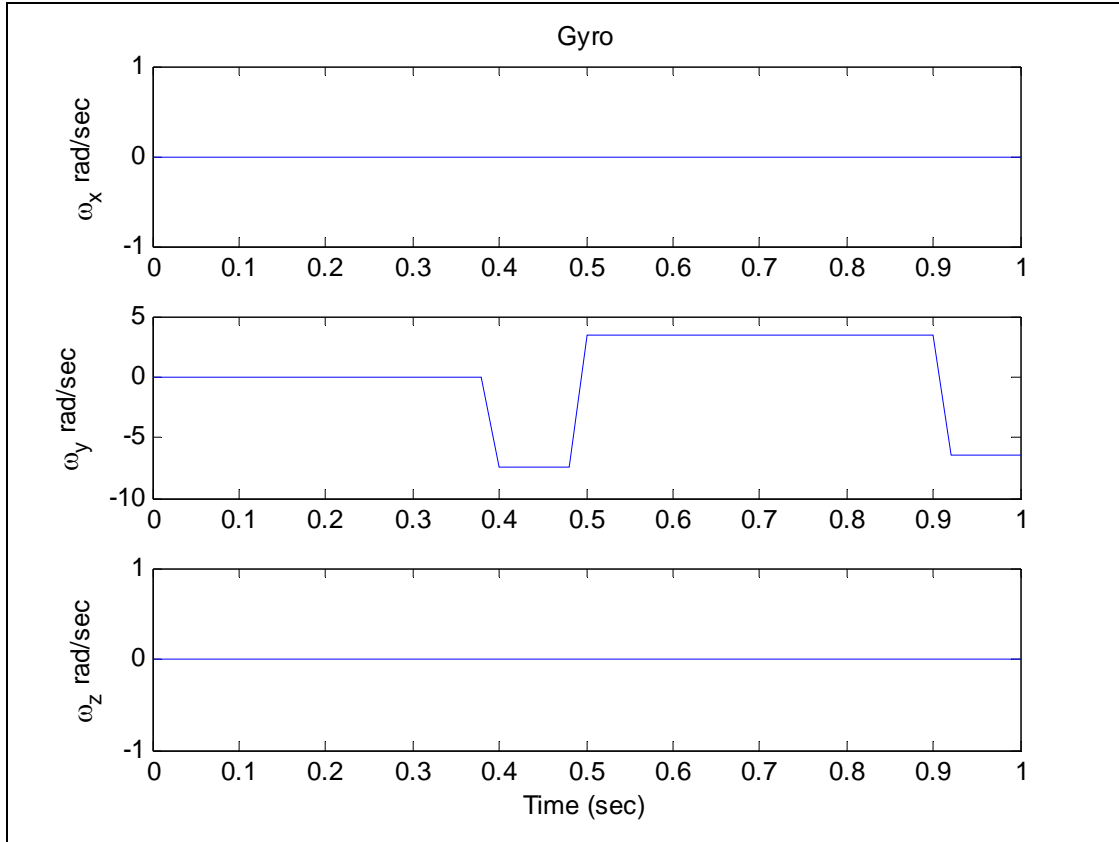
Figure 72.   Gyro measurements for the foot motion model.

Next, we look at the body frame acceleration measured by the foot-mounted IMMU in Figure 73. These plots were created using the navigation frame acceleration model comprised of (4.15) and (4.17), along with the method illustrated in Figure 69. Because the foot motion was constrained as it was in our model, we only have accelerated motion in the $\left\langle x^b\, z^b \right\rangle$ plane. This completes the body frame model of our foot-mounted IMMU. Now it is a simple matter to reproduce this model over as many walking steps as desired to stimulate the PNS with a set of simulated walking data.
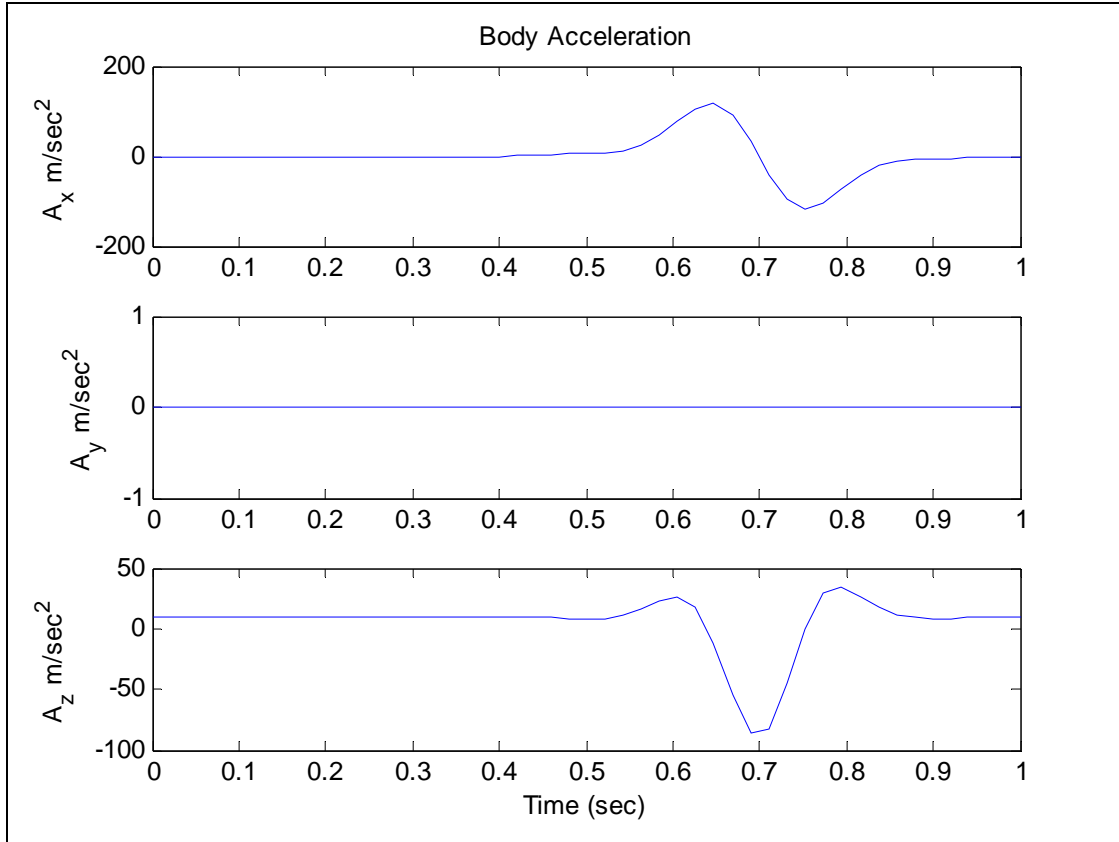
Figure 73.   Body frame acceleration for foot motion model.

As a point of interest, we would also like to make a brief examination of the navigation frame acceleration. Figure 74 provides this acceleration for one walking step in the navigation frame. Recall that this acceleration was derived from our Gaussian models for the foot motion. Integration of these data gives the navigation frame velocity, as shown in Figure 75. The solid line shows the velocity computed from an analytic expression for the velocity. The red dots inside of the black diamonds are the data points computed from the trapezoidal rule integration of the accelerometer data with $f_s = 50$ Hz. Specifically, the red dots were computed using MATLAB's *cumtrapz( )* function, and the black diamonds were computed with our own function. These plots indicate good agreement between the theoretical velocity and that which was computed with the numerical methods.
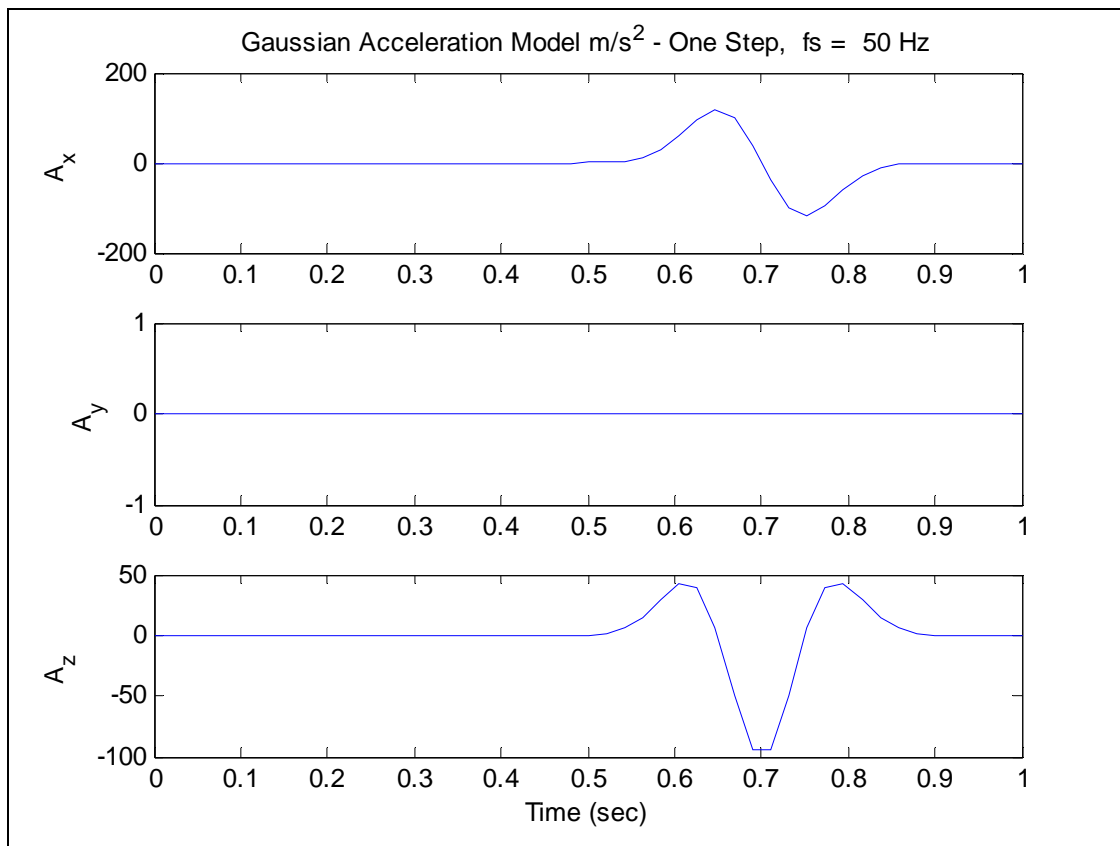
Figure 74.   Navigation frame acceleration from Gaussian foot motion models.
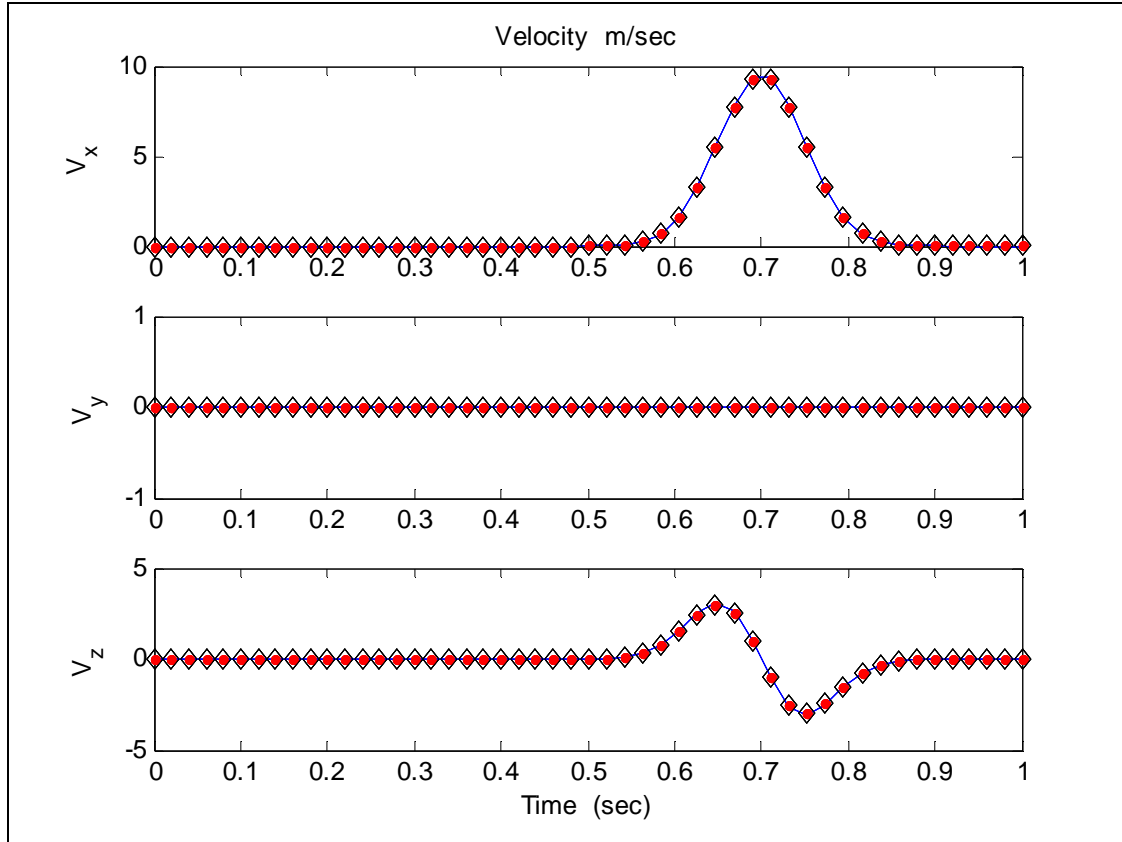
Figure 75.   Navigation frame velocity derived from analytical expression (solid), MATLAB's *cumtrapz( )* function (red dots), and the author's *myTrapZ( )* function (black diamonds).

Lastly, the navigation frame velocity is integrated once more to give the three-dimensional position or displacement. Figure 76 shows this result. The height of the S_x curve is the total horizontal displacement of the foot after one step and equals 179.91 cm, and we had assumed $L_s = 180$ cm, giving a position error of 0.05%. Looking at the S_z curve, the maximum vertical displacement computed with the numerical methods can not be compared with the true maximum vertical displacement because there is no corresponding data point at this location in the curve. However, at the end of the step, the net displacement should be zero. We note that the computed value at the end of the step is 0.176 cm. This suggests that while we have made a good effort to develop a motion model for our simulation, there is some small error that exists within the model that we must be cognizant of when applying these data to the PNS simulation.
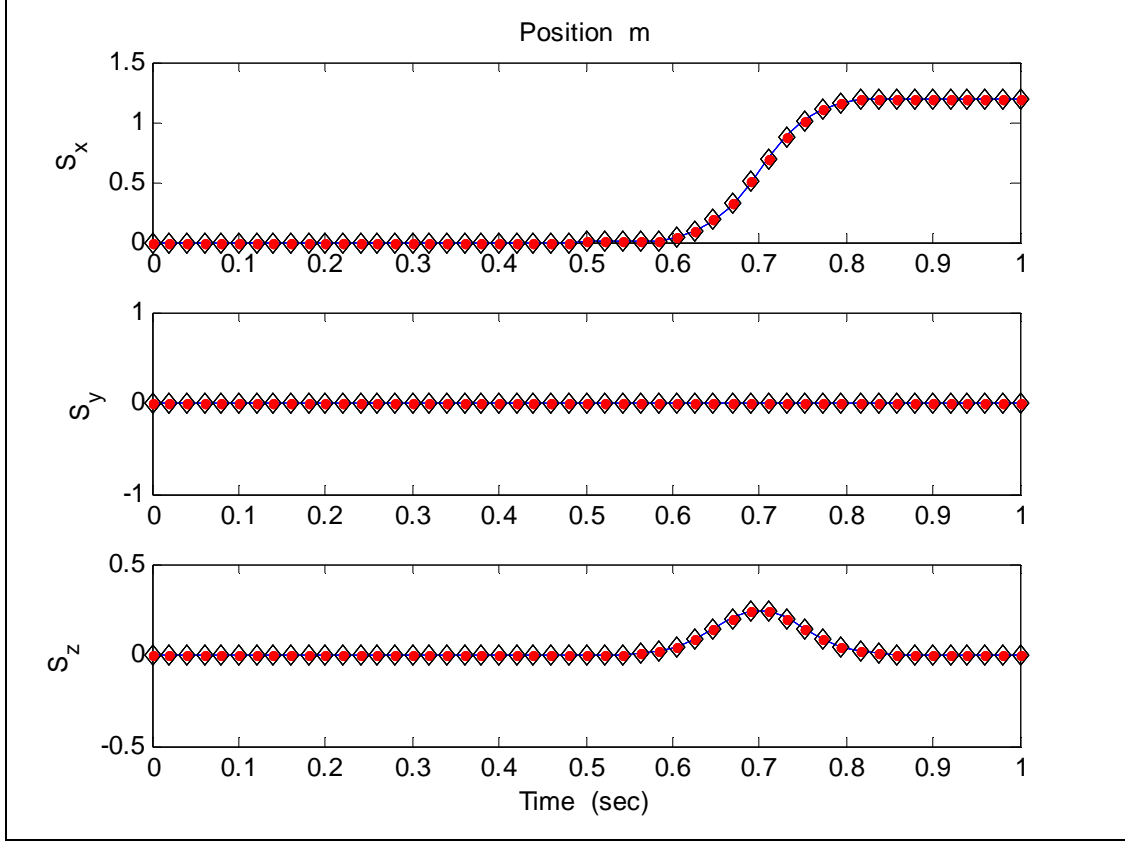
Figure 76.   Navigation frame position derived from analytical expression (solid), MATLAB's *cumtrapz( )* function (red dots), and the author's *myTrapZ( )* function (black diamonds).

D.   NOISE MODEL FOR THE THREE-DIMENSIONAL FOOT MOTION SIMULATION

In the last section, we developed the three-dimensional model for the foot motion using the Gaussian function as a foundation for the velocity and displacement curves. The model gave sensor data from a foot-mounted IMMU in body frame coordinates. In moving forward from this point, it is desirable to include a random component to this model that represents the various errors present in any real-world measurement. This section discusses the work accomplished in this effort to include the effects of calibration error and random noise.

1. Sources of Sensor Error

The output of a given sensor is composed of two parts. One component represents the true value of the physical phenomenon to be quantified—acceleration, angular rate, or the magnetic flux density. The second component in the sensor output is an error, which degrades the overall accuracy of the desired measurement. This error can be further decomposed into two additional parts: a calibration error and a random error. Calibration error is related to the design and manufacturing tolerances of the sensor. Random error, on the other hand, arises as a natural consequence of the physical interactions occurring at the atomic and molecular level of materials within the sensor systems [84].

Generally, after manufacturing and assembly, a sensor undergoes a calibration procedure wherein its output is compared against an input reference. The reference input (or calibration standard) has some specified accuracy that is hopefully traceable to an accepted standard. Associated with the calibration standard is an uncertainty that, consequently, can be extended to the sensor undergoing calibration. Typically this uncertainty is relatively small compared to the input range of the sensor; but it presents a lower bound on the accuracy that can be achieved by a given sensor. Other contributions to the calibration error include null-bias error, scale-factor error, and cross-axis coupling error. Gyroscope accuracy is further compounded by acceleration-dependent bias resulting from the inertia of the gyroscope sensing element [10, pp. 72 and 156–159]. The purpose of the calibration is to mitigate these errors. However, the accuracy of the calibration is influenced by variations in temperature. It also exhibits a random variation in time, which results in the requirement for periodic recalibration of the sensor.

Random error, or more commonly referred to as noise, limits the overall accuracy of the sensor calibration. For magnetometers, the noise is electronic in nature and is generated within the sensing element and its associated electronics. Mechanisms, such as thermal (Johnson) noise, shot noise, and flicker ($1/f$) noise are the result of physical processes occurring within the resistive elements and semi-conductor materials of modern-day electronics [85], [86]. Additionally, MEMS-based sensors are further

impacted by thermal-mechanical noise, also known as Brownian motion [87], [88]. This is due to the random interactions between gas molecules surrounding the miniature mechanical parts of the sensor micro-structures, which are amplified by the sensor electronics.

Sensor noise is typically characterized by its power spectral density (PSD). For cases where the noise power is dominated by Johnson noise, shot noise, or Brownian motion, the PSD appears spectrally flat. On the other hand, flicker noise has a spectrum that is inversely proportional to frequency and may be the dominant noise process at low frequency. Dimensional units associated with sensor noise are in terms of the square of the sensor's unit of measure with respect to unit bandwidth, such as G^2/Hz or $G/\sqrt{\text{Hz}}$ for an accelerometer.

2. A Model for Sensor Noise

To continue the development of the foot motion sensor model, we need an appropriate representation for the error existing within each measurement. MATLAB provides the *randn( )* function, which is the random number generator that produces samples having a Gaussian (normal) distribution. The proposed noise model has the form

$$\mu + \sigma\, randn(\cdot) \tag{4.18}$$

where μ is the mean value of the noise and σ is the standard deviation. To test whether this model is suitable for the generation of sensor noise, it is necessary to compare the PSD of (4.18) to the PSD of the real noise acquired from the 3DM-GX1.

To that end, a set of measurements were collected from the sensors within the 3DM-GX1. While the IMMU sat motionless for approximately 1:35 hours, approximately 297,000 data samples were collected from each of the accelerometers, magnetometers, and gyros within the unit. For the gyros, this measurement can give some good insight of the μ and σ of the noise because these sensors have zero input while they are sitting motionless on the lab bench. Admittedly, there could be some

148

extrinsic rotation or vibration that is present within these measurements, but for these purposes, they are assumed to be negligible. The static measurements from the accelerometers and magnetometers can also be used to gain some knowledge of the sensor noise. However, it must be recognized that these sensors are under the inescapable influence of gravity and the earth's magnetic field. Therefore, the corresponding μ for each sensor measurement represents the mean value of these phenomena, and only the σ from these measurements can give insight into the sensor noise.

In Figure 77, the PSD for one of the accelerometers is shown, which was derived using the methods in [89].[**] The upper plot has the PSD of the sampled data, while the lower plot shows the PSD created from (4.18) using the μ and σ derived from the actual measurement data. Interestingly, these plots have similar spectral qualities suggesting that MATLAB's *randn( )* function will be suitable for modeling the sensor noise. Reading the magnitude of the accelerometer noise power from the upper plot gives an approximate value of $-65\,\mathrm{dBG}^2/\mathrm{Hz}$. This value is converted into linear units, which yields approximately $562\,\mu\mathrm{G}/\sqrt{\mathrm{Hz}}$. It is a reasonable value when compared with the stated figure of $400\,\mu\mathrm{G}/\sqrt{\mathrm{Hz}}$ given in the specification sheet for the 3DM-GX1. Lastly, we make an examination of the sample distribution of the measurement data and our noise model using the histogram plots in Figure 78. Comparison of the upper and lower plots further reinforces the idea of the use of MATLAB's *randn( )* function here.

In Figure 79, the noise from the angular rate sensor in considered. The upper plot shows the PSD for the angular rate sensor measurements under static conditions. The lower plot shows the PSD for the corresponding noise model. Comparing these plots indicates that both processes have similar spectral properties. The noise power level is read directly from these plots giving an approximate value of $-57\,\mathrm{dB}(\mathrm{rad/sec})^2/\mathrm{Hz}$. This figure is converted to an equivalent value of $4.85\,\mathrm{deg}/\sqrt{\mathrm{hr}}$, which compares

---

[**] The PSD was created using MATLAB's *cpsd( )* function. It is based on Welch's averaged modified-periodogram method of spectral estimation. This gives a more accurate representation of the true PSD rather than the DFT of the sampled data. See MATLAB help on *cpsd( )*.

reasonably with the value of $3.5 \, \text{deg}/\sqrt{\text{hr}}$ provided in the manufacturer's specification sheet. Lastly, Figure 80 shows the sample distributions for the measurement data and the noise model data. Comparing these histograms further reinforces the notion that an expression of the form in (4.18) is suitable for use in our MATLAB foot motion model.

For the magnetometer, similar plots were generated, as shown in Figure 81 and Figure 82. Making similar comparisons as before suggests that the proposed noise model is suitable for the magnetometer, as well. It is noted that the manufacturer's specification sheet did not include a noise power density figure for the magnetometer; therefore a comparison with measured data could not be accomplished. The PSD for the measured magnetometer data shows harmonics at the approximate frequencies of 5 Hz, 9 Hz, 17 Hz, and 23 Hz. While the source of these spectral spikes can not be provided with certainty, it is surmised that they may be related to a SET/RESET feature within the magnetometer. This operation requires a periodic pulse of current to be injected through the magnetometer to ensure reliable operation of the sensor [90].
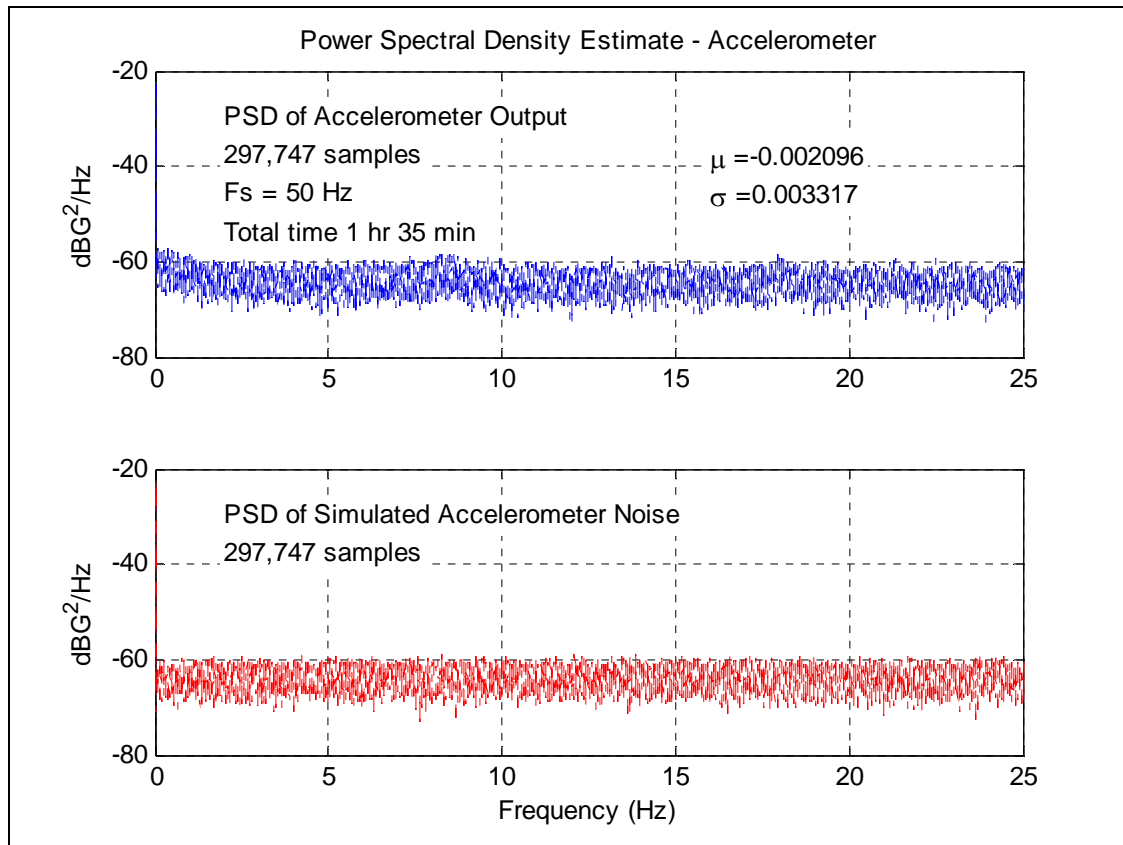
Figure 77. PSD of measured accelerometer output (upper plot) and simulated accelerometer noise model (lower plot).
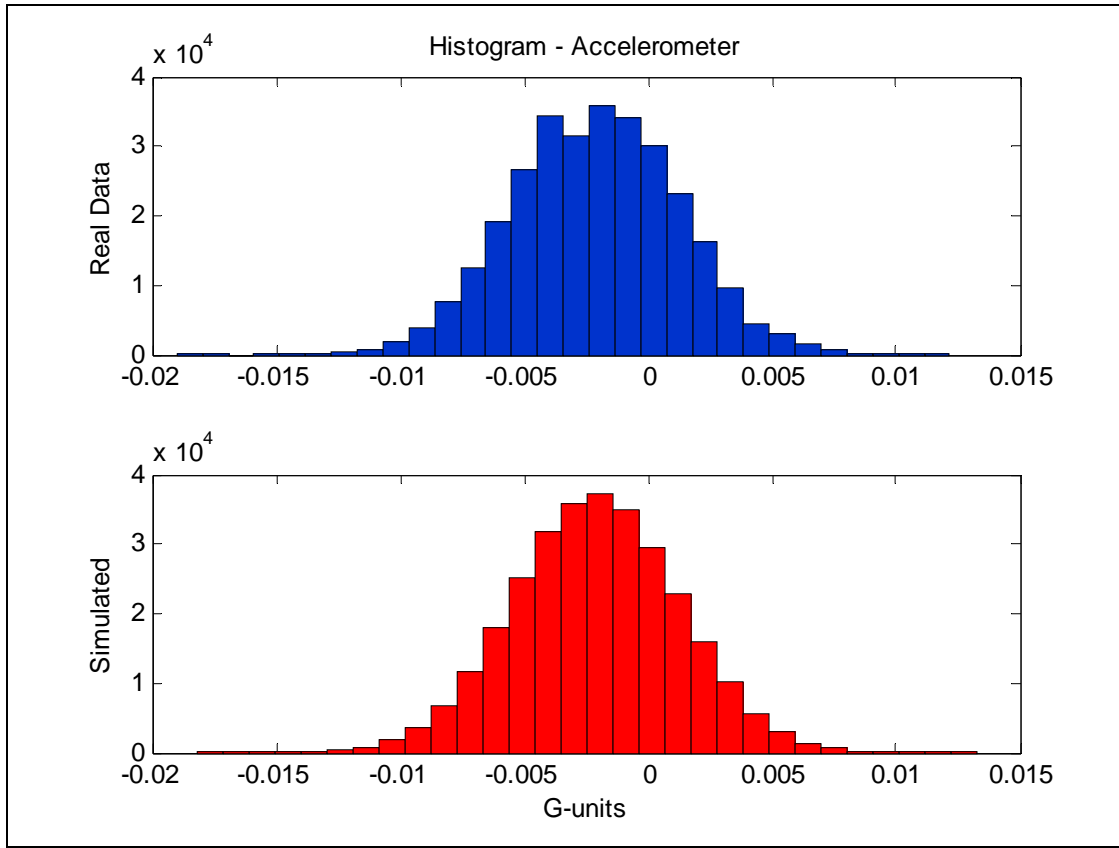
Figure 78. Sample distribution for measured accelerometer output (upper plot) and simulated accelerometer noise model (lower plot).
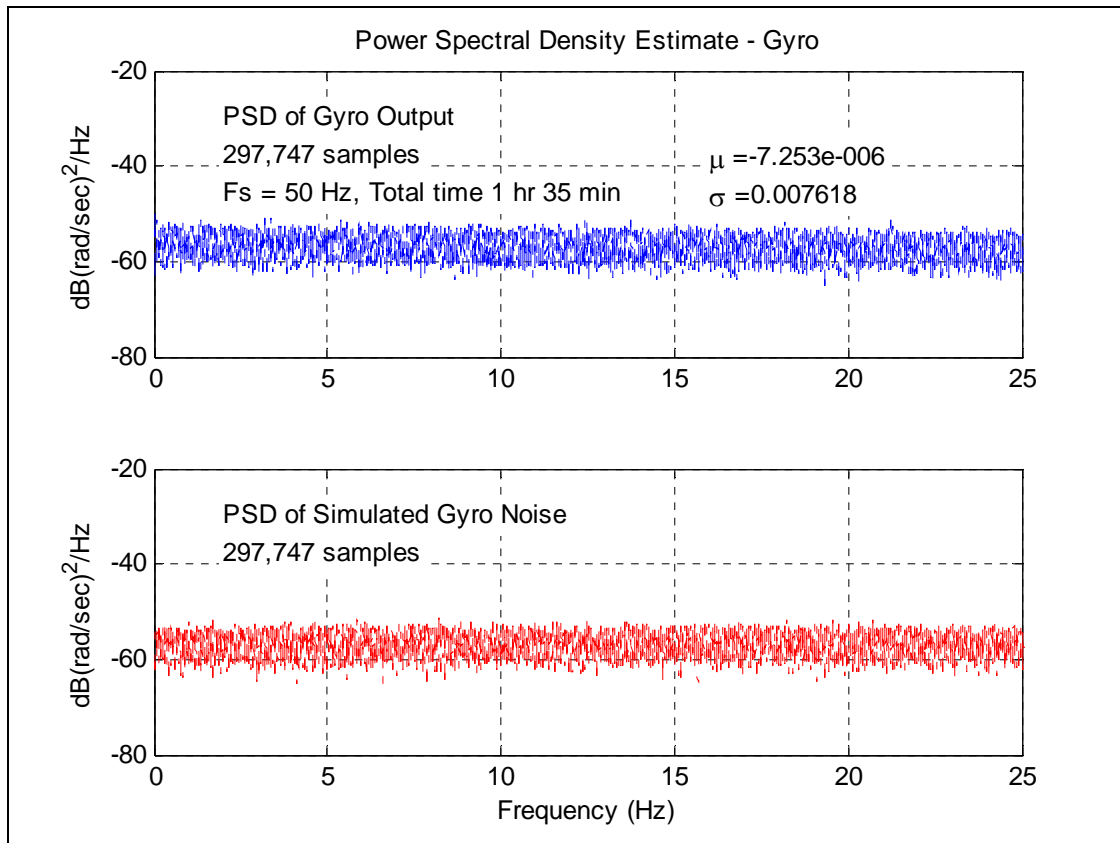
Figure 79.　PSD of measured gyro output (upper plot) and simulated gyro noise model (lower plot).
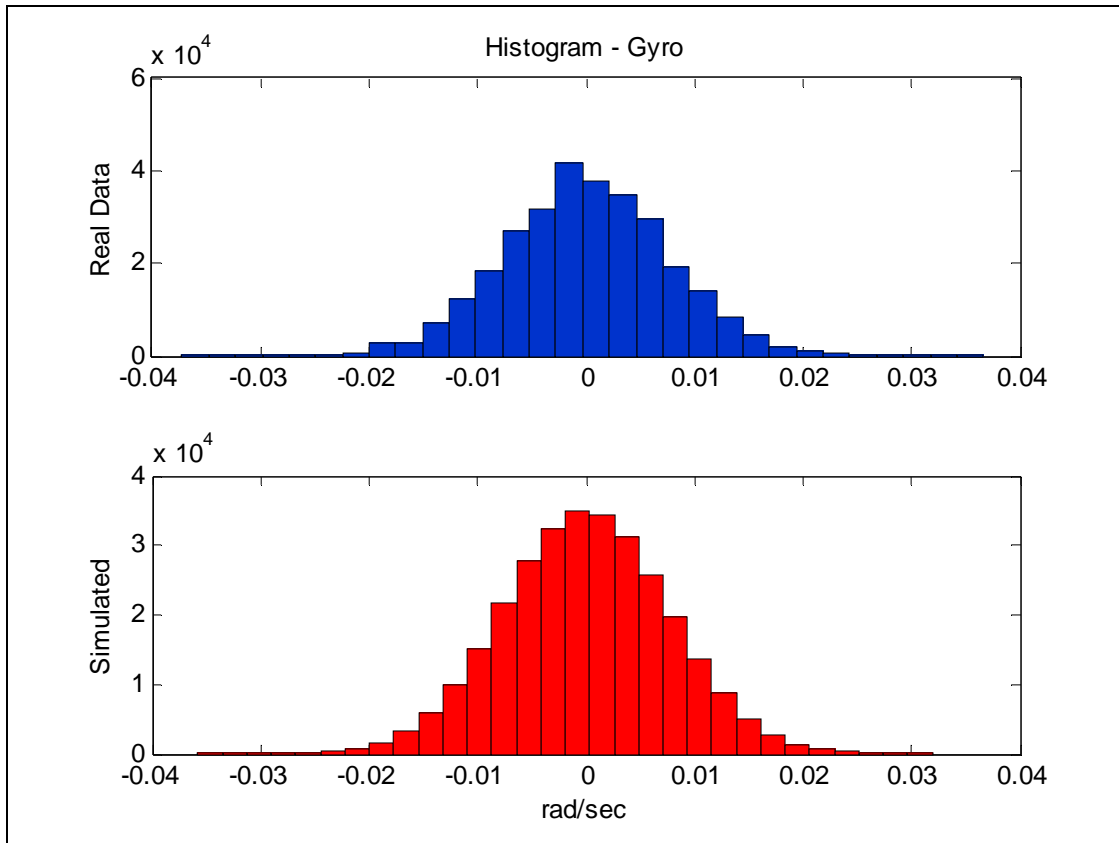
Figure 80.   Sample distribution for measured gyro output (upper plot) and simulated gyro noise model (lower plot).
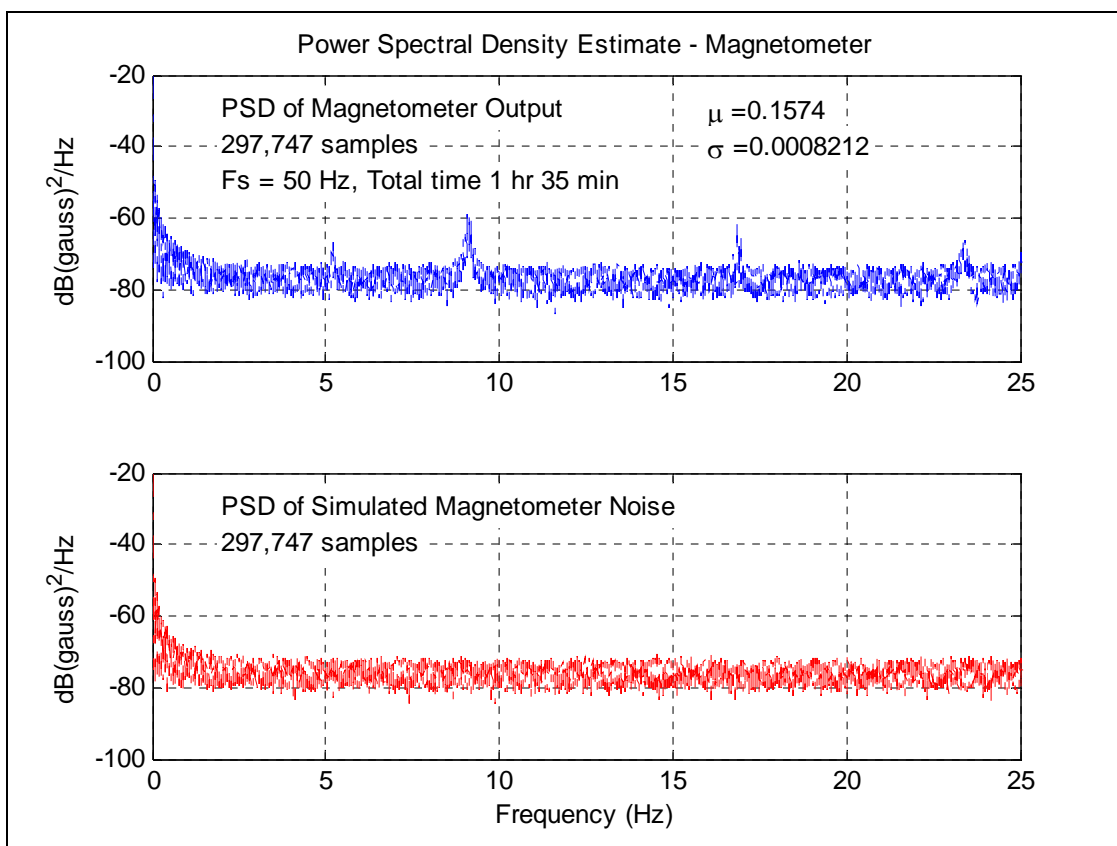
Figure 81.   PSD of measured magnetometer output (upper plot) and simulated magnetometer noise model (lower plot).
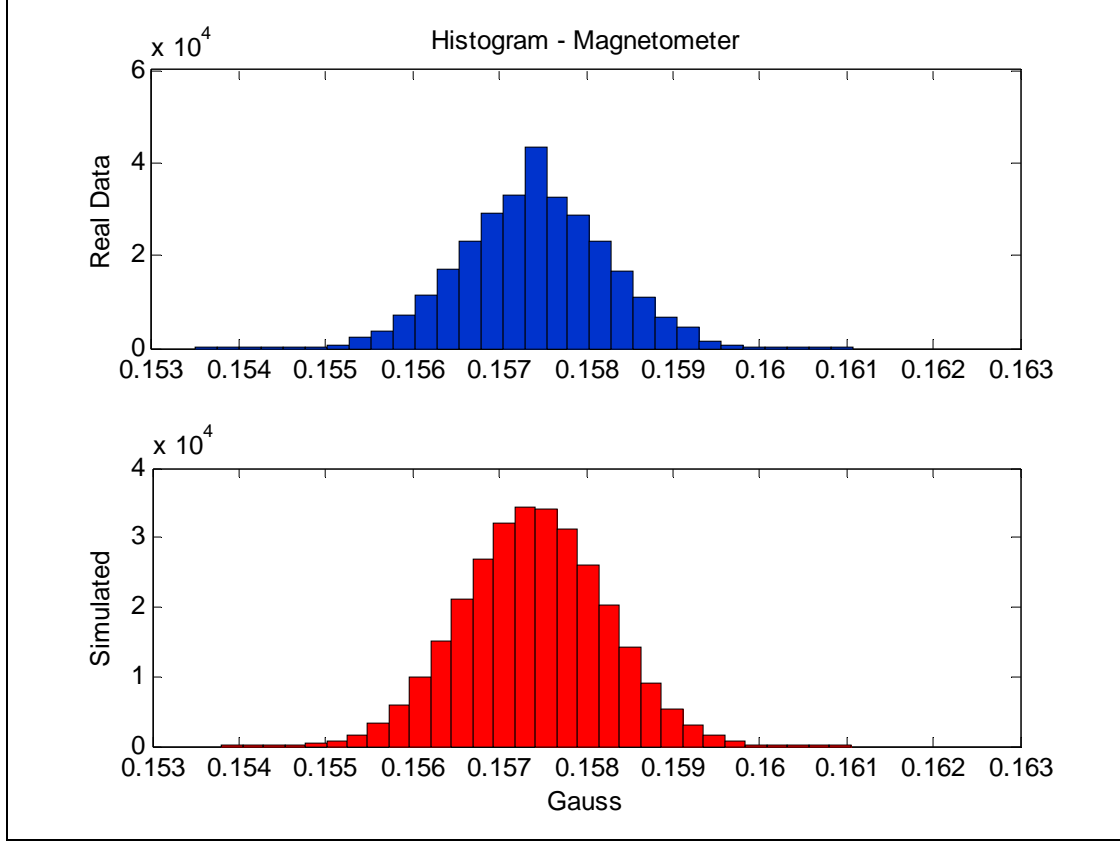
Figure 82.   Sample distribution for measured magnetometer output (upper plot) and simulated magnetometer noise model (lower plot).

E.   PNS PERFORMANCE USING THE THREE-DIMENSIONAL FOOT MOTION MODEL WITH NOISE

Now that a complete three-dimensional model for the foot motion acceleration has been presented, which also includes a random component to simulate the sensor error, we can begin the examination of the PNS performance. For convenience, the main features of the motion model are shown in Table 9. In addition to these features, it is also noted that the walking motion occurs in a straight line in a northerly direction. A useful feature of our model is that the number of walking steps may be easily varied as desired, as well as, μ and σ for the nine sensors within the IMMU.

Table 9.   Summary of foot motion acceleration model.

Model	Gaussian
Stride length	1.2 m
Vertical displacement	0.25 m
Duration of step	1.0 sec
Duration of swing phase	0.4 sec
Sampling frequency	50 Hz
Accelerometer error	$\mu = 0.1\%$ of full scale $\sigma = 0.0325\,\mathrm{m/s^2}$
Magnetometer error	$\mu = 0.1\%$ of full scale $\sigma = 0.8212\times10^{-3}$ Gauss
Gyro error	$\mu = 7.2\times10^{-6}$ rad/s $\sigma = 0.0077\,\mathrm{rad/s}$

To begin examination of the PNS performance, first we consider the case where the walking motion occurs in the absence of any sensor error, as shown in Figure 83. The simulation presented was for a 100-step straight-line walk in the northerly direction. Total distance error was 3.33 meters for the 120-meter walk. In spite of the noiseless sensors used in this simulation, an error of 2.8 % still resulted. The source of this error is due to a number of reasons. It is well known that the selection of numerical integration method and sampling interval play a significant role in the resulting error; however, as was learned from the previous discussion in Section B of this chapter, the particular choice of the acceleration model and the manner in which the samples are distributed also play a role in the final error. Therefore, while it may not be readily determined which of

these factors plays the larger role in the resulting error, it must be acknowledged that there is some degree of error in the present simulation in which error-free sensors are considered.
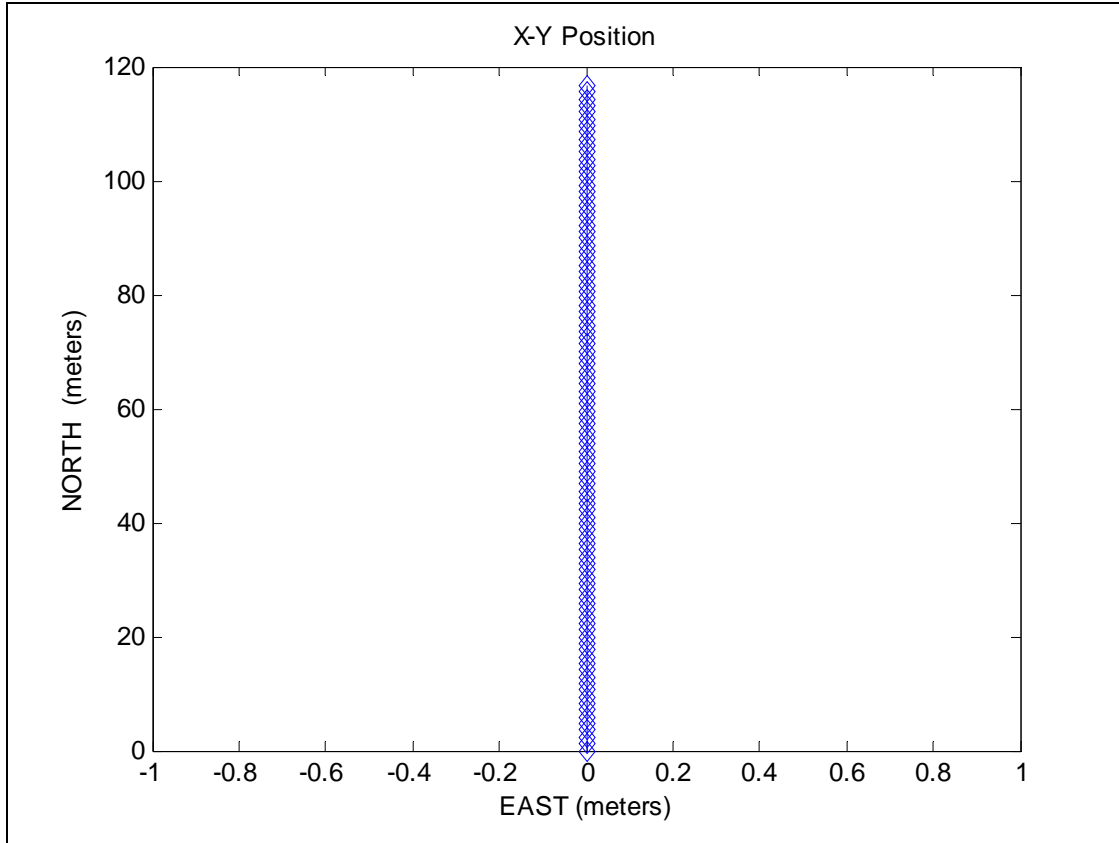
Figure 83.   PNS track of a 100-step straight-line walk in the northerly direction with no sensor error in the IMMU.

Next, we consider the case where sensor error is included in the foot motion model. The following figure examines cases where a proportional amount of sensor error has been included is shown. For these simulations, only a value for σ , which was derived from the measured data for each sensor type, was used, and μ was set to zero for these trials. The plots also show each simulation repeated 50 times to gain some sense of the statistics of the result. A sensor error scale factor was incorporated to examine the effects of increased or decreased sensor noise in the PNS algorithm.

The results of these simulations are shown in Figure 84. Subplot (a) is the case where no sensor noise was included, and is the same result as that shown in the previous figure. Subplots (b), (c) and (d) show the results when the sensor error scaling factor was set to 0.1, 1, and 10, respectively. Consistent with one's intuition, as the sensor noise is increased, there is a corresponding increase in the resulting position error, as can be seen qualitatively in the figure. The spread of the position error in the East/West direction can be seen to increase as the sensor error scale factor is increased. Table 10 shows the pertinent statistics of these simulation results.
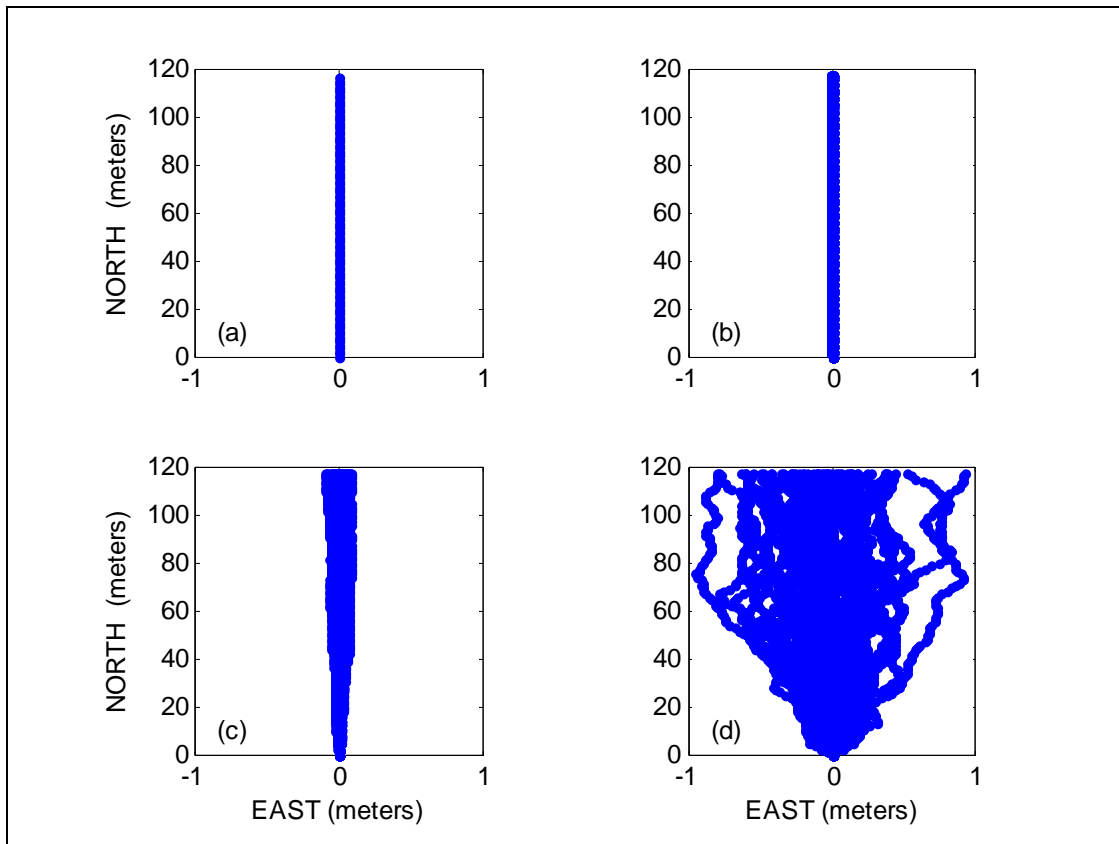
Figure 84.   Simulation results for fifty 100-setep straight-line walks, (a) no sensor error, and sensor error scale factor equal to (b) 0.1, (c) 1, and (d) 10.

Table 10.   PNS error performance due to varying sensor error scale factor.

Sensor Error Scale Factor	East/West Error (meters)		North/South Error (meters)	
	μ	σ	μ	σ
No sensor error	0	---	3.33	---
0.1	0.00041	0.0035	1.75	0.011
1	-0.0040	0.041	1.76	0.012
10	-0.094	0.35	1.79	0.05

Referring to the table above, for the East/West error, the standard deviation of this figure increases in proportion to the sensor error scale factor. For the mean value of the East/West error, on the other hand, we would expect a result near zero, since that is what was used for the sensor error. More simulations would be required to verify whether this is true. Interestingly, the mean value of the North/South error does not seem to depend on the sensor error scale factor, but it is, however, reduced from the case of no sensor error. While it is not determined with certainty, this behavior may be attributed to what is referred to as dithering, wherein noise is intentionally added to a system to achieve an improved performance [91].

Next, we consider the inclusion of μ or sensor bias in the sensor data. For the gyros, the measured value is used in the simulations. However, since it was not possible to measure a corresponding μ for the accelerometers and magnetometers, a nominal value will be used in its place that is proportional to the full scale range of each sensor. A value of 0.1 % of the sensor full scale range is selected. The sensor error scale factor, which only affects σ for each sensor type, is set equal to one. Figure 85 and Table 11 show the results of these simulations. Comparing this figure with the results shown in Figure 84 indicates that the sensor bias introduces a drift or bias into the PNS-computed track.
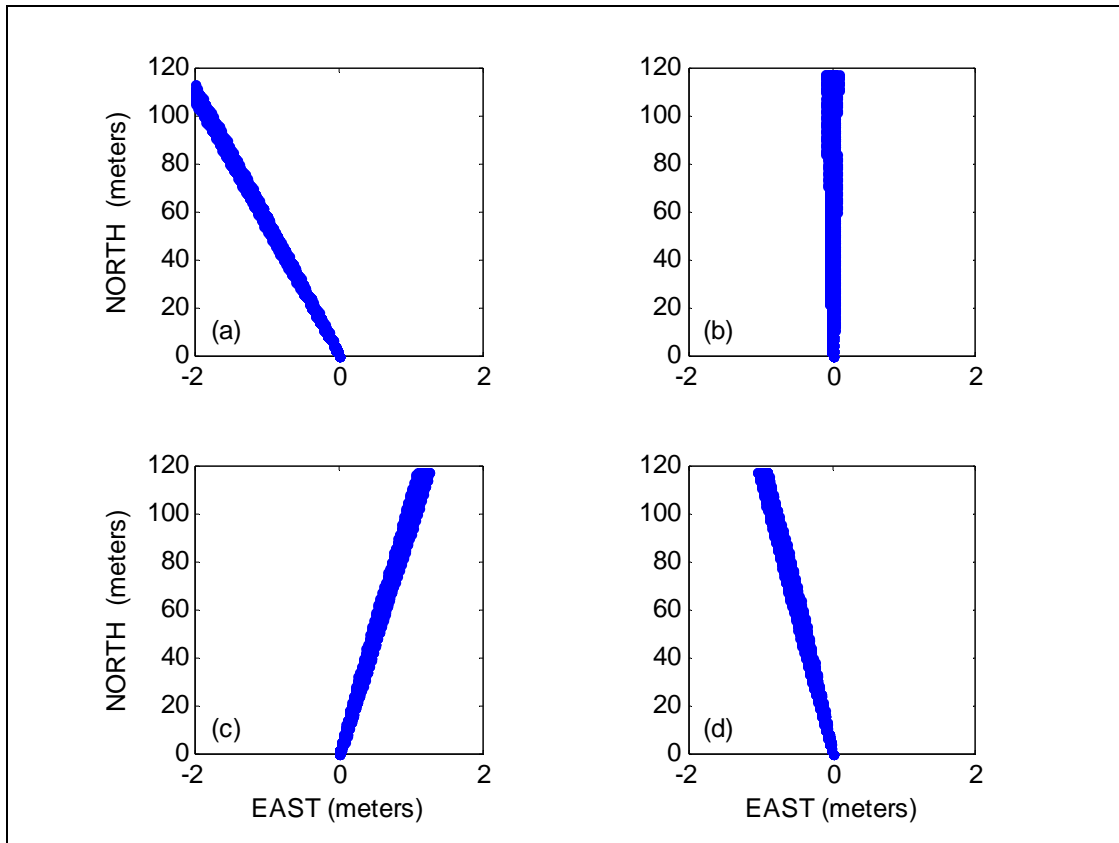
Figure 85.　Simulation results for fifty 100-step straight-line walks with sensor error scale factor equal to one and (a) accelerometer bias only, (b) gyro bias only, (c) magnetometer bias only, and (d) all sensor biases included.

Table 11.　PNS error performance with sensor error scale factor equal to one and varying sensor biases.

Sensor Error Scale Factor = 1.0	East/West Error (meters)		North/South Error (meters)	
	μ	σ	μ	σ
Accel bias (0.1% full scale)	-2.18	0.036	-1.83	0.012
Gyro bias (measured)	-0.0006	0.035	-1.75	0.012
Mag bias (0.1% full scale)	1.17	0.044	-1.76	0.012
All sensor biases included	-0.97	0.036	-1.82	0.011

161

In addition, if one compares Table 11 with the case for sensor error scale factor equal to one in the pervious table, it is noted that the spread, σ, for the East/West error remains relatively unchanged, however, the mean error has been significantly affected by the inclusion of the sensor bias. It would not be entirely appropriate to try to assess the sensitivity of this bias error to the biases introduced into the three sensor types because an accurate measurement for the accelerometer or magnetometer biases could not be acquired, and we arbitrarily chose to use a figure of 0.1% of sensor full scale instead. It is illustrative, nonetheless, the manner in which the sensor error bias impacts the overall error of the PNS.

In the following plots, the effect of the sensor error on the PNS performance is considered with respect to the number of walking steps. Figure 86 shows the East/West error for three different cases: 1) no sensor noise, 2) sensor noise included, but $\mu = 0$, and 3) sensor noise and $\mu \neq 0$. The plot also shows the error (blue diamonds) from three actual walks, each of approximately 300 steps, around an athletic track. The first two cases, these are the simulations having zero noise and the other having zero sensor bias, gave similar error performance. The height of the error bars also is observed to increase with respect to the number of steps taken, which is indicative of the growth or spread in the position error with respect to the number of walking steps. This behavior is certainly consistent with that of inertial navigation systems in general. In the third case, the simulation included a bias error in the sensors. As noted earlier, the sensor biases introduce a drift in some particular direction, which is represented in this plot. In fact, this last simulation result suggests that the PNS performance error may be more sensitive to these sensor bias errors than to the magnitude of the sensor noise.
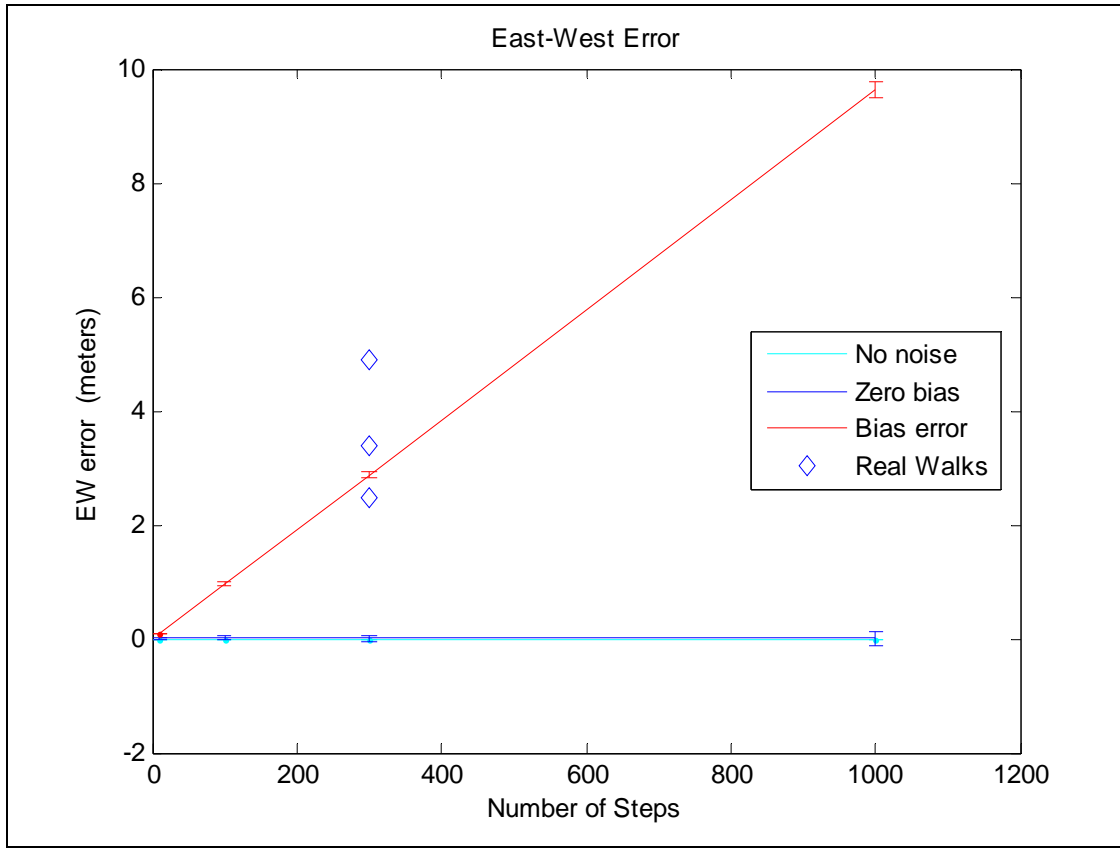
Figure 86.   PNS East-West error with respect to number of walking steps.
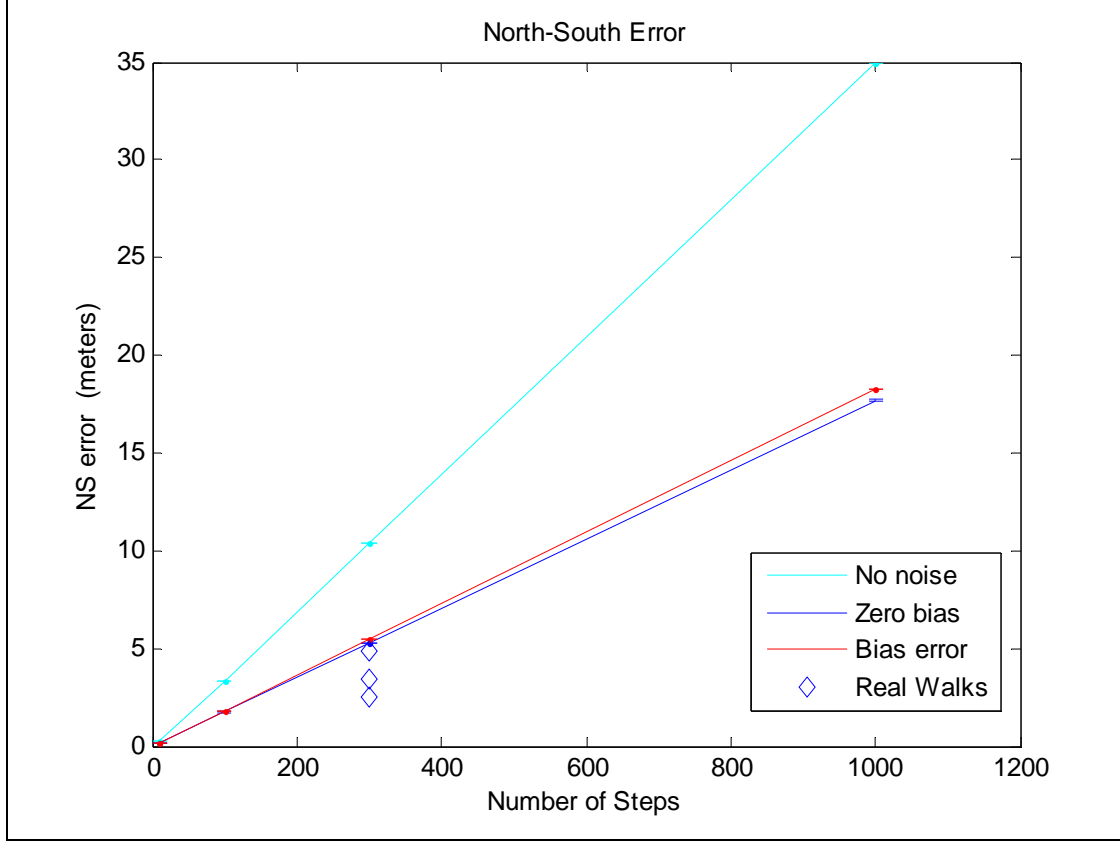
Figure 87.   PNS North-South error with respect to number of walking steps.

F.   PNS PERFORMANCE WITH REAL DATA

Up to this point, we have examined the performance of the PNS algorithm only with simulated data. We learned how the sensor noise (σ) affects the performance of the PNS, and that the spread of the position error will grow with the number of steps taken. It was also observed that the sensor bias (μ) will introduce a drift into the computed position in some direction. It may be further inferred that this quantity may have a more significant impact on the resulting position error than the sensor noise.

Next, in this section we consider the performance of the PNS using actual walking data from the foot-mounted IMMU. With the new algorithm available for use in our PNS, the initial position tracks from Chapter II may now be revisited. The IMMU data from those tracks are applied to the PNS algorithm and compared to the previous results. First, Figure 88 shows the location where many of the walking trials were conducted. It

is a standard athletic track located at Hartnell Community College in Salinas, California. The circumference of the inner lane is 400 meters. Lane seven, where the walks were accomplished, is estimated to be 437.50 meters. All walks were conducted in a counter-clockwise direction. They began and ended at the same point on the track, as shown in the image.

1. PNS with Constant Gain

Figure 89 was generated using the complementary filter set to a constant gain. Three different values were used. Immediately upon inspection of the plot, one sees that the resulting tracks do not resemble the true oval path. When the filter gain was set to $k = 0.15$—recall that this value gave a minimum error in the vertical pendulum—the algorithm does not produce a satisfactory position track. Two other values of gain were considered, $k = 0.001$ and $k = 0.5$. Neither one of these values produced an acceptable result. In fact, when $k = 0.001$, the computed track drifted off in a direction away from the true closed path.

Figure 88.   Athletic track used for PNS walking trials (From [92]).
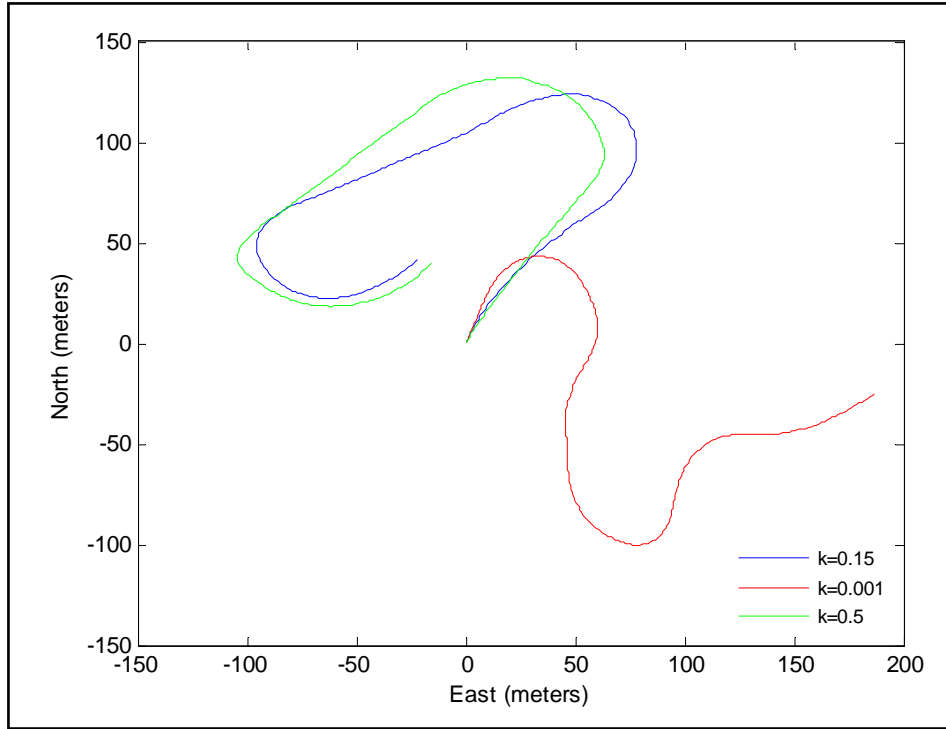
Figure 89.   PNS tracks using a constant-gain complementary filter.

2.   PNS with Adaptive Gain

Next the PNS is evaluated with an adaptive gain strategy. The filter gain will be switched between two values according to the gait-phase detection algorithm. When the foot is in the stance phase, the gain is set to a nominally high value. This is where the motion-induced accelerations are lower, and the FQA produces better results. During the swing phase, the foot is moving through the air experiencing rapidly changing acceleration, and the filter gain is set to a low value such that more of the dynamic quaternion is represented in the filter output.

Figure 90 shows the computed position for the three walks around the athletic track. The dashed lines are those that were produced with the proprietary quaternion. Solid lines represent the tracks computed using our complementary filter with adaptive gain.   Qualitatively, these tracks represent a marked improvement over those computed

using the constant-gain filter and those produced with the proprietary quaternion. The overall shape and orientation of the computed tracks appears very similar to the athletic track shown in Figure 88.
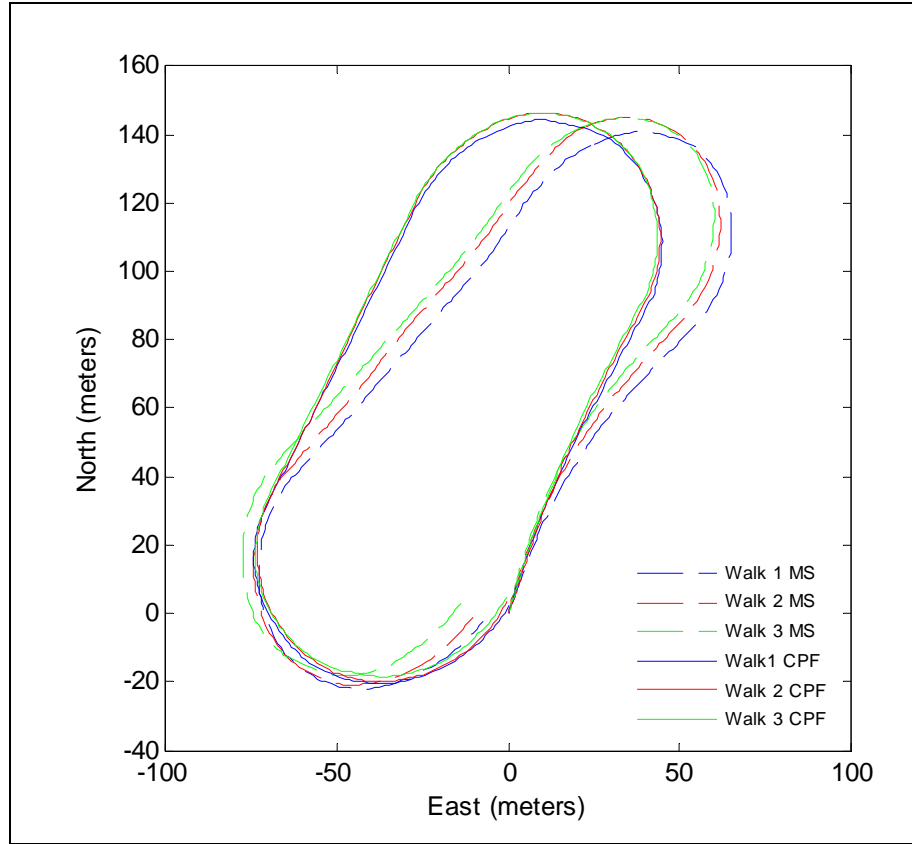
Figure 90.   Comparison of position track using adaptive-gain complementary filter (solid) and proprietary algorithm (dashed).

The following tables make a more quantitative comparison of these position tracks.

Table 12 shows the results for the tracks that were computed using the proprietary quaternion (dashed lines in Figure 90). The Distance column is the computed distance traveled for a given walk. Recall that the estimated path length was 437.50 meters. Using this value, the Distance Error was derived and also included in the table. Another parameter, ΔXY, is the computed position at the end of each walk. Since all walks began

and ended at the same point on the track, this figure represents the radial distance to the origin. The last column is a position error based on the total distance.

Table 13 has the same information as the previous table, but represents the performance of the adaptive-gain complementary filter. Comparing the Distance Error columns from both tables, the adaptive-gain complementary filter has better performance by almost an order of magnitude. Secondly, the last column of each table, which has the position error of distance walked, shows that the new filter reduces this error by almost half.

Table 12.   PNS performance using the proprietary algorithm.

	Proprietary Algorithm			
	Distance (m)	Distance Error	ΔXY (m)	% Error of Distance Walked
Walk 1	445.95	1.9%	7.73	1.8%
Walk 2	446.72	2.1%	10.53	2.4%
Walk 3	446.15	1.9%	14.25	3.3%

Table 13.   PNS Performance using the adaptive-gain complementary filter.

	Adaptive-Gain Complementary Filter			
	Distance (m)	Distance Error	ΔXY (m)	% Error of Distance Walked
Walk 1	438.43	0.21%	2.52	0.58%
Walk 2	439.30	0.41%	3.37	0.77%
Walk 3	438.35	0.19%	4.84	1.10%

G.   SELECTION OF THE APPROPRIATE GAIN

The last section showed that the performance of the PNS is greatly improved when an adaptive gain strategy is utilized. In this approach, two gain values are required, k_s and k_d. The former is used when the accelerations are low, as in the foot's stance phase, while the latter is used during the foot's swing phase. To determine the values of the filter gain that produce the best results, a simple optimization study was accomplished.

During each iteration of the optimization loop, two filter gain values were selected, one for k_s and one for k_d, from a set of possible gains; then the corresponding position error was computed using the PNS algorithm. Each point spanning the range $k_s = \{0.6 ... 1.6\}$ and $k_d = \{0 ... 0.02\}$ was considered in the optimization. Since the track started and ended at the origin, then the final position error was simply

$$\delta p^n = \sqrt{p_x^n(t_f)^2 + p_y^n(t_f)^2} \qquad (4.19)$$

where $p_x^n(t_f)$ is the last value of the computed position in the x^n direction, and $p_y^n(t_f)$ is the last position value in the y^n direction. The vertical direction was not considered because the athletic track was locally flat. Consequently, it was not considered prudent to include the inaccuracies that may exist in the vertical channel in this study.

Figure 91 shows the result of this optimization study. For each pair of gains, k_s and k_d, the computed position error was plotted in the vertical axis of the mesh plot. The horizontal axes are labeled as k_s and k_d. The plot shows that a minimum error is produced when $k_d = 0$ and $k_s = 1.05$. Figure 92 gives a better view of the plot with respect to k_s. It is from here that the value for k_s may be estimated more accurately. The

lowermost curve in this plot corresponds to $k_d = 0$ and $k_s = \{0.6...1.6\}$. Inspection of this curve supports the idea that a value of approximately $k_s = 1.05$ gives the minimum error.
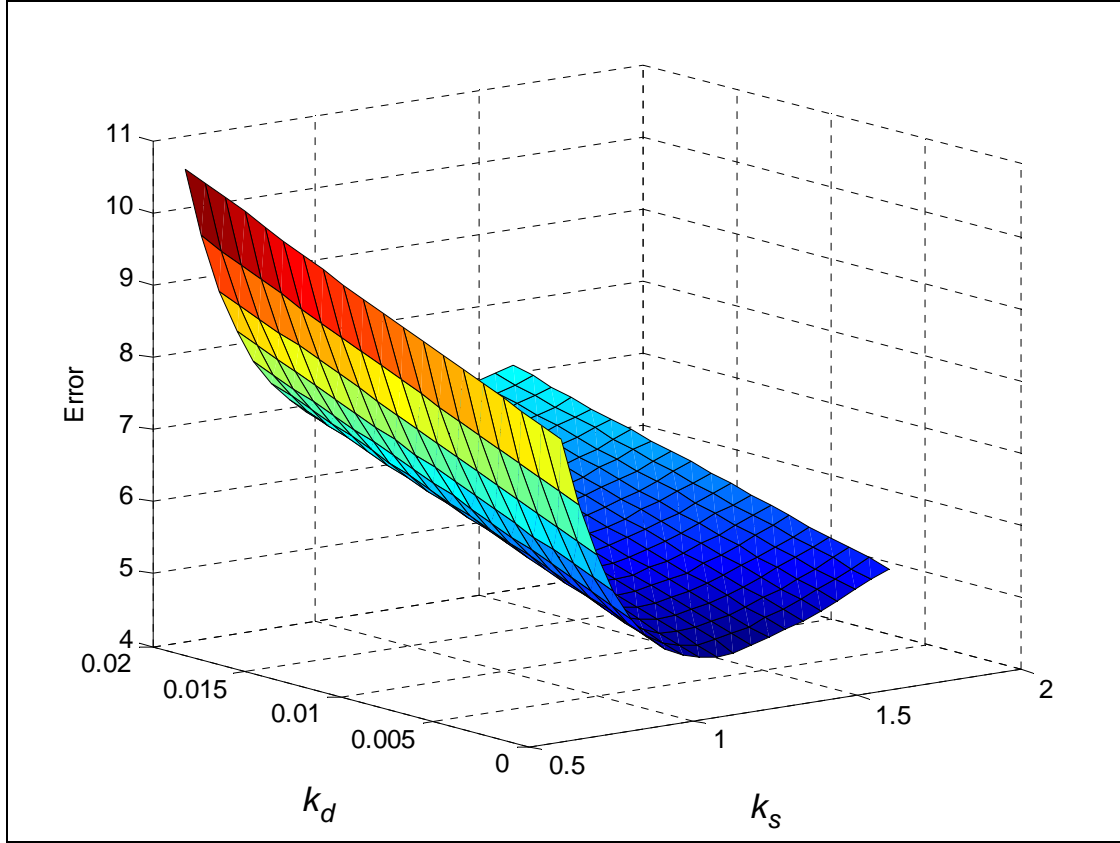
Figure 91.   Optimization of the adaptive gain in the complementary filter.

Comparing these values to the result of the pendulum optimization, where we learned that setting the gain equal to 0.15 gave a minimum pendulum angle error, we see that for walking motion, setting the filter gain to zero ($k_d = 0$) during the swing phase produces better results. During the swing phase, the foot acceleration is changing very rapidly, and the accelerometers output is comprised of a larger part that arises from this motion and a smaller part that comes from the gravity vector. As a result, the FQA gives large errors at this point in the foot motion. In spite of the gyro biases and its associated error, the errors occurring in the FQA during the swing phase assumedly dominates that

170

which arises from the angular rate sensors. Consequently, setting $k_d = 0$ during the swing phase here produces better results than the gain value found in the pendulum motion experiments.

During the stance phase, when the motion-induced accelerations are lower, it is beneficial to have a larger component of the filter output derived form the FQA. Setting $k_s = 1.05$ during this period of the walking motion gives good results. However, as shown in the plot, a value larger than this is not desirable because the error is seen to increase. If the foot velocity is zero during this period, then why should the error increase as more of the FQA quaternion is passed to the filter output? This is possibly due to the fact that during the stance phase of normal walking, while the foot translational velocity is zero, its angular velocity is not. In this phase, the foot is rotating from the heel to the toe in preparation for the next step. If we compare this motion to that of the pendulum, then the foot will experience some normal and tangential acceleration that will affect the overall accelerometer output. Thus, the optimization shows that for this phase of walking motion, it is better to have a blended filter output consisting of both the dynamic and static quaternions.
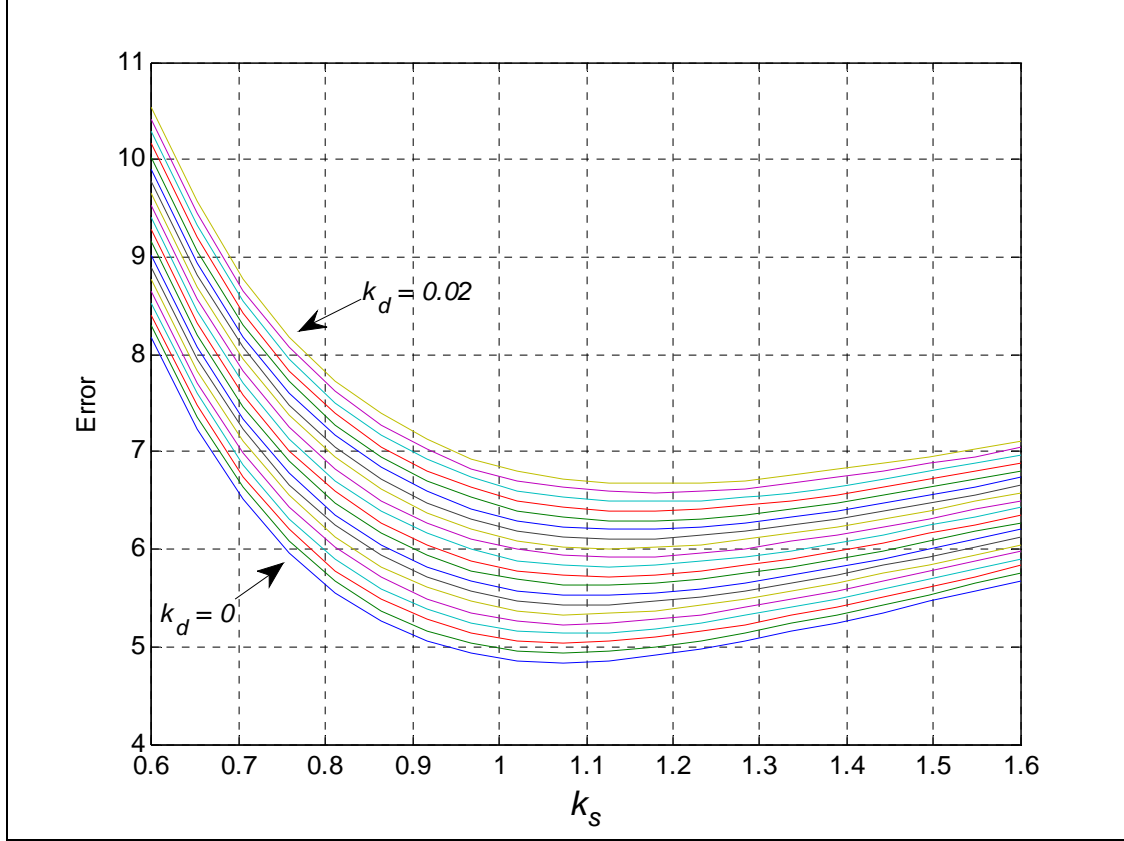
Figure 92.　　Selection of k_s. Minimum error when $k_d = 0$ and $k_s = 1.05$.

H.　ADDITIONAL COMMENTS ON THE PNS PERFORMANCE

In this section, we want to make some final observations on the PNS performance. Figure 93 shows an expanded view of the Start/Stop region of Figure 90. The endpoint for each of the three walks is marked with an 'x' in the figure. It is observed that the endpoints all lie in a region west of the origin. Recalling the impact of the calibration error (μ) introduced into the foot motion model simulations, it is surmised that the fashion in which these endpoints arise is also due to some calibration error or sensor bias existing in the actual IMMU.
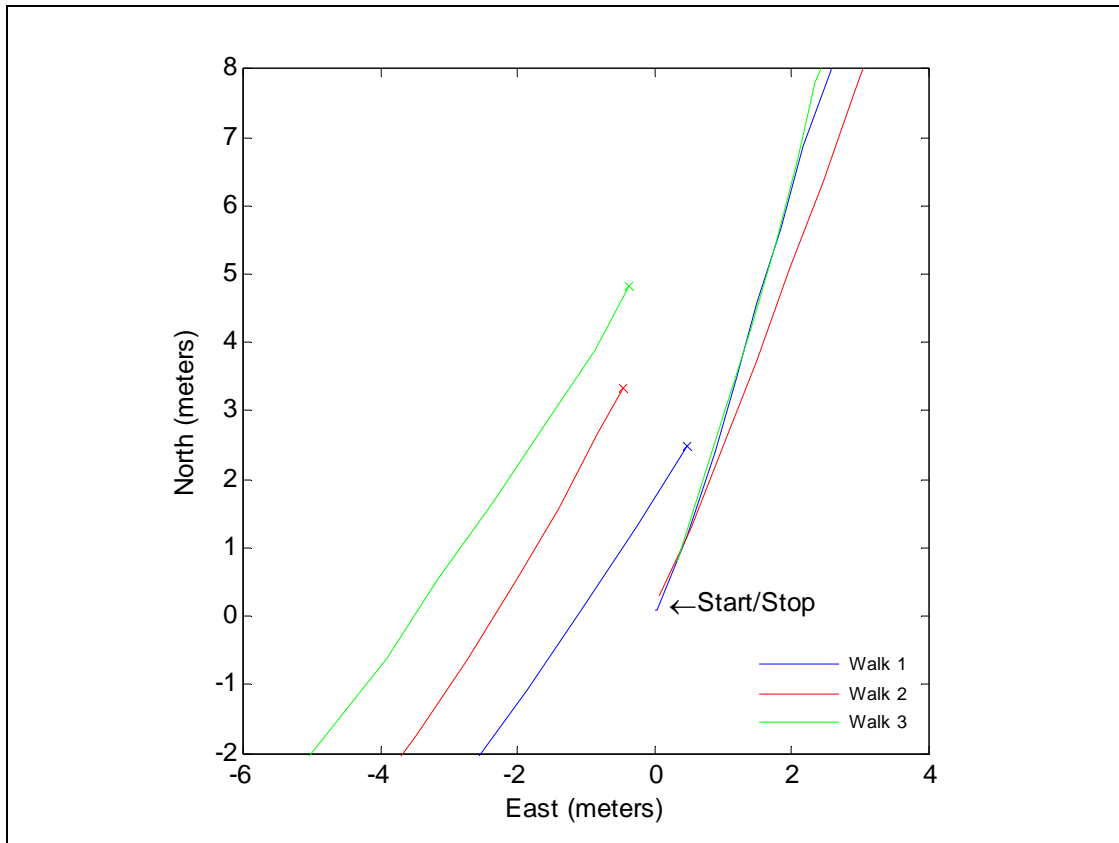
Figure 93.   Zoom of Figure 90. PNS-computed endpoints marked with an 'x'.

In Figure 94, a comparison is made with a track acquired from GPS (shown in black). No quantitative performance has been provided, but this plot is included here to give an overall impression of the PNS performance. In addition to the PNS error, there are two potential sources of error in this plot that must be acknowledged. The first source of error comes from the fact that the PNS track is computed with respect to magnetic north, while the GPS track is with respect to true north. In order for a comparison to be made between the two tracks, the PNS track was rotated by an amount equal to the local angle of declination, the precision of which can not be easily quantified. A second source of error comes from the need to convert the latitude/longitude coordinates derived from GPS into linear distance units of meters. This further requires an estimate of the earth's radius, which is on the order of 6367 km and is a potential source of error if not quantified accurately. In spite of these concerns, the figure illustrates qualitatively that the results from the PNS algorithm are roughly in agreement with the GPS track.
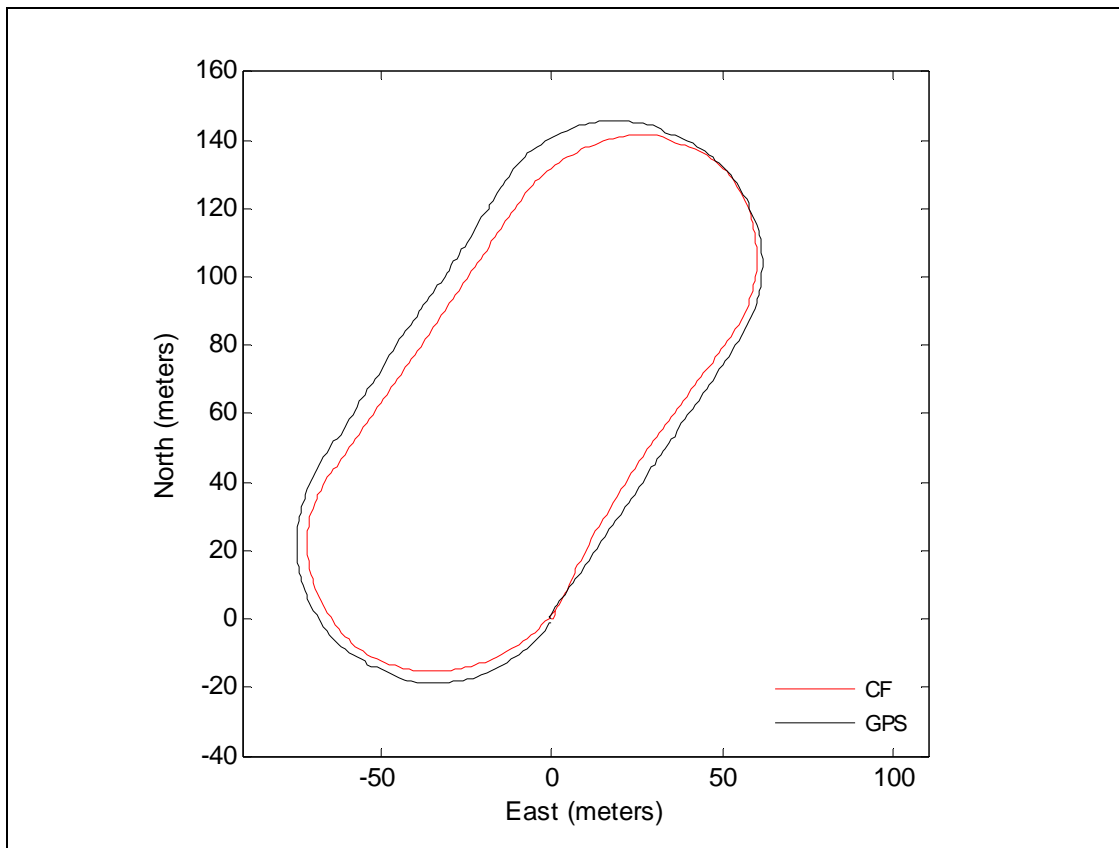
Figure 94.   Comparison of PNS track (red) with GPS track (black).

Figure 95 shows the Microstrain 3DM-GX1, which has been the primary sensor used throughout the scope of this project. Also shown in the figure is a smaller version of an IMMU from MEMSense. The MEMSense nIMU has three sets of orthogonally-mounted accelerometers, magnetometers, and angular rate sensors. It is approximately 90% smaller by volume than the 3DM-GX1.   Data is available to the user through an inter-integrated circuit (I2C) interface at 150 samples per second. Although it does not compute quaternions for the user, as does the 3DM-GX1, its smaller size makes it attractive for this application.

174

Figure 95.   MEMSense nIMU (lower) and Microstrain 3DM-GX1 (upper).

This IMMU was used in several walks around the same athletic track, the results of which are shown in Figure 96. Two observations are made here. First, the resulting plots appear to reproduce the actual walking path around the athletic track, thus reinforcing the utility of the PNS algorithm. A second observation deals with the sampling frequency. In spite of the higher sampling rate provided by this IMMU, the results are not necessarily significantly improved—a point borne out in the simulation study presented earlier in this chapter.
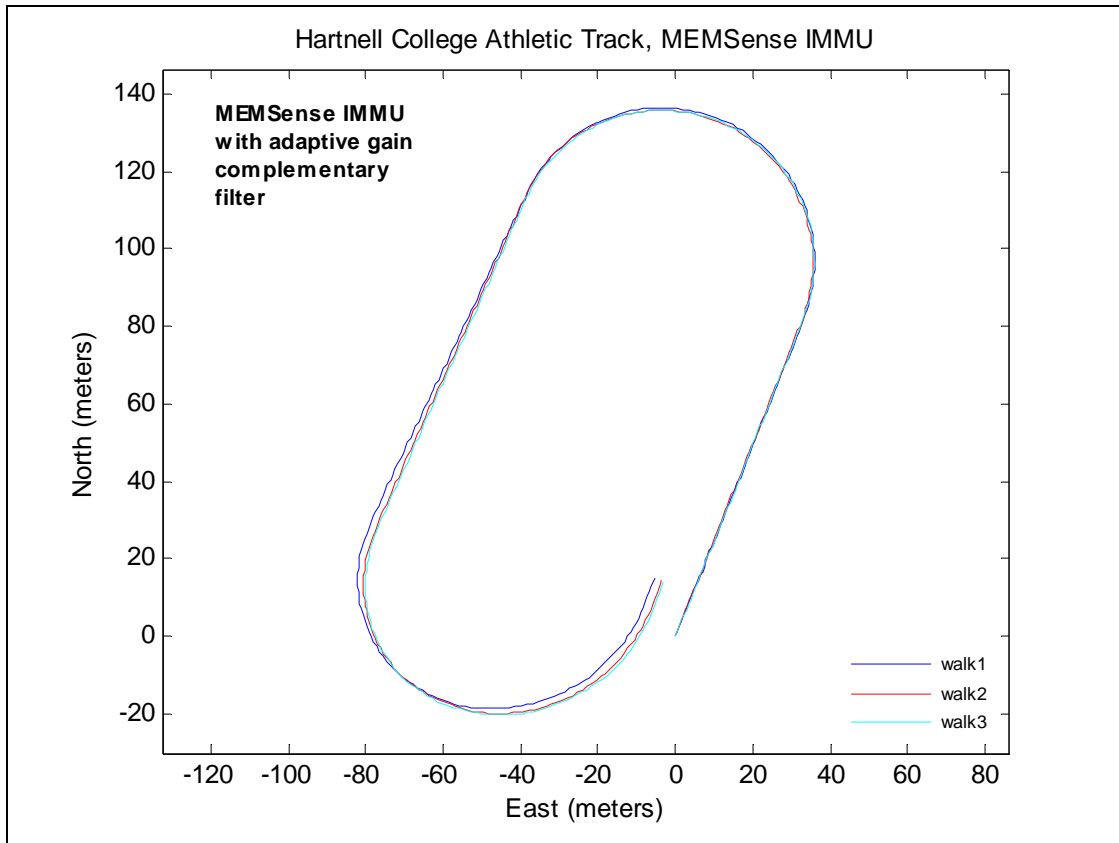
Figure 96.   PNS-computed track using MEMSense IMMU.

One final thought on the PNS performance is given. It deals with the manner in which the endpoints of the computed tracks all fall in the same region with respect to the origin. Figure 97 shows an expanded view of the previous figure. As before, the endpoints are marked with an 'x'; similar to the results when the 3DM-GX1 was used, all three endpoints are clustered in the same area relative to the start/stop point. Recalling the previous simulations using the foot motion acceleration model, this behavior is quite likely due to a degree of uncorrected sensor bias or calibration error within the IMMU. In spite of our best efforts to eliminate these errors with the zero-velocity updates, evidently, some portion still remains. Furthermore, the figure suggests that a larger component of the PNS error is derived from the sensor bias than from the random noise.
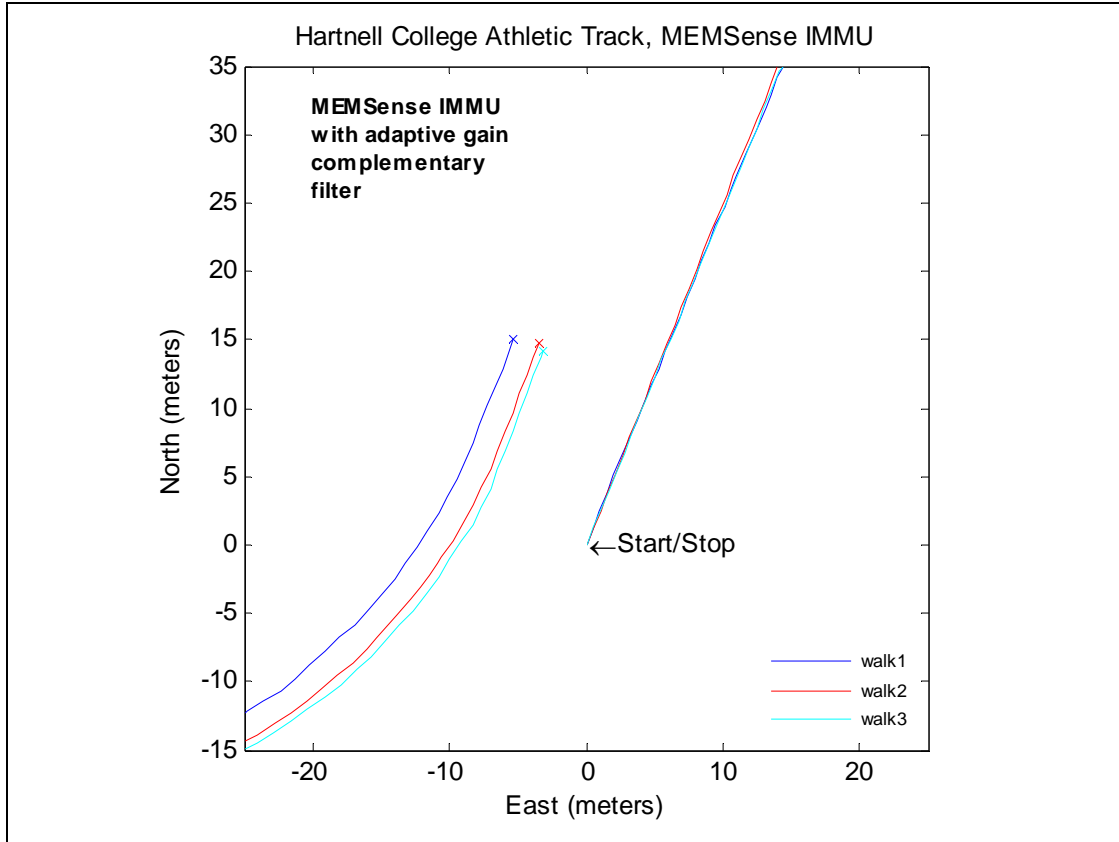
Figure 97.   Zoom of Figure 96. PNS-computed endpoints marked with an 'x'.

I.   SUMMARY

This chapter presented the PNS algorithm and explored its performance through simulations and with the aid of actual walking data. A foot motion model was developed specifically for use in these simulations. It was built upon the Gaussian exponential function. The simulation also included a carefully selected model for the sensor random error. The parameters of the random error were varied to study their impact on the overall performance of the PNS. This chapter also examined various techniques for numerical integration to use in the strapdown portion of the PNS algorithm. The Trapezoidal rule was found to be adequate for this application and the sampling rate of 50 samples-per-second was considered sufficient for normal walking motion.

A qualitative comparison of the PNS with a constant-gain complementary filter and the adaptive-gain complementary filter was also provided. It showed that the latter

approach gave superior performance and created position tracks that were more representative of the true tracks. In the adaptive-gain complementary filter, the gain was adaptively switched between two values in accordance with the particular phase of the gait cycle. An optimization was accomplished using the actual data; it indicated that using $k_d = 0$ and $k_s = 1.05$ gave the minimum position track error.

This chapter concluded by examining the endpoints of the walking trials around the athletic track. The manner in which the endpoints all tended to be grouped together in the same area suggested that there was a component of the sensor error that could not be negated by the zero-velocity updates.

V. A LOCOMOTION INTERFACE FOR THE VIRTUAL ENVIRONMENT

The major theme of this dissertation has been the development of the PNS. The complementary filter and its integration with the strapdown navigation algorithm has been the focus of the discussion to this point. It was during the course of this work that another application for the IMMU came to light. Methods for interaction with virtual environments are essential to enhance the utility of these computer-generated realities. This chapter presents a novel locomotion interface based on the IMMU that allows one to navigate through the virtual environment.

A. BACKGROUND

A virtual reality is a computer-generated environment. Its purpose is to provide either entertainment or some form of training and education. Another application that has gained interest in the medical community is for the treatment of post-traumatic stress disorder in soldiers.

In order for the user of a virtual environment of have a positive and rewarding experience, he/she must have a high sense of presence. This is the subjective measure of one's feeling that he/she really is in the virtual reality. Presence depends on the amount of immersion offered be the virtual environment. Therefore, immersion is the objective measure of the amount of sensory stimuli provided by the virtual environment.

To achieve the desired high levels of presence, researchers have worked to develop immersion devices of various types. These devices are designed to stimulate the senses and promote a more realistic experience within the virtual environment. The most common types of user interfaces are those that are found on almost any desktop having a computer. They are the computer monitor, keyboard, mouse, and speakers. However, these do little to heighten user presence. More advanced types of interfaces have been developed. To display graphics to the user, one of two methods has been used. A head mounted display can be used, which tracks the user's head motion and renders the display consistent with the head orientation (see Figure 3). Alternatively, the virtual environment

can be displayed in a large screen immediately in front of the user, or in other cases, a multi-projector (display) screen can also be utilized. In this approach, the user is presented with a scene that fills his/her peripheral vision as much as possible with two or more large projector screens/displays.

To stimulate the sense of smell while engaged within a virtual environment, the Army developed a device called the "scent collar." This device was worn around the user's neck and dispensed an odor that was relevant to the location within the virtual environment [92]. At appropriate times, the "scent collar" released a scent pertinent to the particular environment to further enhance the user's sense of presence.

In addition to the use of graphics, sound, and smell to increase the sense of user presence in a virtual environment, the control of motion is also just as important. Popular forms of user interfaces for motion control include joysticks and game controllers. However, as studied in [93] and [94], user presence is increased when his/her motions through a virtual environment are similar or identical to those required for the same movement through a real environment. For example, when the user is required to walk or walk-in-place to simulate virtual walking, this results in a greater sense of presence than if the user were required to simply move a joystick or strike one of the arrows on the keyboard to move forward. To this end, other types of motion control devices, or locomotion interfaces, for virtual environments have been developed. Many are variations of treadmill designs, assumedly because this required body motions most like those exhibited in the real world and would most likely result in a high sense of user presence. Other designs are based on step-in-place devices, where the user steps on pads located on the floor to direct his/her motion through the environment.

1. Treadmills

Several examples of locomotion interfaces have been constructed that utilize treadmills. One of the first of this type was developed for the Army by Virtual Space Devices, Inc., see Figure 98 and [95]. This device was called the Omni-Directional Treadmill, or ODT. It allowed the user to move in any direction on the treadmill surface, and through a feedback control mechanism, it maintained the user in a relatively stationary location. A tracking arm attached to the user measured the user's position and

orientation. These data were then passed into the control algorithm to move the treadmill in the appropriate direction, thus keeping the user fixed in the center of the treadmill surface. A novel aspect of this approach was that it incorporated two orthogonal treadmills—one treadmill made up of a number of smaller treadmill belts that were installed orthogonal to the main one. A variation to this approach comes from Iwata [96] in what was called the Torus Treadmill. This version of the locomotion interface used Polhemus position trackers on the user's knees, so the attachment of a tracking arm to the user was not required. This was to give the user greater freedom of movement.

Figure 98.   Omni-directional treadmill (From [98]).

Another very interesting treadmill approach was developed by [97]. Referred to as the Ground Surface Simulator (GSS), this design incorporated the results of two previous projects, the ATLAS [98] and ALF [99]. ATLAS was a treadmill design that was mounted onto a 3-DOF rotating platform. Infra-red reflectors attached to the user's feet were tracked via an infra-red CCD camera. The corresponding foot tracking data were then used to move the treadmill forward and to rotate the entire treadmill in a horizontal plane to simulate changes in the walking direction. The ALF was a floor

design that consisted of an array of movable tiles. When activated, the individual tiles could be raised or lowered to simulate a varying roughness of terrain.

Yet another use of the treadmill for the locomotion interface was created by [100]. This design, called the Sarcos Treadport, was unique in that it used a mechanical tether that was attached to the user to measure position and orientation on the treadmill. This information was used to control the speed of the treadmill as the user walked and to rotate the projected virtual environment when the torso was rotated in a particular direction. The mechanical tether also applied force feedback to the user's torso. In this manner the inertial forces one senses during acceleration and deceleration could be transmitted to the user to enhance the overall sense of presence.

2. Step-In-Place and Gesture Recognition

The use of the treadmill as part of a locomotion interface has been popular because this device allowed the user to move through the virtual environment in a very natural way. However, as was acknowledged in many of the references, in its implementation, a considerable amount of engineering design was required to control the treadmill speed and further, to determine the direction of motion. Other designs have been proposed that do not use the treadmill or a treadmill derivative. These consist of either some type of pad or platform on which the user was required to stand or march in place. The Walking-Pad, as described in [101], measured 45-cm x 45-cm and consisted of an array of 64 switches. As the user marched in place on the pad, the corresponding switches that were activated beneath each foot were used to compute a location for the center-of-gravity on the pad. The position of the center-of-gravity was then used to determine a direction of motion through the virtual environment.

The Virtual Perambulator [102] was a design that required the user to wear a pair of sandals on which a low-friction film had been installed on the sole. The user slid his/her feet across a special floor pad. Polhemus FASTRACK sensors on each foot were used to determine the length and direction of steps as the user slid their feet across the surface. A waist-high stabilizing bar that surrounded the user was utilized for the user to hold while they moved and to provide a measure of safety.

182

In the Step-in-place Turntable [103], the user stood on a 70-cm diameter motorized platform. Pressure sensors in the platform sensed when the user was stepping and propelled the user forward in the virtual environment. To determine direction, infrared markers at the back of the person's waist were monitored by an infrared camera. As the user rotated his/her torso, as if to turn, the relative position of the markers in the camera's field of view registered this rotation. This information then caused the motorized platform to rotate in the opposite direction to bring the user back into view of the large projected screen.

A novel locomotion interface, called CirculaFloor, was developed by [104]. It utilized a set of automatically positioning floor tiles. As the user began to move from the center of the floor tile upon which he stood, the underlying control system would automatically move one of the unused floor tiles into a position to receive the user as they left the first floor tile. The system used ultra-sonic sensors on the floor tiles to monitor their position in the active floor space. The user's position was monitored within the active area with a laser radar system. See Figure 99.

Figure 99.   CirculaFloor designed by Iwata (From [104]).

In [105], a pair of CyberBoots was constructed. Four force sensors were distributed in the insole of each boot. A fuzzy logic algorithm was then implemented to classify the user motion as either leaning or walking for interaction with a virtual object.

In another locomotion interface known as Gaiter, see [48], the system used pressure-sensitive foot switches, along with position and orientation tracking sensors attached at the knees, waist, and head, to move the user through the virtual environment, which was presented in the head mounted display.

B.   SYSTEM DESCRIPTION

At the Naval Postgraduate School, we have developed a locomotion interface for an existing marksmanship training system. In this training system, the user was required to stand in front of a large projector screen (approximately 8 ft x 8 ft) onto which was projected a virtual environment of a fictional urban setting. The user was equipped with a simulated M-16 rifle that shot rounds of laser pulses. Targets that were projected onto the screen were then shot at with the M-16 rifle. A camera monitoring the screen captured the location of the incident laser pulses on the screen for correlation with the actual target location. The locomotion interface, known as MOVESMover, used two IMMU devices—one on each foot. Through a series of foot gestures, the user was free to navigate in a desired direction through the virtual environment. This approach was appropriate for our marksmanship training system because it allowed the user to maintain his position and orientation immediately in front of the projector screen. Furthermore, he could change his direction of walking through the virtual environment without having to rotate any part of his head or torso and possibly take his eyes away from the simulated targets.

In the MOVESMover locomotion interface, the user stood in front of a large projection screen onto which a virtual environment had been displayed. As the user gestured with his/her feet, the projected scene within the virtual environment changed accordingly and provided the user with the perception of movement through the virtual environment. The foot gestures required of the user are shown in Table 14, along with the corresponding movement that resulted in the virtual environment.

Table 14.   MOVESMover foot gestures.

User Foot Gestures	Motion in VE
No foot motion	Not walking
Marching in place	Walking forward
Left foot step, right foot yaw	Walking turn- forward right
Right foot step, left foot yaw	Walking turn- forward left
Right foot step only	Side step right
Left foot step only	Side step left
Right foot yaw only	Turn in place, clockwise
Left foot yaw only	Turn in place, counter-clockwise

Figure 100 shows the system hardware. The user wore one IMMU on each foot, such as the Microstrain 3DM-GX1. A Sony UX180P mobile computer, which was carried by the user in a pouch or backpack, read the sensor data from each foot through a RS232-to-USB interface. The mobile computer executed the custom C++ program referred to as the MOVESMover application in which it accomplished the following tasks: 1) read the sensor data from both feet, 2) decoded the foot gestures into one of the eight motions for the Delta3D virtual environment, and 3) transmitted the commanded movement via wireless network to the Delta3D PC. The Delta3D PC rendered the virtual environment according to the movement information that it received from the mobile computer.
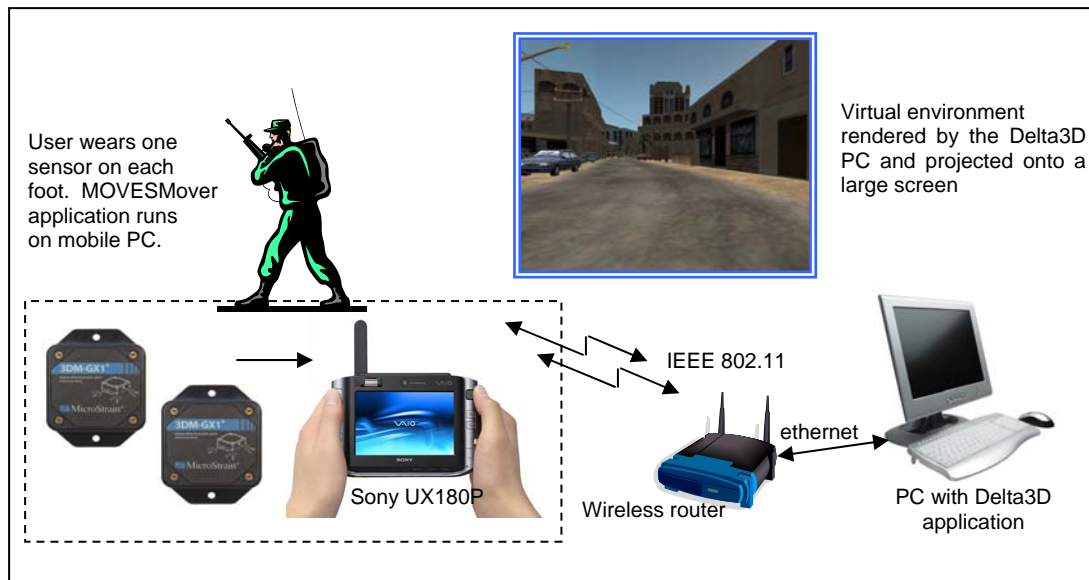
Figure 100.   System hardware used in MOVESMover.

In order to decode the foot gestures into one of the eight motions for movement through the virtual environment, a series of state machines were implemented in the MOVESMover application.   These state machines, as shown in Figure 101, worked together to produce one of the eight possible movements. As an illustration of how these state machines worked together, the Swing/Stance state machine for the left foot identified periods of foot swing and foot stance. Then the Motion/~Motion state machine for the same foot determined whether the foot was in a general state of motion over one or more cycles of the Swing/Stance state machine. An identical pair of state machines was created for the right foot. In this manner, it was possible to determine sustained periods of foot motion for each foot.

If the user gestured in a repeated twisting motion (by an outward rotation of the ankle so that the foot rotated in a plane parallel to the ground), the Yaw/~Yaw state machine was triggered. One state machine of this type was created for each foot. These state machines, along with the Motion/~Motion state machines for both feet, worked together in what was referred to as the Overall state machine to classify the foot gestures into one of eight movements through the virtual environment.
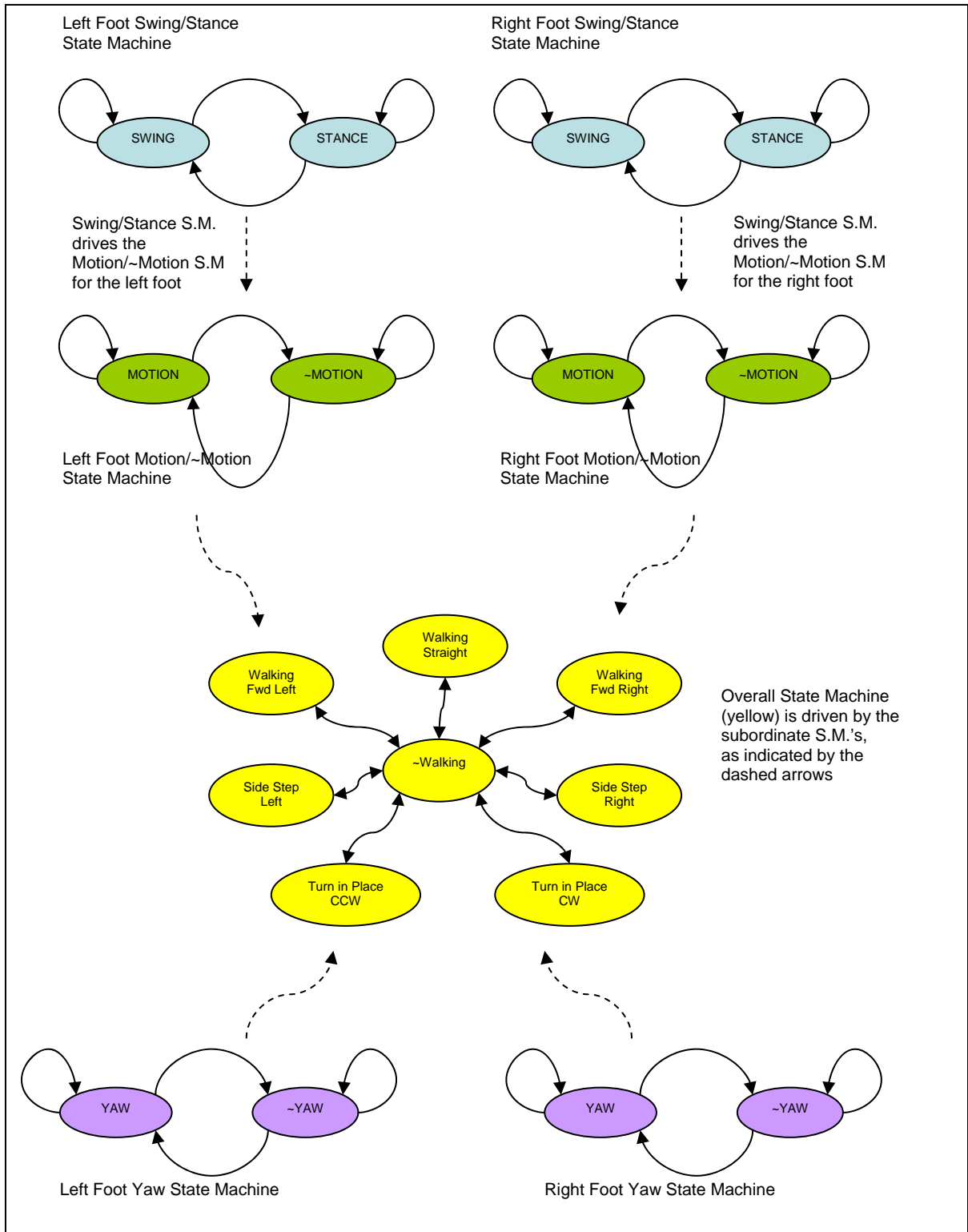
Figure 101.   State machines for the MOVESMover locomotion interface.

In Figure 102, a portion of the state machine operation in shown. It shows the angular rate data for three steps of the left foot (Figure 102a). Through experiment, it was learned that using the foot angular rate instead of acceleration produced more consistent identification of the periods of foot swing and foot stance. Figure 102b shows the cycles of the Swing/Stance state machine over the three steps. This state machine compared the angular rate with a specified threshold, which was also determined experimentally. If the angular rate exceeded the threshold for a defined period of time, the state machine switched into the Swing state. Alternatively, if the angular rate fell below the established threshold for a period of time, the state machine switched to the Stance state. Subsequently, the Motion/~Motion state machine used the status of the Swing/Stance state machine to make its determination of sustained foot motion, as observed in Figure 102c. It accomplished this by considering whether the Swing/Stance state machine was persistent in the Stance state over an interval of time. Furthermore, if the Swing/Stance state machine switched to the Swing state, the Motion/~Motion state machine immediately changed into the Motion state.

The operation of the yaw state machine is shown in Figure 103. It shows the foot yaw angle data. This parameter was derived from the sensor's computed orientation (i.e. quaternion). In Figure 103a, the user was executing a series of quick ankle twists. As shown, there existed an approximate offset of (-)2.5 radians in this sample of data. It was in essence the horizontal direction in which the foot sensor was oriented with respect to a North-East-Down coordinate system when the foot was in the Stance state. On occasion, this offset was also observed to exhibit a slow wander. It was surmised that this behavior resulted from the sensor's orientation algorithm and its difficulty to track the erratic foot motions. To alleviate this problem, a first-order high-pass filter was used on the foot yaw data. This filter was implemented as shown below with $\alpha = 0.9$.

$$y_k = \alpha \left(y_{k-1} + x_k - x_{k-1} \right) \tag{5.1}$$
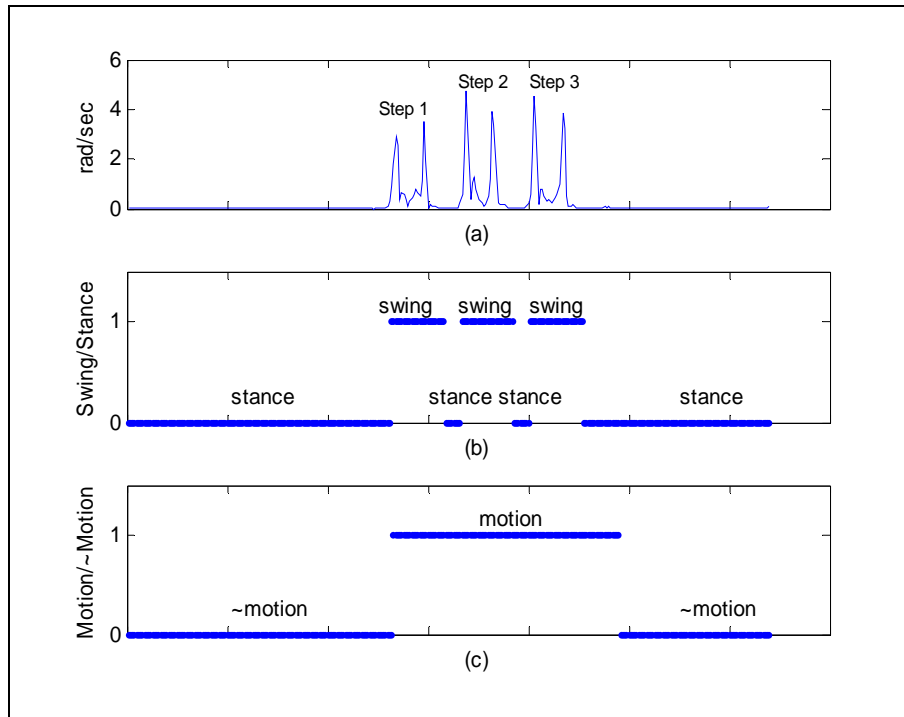
Figure 102. Three steps of the left foot and classification by the corresponding state machines.
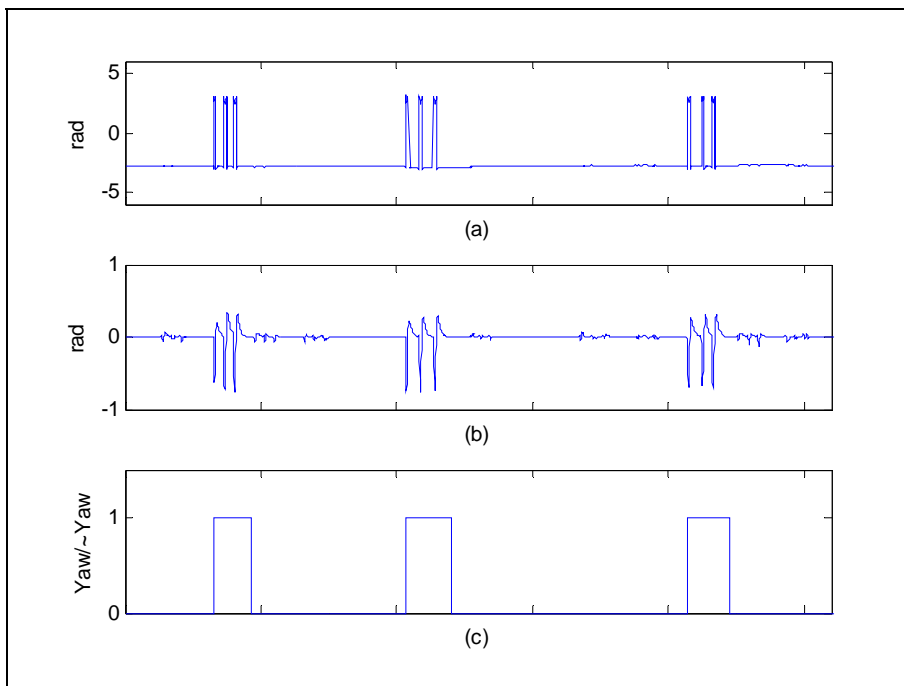
Figure 103. Filtering of the foot yaw data and classification by the Yaw/~Yaw state machine.

189

The resulting filter attenuated all frequencies below approximately 0.5 Hz (Fs = 30 Hz), and Figure 103b shows the filtered foot yaw with the offset removed. This data was then used in the Yaw/-Yaw state machine. It was compared with a threshold and the Yaw state was set accordingly, as shown in Figure 103c.

During each program cycle, the Overall state machine used the current status of the four collaborating state machines to make its determination of the movement through the virtual environment. The result was then transmitted via a network UDP packet to the Delta3D PC, which in turn rendered the virtual environment for the user. The transmitted data consisted of two short data types. The first parameter was an integer value between 0 and 7 that corresponded to one of the motions shown in Table 14. The other parameter corresponded to a speed to which the user moved through the virtual environment. This latter parameter was a fixed value, thus it was not computed from the rate of movement of the user's foot gestures. Experiment and data analysis to compute a user's speed through measurement of the rate of one's foot gestures failed to yield any good results. The sample rate of approximately 30 Hz from each sample proved insufficient to achieve accurate measurements of rates of one's foot gestures.

C.   SUMMARY

We have developed a low-cost locomotion interface for a virtual reality marksmanship trainer. The MOVESMover locomotion interface required the user to utilize foot gestures for motion control through the virtual environment. Admittedly, the ideal locomotion interface would have been one that required the user to walk as in the real world. However, since this was not possible for our application, a good engineering compromise was achieved with our approach. In addition to low-cost, the MOVESMover locomotion interface was easily implemented in that it used commercial off-the-shelf equipment and only required the development of a custom computer program to decode the sensor data appropriately. Because the foot-worn sensors were inertial/magnetic, there was no requirement for the installation of any infrastructure, other than the wireless network to transmit the data. The MOVESMover locomotion interface was demonstrated at the MOVES Institute Open House in July 2008. Preliminary trials

of the interface indicated that after approximately two or three minutes, users who tried the locomotion interface became accustomed to the required foot gestures and moved confidently through the virtual environment.

THIS PAGE INTENTIONALLY LEFT BLANK

VI. CONCLUSION AND RECOMMENDATIONS

This chapter provides final conclusions and summarizes the major contributions of this dissertation. Recommendations for future work are also given here. The main theme of this body of work concerned the Personal Navigation System (PNS), which gave the user a capability of tracking one's position in GPS-denied environments. Another component of this effort was the development of a locomotion interface for a virtual environment. Both of these elements described within this dissertation utilized the miniature inertial/magnetic measurement unit (IMMU).

A. SUMMARY OF CONTRIBUTIONS

The primary accomplishment of this dissertation was the design and development of the Personal Navigation System (PNS) to track one's position during normal walking. In this implementation, a miniature inertial/magnetic measurement unit (IMMU) was utilized. These devices were based on MEMS technology and were small, lightweight, low-cost, and low-power. However, they suffered from an added amount of sensor error that was greater than that found in navigation-grade inertial measurement units designed for military and commercial applications. Consequently, straightforward use of the miniature IMMU with the well-known strapdown navigation algorithm in a personal navigation application would lead to rapidly increasing position error. For this reason, a new navigation algorithm was designed and tested to mitigate the degraded performance of the miniature IMMU.

The new PNS algorithm was adapted from the strapdown navigation algorithm and integrated three additional component algorithms. One of these components was an error-correction technique known as zero-velocity updates, which was used to negate the accumulation of error in the computed velocity that had resulted from the integration of the error in the foot-mounted sensor. Another critical component was the quaternion-based complementary filter. Designed specifically for the PNS, it employed an adaptive gain-switching strategy and provided the dynamic foot attitude estimate required for the strapdown navigation algorithm. Lastly, the gait-phase detection algorithm was also

incorporated. It identified the instances of the foot stance and swing, which were required for operation of the complementary filter and the zero-velocity updates.

A significant contribution in support of the PNS development was a measured improvement in the dynamic performance of the Factored Quaternion Algorithm (FQA) through its integration in the quaternion-based complementary filter resulting in an algorithm that facilitated the completion of the PNS. The composite algorithm gave an intuitive and straightforward method for attitude estimation suitable for applications beyond those of the PNS application. Testing of the attitude filter was accomplished by simulation and through the use of an instrumented pendulum built in the laboratory.

The quaternion-based complementary filter incorporated a novel gain-switching scheme that leveraged the natural features of normal biped walking. This approach was shown to give improved performance in the PNS over a filter utilizing a constant gain. Additionally, in support of this contribution a gain optimization was performed using experimental data to identify the best values for the filter static gain, k_s, and the dynamic gain, k_d, that resulted in the minimum position error.

The gait-phase detection algorithm identified instances of foot stance and swing with a demonstrated high degree of accuracy. Furthermore, it signaled the appropriate times to employ the zero-velocity updates and also indicated when the gain should be switched within the complementary filter.

This work also described the development of a foot motion model. Based on the Gaussian exponential function, it provided a means for simulation of the PNS and gave insight into the performance of the navigation algorithm. The model also included a component of sensor error, which was validated through experimental measurement and analysis.

An investigation of the numerical methods suitable for the PNS algorithm was also accomplished. Through simulation and experiment, the Trapezoidal rule was shown to give satisfactory results for the strapdown portion of the PNS application, and Euler's method was appropriate for the complementary filter. Furthermore, this work also highlighted the fact that data sampling rates on the order of 50 samples-per-second were adequate for a PNS utilized in normal walking conditions.

194

As an incidental by-product of this effort, a novel utilization for the IMMU was also developed—a locomotion interface for a virtual environment. As in the PNS application, it used the shoe-worn IMMU. In this application, however, two IMMUs were required, one to be worn on each foot. A set of foot gestures were conceived and a custom software program was developed to decode the user's foot motions. This unique interface, referred to here as MOVESMover, gave the user freedom to navigate through virtual environments utilizing large projection displays in which the user was required to remain in front of the screen. Specifically, the locomotion interface was designed for a military marksmanship training system that projected virtual targets onto a large projection display located immediately in front of the trainee.

B. RECOMMENDATIONS FOR FUTURE WORK

It is noted that the PNS was not without its limitations. Firstly, the PNS was only demonstrated for normal biped walking. Locomotion by other means (i.e. limping, skipping, hopping) was not considered in this dissertation, but are topics for further study and development. Performance of the PNS was initially examined for the case of running motion. It was found that the data sample rate was insufficient to identify the necessary features of this type of locomotion and was not considered beyond this point. IMMUs providing higher sampling rates may be worthwhile avenues for investigation, as well as, tailoring the gait-phase detection algorithm with additional features to recognize the onset of running and other forms of biped locomotion.

Another operational limitation of the PNS deals with the walking surface. Only flat, level walking surfaces were examined, such as, concrete or other types of manufactured flooring (tile, rubberized asphalt). Walking on softer surfaces, grass for example, made it difficult for the gait-phase detection algorithm to determine the principal features of natural walking motion and prevented the other components of the PNS from operating properly. Further investigation and study is required here to build up this capability within the gait-phase detection algorithm.

PNS performance in terms of heading accuracy is mainly determined by the magnetometer. This sensor, however, is known to be susceptible to magnetic disturbances arising from hard-iron or soft-iron interference. A thorough examination of

this performance limitation was not accomplished, but is recommended for future work. It is suggested that further testing be accomplished in a space where the local magnetic field can be controlled or quantified so that this type of interference on the PNS performance can be assessed in greater detail. Furthermore, possible solutions to address this limitation could come in the form of an additional sensor, such as, a high-end angular rate sensor (fiber-optic gyro) to measure heading rates-of-change. Yet another approach could involve an examination of the sudden change in the magnetic field due to some interference and correlate this to angular rate measurements. It is surmised here that a true heading change would be sensed by the magnetometers, as well as, some component of the angular rate sensors. On the other hand, if the magnetometers exhibit some change in their output due to some anomalous interference, the angular rate sensors being insensitive to the interference would not give any representation of this and could serve as an indication of the degraded magnetometer performance. Additional features could be integrated into the PNS algorithm rooted in these ideas and lead to a more robust navigation system in regions prone to magnetic interference.

While not a limitation of the PNS algorithm, another source of potential improvement in the overall system deals with the accuracy of the IMMU. Recalling the figures showing the computed paths around the athletic tracks, they exhibited the behavior that the endpoints tended to cluster in the same region with regard to the origin. Furthermore, it was indicated that this pattern was due to the sensor bias, and in spite of our best efforts to eliminate these errors with the zero-velocity updates, there was still some part of the bias error that could not be removed. It is put forward that this remaining error may be addressed through a rigorous calibration of the IMMU sensors. A study of accepted calibration procedures is necessary and an understanding of the complex relationship between sensor calibration accuracy and other factors including temperature and materials aging, among others is warranted.

Many navigation systems incorporate the Kalman filter to improve the overall accuracy of the computed position. All of these solutions require the use of an additional navigational aid, such as GPS, to provide measurements of some or all of the components of the Kalman filter state vector. Since a main motivation of this work was for

196

navigation in GPS-denied environments, the integration of the Kalman filter was not pursued here. Alternatively, it has been suggested that the zero-velocity updates could be used in some form to serve as the required navigational aid for the Kalman filter algorithm. While this idea was not pursued in any detail in this work, it is nonetheless a very interesting and worthwhile area for further investigation.

The preceding discussion and recommendations were not meant to be comprehensive. Admittedly, there remains a great deal of additional capabilities required before a PNS suitable for military application would be available.

THIS PAGE INTENTIONALLY LEFT BLANK

LIST OF REFERENCES

[1]   "Navigation," *Encyclopedia Britannica*, 15th ed. vol. 24, pp. 756–766.

[2]   N. Grice, "Sailing the polynesian sky," *Odyssey*, April 2004, vol. 13, iss. 4, p. 43.

[3]   E. Amcoff, "Mobile phones are packing more GPS features," *The Wall Street Journal*, March 23, 2006, p. D2.

[4]   M. Lehtinen, A. Happonen, and J. Ikonen, "Accuracy and time to fix using consumer-grade GPS receivers," *Software, Telecommunications and Computer Networks, 2008. SoftCOM 2008, 16th International Conference*, September 25–27, 2008, pp. 334–340.

[5]   M. S. Braasch and A. J. van Dierendonck, "GPS receiver architectures and measurements," *Proceedings of the IEEE*, vol. 87, iss. 1, January 1999, pp. 48–64.

[6]   A. B. Chatfield, *Fundamentals of High Accuracy Inertial Navigation*, Volume 174 Progress in Astronautics and Aeronautics, American Institute of Aeronautics and Astronautics, Inc., 1997, pp. xiii.

[7]   R. G. Brown, *Introduction to Random Signal Analysis and Kalman Filtering*. New York: John Wiley & Sons, 1983.

[8]   M. Kayton, "Navigation Systems," in *The Electrical Engineering Handbook*, R. C. Dorf, Ed. CRC Press, 1993.

[9]   G. R. Pitman Jr., *Inertial Guidance*. New York: John Wiley & Sons, 1962.

[10]   D. Titterton and J. Weston, *Strapdown Inertial Navigation Technology, 2nd ed.*, The Institution of Electrical Engineers, Michael Faraday House, United Kingdom, and The American Institute of Aeronautics and Astronautics, USA, 2004.

[11]   N. Maluf, *An Introduction to Microelectromechanical Systems Engineering*. Massachusetts: Artech House, 2000.

[12]   H. Weinberg, H., "MEMS sensors are driving the automotive industry," *Sensors Magazine*, February 1, 2002.

[13]   D. Breed et al., "Method and System for Controlling a Vehicle," U.S. Patent No. 7,085,637, August 1, 2006.

[14]   R. A. Wood, "High-performance infrared thermal imaging with monolithic silicon focal planes operating at room temperature," *Electron Devices Meeting, 1993. Technical Digest., International*, December 5–8, 1993, pp. 175–177.

[15]   R. P. Lyle and D. Walters, "Commercialization of silicon-based gas sensors," *Solid State Sensors and Actuators, 1997. Transducers '97 Chicago, 1997 International Conference*, vol. 2, June 16–19, 1997, pp. 975–978.

[16]   Knowles Acoustics, "SiSonic surface mount microphones," July 2003, [Online]. Available: http://www.knowlesacoustics.com/images/pdf/white/Surfacemount.pdf [Accessed: December 1, 2006].

[17]   L. J. Hornbeck, "Frame Addressed Spatial Light Modulator," U.S. Patent No. 4,615,595, October 7, 1986.

[18]   Texas Instruments, "Digital light processing technology," [Online]. Available: http://www.dlp.com/ [Accessed: May 3, 2010].

[19]   E. Bassous, "Nozzles Formed in Monocrystalline Silicon," U.S. Patent 3,921,916, November 25, 1975.

[20]   E. Bassous et al., "Jet Nozzle Structure for Electrohydrodynamic Droplet Formation and Ink Jet Printing System Therewith," U.S. Patent No. 3,949,410, April 6, 1976.

[21]   C. Chiou et al., "Ink Jet Nozzle Structure," U.S. Patent No. 3,958,255, May 18, 1976.

[22]   W. A. Wan and M. Lim, M., "Fiber optic Switch Using MEMS," U.S. Patent No. 6,477,290, November 5, 2002.

[23]   Yammamoto et al., "Optical Switch Using Tilt Mirrors," U.S. Patent No. 6,044,705, August 6, 2002.

[24]   Dautartas et al., "Self-aligning 1xN Rotary Optical Switch," U.S. Patent No. 6,320,997, November 20, 2001.

[25]   Rosa et al., "Method for an Optical Switch on a Silicon on Insulator Substrate," U.S. Patent No. 6,632,374, October 14, 2003.

[26]   S. Lucyszyn, "Review of radio frequency microelectromechanical systems technology," *Science, Measurement and Technology, IEE Proceedings,* vol. 151, iss. 2, 2004, pp. 93–103.

[27]   S. D. Senturia, *Microsystem Design*. Kluwer Academic Publishers, 2000.

[28]   D. Tuite, "Motion-Sensing MEMS gyros and accelerometers are everywhere," *Electronic Design*, vol. 57, no. 14, July 9, 2009.

[29]   J. L. Marins, X. Yun, E. R. Bachmann, R. B. McGhee, and M. J. Zyda, "An extended Kalman filter for quaternion-based orientation estimation using MARG sensors," *Intelligent Robots and Systems, 2001. Proceedings, 2001 IEEE/RSJ International Conference*, October 29–November 3, 2001, vol. 4, pp. 2003–2011.

[30]   Analog Devices, Inc., "ADXL325: small, low-power, 3-axis +/-5g accelerometer," [Online]. Available: http://www.analog.com/en/sensors/inertial-sensors/adxl325/products/product.html [Accessed: May 3, 2010].

[31]   Analog Devices, Inc., "ADXRS610: +/-300 deg/sec angular rate sensor," [Online]. Available: http://www.analog.com/en/sensors/inertial-sensors/adxrs610/products/product.html [Accessed: May 3, 2010].

[32]   Northrop-Grumman, "LN-200 inertial measurement unit," [Online]. Available: http://www.es.northropgrumman.com/solutions/ln200/ [Accessed: May 3, 2010].

[33]   W. Stockwell, "Angle random walk," [Online]. Available: http://www.xbow.com/Support/Support_pdf_files/AngleRandomWalkAppNote.pdf [Accessed: May 3, 2010].

[34]   E. Ogg, "GPS finding its way to the mainstream," November 15, 2006. [Online]. Available: http://news.cnet.com/GPS-finding-its-way-to-the-mainstream/2100-1041_3-6135918.html [Accessed: May 3, 2010].

[35]   Q. Ladetto and B. Merminod, "In step with INS," *GPS World*, October 2002, pp. 30–38.

[36]   "VisuAide unveils Trekker 2.0," *Satellite Today*. Potomac, March 18, 2004, vol. 3, iss. 52, p. 4.

[37]   "Medical Devices: SWAN system provides wearable audio navigation technology for visually impaired," *Medical Devices and Surgical Technology Week*, Atlanta, September 10, 2006, p. 304.

[38]   Honda, "ASIMO, the Honda humanoid robot," [Online]. Available: http://world.honda.com/ASIMO/ [Accessed: May 3, 2010].

[39]   E. R. Bachmann, "Inertial and magnetic tracking of limb segment orientation for inserting humans into synthetic environments," PhD dissertation, Naval Postgraduate School, Monterey, California, December 2000.

[40]   X. Yun, C. Aparacio, E. R. Bachmann, and R. B. McGhee, "Implementation and experimental results of a quaternion-based Kalman filter for human body motion tracking," *Robotics and Automation, 2005. ICRA 2005. Proceedings of the 2005 IEEE International Conference,* April 18–22, 2005, pp. 317–322.

[41]   X. Yun, E. R. Bachmann, A. Kavousanos-Kavousanakis, F. Yildiz, and R. B. McGhee, "Design and implementation of the MARG human body motion tracking system," *Intelligent Robots and Systems, 2004. (IROS 2004). Proceedings. 2004 IEEE/RSJ international Conference*, vol. 1, September 28–October 2, 2004, pp. 625–630.

[42]   E. R. Bachmann, X. Yun, D. McKinney, R. B. McGhee, and M. J. Zyda, "Design and implementation of MARG sensors for 3-DOF orientation measurement of rigid bodies," *Robotics and Automation, 2003. Proceedings. ICRA '03. IEEE International Conference,* vol. 1, September 14–19, 2003, pp. 1171–1178.

[43]   I. Pantazis, "Tracking human walking using MARG sensors," M.S. thesis, Naval Postgraduate School, Monterey, California, June 2005.

[44]   M. Zyda, "From visual Simulation to virtual reality to games," *Computer*, vol. 38, no. 9, September 2005, pp. 25–32.

[45]   S. Sanborn, "3-D simulation: coming soon to a net near you," *InfoWorld*, vol. 23, no. 6, February 2001, p. 32.

[46]   P. Tucker, "Virtual health," *The Futurist*, vol. 42, no. 5, 2008, pp. 60–61.

[47]   "Living a second life online," *Newsweek*, vol. 152, no. 4, July 28, 2008.

[48]   J. N. Templeman, P. S. Denbrook, and L. E. Sibert, "Virtual locomotion: walking in place through virtual environments," *Presence*, vol. 8, no. 6, December 1999, pp. 598–617.

[49]   A. Sternstein, "Astronauts to board virtual reality video game," *Federal Computer Week*, vol. 20, no. 31, pp. 58–59.

[50]   D. Knott, "Tangible benefits of virtual reality," *Oil and Gas Journal*, vol. 94, no. 13, p. 30.

[51]   B. Stackpole, "Military broadens use of virtual reality," *Design News*, January 7, 2008.

[52]   J. A. Vargas, "Virtual reality prepares soldiers for real war," *Washington Post*, February 14, 2006, p. A01.

[53]   "Australian army receives state-of-the-art tank simulation systems," *Defense Daily International*, vol. 7, no. 33, August 2006, p. 1.

[54]   "Lockheed Martin: Lockheed Martin receives $23.4 million contract modification to update formal training unit for C-130 aircrews," *Computers, Networks, & Communications*, vol. 321, July 2008.

[55]   G. M. Reger and G. A. Grahm, "Virtual reality exposure therapy for active duty soldiers," *Journal of Clinical Psychology*, Brandon, August 2008, vol. 64, iss. 8, p. 940.

[56]   S. Halpern, "Virtual Iraq: annals of psychology," *The New Yorker*, vol. 84, no. 14, May 2008.

[57]   D. A. Bowman and R. P. McMahn, "Virtual reality: how much immersion is enough?" *Computer*, vol. 40, iss. 7, July 2007, pp. 36–43.

[58]   J. A. DeLisa, "Gait analysis in the science of rehabilitation, monograph 002," Department of Veterans Affairs–Veterans Health Administration, 1998.

[59]   G. A. L. Meijer, K. R. Westerterp, F. M. H. Verhoeven, H. B. M. Koper, and F. ten Hoor, "Methods to assess physical activity with special reference to motion sensors and accelerometers," *IEEE Transactions on Biomedical Engineering*, vol. 38, no. 3, March 1991, pp. 221–229.

[60]   N. F. Troje, "Decomposing biological motion: a framework for analysis and synthesis of human gait patterns," *Journal of Vision* (2002) vol. 2, pp. 371–387.

[61]   I. P. I. Pappas, M. R. Popovic, T. Keller, V. Dietz, and M. Morari, "A reliable gait phase detection system," *IEEE Transactions on Neural Systems and Rehabilitation Engineering*, vol. 9, no. 2, June 2001, pp.113–125.

[62]   S. W. Lee and K. Mase, "Recognition of walking behaviors for pedestrian navigation," *Control Applications, 2001 (CCA '01). Proceedings of the 2001 IEEE Int'l Conference,* September 5–7, 2001, pp. 1152 –1155.

[63]   S. W. Lee, K. Mase, and K. Kogure, "Detection of spatio-temporal gait parameters by using wearable motion sensors," *Proceedings of the 2005 IEEE Engineering in Medicine and Biology 27th Annual Conference*, Shanghai, China, September 1–4, 2005, pp. 6836–6839.

[64]   S. W. Lee and K. Mase, "Activity and location recognition using wearable sensors," *Pervasive Computing, IEEE,* vol. 1, iss. 3, July–September 2002, pp. 24–32.

[65]   K. Sagawa, H. Inooka, and Y. Satoh, "Non-restricted measurement of walking distance," *Systems, Man, and Cybernetics, 2000 IEEE Conference,* vol. 3, October 8–11, 2000, pp. 1847–1852.

[66]   A. M. Sabatini, C. Martelloni, S. Scapellato, and F. Cavallo, "Assessment of walking features from foot inertial sensing," *IEEE Transactions on Biomedical Engineering*, vol. 52, no. 3, March 2005, pp. 486–494.

[67]   F. Cavallo, A. M. Sabatini, and V. Genovese, "A step toward GPS/INS personal navigation systems: real-time assessment of gait by foot inertial sensing," *Intelligent Robots and Systems, 2005 (IROS 2005), 2005 IEEE/RSJ International Conference,* pp. 1187–1191.

[68]   C. Randell, C. Djiallis, and H. Muller, "Personal position measurement using dead reckoning," *Wearable Computers, 2003. Proceedings, Seventh IEEE International Symposium,* October 18–21, 2005, pp. 166–172.

[69]   H. Moore, "Networked humanoid avatar driven by MARG sensors," M.S. thesis, Naval Postgraduate School, Monterey, California, September 2006.

[70]   J. Shaver, "PC104 control environment development and use for testing the dynamic accuracy of the Microstrain 3DM-GX1 sensor," M.S. thesis, Naval Postgraduate School, Monterey, California, June 2007.

[71]   L. Lee, and V. N. Krovi, "Musculoskeletal simulation-based parametric study of optimal gait frequency in biped locomotion," *Proceedings of the 2nd Biennial IEEE/RAS-EMBS International Conference on Biomedical Robotics and Biomechatronics*, Scottsdale, Arizona, USA, October 19–22, 2008, pp. 345–359.

[72]   M. Pandy, "Simple and complex models for studying muscle function in walking," *Philosophical Transactions of the Royal Society Biological Sciences*, 2003, vol. 358, pp. 1501–1509.

[73]   A. D. Kuo, "A simple model of bipedal walking predicts the preferred speed—step length relationship," *Journal of Biomechanical Engineering*, June 2001, vol. 123, pp. 264–269.

[74]   R. McKern and H. Musoff, "Strapdown attitude algorithms from a geometric viewpoint," *Journal of Guidance, Control, and Dynamics*, 1981, vol. 4, no. 5, pp. 657–661.

[75]   S. C. Garg, L. D. Morrow, and R. Mamen, "Strapdown navigation technology: a literature survey," *Journal of Guidance, Control, and Dynamics*, 1978, vol. 1, no. 3, pp. 161–172.

[76]   J. R. Wertz, *Spacecraft Attitude Determination and Control*. Holland: D. Reidel Publishing Company, 1978.

[77]   M. D. Shuster and S. D. Oh, "Three-axis attitude determination from vector observations," *Journal of Guidance and Control*, vol. 4, no. 1, January–February 1981, pp. 70–77.

[78]   J. E. Keat, "Analysis of least-squares attitude determination routine DOAOP," Computer Sciences Corp., Report CSC/TM-77/6034, National Aeronautics Space Administration, Goddard Space Flight Center, February 1977.

[79]   X. Yun, E. R. Bachmann, and R. B. McGhee, "A simplified quaternion-based algorithm for orientation estimation from earth gravity and magnetic field measurements," *IEEE Transactions on Instrumentation and Measurement*, vol. 57, no. 3, March 2008, pp. 638–650.

[80]   J. B. Kuipers, *Quaternions and Rotation Sequences*. New Jersey: Princeton University Press, 1999.

[81]   Microstrain, Inc., "3DM-GX1 hard iron calibration, ver. 3.1.00," September 19, 2005. [Online], Available: http://www.microstrain.com/pdf/3DM-GX1%20Hard%20Iron%20Calibration.pdf [Accessed: May 3, 2010].

[82]   S. C. Chapra and R. P. Canale, *Numerical Methods for Engineers*, *2nd ed.*, McGraw-Hill Publishing Co., New York, 1985, pp. 476–505.

[83]   C. F. Gerald and P. O. Wheatley, *Applied Numerical Analysis, 6th ed.* Massachusetts: Addison-Wesley, 1999.

[84]   F. Mohd-Yasin, D. J. Nagel, C. E. Korman, "Noise in MEMS", *Measurement Science and Technology*, vol. 21, iss. 1, Article Number 012001, January 2010.

[85] H. J. Reich, J. G. Skalnik, and H. L. Krauss, *Theory and Applications of Active Devices*. D. Van Nostrand Company, 1966.

[86] S. M. Sze, *Physics of Semiconductor Devices*. New York: John Wiley & Sons, 1969.

[87] T. B. Gabrielson, "Mechanical-thermal noise in micromachined acoustic and vibration sensors,*" IEEE Transactions on Electron Devices*, vol. 40, no. 5, May 1993, pp. 903–909.

[88] R. P. Leland, "Mechanical-thermal noise in MEMS gyroscopes," *IEEE Sensors Journal*, vol. 5, no. 3, June 2005, pp. 493–500.

[89] A. V. Oppenheim and R. S. Schafer, *Discrete-Time Signal Processing*. New Jersey: Prentice Hall, 1989.

[90] Honeywell, "HMC1043 3-Axis Magnetic Sensor," [Online]. Available: http://www.ssec.honeywell.com/magnetic/datasheets/hmc1043.pdf [Accessed: March 8, 2010].

[91] S. P. Lipshitz, R. A. Wannamaker, and J. Vanderkooy, "Quantization and dither: a theoretical survey," *J. Audio Eng. Soc.,* vol. 40, no. May 5, 1992, pp. 355–375.

[92] R. Tortell, D. P. Luigi, A. Dozios, S. Bouchard, J. F. Morie, and D. Illan, "The effects of scent and game play experience on memory of a virtual environment," *Virtual Reality*, vol. 11, iss. 1, March 2007, pp. 61–68.

[93] M. Slater, M. Usoh, and A. Steed, "Taking steps: the influence of a walking technique on presence in virtual reality," *ACM Transactions on Computer-Human Interaction*, vol. 2, no. 3, September 1995, pp. 201–219.

[94] M. Usoh, K. Arthur, M. C. Whitton, R. Bastos, et al., "Walking > walking-in-place > flying, in virtual environments," in *Proceedings of the 26th Annual Conference on Computer Graphics and Interactive Techniques*, 1999, pp. 359–364.

[95] R. P. Darken, W. R. Cockayne, and D. Carmien, "The omni-directional treadmill: a locomotion device for virtual worlds," in *Proceedings of the 10th Annual ACM Symposium on User Interface Software and Technology*, Banff, Alberta Canada, October 14–17, 1997, UIST '97. ACM, New York, NY, pp. 213–221.

[96] H. Iwata, "The torus treadmill: realizing locomotion in VEs," *IEEE Computer Graphics and Applications*, vol. 19, iss. 6, November–December, 1999, pp. 30–35.

[97]   H. Noma, T. Sugihara, and T. Miyasato, "Development of ground surface simulator for Tel-E-Merge system," *IEEE Virtual Reality Proceedings*, March 18–22, 2000, pp. 217–224.

[98]   H. Noma and T. Miyasato, "Design for locomotion interface in a large scale virtual environment, ATLAS: ATR locomotion interface for active self motion," *Proceedings of the ASME Dynamic Systems and Control Division*, Anaheim, CA, USA, November 15–20, 1998, pp. 111–118.

[99]   T. Sugihara and T. Miyasato, "The terrain surface simulator ALF (Alive! Floor)," *Proc. of VRSJ ICAT'98*, 1998, pp. 170–174.

[100]   J. Hollerbach, D. Grow, and C. Parker, "Developments in locomotion interfaces," *Rehabilitation Robotics, 2005, ICORR 9th International Conference*, June 28–July 1, 2005, pp. 522–525.

[101]   L. Bouguila, F. Evequoz, M. Courant, and B. Hirsbrunner, "Walking-pad: a step-in-place locomotion interface for virtual environments," *Proceedings of the 6th International Conference on Multimodal Interfaces*, ICMI 2004, October 13 –15, 2004, pp. 77–81.

[102]   H. Iwata and T. Fuji, "Virtual perambulator: a novel interface device for locomotion in virtual environment," *Virtual Reality Annual International Symposium, 1996, Proceedings of the IEEE 1996*, March 30–April 3, 1996, pp. 60–65.

[103]   L. Bouguila, M. Ishii, and M. Sato, "Realizing a new step-in-place locomotion interface for virtual environment with large display system," *ACM International Conference Proceedings Series: Vol. 23, Proceedings of the Workshop on Virtual Environments 2002*, pp. 197–207.

[104]   H. Iwata, H. Yano, H. Fukushima, and H. Noma, "CirculaFloor [locomotion interface]," *IEEE Computer Graphics and Applications*, vol. 25, iss. 1, January–February 2005, pp. 64–67.

[105]   I. Choi and C. Ricci, "Foot-mounted gesture detection and its application in virtual environments," *Systems, Man, and Cybernetica, 1997, 'Computational Cybernetics and Simulation.' 1997 IEEE International Conference*, vol. 5, October 12–15, 1997, pp. 4248–4253.

THIS PAGE INTENTIONALLY LEFT BLANK

INITIAL DISTRIBUTION LIST

1.   Defense Technical Information Center
        Fort Belvoir, Virginia

2.   Dudley Knox Library
        Naval Postgraduate School
        Monterey, California

3.   Chairman, Code ECE
        Naval Postgraduate School
        Monterey, California

4.   Professor Xiaoping Yun
        Naval Postgraduate School
        Monterey, California

5.   Professor Murali Tummala
        Naval Postgraduate School
        Monterey, California

6.   Professor David C. Jenn
        Naval Postgraduate School
        Monterey, California

7.   Professor Carlos F. Borges
        Naval Postgraduate School
        Monterey, California

8.   Professor Emeritus Harold Titus
        Naval Postgraduate School
        Monterey, California

9.   James Calusdian
        Naval Postgraduate School
        Monterey, California